

**Photoactivated Hydrosilylation of Alkenes using
Platinum(II) Salicylaldimine Phenylpyridine
Complexes**

Helena Lancaster

PhD

University of York

Chemistry

March 2024

Abstract

Photoactivated catalysts for the hydrosilylation of silanes and alkenes offer spatial and temporal control in manufacturing processes that require silicone curing. This thesis presents the development of a series of Pt(II) (salicylaldimine)(phenylpyridine) [Pt(sal)(ppy)] complexes as photoactivated hydrosilylation catalysts.

Chapter two outlines the rationale behind the design and synthesis of the [Pt(sal)(ppy)] complexes **1a–1g** as latent precatalysts for photoactivated hydrosilylation. The key spectroscopic and structural features are presented to link the molecular structure to the catalytic performance.

Chapter three presents the development of a model hydrosilylation reaction that serves as a platform for probing reaction kinetics and mechanistic details using in situ ^1H NMR spectroscopy. The utilisation of complexes **1a–1g** as precatalysts in the model reaction under both thermal and photoactivated conditions is explored, and the structure of the phenylpyridine and salicylaldimine ligands is correlated with the catalytic activity. Many of these precatalysts were found to show excellent thermal latency and rapid (10 s) activation upon exposure to UV-light. Through a systematic examination of different alkene substrates, this chapter also elucidates the impact of substrate structure on the catalytic activity and selectivity when using precatalyst **1b**. This chapter concludes by showcasing the ability of several precatalysts to cure the industrially used siloxane polymer substrates, highlighting their practical application.

In chapter four, the mechanistic intricacies of photoactivated hydrosilylation reactions using precatalysts **1a** and **1b** are investigated. Through a combination of poisoning experiments, kinetic studies, isotope labelling experiments and kinetic modelling, a mechanism is proposed based on an active homogeneous catalyst where reductive elimination is the turnover limiting step.

Chapter five outlines the key conclusions and potential directions for further exploration, and chapter six contains all experimental information.

List of Contents

Abstract	2
List of Contents	3
List of Tables	10
List of Figures	12
List of Schemes	29
Acknowledgements	32
Author's Declaration	34
Chapter 1 – Introduction.....	35
1.1 Preamble.....	35
1.2 The hydrosilylation reaction	35
1.2.1 The Chalk-Harrod mechanism for hydrosilylation	43
1.2.2 The modified Chalk-Harrod mechanism for hydrosilylation.....	49
1.2.3 The Seitz–Wrighton mechanism for hydrosilylation	50
1.2.4 The Two-Silicon mechanism for hydrosilylation.....	52
1.2.5 Hydrosilylation reactions involving colloidal platinum.....	54
1.3 Silane activation.....	57
1.3.1 Comparison between C–H and Si–H activation.....	57
1.3.2 Bonding in metal silyl hydride and η^2 –silane complexes.....	58
1.3.3 Si–H activation by metal nanoparticles	59
1.4 Photoactivated catalysts for hydrosilylation.....	62
1.4.1 Oxalate complexes.....	63

1.4.2	Platinum bis(β -diketonates).....	65
1.4.3	Trimethyl(β -dicarbonyl) platinum(IV) complexes	68
1.4.4	Cyclopentadienyl-platinum complexes	70
1.5	Summary and outlook.....	73
Chapter 2 – Synthesis, Structure and Characterisation of Pt(II) Complexes for Hydrosilylation		
.....		75
2.1	Preamble	75
2.2	Platinum-based catalysts for hydrosilylation	77
2.3	Light-initiated catalysts for hydrosilylation	80
2.4	Preparation and characterisation of Pt(ppy)(dmsO)Cl complexes	89
2.4.1	NMR characterisation of Pt(ppy)(dmsO)Cl complexes	91
2.4.2	UV-vis spectroscopic data of Pt(ppy)(dmsO)Cl complexes	93
2.5	Preparation and characterisation of Schiff base ligands	95
2.5.1	NMR characterisation of Schiff base ligands.....	96
2.5.2	UV-vis spectroscopic data of Schiff base ligands.....	98
2.6	Preparation and Characterisation of Pt(sal)(ppy) complexes.....	99
2.6.1	NMR characterisation of Pt(sal)(ppy) complexes.....	101
2.6.2	UV-vis spectroscopic data of Pt(sal)(ppy) complexes	104
2.6.3	Crystal structures of Pt(sal)(ppy) complexes	107
2.7	Summary and Conclusions	110
Chapter 3 – Reactivity of the Pt(sal)(ppy) Complexes in Thermal and Photoactivated Hydrosilylation Reactions		
.....		113
3.1	Preamble	113

3.2	Latent reaction kinetics	113
3.3	Reaction monitoring by NMR spectroscopy	119
3.4	Optimised model hydrosilylation reaction	123
3.5	Optimised set-up for reaction monitoring by NMR spectroscopy.....	130
3.6	Performance of Pt(sal)(ppy) complexes in thermal and photoactivated hydrosilylation reactions.....	132
3.6.1	Precatalyst 1a	132
3.6.2	Precatalyst 1b	135
3.6.3	Precatalyst 1c	137
3.6.4	Precatalyst 1d	138
3.6.5	Precatalyst 1e	139
3.6.6	Precatalyst 1f.....	141
3.6.7	Precatalyst 1g	142
3.6.8	Precatalyst 1h	143
3.6.9	Precatalyst 1i	145
3.6.10	Summary of precatalyst screening.....	146
3.7	Effect of varying the catalyst loading.....	148
3.8	Substrate scope using precatalyst 1b	152
3.8.1	Vinyltrimethoxysilane.....	154
3.8.2	3-Buten-2-one	158
3.8.3	Styrene	160
3.8.4	4-methoxystyrene	162
3.8.5	Oct-1-ene.....	164

3.8.6	Substrates inert to hydrosilylation in the model system	168
3.8.7	Recharges with inert substrates.....	170
3.9	Comparison to the commercial catalyst.....	173
3.9.1	Curing times in commercial substrates.....	173
3.9.2	Thermal stability studies.....	176
3.10	Conclusions	177
Chapter 4 – Mechanistic Studies on the Hydrosilylation Reaction.....		181
4.1	Preamble	181
4.2	Identifying the nature of the active species.....	189
4.3	Determining order in silane	195
4.3.1	Using precatalyst 1a	195
4.3.2	Using precatalyst 1b.....	201
4.3.3	Using precatalyst 1b at 0.000025 M	205
4.3.4	Using precatalyst 1b with vinyltrimethoxysilane as the alkene substrate	207
4.3.5	Recharging using precatalyst 1a.....	210
4.3.6	Recharging using precatalyst 1b	212
4.4	Determining order in alkene	213
4.4.1	Using precatalyst 1a.....	213
4.4.2	Using precatalyst 1b.....	217
4.5	Adding substrates before and after irradiation	219
4.6	Effect of alkene on the active species	222
4.7	² H NMR studies	226
4.7.1	Thermal hydrosilylation using deuterio MD'M.....	228

4.7.2	Photoactivated hydrosilylation using deuterio MD'M	233
4.8	Proposed mechanism for photoactivated hydrosilylation using COPASI.....	238
4.9	Conclusions.....	246
Chapter 5 – Conclusions and Future Directions.....		249
5.1	Key Conclusions	249
5.2	Future Directions	255
5.2.1	Combining the precatalyst with inhibitors	255
5.2.2	Expanding the substrate scope	255
5.2.3	Time-resolved spectroscopic methods for identifying the active species	256
Chapter 6 – Experimental methods		258
6.1	General techniques.....	258
6.1.1	Nuclear Magnetic Resonance (NMR) spectroscopy	258
6.1.2	Ultraviolet–visible spectroscopy	258
6.1.3	Mass spectrometry.....	259
6.1.4	Elemental microanalysis.....	259
6.1.5	Transmission Electron Microscopy.....	259
6.1.6	Differential Scanning Calorimetry	259
6.2	UV photoreactor	260
6.3	Catalytic procedures	260
6.3.1	Reagents	260
6.3.2	Method for in-situ reaction monitoring.....	261
6.4	Chapter Two Experimental	262

6.4.1	Synthesis and characterisation of $[\text{Pt}\{\text{NC}_5\text{H}_4\text{-6-(4'-R-C}_6\text{H}_3)\}\text{Cl}(\kappa_1\text{-S-dmsO})]$ complexes	262
6.4.2	Synthesis and characterisation of Schiff base ligands.....	265
6.4.3	Synthesis and characterisation of Pt(sal)(ppy) complexes.....	272
6.5	Chapter Three Experimental	282
6.5.1	Performance of Pt(sal)(ppy) complexes in thermal and photoactivated hydrosilylation reactions.....	282
6.5.2	Substrate scope.....	282
6.5.3	Recharges with inert substrates.....	284
6.5.4	Curing times in commercial substrates.....	285
6.5.5	Thermal stability studies.....	285
6.6	Chapter Four Experimental	286
6.6.1	Tests for determining the active species.....	286
6.6.2	Determining order in silane	286
6.6.3	Recharges.....	287
6.6.4	Determining order in alkene	287
6.6.5	Adding substrates before and after irradiation.....	287
6.6.6	Experiments to determine the effect of alkene on the active species	288
6.6.7	Preparation of d_1 -hexamethylsiloxymethylsilane	288
6.6.8	Hydrosilylation reactions using d_1 -hexamethylsiloxymethylsilane	289
6.6.9	Recharge of the solution using d_1 -hexamethylsiloxymethylsilane.....	289
6.7	Crystallographic data.....	290
	Appendix	291

Abbreviations..... 295

References 298

List of Tables

Table 2.1. Selected ^1H NMR shifts (ppm) with $ \text{}^1\text{H}-^1\text{H} $ and $ \text{}^1\text{H}-^{195}\text{Pt} $ coupling constants (Hz) of synthesised dmsO complexes measured in d_2 -dichloromethane at 600 MHz.....	93
Table 2.2. Selected bands and absorption coefficients within the UV–vis spectra of 1-dmsO , 2-dmsO and 3-dmsO	95
Table 2.3. Selected ^1H NMR shifts (ppm) of synthesised Schiff base ligands (L-a–L-i) measured in d_2 -dichloromethane at 600 MHz.	98
Table 2.4. Selected absorption bands within the UV–vis spectra of Schiff base ligands (L-a–L-i).	99
Table 2.5. Selected ^1H NMR shifts (ppm) with $ \text{}^1\text{H}-^1\text{H} $ and $ \text{}^1\text{H}-^{195}\text{Pt} $ coupling constants (Hz) of synthesised Pt(sal)(ppy) complexes (1a–1i) measured in d_2 -dichloromethane at 600 MHz.....	103
Table 2.6. Selected absorption bands and absorption coefficients within the UV–vis spectra of Pt(sal)(ppy) complexes (1a–1i).	107
Table 2.7. Selected bond distances and bond angles for Pt(sal)(ppy) complexes 1a , 1b , 1f and 1g	110
Table 3.1. Absorption coefficients at 365 nm in the UV-vis spectra of precatalysts 1a–1i	130
Table 3.2. Comparison of precatalyst performance in the model hydrosilylation reaction between MD'M and VTMS under thermal and photoactivated conditions. Reaction conditions (0.0025 M precatalyst, 0.8 – 1.0 M MD'M , 0.8 – 1.0 M VTMS in d_2 -dichloromethane).....	148
Table 3.3. Initial rates extracted from the first five data points following irradiation in the photoactivated hydrosilylation reaction between MD'M and VTMS using precatalyst 1b at varied loadings (0.0025 mol% – 0.25 mol%) with 120 s irradiation.	150
Table 3.4. Comparisons of selectivity and ToF_{app} using precatalyst 1b in the photoactivated hydrosilylation reaction of MD'M with a variety of alkenes. Reaction conditions (0.0025 M 1b , 0.8 – 1.2 M MD'M and 0.8 – 1.2 M alkene in d_2 -dichloromethane, left for ~1 h thermally, then irradiated for 120 s).	153

Table 3.5. Comparisons of the cure times using a variety of precatalysts in the photoactivated hydrosilylation reaction of HMS and DMS	175
Table 4.1. Initial rates extracted from the first 5 data points following irradiation in the hydrosilylation reaction between MD'M and VTMS using 1a as a precatalyst. Reaction conditions as detailed in section 4.5.	221
Table 4.2. Experimental details of [VTMS] and [MD'M] used for the COPASI model using precatalyst 1b , and resulting, iterated, $[\text{cat}]_{\text{effective}}$ used in the fitting. Conditions as detailed in Figure 4.47.	241
Table 4.3. Experimental details of [VTMS] and [MD'M] used for the COPASI model using precatalyst 1a , and resulting, iterated, $[\text{cat}]_{\text{effective}}$ used in the fitting. Conditions as detailed in Figure 4.47.	241

List of Figures

Figure 1.1. Karstedt's catalyst (i-2). ¹⁸	37
Figure 1.2. Marko's catalysts (i-3–i-5) bearing imidazolyl carbene ligands.	38
Figure 1.3. Series of (salicylaldiminato)methylnickel complexes (i-13–i-16) as hydrosilylation catalysts. ²⁵	41
Figure 1.4. Bonding interaction of Si–H with metals.	58
Figure 1.5. Complex i-54 linked to a silica support to form i-55	64
Figure 1.6. Dimeric structure of trimethyl(β -dicarbonyl) platinum(IV) (i-65) complexes found to be photocatalysts for the hydrosilylation of silicone polymers.	69
Figure 1.7. Industrial silicone polymers (i-66 and i-67).	69
Figure 1.8. Structure of $(\eta^5\text{-C}_5\text{H}_4\text{CH}_3)\text{Pt}^{\text{IV}}(\text{CH}_3)_3$ (i-68) as a photoactivated hydrosilylation catalyst along with the structures of 2-chlorothioxanthen-9-one (i-69) photosensitiser and the industrial silicone polymers (i-70 and i-71).	71
Figure 1.9. Photosensitisers used to facilitate hydrosilylation.	72
Figure 2.1. Monthly average metal prices between 2019 and 2024 in \$ / troy oz (1 troy oz = 31.1 g). Average prices: Pt , \$962.52, Pd , \$1,923.79, Rh , \$11,366.34, Ir , \$3,487.52, Ru , \$420.89. ¹⁰¹ .	78
Figure 2.2. Selected platinum-based thermal hydrosilylation catalysts. ^{13,18,20,105}	79
Figure 2.3. Manganese(I) NHC complexes as photoactivated hydrosilylation catalysts. ¹⁰⁶	81
Figure 2.4. Iron(II) NHC complexes as photoactivated hydrosilylation catalysts. ¹⁰⁷	82
Figure 2.5. Selected platinum-based photoactivated hydrosilylation catalysts. ^{54,78,79,81,84}	84
Figure 2.6. Further developments of platinum-based photoactivated hydrosilylation catalysts. ^{71,72,97,112}	86
Figure 2.7. Thermal and photochemical hydrosilylation results under various conditions using Mata's complexes, 2.24a and 2.24b	87
Figure 2.8. Proposed mechanism for photohydrosilylation using Mata's complexes. ⁷²	88
Figure 2.9. General structure and advantages of complexes synthesised herein.	89

Figure 2.10. dmsO complexes synthesised herein (% yield). ^{121,122}	91
Figure 2.11. ¹ H NMR spectrum of 1-dmsO with insets to show platinum satellites (600 MHz, <i>d</i> ₂ -dichloromethane, 298 K).	93
Figure 2.12. UV–vis absorption spectra of 1-dmsO , 2-dmsO and 3-dmsO in dichloromethane (1.6 x 10 ⁻⁵ M).	94
Figure 2.13. Schiff base ligands (L-a–L-i) synthesised herein (% yield). ^{128,129,130,131,132}	96
Figure 2.14. ¹ H NMR spectrum of L-a (600 MHz, <i>d</i> ₂ -dichloromethane, 298 K).	97
Figure 2.15. UV–Vis absorption spectra and absorption coefficients of Schiff base ligands (L-a–L-i) in dichloromethane (1.6 x 10 ⁻⁵ M).	99
Figure 2.16. Pt(sal)(ppy) complexes (1a–1i) synthesised herein (% yield). ^{113,114}	101
Figure 2.17. ¹ H NMR spectra of 1a (top) with insets to show platinum satellites and L-a (bottom) (600 MHz, <i>d</i> ₂ -dichloromethane, 298 K).	102
Figure 2.18. ¹³ C{ ¹ H} NMR spectrum of 1a with insets to show ¹³ C– ¹⁹ F coupling (151 MHz, <i>d</i> ₂ -dichloromethane, 298 K).	104
Figure 2.19. UV–Vis absorption spectra of Pt(sal)(ppy) complexes (1a–1i) in dichloromethane (1.6 x 10 ⁻⁵ M).	106
Figure 2.20. Crystallographically determined structures of 1a , 1b , 1f and 1i . Ellipsoids are shown at the 50% probability level and hydrogen atoms are omitted for clarity.	109
Figure 3.1. Commonly used inhibitors to achieve latent reaction kinetics in the hydrosilylation reaction.	114
Figure 3.2. Selected examples of dormant platinum complexes used to exploit latent reaction kinetics.	116
Figure 3.3. Characteristic concentration-time profiles showing ideal latent reaction kinetics upon UV-triggering (1) and non-ideal reaction kinetics (2 – 4).	119
Figure 3.4. ¹ H NMR spectrum of MD'M (600 MHz, <i>d</i> ₂ -dichloromethane, 298 K).	125
Figure 3.5. ¹ H NMR spectrum of VTMS (600 MHz, <i>d</i> ₂ -dichloromethane, 298 K).	126

- Figure 3.6.** Representative ^1H NMR spectrum of the beta product formed in the photoactivated hydrosilylation reaction between **MD'M** and **VTMS** when using precatalyst **1b** (600 MHz, d_2 -dichloromethane, 298 K). Reaction conditions (0.93 M **MD'M** and 0.93 M **VTMS**, left for ~ 1 h thermally, then irradiated for 120 s)..... 127
- Figure 3.7.** ^{29}Si NMR spectra of **VTMS** (bottom), **MD'M** (middle) and beta product (top) formed in the photoactivated hydrosilylation reaction between **MD'M** and **VTMS** when using precatalyst **1b** (119.2 MHz, d_2 -dichloromethane, 298 K). Reaction conditions (0.93 M **MD'M** and 0.93 M **VTMS**, left for ~ 1 h thermally, then irradiated for 120 s). 128
- Figure 3.8.** ^{29}Si - ^1H HMBC spectrum of the beta product formed in the photoactivated hydrosilylation reaction between **MD'M** and **VTMS** when using precatalyst **1b** (119.2, 600.1 MHz, d_2 -dichloromethane, 298 K). Reaction conditions (0.93 M **MD'M** and 0.93 M **VTMS**, left for ~ 1 h thermally, then irradiated for 120 s)..... 129
- Figure 3.9.** 365 nm LED array used in all photoactivated kinetic studies. Left – arrangement of LEDs. Right – NMR tube inserted into the LED array which is connected to the compressed air for temperature control, and a timer to set the irradiation time. 130
- Figure 3.10.** Representative stacked ^1H NMR spectra of the in-situ thermal hydrosilylation reaction between **MD'M** and **VTMS** over time to show distinctive signals of **MD'M**, **VTMS**, mesitylene and the beta product. The inset shows the ethylene signals of the beta product (600 MHz, d_2 -dichloromethane, 298 K). Reaction conditions (0.93 M **MD'M** and 0.93 M **VTMS**). .. 131
- Figure 3.11.** Left – concentration-time profile of **MD'M** and **VTMS** consumption and beta product formation during the thermal hydrosilylation reaction using **1a** as a precatalyst. Right – concentration-time profile of beta product formation during the photoactivated hydrosilylation reaction using **1a** as a precatalyst, with 10, 60 and 120 s irradiation. Reaction conditions as detailed in section 3.6. All photoactivated plots are time-shifted to 5000 s to show the same latency period. The table shows the initial rates extracted from the first five data points after catalytic activity has been established. 133

Figure 3.12. In-situ ^1H NMR spectra of the photoactivated hydrosilylation reaction between **MD'M** and **VTMS** using **1a** as a precatalyst (400 MHz). Reaction conditions (0.0025 M **1a**, 1.0 M **MD'M**, 1.0 M **VTMS** in d_2 -dichloromethane, 120 s irradiation with 365 nm LED, 298 K). The bottom spectrum is the reaction mixture at the start of catalysis and the top spectrum is at the end of catalysis. The inset shows that there is no observable change in the catalyst after hydrosilylation..... 135

Figure 3.13. Left – concentration-time profile of **MD'M** and **VTMS** consumption and beta product formation during the thermal hydrosilylation reaction using **1b** as a precatalyst. Right – concentration-time profile of beta product formation during the photoactivated hydrosilylation reaction using **1b** as a precatalyst, with 10, 60 and 120 s irradiation. Reaction conditions as detailed in section 3.6. All photoactivated plots are time-shifted to 4000 s to show the same latency period. The table shows the initial rates extracted from the first five data points after catalytic activity has been established..... 136

Figure 3.14. Left – concentration-time profile of **MD'M** and **VTMS** consumption and beta product formation during the thermal hydrosilylation reaction using **1c** as a precatalyst. Right – concentration-time profile of beta product formation during the photoactivated hydrosilylation reaction using **1c** as a precatalyst, with 10 and 120 s irradiation. Reaction conditions as detailed in section 3.6. Photoactivated plots are time-shifted to 3700 s to show the same latency period. The table shows the initial rates extracted from the first five data points after catalytic activity has been established..... 137

Figure 3.15. Left – concentration-time profile of **MD'M** and **VTMS** consumption and beta product formation during the thermal hydrosilylation reaction using **1d** as a precatalyst. Right – concentration-time profile of **MD'M** and **VTMS** consumption and beta product formation during the photoactivated hydrosilylation reaction using **1d** as a precatalyst, with 10 s irradiation. Reaction conditions as detailed in section 3.6. The table shows the initial rates extracted from the first five data points after catalytic activity has been established..... 138

Figure 3.16. Left – concentration-time profile of **MD'M** and **VTMS** consumption and beta product formation during the thermal hydrosilylation reaction using **1e** as a precatalyst. Right – concentration-time profile of **MD'M** and **VTMS** consumption and beta product formation during the photoactivated hydrosilylation reaction using **1e** as a precatalyst, with 10 s irradiation. Reaction conditions as detailed in section 3.6. The table shows the initial rates extracted from the first five data points after catalytic activity has been established. 140

Figure 3.17. Left – concentration-time profile of **MD'M** and **VTMS** consumption and beta product formation during the thermal hydrosilylation reaction using **1f** as a precatalyst. Right – concentration-time profile of **MD'M** and **VTMS** consumption and beta product formation during the photoactivated hydrosilylation reaction using **1f** as a precatalyst, with 120 s irradiation. Reaction conditions as detailed in section 3.6. The table shows the initial rates extracted from the first five data points after catalytic activity has been established. 141

Figure 3.18. Left – concentration-time profile of **MD'M** and **VTMS** consumption and beta product formation during the thermal hydrosilylation reaction using **1g** as a precatalyst. Right – concentration-time profile of **MD'M** and **VTMS** consumption and beta product formation during the photoactivated hydrosilylation reaction using **1g** as a precatalyst, with 120 s irradiation. Reaction conditions as detailed in section 3.6. The table shows the initial rates extracted from the first five data points after catalytic activity has been established. 142

Figure 3.19. Left – concentration-time profile of **MD'M** and **VTMS** consumption and beta product formation during the thermal hydrosilylation reaction using **1h** as a precatalyst. Right – concentration-time profile of **MD'M** and **VTMS** consumption and beta product formation during the photoactivated hydrosilylation reaction using **1h** as a precatalyst, with 10 s irradiation. Reaction conditions as detailed in section 3.6. The table shows the initial rates extracted from the first five data points after catalytic activity has been established. 144

Figure 3.20. Left – concentration-time profile of **MD'M** and **VTMS** consumption and beta product formation during the thermal hydrosilylation reaction using **1i** as a precatalyst. Right – concentration-time profile of **MD'M** and **VTMS** consumption and beta product formation during

the photoactivated hydrosilylation reaction using **1i** as a precatalyst, with 10 s irradiation. Reaction conditions as detailed in section 3.6. The table shows the initial rates extracted from the first five data points after catalytic activity has been established..... 145

Figure 3.21. Concentration-time profiles of beta product formation during the photoactivated hydrosilylation reaction using **1b** as a precatalyst at varied loadings with 120 s irradiation. Reaction conditions (0.0025, 0.025 and 0.25 mol% **1b**, 0.93 M **MD'M** and 0.93 M **VTMS** in d_2 -dichloromethane). All plots are time-shifted to 4600 s to show the same latency period. 149

Figure 3.22. Concentration-time profiles of beta product formation during the photoactivated hydrosilylation reaction using **1b** as a precatalyst at 0.0025 mol% with 120 and 600 s irradiation, and at 0.25 mol% with 120 s irradiation. Reaction conditions (0.0025 and 0.25 mol% **1b**, 0.93 M **MD'M** and 0.93 M **VTMS** in d_2 -dichloromethane). All plots are time-shifted to show the same latency period. 151

Figure 3.23. ^1H NMR spectrum of the alpha and beta products formed in the photoactivated hydrosilylation reaction of **MD'M** and **VTMOS** using precatalyst **1b** (400 MHz, d_2 -dichloromethane, 298 K). Reaction conditions (0.0025 M **1b**, 1.0 M **MD'M**, 1.0 M **VTMOS**, left for ~ 1 h thermally then irradiated for 120 s). 155

Figure 3.24. ^{29}Si NMR spectra of **VTMOS** (bottom), **MD'M** (middle) and alpha and beta products (top) formed in the photoactivated hydrosilylation reaction between **MD'M** and **VTMOS** using precatalyst **1b** (119.2 MHz, d_2 -dichloromethane, 298 K). Reaction conditions (0.0025 M **1b**, 1.0 M **MD'M** and 1.0 M **VTMOS**, left for ~ 1 h thermally, then irradiated for 120 s). 156

Figure 3.25. ^{29}Si - ^1H HMBC spectrum of the alpha and beta products formed in the photoactivated hydrosilylation reaction between **MD'M** and **VTMOS** using precatalyst **1b** (119.2, 600.1 MHz, d_2 -dichloromethane, 298 K). Reaction conditions (0.0025 M **1b**, 1.0 M **MD'M** and 1.0 M **VTMOS**, left for ~ 1 h thermally, then irradiated for 120 s). 157

Figure 3.26. Left – concentration-time profile of **MD'M** and **VTMOS** consumption and alpha and beta product formation during the photoactivated hydrosilylation reaction using **1b** as a precatalyst. Right – linear fits for the alpha and beta products for the first 5 data points following

irradiation to determine the initial rates. Reaction conditions (0.0025 M **1b**, 1.1 M **MD'M** and 1.1 M **VTMOS** in *d*₂-dichloromethane, left for ~1 h thermally then irradiated for 120 s). The table shows the initial rates for alpha and beta product formation..... 158

Figure 3.27. ¹H NMR spectrum of the alpha and beta products formed in the photoactivated hydrosilylation reaction of **MD'M** and **3-Buten-2-one** using precatalyst **1b** (400 MHz, *d*₂-dichloromethane, 298 K). Reaction conditions (0.0025 M **1b**, 1.2 M **MD'M**, 1.2 M **3-Buten-2-one**, left for ~1 h thermally then irradiated for 120 s). 159

Figure 3.28. Left – concentration-time profile of **MD'M** and **3-Buten-2-one** consumption and alpha and beta product formation during the photoactivated hydrosilylation reaction using **1b** as a precatalyst. Right – linear fits for the alpha and beta products for the first 5 data points following irradiation to determine the initial rates. Reaction conditions (0.0025 M **1b**, 1.2 M **MD'M** and 1.2 M **3-Buten-2-one** in *d*₂-dichloromethane, left for ~1 h thermally then irradiated for 120 s). The table shows the initial rates for alpha and beta product formation..... 160

Figure 3.29. ¹H NMR spectrum of the alpha and beta products formed in the photoactivated hydrosilylation reaction of **MD'M** and **styrene** using precatalyst **1b** (400 MHz, *d*₂-dichloromethane, 298 K). Reaction conditions (0.0025 M **1b**, 1.2 M **MD'M**, 1.2 M **styrene**, left for ~1 h thermally then irradiated for 120 s)..... 161

Figure 3.30. Left – concentration-time profile of **MD'M** and **styrene** consumption and alpha and beta product formation during the photoactivated hydrosilylation reaction using **1b** as a precatalyst. Right – linear fits for the alpha and beta products for the first 5 data points following irradiation to determine the initial rates. Reaction conditions (0.0025 M **1b**, 1.2 M **MD'M** and 1.2 M **styrene** in *d*₂-dichloromethane, left for ~1 h thermally then irradiated for 120 s). The table shows the initial rates for alpha and beta product formation..... 162

Figure 3.31. ¹H NMR spectrum of the alpha and beta products formed in the photoactivated hydrosilylation reaction of **MD'M** and **4-methoxystyrene** using precatalyst **1b** (400 MHz, *d*₂-dichloromethane, 298 K). Reaction conditions (0.0025 M **1b**, 0.93 M **MD'M**, 0.93 M **4-methoxystyrene**, left for ~1 h thermally then irradiated for 120 s)..... 163

- Figure 3.32.** Left – concentration-time profile of **MD'M** and **4-methoxystyrene** consumption and alpha and beta product formation during the photoactivated hydrosilylation reaction using **1b** as a precatalyst. Right – linear fits for the alpha and beta products for the first 5 data points following irradiation to determine the initial rates. Reaction conditions (0.0025 M **1b**, 0.93 M **MD'M** and 0.93 M **4-methoxystyrene** in *d*₂-dichloromethane, left for ~1 h thermally then irradiated for 120 s). The table shows the initial rates for alpha and beta product formation. 164
- Figure 3.33.** ¹H NMR spectrum of the beta and isomerisation products formed in the in-situ hydrosilylation reaction of **MD'M** and **oct-1-ene** using precatalyst **1b** (400 MHz, *d*₂-dichloromethane, 298 K). Reaction conditions (0.0025 M **1b**, 1.1 M **MD'M**, 1.1 M **oct-1-ene**, left for ~1 h thermally then irradiated for 120 s). 165
- Figure 3.34.** ²⁹Si NMR spectra of **MD'M** (bottom) and beta product (top) formed in the hydrosilylation reaction between **MD'M** and **oct-1-ene** using precatalyst **1b** (119.2 MHz, *d*₂-dichloromethane, 298 K). 166
- Figure 3.35.** Left – concentration-time profile of **MD'M** and **oct-1-ene** consumption and beta and isomerisation product formation during the photoactivated hydrosilylation reaction using **1b** as a precatalyst. Right – linear fits for the beta and isomerisation products for the first 4 data points following irradiation to determine the initial rates. Reaction conditions (0.0025 M **1b**, 1.1 M **MD'M** and 1.1 M **oct-1-ene** in *d*₂-dichloromethane, left for ~1 h thermally then irradiated for 120 s). The table shows the initial rates for beta and isomerisation product formation. 167
- Figure 3.36.** Concentration-time profiles of **MD'M** and inert alkenes in the photoactivated hydrosilylation reaction. Reaction conditions (0.0025 M **1b**, 0.8 – 1.4 M **MD'M** and 0.8 – 1.4 M **alkene** in *d*₂-dichloromethane, left for ~1 h thermally then irradiated for 120 s)..... 168
- Figure 3.37.** Products formed in the hydrosilylation reaction between **MD'M** and **norbornadiene** using Karstedt's catalyst (0.05 mol%).¹⁶³ 169
- Figure 3.38.** Concentration-time profile of **MD'M** and **VTMS** consumption and beta product formation during the photoactivated hydrosilylation reaction between **MD'M** and **VTMS**, recharged with **MD'M** and **cyclohexene** upon completion. Reaction conditions (0.0025 M **1b**,

0.93 M MD'M , 0.93 M VTMS , irradiated 120 s then recharged with 1.2 M MD'M and 1.2 M cyclohexene upon completion.	170
Figure 3.39. Concentration-time profile of MD'M and VTMS consumption and beta product formation during the photoactivated hydrosilylation reaction between MD'M and VTMS , recharged with MD'M and trans-2-octene upon completion. Reaction conditions (0.0025 M 1b , 0.93 M MD'M , 0.93 M VTMS , left for ~1 h thermally then irradiated 120 s. Recharged with 0.93 M MD'M and 0.93 M trans-2-octene upon completion.	171
Figure 3.40. Concentration-time profile of MD'M and VTMS consumption and beta product formation during the photoactivated hydrosilylation reaction between MD'M and VTMS , recharged with MD'M and norbornadiene upon completion. Reaction conditions (0.0025 M 1b , 0.93 M MD'M , 0.93 M VTMS , left for ~1 h thermally then irradiated 120 s. Recharged with 0.93 M MD'M and 0.93 M norbornadiene upon completion.....	172
Figure 3.41. Structures of commercially used methylhydrosiloxane / dimethylsiloxane copolymer (HMS) and vinyl-terminated polydimethylsiloxane (DMS) substrates.....	173
Figure 3.42. 300 W Xe arc lamp with water cooled chamber 110 mm away from the cuvette. The cuvette contains the catalyst solution and HMS / DMS polymers.	174
Figure 3.43. Inverted cuvette after curing the precatalyst in the HMS / DMS formulation.....	174
Figure 3.44. Thermal DSC analysis of the cure temperature of 6.8 HMS : 100 DMS in the presence of selected precatalysts.	176
Figure 4.1. Model hydrosilylation reaction chosen for the mechanistic study.....	181
Figure 4.2. Left – concentration-time profile of beta product formation during the thermal hydrosilylation reaction between MD'M and VTMS using 1b as a precatalyst with a drop of Hg(0) added after ~20,000 seconds. Right – concentration-time profile of beta product formation in the corresponding non-poisoned thermal hydrosilylation reaction overlaid with the poisoned experiment. Reaction conditions as detailed in section 4.2.	190
Figure 4.3. Left – concentration-time profile of beta product formation during the photoactivated hydrosilylation reaction between MD'M and VTMS using 1b as a precatalyst with a drop of Hg(0)	

added after 40% conversion. Right – concentration-time profile of beta product formation in the corresponding non-poisoned photoactivated hydrosilylation reaction overlaid with the poisoned experiment. Substrate concentrations for non-poisoned experiment: 0.86 M MD'M and 0.86 M VTMS . Substrate concentrations for poisoned experiment: 0.86 M MD'M and 0.93 M VTMS . Plots are time-shifted to 6000 s to show the same latency period. Reaction conditions as detailed in section 4.2, with 10 s irradiation.....	191
Figure 4.4. Left – concentration-time profile of beta product formation during the thermal hydrosilylation reaction between MD'M and VTMS using 1b as a precatalyst with DBCOT added after 20,000 seconds. Right – concentration-time profile of beta product formation in the corresponding non-poisoned thermal hydrosilylation reaction overlaid with the poisoned experiment. Reaction conditions as detailed in section 4.2.	192
Figure 4.5. Left – concentration-time profile of beta product formation during the photoactivated hydrosilylation reaction between MD'M and VTMS using 1b as a precatalyst with DBCOT added after 10,000 seconds. Right – concentration-time profile of beta product formation in the corresponding non-poisoned photoactivated hydrosilylation reaction overlaid with the poisoned experiment. Substrate concentrations for non-poisoned experiment: 0.86 M MD'M and 0.86 M VTMS . Substrate concentrations for poisoned experiment: 0.86 M MD'M and 0.93 M VTMS . Reaction conditions as detailed in section 4.2, with 10 s irradiation.....	193
Figure 4.6. TEM images of the post-catalysis mixture (2 h). Reaction conditions as detailed in section 4.2, with 10 s irradiation.....	194
Figure 4.7. DLS data of the post-catalysis mixture (2 h). Reaction conditions as detailed in section 4.2, with 10 s irradiation.	194
Figure 4.8. Concentration-time profiles of beta product formation during the photoactivated hydrosilylation reaction between MD'M and VTMS using 1a as a precatalyst. Reaction conditions as detailed in section 4.3.1, with 10 s irradiation. All plots are time-shifted to 4300 s to show the same latency period. The table shows the initial rates extracted from the first 5 data points following irradiation.....	196

Figure 4.9. Rate-concentration profiles for half, first and second order in MD'M using the rates for beta product formation in the photoactivated hydrosilylation reaction between MD'M and VTMS with precatalyst 1a . Reaction conditions as detailed in section 4.3.1, with 10 s irradiation.	197
Figure 4.10. Concentration-time profiles of beta product formation during the photoactivated hydrosilylation reaction between MD'M and VTMS using 1a as a precatalyst. Reaction conditions as detailed in section 4.3.1, with 60 s irradiation. All plots are time-shifted to 4000 s to show the same latency period. The table shows the initial rates extracted from the first 3 data points following irradiation.	198
Figure 4.11. Rate-concentration profiles for half, first and second order in MD'M using the rates for beta product formation in the hydrosilylation reaction between MD'M and VTMS with precatalyst 1a . Reaction conditions as detailed in section 4.3.1, with 60 s irradiation.....	199
Figure 4.12. Concentration-time profiles of beta product formation during the photoactivated hydrosilylation reaction between MD'M and VTMS using 1a as a precatalyst. Reaction conditions as detailed in section 4.3.1, with 120 s irradiation. All plots are time-shifted to 4500 s to show the same latency period. The table shows the initial rates extracted from the first 3 data points following irradiation.	200
Figure 4.13. Rate-concentration profiles for half, first and second order in MD'M using the rates for beta product formation in the hydrosilylation reaction between MD'M and VTMS with precatalyst 1a . Reaction conditions as detailed in section 4.3.1, with 120 s irradiation.....	201
Figure 4.14. Concentration-time profiles of beta product formation during the photoactivated hydrosilylation reaction between MD'M and VTMS using 1b as a precatalyst. Reaction conditions as detailed in section 4.3.1, with 10 s irradiation. All plots are time-shifted to 3300 s to show the same latency period. The table shows the initial rates extracted from the first 5 data points following irradiation.	202

- Figure 4.15.** Rate-concentration profiles for half, first and second order in **MD'M** using the rates for beta product formation in the hydrosilylation reaction between **MD'M** and **VTMS** with precatalyst **1b**. Reaction conditions as detailed in section 4.3.1, with 10 s irradiation. 203
- Figure 4.16.** Concentration-time profiles of beta product formation during the photoactivated hydrosilylation reaction between **MD'M** and **VTMS** using **1b** as a precatalyst. Reaction conditions (0.0025 M **1b**, 0.11, 0.22, 0.44, 0.88 and 1.76 M **MD'M**, 0.88 M **VTMS** in d_2 -dichloromethane, left for ~1 h thermally then irradiated 120 s with 365 nm LED, 298 K). All plots are time-shifted to 4200 s to show the same latency period. The table shows the initial rates extracted from the first 5 data points following irradiation. 204
- Figure 4.17.** Rate-concentration profiles for half, first and second order in **MD'M** using the rates for beta product formation in the hydrosilylation reaction between **MD'M** and **VTMS** with precatalyst **1b**. Reaction conditions (0.0025 M **1b**, 0.11, 0.22, 0.44, 0.88 and 1.76 M **MD'M**, 0.88 M **VTMS** in d_2 -dichloromethane, left for ~1 h thermally then irradiated 120 s with 365 nm LED, 298 K). 205
- Figure 4.18.** Concentration-time profiles of beta product formation during the photoactivated hydrosilylation reaction between **MD'M** and **VTMS** using **1b** as a precatalyst. Reaction conditions as detailed in section 4.3.3. All plots are time-shifted to 3600 s to show the same latency period. The table shows the initial rates extracted from the first 5 data points following irradiation. 206
- Figure 4.19.** Rate-concentration profiles for half, first and second order in **MD'M** using the rates for beta product formation in the hydrosilylation reaction between **MD'M** and **VTMS** with precatalyst **1b**. Reaction conditions as detailed in section 4.3.3. 207
- Figure 4.20.** Concentration-time profiles of beta product formation during the photoactivated hydrosilylation reaction between **MD'M** and **VTMOS** using **1b** as a precatalyst. Reaction conditions as detailed in section 4.3.4, with 120 s irradiation. All plots are time-shifted to 3000 s to show the same latency period. The table shows the initial rates extracted from the first 5 data points following irradiation. 208

Figure 4.21. Rate-concentration profiles for half, first and second order in MD'M using the rates for beta product formation in the hydrosilylation reaction between MD'M and VTMOS with precatalyst 1b . Reaction conditions as detailed in section 4.3.4, with 120 s irradiation.	209
Figure 4.22. Bonding of vinylsilanes to metal centres.....	210
Figure 4.23. Concentration-time profiles of beta product formation during the photoactivated hydrosilylation reaction using 1a between MD'M and VTMS with a recharge of the same amount of MD'M and VTMS after completion. Reaction conditions as detailed in section 4.3.5. All plots are time-shifted to 4200 s to show the same latency period. The table shows the initial rates extracted from the first 5 data points following the recharge.	211
Figure 4.24. Concentration-time profiles of beta product formation during the photoactivated hydrosilylation reaction using 1b between MD'M and VTMS with a recharge of the same amount of MD'M and VTMS after completion. Reaction conditions as detailed in section 4.3.6. All plots are time-shifted to 3900 s to show the same latency period. The table shows the initial rates extracted from the first 5 data points following the recharge.	212
Figure 4.25. Concentration-time profiles of beta product formation during the photoactivated hydrosilylation reaction between MD'M and VTMS using 1a as a precatalyst. Reaction conditions as detailed in section 4.4.1, with 10 s irradiation. All plots are time-shifted to 4500 s to show the same latency period. The table shows the initial rates extracted from the first 5 data points following irradiation.	214
Figure 4.26. Rate-concentration profiles for negative first, half, first and second order in VTMS using the rates for beta product formation in the hydrosilylation reaction between MD'M and VTMS with precatalyst 1a . Reaction conditions as detailed in section 4.4.1, with 10 s irradiation.	215
Figure 4.27. Concentration-time profiles of beta product formation during the photoactivated hydrosilylation reaction between MD'M and VTMS using 1a as a precatalyst. Reaction conditions as detailed in section 4.4.1, with 120 s irradiation. All plots are time-shifted to 4500 s to show	

the same latency period. The table shows the initial rates extracted from the first 5 data points following irradiation.....	216
Figure 4.28. Rate-concentration profiles for negative first, half, first and second order in VTMS using the rates for beta product formation in the hydrosilylation reaction between MD'M and VTMS with precatalyst 1a . Reaction conditions as detailed in section 4.4.1, with 120 s irradiation.	217
Figure 4.29. Concentration-time profiles of beta product formation during the photoactivated hydrosilylation reaction between MD'M and VTMS using 1b as a precatalyst. Reaction conditions as detailed in section 4.4.2, with 10 s irradiation. All plots are time-shifted to 3200 s to show the same latency period. The table shows the initial rates extracted from the first 5 data points following irradiation.....	218
Figure 4.30. Rate-concentration profiles for negative first, half, first and second order in VTMS using the rates for beta product formation in the hydrosilylation reaction between MD'M and VTMS with precatalyst 1b . Reaction conditions as detailed in section 4.4.2, with 10 s irradiation.	219
Figure 4.31. Concentration-time profiles of beta product formation during the photoactivated hydrosilylation reaction between MD'M and VTMS using precatalyst 1a . Reaction conditions as detailed in section 4.5. Blue: precatalyst 1a irradiated 10 s then added MD'M and VTMS , black: precatalyst 1a and MD'M irradiated 10 s then added VTMS , pink: precatalyst 1a , MD'M and VTMS irradiated 10 s, purple: precatalyst 1a and VTMS irradiated 10 s then added MD'M ...	220
Figure 4.32. Proposed (generic) structures of the active catalyst species in platinum-catalysed hydrosilylation according to the literature. ^{2,19,183} Kühn noted that addition spectator ligands should be thought of as part of the species denoted as [Pt].....	221
Figure 4.33. Concentration-time profiles of beta product formation and MD'M and VTMS consumption during the photoactivated hydrosilylation reaction between MD'M and VTMS with cyclohexene doped in. Reaction conditions as detailed in section 4.6.	223

Figure 4.34. Proposed active species formed from precatalyst 1b in the hydrosilylation reaction between MD'M and VTMS . Spectator ligands should be thought of as part of the species denoted as [Pt].	224
Figure 4.35. Concentration-time profiles of beta product formation and MD'M and VTMS consumption during the photoactivated hydrosilylation reaction between MD'M and VTMS with trans-2-octene doped in. Reaction conditions as detailed in section 4.6.	224
Figure 4.36. Concentration-time profiles of MD'M , VTMS and norbornadiene during the attempted photoactivated hydrosilylation reaction between MD'M and VTMS with norbornadiene doped in. Reaction conditions as detailed in section 4.6.	225
Figure 4.37. ^2H NMR spectrum of deuterio MD'M (92 MHz, dichloromethane, 298 K).	227
Figure 4.38. ^1H NMR spectrum of deuterio MD'M (600 MHz, d_2 -dichloromethane, 298 K).	227
Figure 4.39. Concentration-time profiles of beta product formation during the thermal hydrosilylation reaction between MD'M and VTMS (pink) and deuterio MD'M and VTMS (black) using 1a as a precatalyst. Reaction conditions as detailed in section 4.7.1.	228
Figure 4.40. Simplified Chalk-Harrod mechanism. ³³	230
Figure 4.41. Concentration-time profiles of beta product formation during the thermal hydrosilylation reaction between MD'M and VTMS (pink) and deuterio MD'M and VTMS (black) using 1b as a precatalyst. Reaction conditions as detailed in section 4.7.1.	231
Figure 4.42. In-situ stacked ^2H NMR spectra of the thermal hydrosilylation reaction between deuterated MD'M and VTMS using 1b as a precatalyst (92 MHz, dichloromethane, 298 K). Reaction conditions as detailed in section 4.7.1.	232
Figure 4.43. Overlaid ^1H (600 MHz, CD_2Cl_2 , 298 K) and ^2H (92 MHz, dichloromethane, 298 K) NMR spectra at the end of the thermal hydrosilylation reaction between MD'M and VTMS (light blue) and deuterio MD'M and VTMS (dark blue) using 1b as a precatalyst. Reaction conditions as detailed in section 4.7.1.	233
Figure 4.44. Concentration-time profiles of beta product formation during the photoactivated hydrosilylation reaction between MD'M and VTMS (pink) and deuterio MD'M and VTMS (black)	

using 1b as a precatalyst. Reaction conditions as detailed in section 4.7.2. All plots are time-shifted to 3300 s to show the same latency period. The table shows the initial rates extracted from the first 5 data points following irradiation.....	234
Figure 4.45. In-situ stacked ^2H NMR spectra of the photoactivated hydrosilylation reaction between deuterated MD'M and VTMS using 1b as a precatalyst (92 MHz, dichloromethane, 298 K). Reaction conditions as detailed in section 4.7.2.....	235
Figure 4.46. Concentration-time profiles for beta product formation during the photoactivated hydrosilylation reaction between deuterio MD'M and VTMS with a recharge of the same amount of protio MD'M and VTMS after completion. The table shows the initial rates extracted from the first 5 data points following irradiation, and after the recharge. Reaction conditions as detailed in section 4.7.2.1.....	237
Figure 4.47. Concentration-time profiles of beta product formation for a variety of starting concentrations of MD'M and VTMS (~ 0.5 M to 2 M) using pre-catalyst 1b (0.0025 M, 10 s irradiation time) Open circles = experimental data, solid lines = holistically simulated data derived from the catalytic manifold outlined in . Data are time shifted to remove the latent periods prior to irradiation. Inset shows the first 5000 s for experiments with an excess of MD'M that show the increase in rate of turnover with time.....	240
Figure 4.48. COPASI simulated models for the concentration of beta product, using the derived rate constants from fitting 1b (Figure 4.49) at three different $[\text{cat}]_{\text{effective}}$ ● = 1.2×10^{-5} M; ■ = 6.0×10^{-6} M; ▲ = 3.0×10^{-6} M; $[\text{VTMS}] = 0.81$ M; $[\text{MD'M}] = 0.84$ M. Simulated post irradiation. Inset: (top) expansion of the first 5000 s of simulation, showing the three different starting $[\text{cat}]_{\text{effective}}$ and linear fits. Inset (bottom): relationship between simulated rates and $[\text{cat}]_{\text{effective}}$	242
Figure 4.49. Initial rates, post induction period, versus irradiation time for precatalyst 1a and 1b . Reaction conditions as detailed in section 4.3.....	243
Figure 4.50. Relationship of $[\text{VTMS}]$ and $[\text{MD'M}]$ to $[\text{cat}]_{\text{effective}}$ for pre-catalysts 1b (light grey) and 1a (dark grey).....	243

Figure 5.1. Pt(sal)(ppy) complexes synthesised herein (1a – 1i) and used as precatalysts for the hydrosilylation reaction.	251
Figure 5.2. Alternative unsaturated substrates to test in the model reaction based on alkynes, carbonyls and conjugated dienes.	255
Figure 5.3. Alternative silanes to test in the model reaction based on alkylsilanes, phenylsilanes and chlorosilanes.	256
Figure A.1. Expanded region of the latency period in the thermal hydrosilylation reaction detailed in Figure 3.11.	291
Figure A.2. Concentration-time profiles of beta product formation during the photoactivated hydrosilylation reaction between MD'M and VTMS using 1b as a precatalyst. Reaction conditions as detailed in section 4.3.2, with 60 s irradiation. All plots are time-shifted to 3000 s to show the same latency period. The table shows the initial rates extracted from the first 5 data points following irradiation.	291
Figure A.3. Concentration-time profiles of beta product formation during the photoactivated hydrosilylation reaction between MD'M and VTMS using 1a as a precatalyst. Reaction conditions as detailed in section 4.4.1, with 60 s irradiation. All plots are time-shifted to 4500 s to show the same latency period. The table shows the initial rates extracted from the first 5 data points following irradiation.	292
Figure A.4. Rate-concentration profiles for half, first and second order in VTMS using the rates for beta product formation in the hydrosilylation reaction between MD'M and VTMS with precatalyst 1a . Reaction conditions as detailed in section 4.4.1, with 60 s irradiation.	292
Figure A.5. Concentration-time profiles of beta product formation during the photoactivated hydrosilylation reaction between MD'M and VTMS using 1b as a precatalyst. Reaction conditions as detailed in section 4.4.2, with 120 s irradiation. All plots are time-shifted to 3200 s to show the same latency period. The table shows the initial rates extracted from the first 5 data points following irradiation.	293

List of Schemes

Scheme 1.1. The hydrosilylation reaction.....	35
Scheme 1.2. The hydrosilylation reaction between oct-1-ene and trichlorosilane using diacetylperoxide as the catalyst.....	36
Scheme 1.3. The hydrosilylation reaction between pent-1-ene and trichlorosilane using Speier's catalyst.....	36
Scheme 1.4. Regio- and chemoselectivity of hydrosilylation reactions using i-5 compared to Karstedt's catalyst (i-2). ²⁰	39
Scheme 1.5. The hydrosilylation reaction between hexamethylsiloxymethylsilane and oct-1-ene catalysed by divinylsiloxane platinum(0) complexes (i-9–i-12) with ylide-functionalised phosphines. The table shows the percentage conversion of substrates to the anti-Markovnikov product (i-8).	40
Scheme 1.6. The hydrosilylation reaction between diethylsilane and oct-1-ene catalysed by i-13–i-16 . The table shows the percentage conversion to the single (i-17) and double (i-18) hydrosilylation products.....	42
Scheme 1.7. Common side-reactions accompanying hydrosilylation.	43
Scheme 1.8. Proposed mechanism for hydrosilylation by Chalk and Harrod in 1965. ³³	44
Scheme 1.9. Deuterium scrambling in cyclohexene in the hydrosilylation reaction with trichlorosilane using Karstedt's catalyst. ²	45
Scheme 1.10. Catalytic cycle for the hydrosilylation of cyclohexene as proposed by Kühn and colleagues. ²	46
Scheme 1.11. Deuterium scrambling products observed in the hydrosilylation reaction between deuterated trichlorosilane and oct-1-ene, using Karstedt's catalyst. ²	46
Scheme 1.12. Kühn's revised Chalk–Harrod mechanism accounting for the product distribution observed when using deuterated substrates. ² After decoordination of the isomerisation product	

(V ₁₅), the corresponding platinum hydride rather than the deuteride would be formed (omitted for clarity).	47
Scheme 1.13. The modified Chalk–Harrod mechanism proposed by Wrighton in 1981.	49
Scheme 1.14. Proposed mechanism for hydrosilylation by Seitz and Wrighton in 1988.	51
Scheme 1.15. Reductive elimination of the alkyl and hydrido ligands from Co(CO) ₃ MeSiMe ₃ H (i-39).....	52
Scheme 1.16. Two silicon cycle for hydrosilylation, proposed by Duckett and Perutz in 1992... 53	
Scheme 1.17. The photoactivated hydrosilylation reaction catalysed by CpPtMe ₃ (i-48).	54
Scheme 1.18. Photolysis of CpPtMe ₃ (i-48) in the presence of HMe ₂ SiOSiMe ₃ to form the bis(silyl) hydride species (i-49).....	55
Scheme 1.19. Boardman’s mechanistic proposal for platinum colloid formation. ⁵⁴	56
Scheme 1.20. The hydrosilylation reaction catalysed by a heterogeneous catalyst.	60
Scheme 1.21. The hydrosilylation reaction between PMHS and oct-1-ene catalysed by platinum nanoparticles. The table shows the percentage conversion to the hydrosilylation product as well as the percentage of oct-1-ene isomerisation.....	61
Scheme 1.22. UV-irradiation of transition-metal oxalate complexes.....	63
Scheme 1.23. Photochemical reductive elimination of the oxalate ligand from Pt(PEt ₃) ₂ (C ₂ O ₄) (i-54).....	64
Scheme 1.24. Formation of active catalysts using Pt(acac) ₂ (i-56).....	66
Scheme 1.25. Reaction of Pt(hfac) ₂ (i-63) in the presence of ethene under UV-irradiation to form Pt(hfac) ₂ (η ² -C ₂ H ₄) (i-64).	67
Scheme 1.26. Formation of hyperbranched polycarbosilanes using either Karstedt’s catalyst (i-2) thermally or Pt(acac) ₂ (i-56) under photochemical conditions.	68
Scheme 2.1. Hydrosilylation of cyclohexanone with Wilkinson’s catalyst (top), Pd(PPh ₃) ₄ catalysed hydrosilylation of 1,3-pentadiene (middle) and [Ir(COD)Cl] ₂ catalysed hydrosilylation of allyl chloride.	77
Scheme 2.2. Synthetic route towards 1-dmso , 2-dmso and 3-dmso	91

Scheme 2.3. General synthesis of Schiff base ligands (L-a–L-i). ¹²⁷	96
Scheme 2.4. General synthesis of Pt(sal)(ppy) complexes (1a–1i).	100
Scheme 3.1. Proposed mechanism for conversion of the platinum di- ω -alkenyl complex into the active catalyst. ⁷³	117
Scheme 3.2. Model hydrosilylation reaction used for kinetic studies under thermal (top) and photoactivated (bottom) conditions.	123
Scheme 4.1. Proposed mechanism for the observed rate acceleration of Osborn’s catalysts compared to Karstedt’s catalyst.	186
Scheme 4.2. Ligand exchange of Karstedt’s catalyst when exposed to olefin substrates. ²	187
Scheme 4.3. Different proposed active species depending on the binding strength of the alkene. The depicted alkene represents dtvms on Karstedt’s catalyst and the alkene substrate for hydrosilylation. ²	188
Scheme 4.4. Synthesis of deuterio MD’M	226
Scheme 4.5. Simplified catalytic cycle, showing the modelled elementary steps, associated intermediates and selected equilibrium constants as simulated using COPASI. The precise speciation of the catalyst is undetermined (i.e. oxidation state, charge, and identity of X).....	239
Scheme 4.6. Suggested mechanism of photoactivation of the precatalysts. X = SiR’ ₃ or another anionic ligand.	245
Scheme 4.7. Suggested mechanism for photoactivated hydrosilylation. For simplicity, ligand X in the active species is assumed to be a neutral ligand, but its identity remains unresolved.	246
Scheme 5.1. Suggested mechanism for photoactivated hydrosilylation.	254

Acknowledgements

I must begin by stating what an absolute privilege it has been to be supervised by three of the most incredible academics in inorganic chemistry! Andy – your unwavering support, upholding of high standards and clear direction have truly made this project what it is. Simon – thank you for your insights, and most of all, for fixing NMR 1 every time it was playing up! Robin – your thoughtful contributions have added so much value to this project. I will be forever indebted to each of you for your guidance, encouragement, and kindness. I hope that one day, I can pay forward all that you have given to me.

To Laura and Sam, thank you for making me feel so welcome during my visit to JMTC. I have thoroughly enjoyed having an industry focused project and your contributions have been invaluable for driving the project forwards. Thanks, must also go to Johnson Matthey, for providing funding for this project.

No small thanks must go to Chris Rhodes, for his outstanding work in the design and manufacture of the LED photoreactor. I also owe a huge thank you, to all of the amazing technical staff at York.

Perhaps the best thing about being co-supervised is having the pleasure of being surrounded by two wonderful research groups. To *all* of the Weller and Duckett groups, past and present, it has been an honour to share so many happy times with you. From Tim and James' bromance, Cameron's unusual (to say the least) lunch combo's, Laurence's consumption of *anything* so long that it's >5 days past expiry, to David's refusal to wear absolutely anything weather appropriate – it's been a real joy to be a part of. A special mention must go to you, Joe, for being the kindest, most supportive friend over these three happy years. I feel incredibly lucky to have such a funny and upstanding friend as you, and I am elated to be attending your wedding this year to beautiful Thea. To Chloe, my duck, we've shared such a special bond from the second you joined the group. I so enjoyed our romantic retreat / NMR symposium in Bath. To Mat and Chloe, an absolute highlight of this PhD journey was the waterpark in Prague! What a blast we had. Pav, I will forever miss our renditions of the Katy Perry classics, but more importantly, our regular trips to B&M to

buy coffee sachets. Callum, I will miss watching you push deadlines to the absolute minute and wondering how to make posh coffee with you. Aminata, thank you for your directness, your elegance, and impeccable fashion sense. You are missed deeply. To all the lovely MChem and new PhD students, Matt W, Kat, Jack, Rebecca, Orry and Anna, you all fit so perfectly into the group right away. I know that you will all be incredibly successful in whatever you go on to do.

I have had the absolute pleasure of being supported by some fantastic post-docs and technical staff during my time at York. Sam, your support at the very start really helped me settle into the lab during the unsettling times of the pandemic. Claire B, your resilience and work ethic have been truly inspiring. Matt, you are the most fantastic chemist (wizard) I have ever known, and I wish you all the best in your new role! Big Kris, thank you for sharing your boundless knowledge on platinum chemistry with me, and for bringing so much fun to the lab. Claire C, we have had such a laugh, and your support has seen me through many tiring days. Vicky A, thanks for keeping *everything* and *everyone* in check, despite our continuous reluctance to engage with the building clean. Vicky L, thank you for taking on the role of the work mum and making sure that everyone is happy! I will miss each of you deeply.

To my best friends: Keeley, Jess, Tom and Kerry. We have shared so many happy times together, and I am so grateful to you for keeping me grounded. Thank you for believing in me when I haven't believed in myself.

To my wonderful boyfriend, Ben. Where would I be without you? Thank you for your endless support and encouragement, for your comfort, and for never complaining about picking me up from the library in the middle of the night. I could go on forever, but you know how it is. You are truly amazing.

Last but certainly not least, to my wonderful Nana and Dad. Thank you always, for your warmth, for putting my happiness above your own, and for being all-round exemplary role models. You have made it all possible.

Author's Declaration

I declare that this thesis is a presentation of original work, and I am the sole author. This work has not previously been presented for a degree or other qualification at this University or elsewhere. All sources are acknowledged as references.

Portions of the work have been disclosed in a patent: Laura J. Ashfield, Simon B. Duckett, Helena G. Lancaster, Robin N. Perutz, Andrew S. Weller, PCT/GB2022/051574, Hydrosilylation Catalysts, June 21, 2022.

Much of the work discussed has been presented for publication: Helena G. Lancaster, Joe C. Goodall, Samuel P. Douglas, Laura J. Ashfield, Simon B. Duckett, Robin N. Perutz, Andrew S. Weller. "Platinum(II) Phenylpyridine Schiff Base Complexes as Latent, Photoactivated, Alkene Hydrosilylation Catalysts." *ACS Catal.*, 2024, *under review*.

Helena G. Lancaster

March 2024

Chapter 1 – Introduction

1.1 Preamble

This doctoral thesis presents the research findings from a PhD project which has been carried out in collaboration with Johnson Matthey. The overarching aim of this research is to develop platinum-based catalysts for use in the photoactivated hydrosilylation reaction. Following the details of the synthesis and characterisation of a series of Pt(II) complexes as photoactivated hydrosilylation precatalysts (chapter two), a detailed kinetic and mechanistic study (chapters three and four) will be presented. In this context, this first chapter describes the general background of the hydrosilylation reaction, focussing in particular on the commercial importance of hydrosilylation, the mechanistic pathways that have been proposed and the development of photoactivated hydrosilylation catalysts.

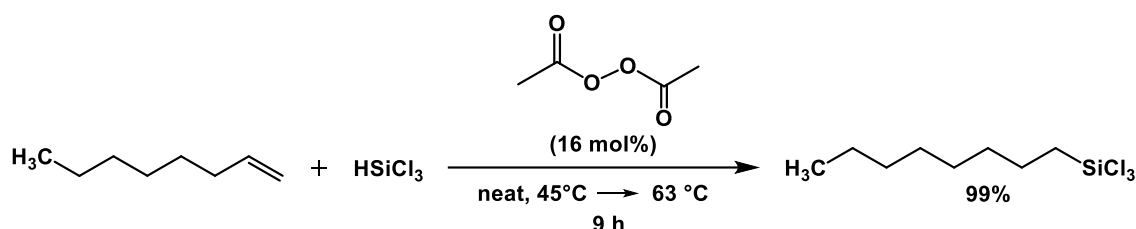
1.2 The hydrosilylation reaction

Hydrosilylation is an important addition reaction of an Si–H bond across unsaturated organic moieties, such as alkenes and alkynes, to form organofunctional silanes and silicones (Scheme 1.1). The reaction is characterized by its excellent atom-efficiency and broad substrate scope, making it a fundamental transformation for both industrial processes and academic research.^{1,2} Commercially, hydrosilylation reactions are employed in the production of functional polymers^{3,4,5} and for applications such as silicone release coatings, baby bottle teats and automotive gaskets.^{6,7,8,9}



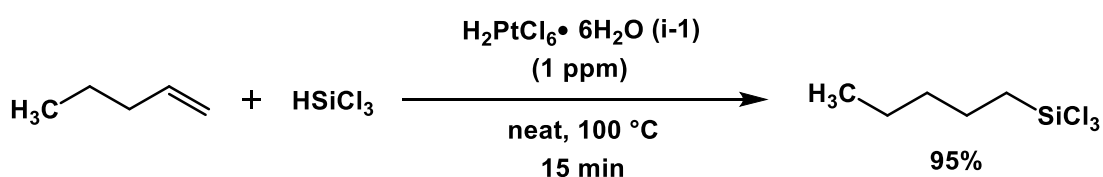
Scheme 1.1. The hydrosilylation reaction.

The first hydrosilylation reaction was reported in 1947, where *n*-octyltrichlorosilane was prepared from oct-1-ene and trichlorosilane in the presence of diacetyl peroxide (Scheme 1.2).¹⁰ This reaction pathway relies on the decomposition of the peroxide to act as a radical initiator, enabling a free radical chain mechanism. Despite good yields of product being obtained, certain disadvantages are resident in the use of peroxides to facilitate hydrosilylation reactions, including many substrates being unable to tolerate the forcing reaction conditions. It is not surprising then, that these methods find little use in the industries of today.



Scheme 1.2. The hydrosilylation reaction between oct-1-ene and trichlorosilane using diacetylperoxide as the catalyst.

In 1953, a catalyst composed of platinum supported on charcoal was found to be effective in catalysing hydrosilylation reactions under much milder conditions and with lower amounts of catalyst.¹¹ This early recognition of the ability of platinum to activate Si–H bonds preceded the breakthrough of Speier’s pioneering work in 1957, when he introduced $\text{H}_2\text{PtCl}_6 \cdot 6\text{H}_2\text{O}$ (**i-1**) as a very effective hydrosilylation catalyst (Scheme 1.3).^{12,13} Catalyst loadings for **i-1** can drop as low as 10^{-5} – 10^{-8} moles catalyst per mole of substrate (10^{-3} – 10^{-6} mol%).¹⁴ In spite of the high cost of platinum, **i-1** is used on a large scale for industrial hydrosilylation, owing to its extremely high turnover number (TON) and turnover frequency (TOF).¹



Scheme 1.3. The hydrosilylation reaction between pent-1-ene and trichlorosilane using Speier’s catalyst.

However, **i-1** presents several limitations, namely long induction periods and poor selectivity when using internal alkenes. For example, pent-2-ene is isomerised to the terminal alkene prior to hydrosilylation, which affords 1-silylpentene in high yields.¹⁵ Furthermore, when used on a large scale, *in situ* reduction of hexachloroplatinic acid to give the active platinum(0) catalyst can be unpredictable, which after the long induction period can lead to a sudden and potentially dangerous exotherm.¹⁶ The dissipation of heat is ineffective in large scale reactors and the sudden exotherm can result in thermal degradation of the active catalyst or potential explosions.¹⁷

Such drawbacks provided the impetus to further develop different platinum-based hydrosilylation catalysts and this was achieved by Karstedt utilising a platinum(0) complex with 1,1,3,3-tetramethyl-1,3-divinylsiloxane as a ligand (**i-2**) (Figure 1.1).¹⁸ This catalyst demonstrated a tremendous improvement in reactivity compared to any other previously reported catalyst and turnover rates of millions / hour are often seen for the hydrosilylation of olefins.² Owing to its higher activity, greater selectivity towards hydrosilylation products and much shorter induction period, **i-2** largely replaced **i-1** for large scale industrial processes such as the crosslinking of silicon rubber, and it remains the benchmark system for new hydrosilylation catalysts today.⁴

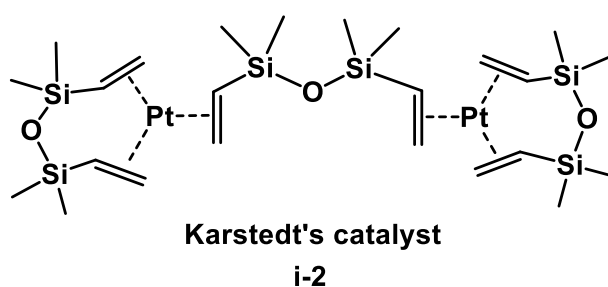


Figure 1.1. Karstedt's catalyst (**i-2**).¹⁸

In spite of **i-2** being the most versatile and established catalyst for hydrosilylation, it also presents some limitations, including alkene isomerisation and the reduction of alkenes to alkanes. The divinylsiloxane ligand is also labile and leads to facile decomposition to platinum colloids upon

prolonged storage or during catalysis, which can lead to discolouration of end products.¹⁹ Induction periods are still observed using **i-2** because the supporting vinylsiloxane ligands often bind more strongly to platinum than the unsaturated substrate. It has been reported that during the induction period, the supporting vinylsiloxane ligands are removed by ligand exchange or hydrosilylation.² Another issue is that **i-2** is only commercially available as a highly diluted solution since it forms platinum black in the absence of excess olefin stabiliser. This renders it unsuitable for typical laboratory experiments that underpin kinetic and mechanistic investigations, such as characterisation or isolation of intermediates.

These drawbacks spurred research into the development of new hydrosilylation precatalysts with improved stability. To circumvent the issue of ligand lability leading to colloid formation, Marko and coworkers employed robust σ -donor ligands and prepared platinum(0) complexes bearing an imidazolyl carbene ligand and a single divinylsiloxane (complexes **i-3–i-5**) (Figure 1.2).²⁰

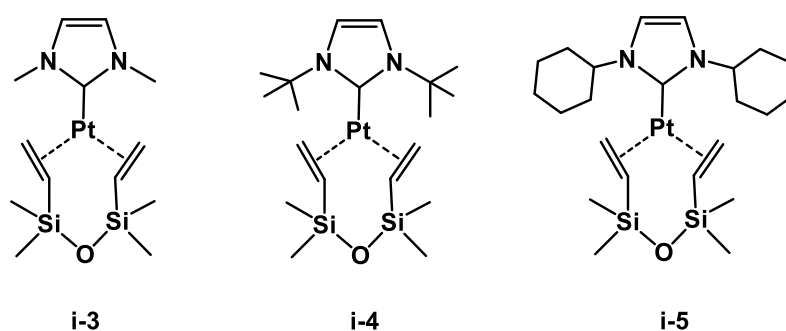
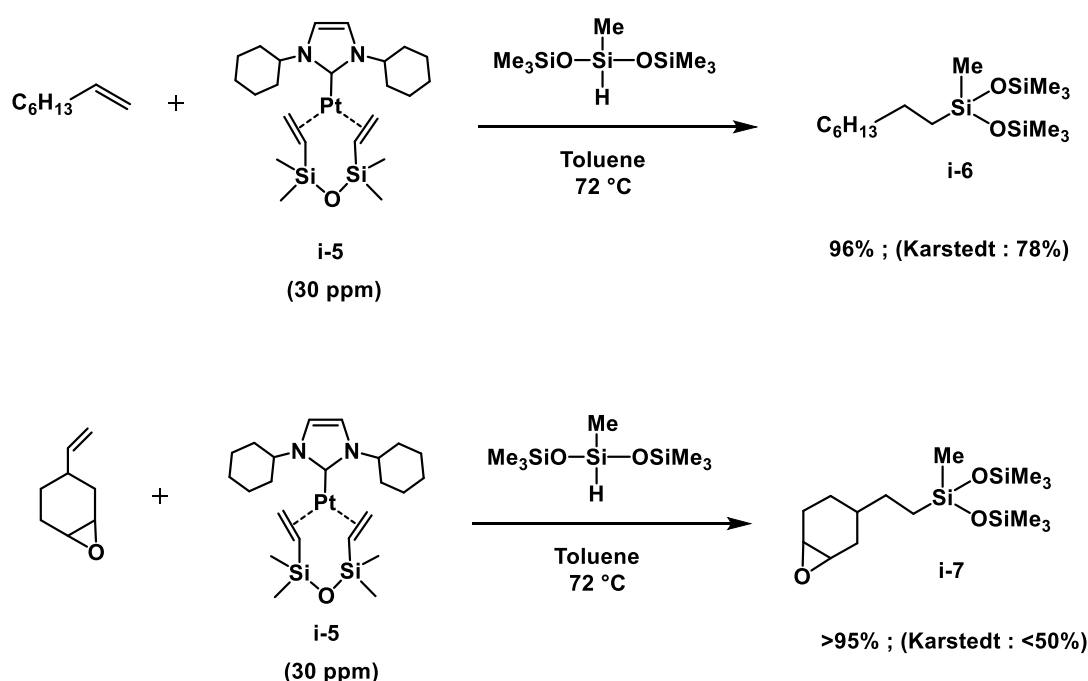


Figure 1.2. Marko's catalysts (**i-3–i-5**) bearing imidazolyl carbene ligands.

Despite **i-5** being slightly less reactive than Karstedt's catalyst in the model hydrosilylation reaction between oct-1-ene and hexamethylsiloxymethylsilane using a catalyst loading of 30 ppm, the amount of undesired side products was greatly reduced, and no colloidal platinum was observed (Scheme 1.4).²⁰ It is noteworthy that **i-5** is completely regioselective in the model reaction, forming only the anti-Markonikov hydrosilylation product (**i-6**) in 96% yield, in contrast to Karstedt's catalyst which formed 78% **i-6**, along with 15% isomerised product and 7% reduced

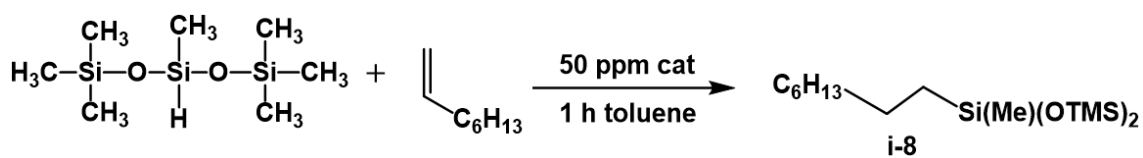
alkene. The hydrosilylation of the epoxide using **i-5** afforded the anti-Markovnikov product (**i-7**) in >95% yield, in contrast to Karstedt's catalyst which formed **i-7** in <50% yield, along with >35% decomposition material resulting from the opening / polymerisation of the sensitive epoxide function. In addition to improved stability during catalysis, Marko's complexes also offer bench stability and remarkable selectivity to a wide range of functional groups such as alcohols, silyl ethers and ketones.⁴ This success prompted the development of a large variety of N-heterocyclic carbene (NHC) based platinum precatalysts with more sterically encumbering NHC ligands and different alkene co-ligands.^{21,22}



Scheme 1.4. Regio- and chemoselectivity of hydrosilylation reactions using **i-5** compared to Karstedt's catalyst (**i-2**).²⁰

More recently, Gessner and coworkers reported a variety of divinylsiloxane platinum(0) complexes with ylide-functionalised phosphines (**i-9–i-12**) (Scheme 1.5).²³ These complexes are air and moisture stable and do not require storage with excess alkene as a stabiliser, which represents a significant advantage over Karstedt's catalyst. In a model reaction between hexamethylsiloxymethylsilane and oct-1-ene at 50 ppm catalyst loading, complexes **i-9–i-12** showed excellent selectivity toward the anti-Markovnikov product (**i-8**), comparable with

Karstedt's catalyst. Furthermore, all of these complexes were effective in catalysing the hydrosilylation reaction of a variety of substrates at catalyst loadings between 50–200 ppm, including norbornene and vinyl epoxides. A further advantage of complexes **i-9–i-12** is that they are effective hydrosilylation catalysts at 40 °C, as many other catalysts require heating to temperatures >80 °C to effect hydrosilylation.¹



Catalyst	Conversion to i-8 (%)
i-9 R ¹ = Cy, R ² = Me	62
i-10 R ¹ = <i>t</i> Bu, R ² = Me	>99
i-11 R ¹ = Cy, R ² = Ph	>99
i-12 R ¹ = Cy, R ² = <i>o</i> Tol	97
Karstedt's	>99

Scheme 1.5. The hydrosilylation reaction between hexamethylsiloxymethylsilane and oct-1-ene catalysed by divinyl-disiloxane platinum(0) complexes (**i-9–i-12**) with ylide-functionalised phosphines. The table shows the percentage conversion of substrates to the anti-Markovnikov product (**i-8**).

To date, the catalytic activity of platinum-based systems is unparalleled which renders them first choice for industrial hydrosilylation.¹ However, the high cost and diminishing reserves of noble metal catalysts has prompted extensive research into using earth-abundant transition metal-based catalysts.³ There is a wealth of literature detailing the studies of complexes based on nickel,^{24,25} iron²⁶ and cobalt^{27,28} that find use as hydrosilylation catalysts. It is worth noting that, generally, first-row transition metals have been reported to be poor hydrosilylation catalysts compared to their platinum analogues. For example, the nickel equivalent of Karstedt's catalyst was prepared, and the dominant reaction was dehydrogenative silylation of alkenes leading to unsaturated products, with hydrosilylation being a secondary pathway.²⁹ Nevertheless, research

efforts in recent years have led to the development of nickel-based hydrosilylation catalysts with improved activity.^{25, 30}

A noteworthy example of a recent nickel catalysed hydrosilylation was reported by Shimada and coworkers in 2015.²⁵ In this work, a series of (salicylaldiminato)methylnickel complexes (**i-13–i-16**) were prepared as hydrosilylation catalysts, as show in Figure 1.3. These complexes were tested in a model hydrosilylation reaction between diethylsilane and oct-1-ene (Scheme 1.6). Complexes **i-13a** and **i-13b** showed very high activity and good selectivity toward the monohydrosilylation product. The relatively lower activities of complexes **i-14** and **i-15** were attributed to the bulky aryl substituent on the imino-*N* atom in **i-14** and the strongly coordinating 4-dimethylaminopyridine in **i-15**. It was found that complex **i-16** was unreactive even at elevated temperatures. Despite previous nickel complexes suffering from limited substrate scope and improper reaction selectivity when employed as hydrosilylation catalysts, Shimada demonstrated that these complexes were also applicable for the hydrosilylation of amino- and sulfur-functionalised alkenes. This work, along with other studies, offers promise for the development of commercially viable non-precious metal catalysts for hydrosilylation.^{31,32}

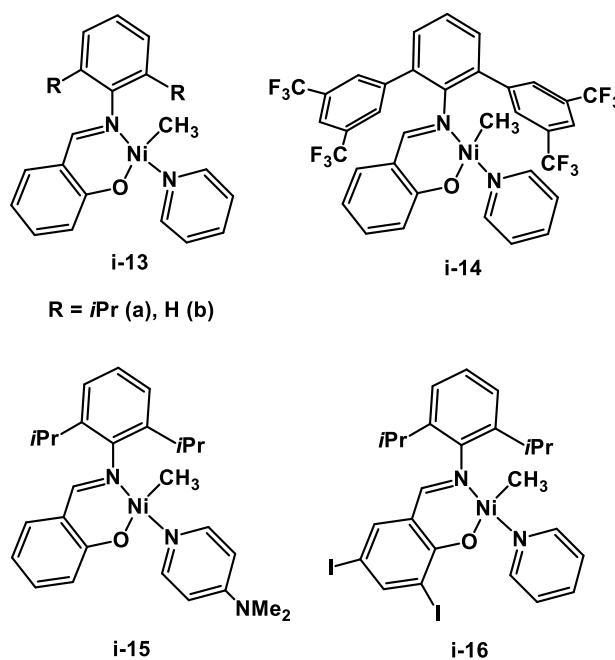
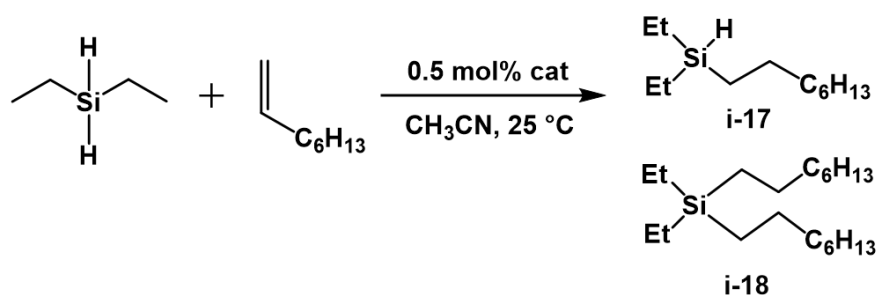


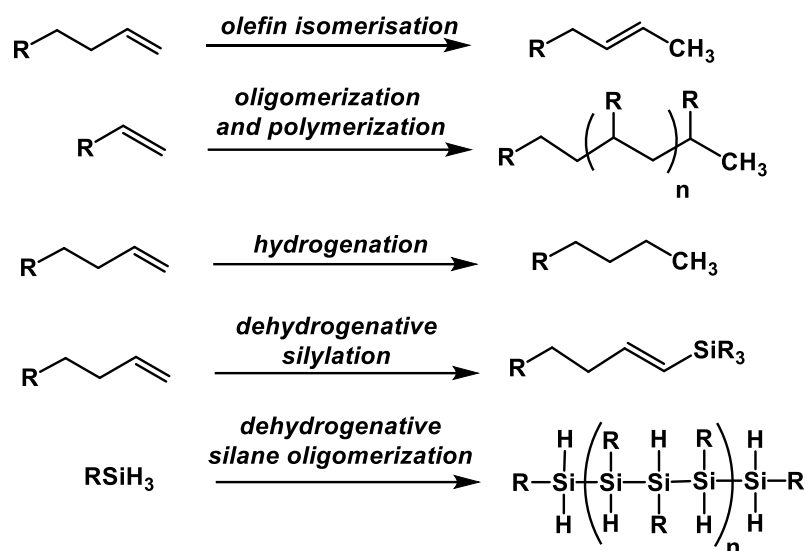
Figure 1.3. Series of (salicylaldiminato)methylnickel complexes (**i-13–i-16**) as hydrosilylation catalysts.²⁵



Catalyst	Time (h)	Product yield (%)	
		i-17	i-18
i-13a	1	93	4
i-13b	1.3	90	2
i-14	8	88	5
i-15	2.5	92	4
i-16	24	0	0

Scheme 1.6. The hydroosilylation reaction between diethylsilane and oct-1-ene catalysed by **i-13**–**i-16**. The table shows the percentage conversion to the single (**i-17**) and double (**i-18**) hydroosilylation products.

One major challenge in transition metal catalysed hydroosilylation today is that it is often accompanied by side-reactions such as olefin isomerisation, oligomerisation, polymerisation, hydrogenation, dehydrogenative silylation as well as dehydrogenative silane oligomerisation (Scheme 1.7).⁷ There is significant cost associated with these side-reactions commercially, as the desired products have to be separated from the co-products. Furthermore, the side-reactions observed are dependent on the identity of the catalyst as well as the substrates and reaction conditions. As such, studies have been devoted to understanding the mechanisms for hydroosilylation, in order to minimise by-products and design systems with high activity and selectivity. Another important question is whether catalysis occurs homogeneously or heterogeneously, especially in light of the fact that several examples of immobilised platinum nanoparticles on supports have proved to be excellent hydroosilylation catalysts.⁸ Addressing these major questions is important as it helps to refine catalysts, reduce loadings, and mitigate against excessive residual catalyst in the product.

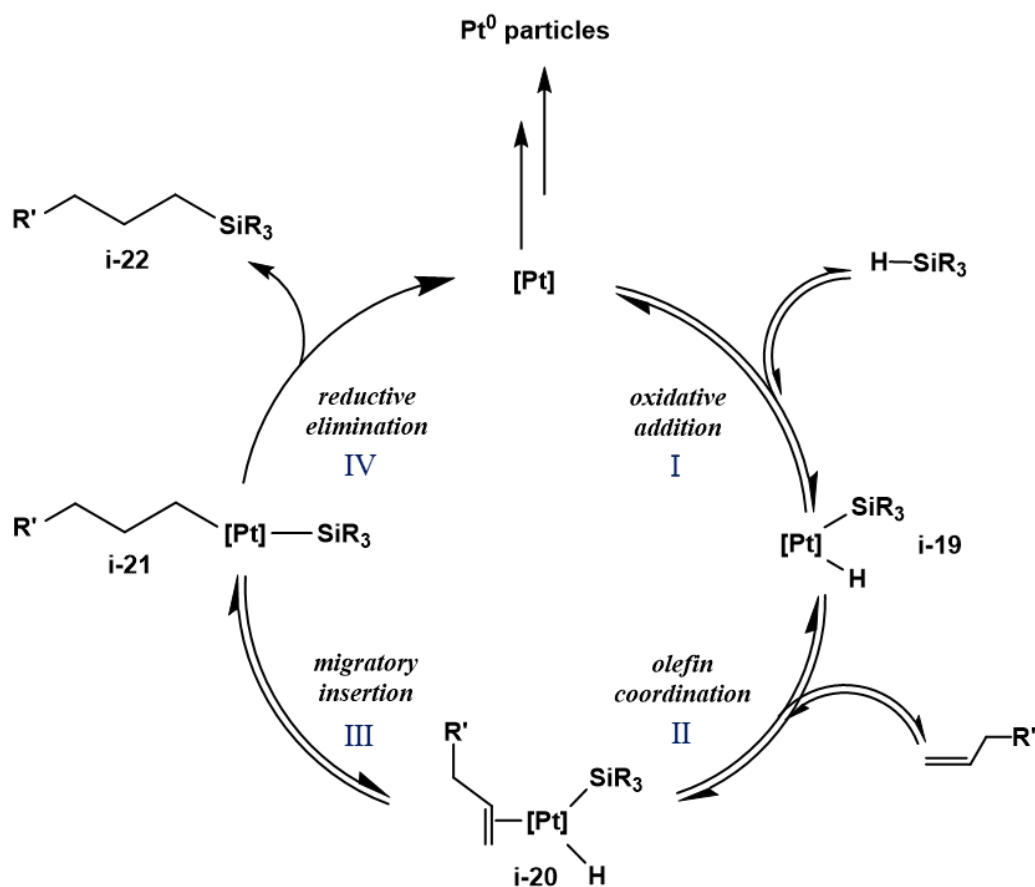


Scheme 1.7. Common side-reactions accompanying hydrosilylation.

1.2.1 The Chalk-Harrod mechanism for hydrosilylation

The Chalk-Harrod mechanism was proposed in 1965 and continues to be the most commonly accepted mechanism for platinum-catalysed hydrosilylation (Scheme 1.8).³³ This proceeds via oxidative addition (step I) of the Si–H bond to a catalytically active transition metal centre, to give a metal silyl hydride intermediate (**i-19**). This is then followed by olefin coordination (step II) to form **i-20**) and migratory insertion (step III) of the olefin into the Pt–H bond to yield a metal alkyl silyl intermediate (**i-21**). Rate-determining and irreversible reductive elimination of the alkyl and silyl groups (step IV) to form the organosilane product (**i-22**) completes the cycle and regenerates the active catalyst. Insertion of the coordinated olefin into the Pt–H bond rather than the Pt–Si bond has been inferred from a variety of experimental observations and also theoretical studies.^{34,35} Most hydrosilylation reactions that have employed Karstedt's or Speier's catalyst generate exclusively the product of anti-Markovnikov addition (**i-22**). In order to form **i-22**, olefin insertion into the Pt–H bond occurs to generate the terminally-bound alkyl complex (**i-21**). Complementary isotope labelling studies have shown rapid deuterium / hydrogen

scrambling into the olefin substrate, which provides further evidence for the rapid and reversible migratory insertion of olefins into the Pt–H bond prior to reductive elimination.³⁶

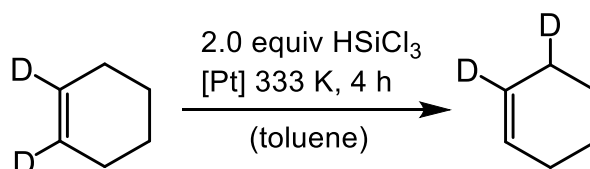


Scheme 1.8. Proposed mechanism for hydrosilylation by Chalk and Harrod in 1965.³³

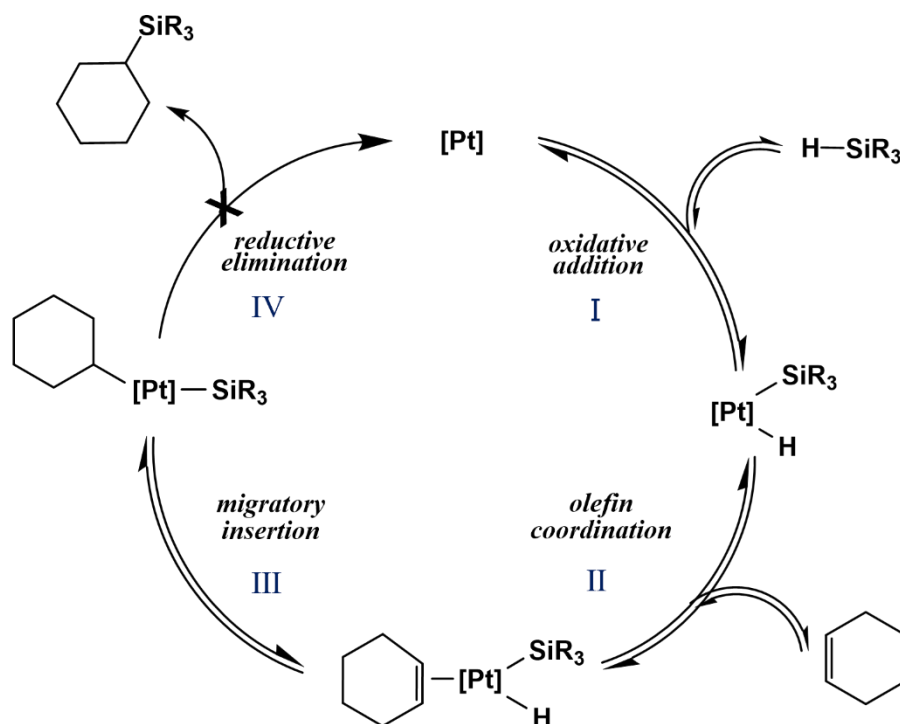
Despite the hydrosilylation reaction having been practised in industry for almost sixty years, development of the steps involved in the catalytic cycle have been laborious and slow, which is attributed to the elusive nature of highly active intermediates. Nonetheless, there are many studies that have corroborated the mechanism proposed in 1965, for which a few selected examples are presented. Lewis and Stein proposed that the active catalyst is a homogeneous platinum complex when using Karstedt's precatalyst, on the basis that platinum colloids were not observed during catalysis and mercury did not inhibit the reaction, although it is a known poison for heterogeneous catalysts.¹⁹ Employing Crabtree's and Anton's³⁷ method of using the bulky and tub-shaped dibenzo[*a,e*]cyclooctatetraene (DBCOT) ligand to bind with and sterically

encumber transition metal complexes, Osborn showed that their Karstedt-based catalyst systems were significantly inhibited by DBCOT, but not by mercury.³⁸ Moreover, Lewis reported the presence of intermediates with both Pt–C and Pt–Si bonds during catalysis, via extended X-ray absorption fine structure (EXAFS) analysis. It was postulated that the absence of Pt–Pt bonds during the most active period of catalysis was evidence that only mononuclear Pt species are catalytically active. All of these observations are consistent with the mechanism put forward by Chalk and Harrod in 1965.³³

More recently, Kühn and colleagues revisited the Chalk-Harrod mechanism in an extensive study using Karstedt's catalyst.² It has been generally accepted that internal double bonds are far less reactive toward hydrosilylation than terminal olefins because of steric hinderance. However, this has not accounted for the reluctance of cyclohexene to undergo hydrosilylation whilst the same reaction using norbornene proceeds readily under mild conditions.^{39,40} To shine light on this concept, Kühn and co-workers conducted a series of ²H-labelling experiments to pinpoint the rate-limiting steps of hydrosilylation reaction (Scheme 1.9). Interestingly, they found that when monitoring the ²H NMR of the reaction between trichlorosilane and 1,2-dideuterocyclohexene in the presence of Karstedt's catalyst, the double bond scrambles around the C₆ cycle. This demonstrates that there is successful insertion of cyclohexene into the Pt–H bond (shown by step III in Scheme 1.10) and is supportive of the reductive elimination of product being the rate limiting step.

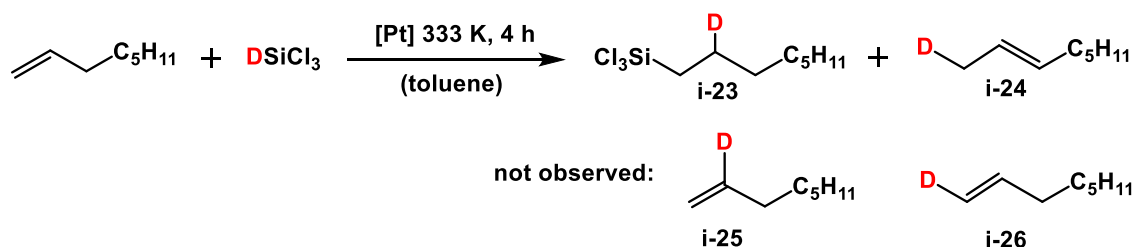


Scheme 1.9. Deuterium scrambling in cyclohexene in the hydrosilylation reaction with trichlorosilane using Karstedt's catalyst.²



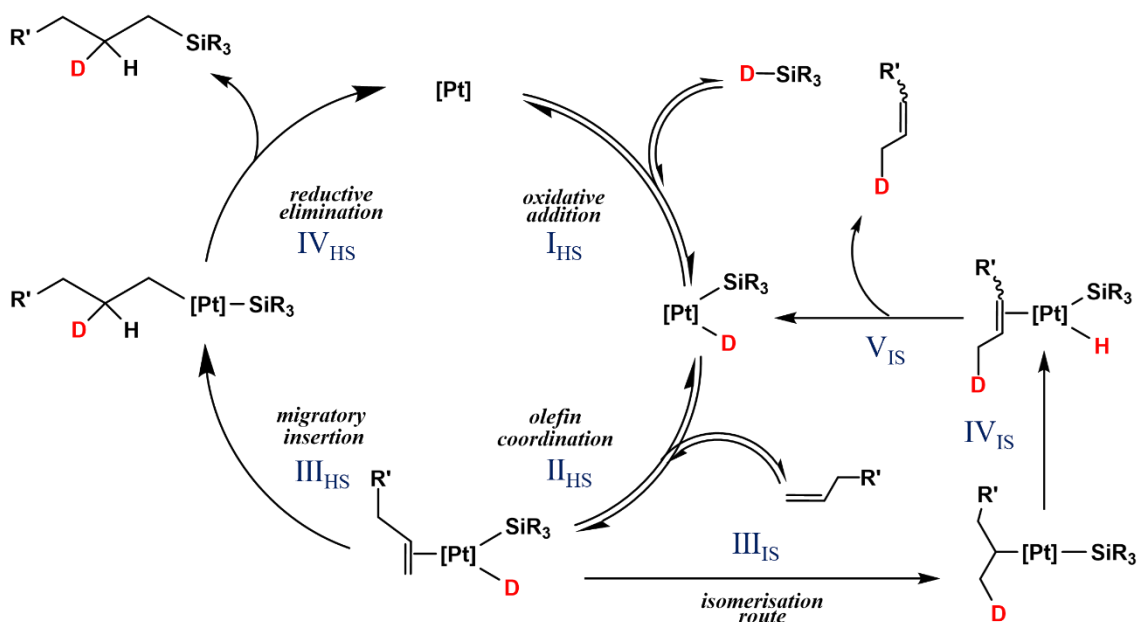
Scheme 1.10. Catalytic cycle for the hydrosilylation of cyclohexene as proposed by Kühn and colleagues.²

A separate experiment by Kühn using deuterated trichlorosilane and oct-1-ene as substrates illustrated that there was no scrambling of deuterium about the olefinic positions, but only at the C2 position of the hydrosilylation product (**i-23**) and the terminal CH₃ group of the isomerization product (**i-24**) (Scheme 1.11). The fact that no scrambling of deuterium into the olefinic methylene groups of oct-1-ene (**i-25** and **i-26**) was observed demonstrates that the migratory insertion step cannot truly be reversible in this particular set-up.



Scheme 1.11. Deuterium scrambling products observed in the hydrosilylation reaction between deuterated trichlorosilane and oct-1-ene, using Karstedt's catalyst.²

That olefin insertion into the Pt–H bond cannot be considered reversible is contradictory to the Chalk–Harrod mechanism.³³ Therefore, as a modification to this long-established mechanism, Kühn proposed that the insertion step is succeeded by two alternative competing reactions, hydrosilylation or isomerisation (Scheme 1.12). Depending on the overall energy profiles, the intermediate present following olefin coordination will either isomerise to afford deuterated olefin (steps III_{IS}, IV_{IS} and V_{IS}), or undergo migratory insertion and reductive elimination (steps III_{HS} and IV_{HS}) to yield hydrosilylation product. In this case, it seems that cyclohexene proceeds via the isomerisation route whilst oct-1-ene favours the hydrosilylation route.



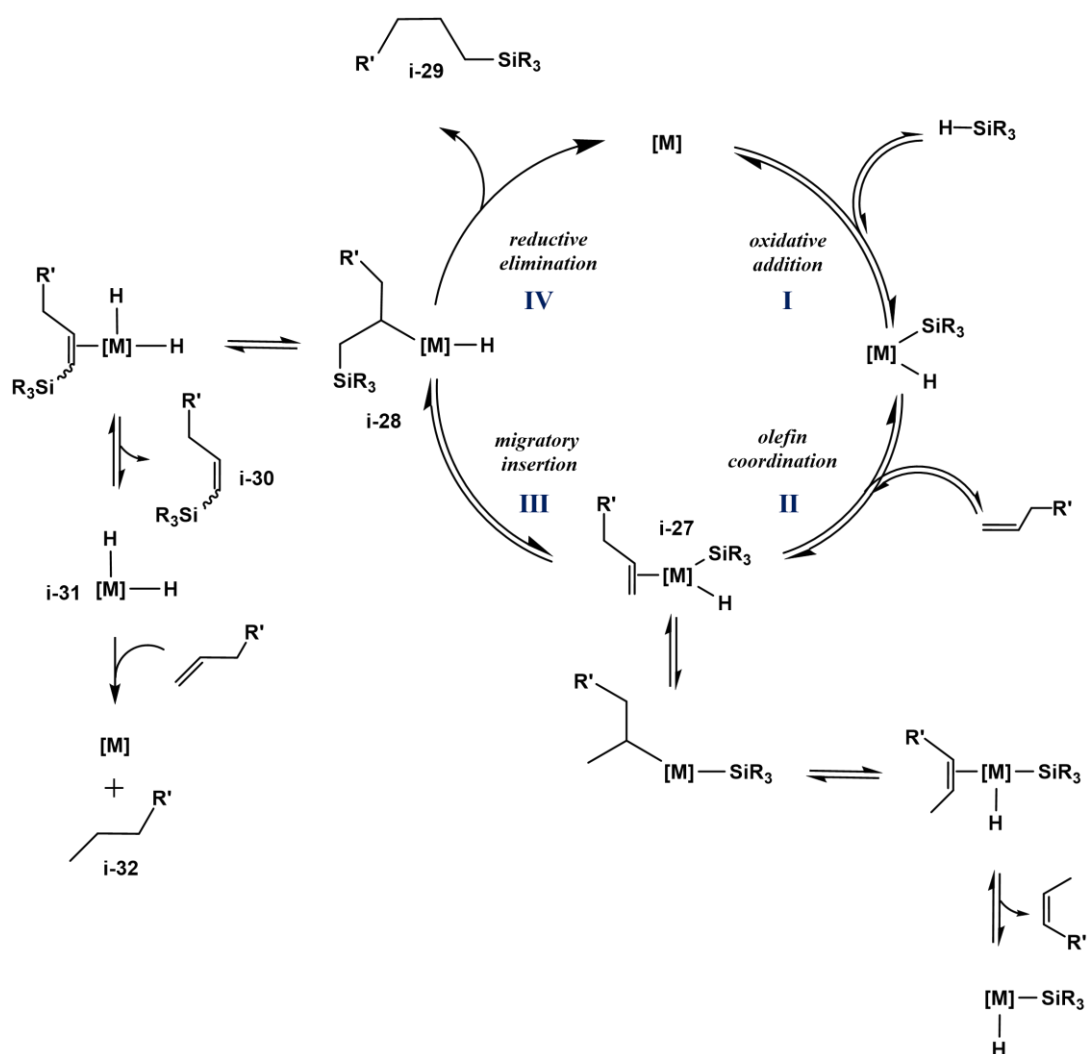
Scheme 1.12. Kühn's revised Chalk–Harrod mechanism accounting for the product distribution observed when using deuterated substrates.² After decoordination of the isomerisation product (V_{IS}), the corresponding platinum hydride rather than the deuteride would be formed (omitted for clarity).

To further consolidate their proposal that insertion of the olefin into the Pt–H bond is not truly reversible, Kühn and co-workers demonstrated a primary kinetic isotope effect in the hydrosilylation reactions of both norbornene and oct-1-ene with H/DSiCl₃. The values obtained were $k_H/k_D = 2.4$ (1) (norbornene) and 3.9 (4) (oct-1-ene) which was consistent with the values

reported by Pregosin ($k_H/k_D = 3.6$ (2)) for the hydrosilylation of styrene with triethylsilane using *cis*-[PtCl₂(PhCH = CH₂)₂] as the catalyst.⁴¹ The observed primary kinetic isotope effect is indicative of Pt–H or Si–H bond breakage prior to or during the rate-limiting step. Despite Lewis, Stein and co-workers¹⁹ attributing the isotope effect using Karstedt's catalyst to the Si–H bond breaking prior to or during the rate limiting step, Kühn proposed that the observed isotope effect should be interpreted as characteristic of the rate-limiting nature of the migratory insertion step.² This was on the basis that oxidative addition of SiR₃–H to Karstedt's 16 valence electron (VE) complex should occur readily to yield the 18 VE Pt (II) complex [Pt(H)(SiR₃)(olefin)₃]. In addition to this, the fact that 1,2-dideuterocyclohexene was isomerized only after the addition of silane corroborates this notion that formation of the active catalyst involves a facile addition of silane to platinum. Taken together with the previous literature which supports a rapid reaction of Karstedt's catalyst with hydrosilane,^{9,42} this eliminates oxidative addition of SiR₃–H to platinum as the rate determining step of the reaction. It was thus concluded that the true rate-limiting step is migratory insertion of the olefin into the Pt–H bond. Kühn and co-workers further verified that the insertion step was rate limiting by showing that the resting state *in situ* was a platinum hydride (deuteride) species. A Pt–²H species was observed by exposing Karstedt's catalyst to 5 equiv. of norbornene or oct-1-ene, respectively and 10 equiv. of deuterated trichlorosilane, before inserting into a spectrometer cooled to 193 K. The signals of the platinum deuterides were observed at $\delta = -26.3$ ppm (oct-1-ene) and -29.3 ppm (norbornene), which are in the expected range for Pt–²H groups.⁴³ Overall, Kühn's important revisions of the Chalk–Harrod mechanism are 1) the introduction of a separate bypath for the isomerisation of terminal olefins and 2) the assignment of the rate determining step to the insertion of the olefin into the Pt–H bond. It is important to note that this conclusion applies to the combination of substrates studied and may not hold for all substrates or all catalysts.

1.2.2 The modified Chalk-Harrod mechanism for hydrosilylation

Wrighton et al. were the first to propose a modification of the Chalk–Harrod mechanism, on the basis of the observation of vinylsilanes in hydrosilylation catalysed by $\text{Fe}(\text{CO})_5$ (Scheme 1.13).⁴⁴ They postulated that migratory insertion of the olefin into the M–H bond could be slower than migratory insertion into the M–Si bond. Wrighton found that upon excitation of the $\text{Fe}(\text{CO})_5$ complex, pent-1-ene and triethylsilane were converted to a mixture of alkane, alkylsilane and vinylsilane products. Wrighton’s modified mechanism provides a plausible pathway for the formation of vinylsilanes, which are not accounted for in the original Chalk–Harrod mechanism.³³

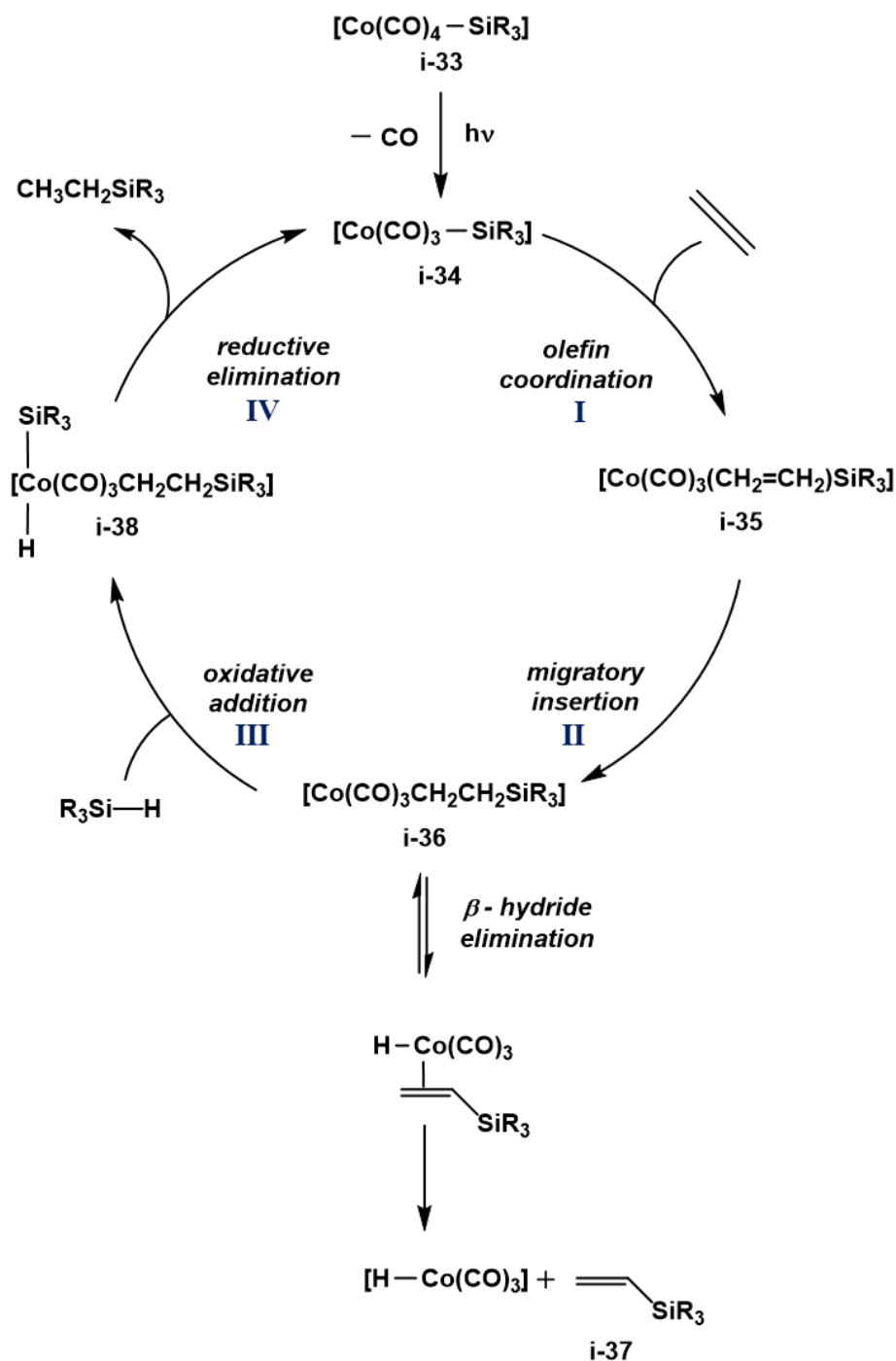


Scheme 1.13. The modified Chalk–Harrod mechanism proposed by Wrighton in 1981.

In the modified Chalk–Harrod mechanism, it is proposed that the formation of the Si–C bond is a result of olefin insertion into the M–Si bond of **i-27** rather than the M–H bond. Subsequent C–H reductive elimination from **i-28** (step **IV**) yields the hydrosilylation product (**i-29**). Alternatively, β -hydride elimination from **i-28** produces a vinylsilane (**i-30**) and a dihydride (**i-31**) that reacts with further alkene to form an alkane (**i-32**). Braunstein and Knorr noted that olefin insertion into an M–Si bond can be viewed as silyl group migration onto a coordinated olefin.⁴⁵

1.2.3 The Seitz–Wrighton mechanism for hydrosilylation

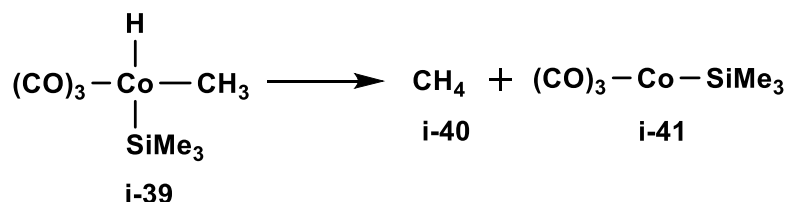
Seitz and Wrighton later provided more evidence for silyl group migration in the photoactivated hydrosilylation of alkenes.⁴⁶ Upon near-UV photolysis of $\text{Co}(\text{CO})_4\text{SiEt}_3$ (**i-33**) in a matrix of either ethene or methylcyclohexane at 77 K, a CO ligand is lost to yield the coordinatively unsaturated 16 electron $\text{Co}(\text{CO})_3\text{SiEt}_3$ complex (**i-34**) (Scheme 1.14). This is succeeded by the coordination of ethene (step **I**) to form $\text{Co}(\text{CO})_3(\text{CH}_2=\text{CH}_2)(\text{SiR}_3)$ (**i-35**), as observed by ^1H NMR spectroscopy. The next step is insertion of ethene (step **II**) into the Co–Si bond, to form **i-36**. Subsequent β -hydride elimination from **i-36** yields vinyl(triethyl)silane (**i-37**), which was detected in the reaction mixture by gas chromatography. This accounts for the observation of vinylsilane products, which are common by-products in hydrosilylation reactions and are not accounted for in the Chalk–Harrod mechanism.³³ This result is also consistent with the finding that photolysis of $\text{Co}(\text{CO})_4\text{SiEt}_3$ in the presence of pent-1-ene yields triethyl(pentenyl)silane.⁴⁷ Oxidative addition of silane to **i-36** (step **III**) to form **i-38**, followed by reductive elimination of the C–H bond (step **IV**) completes the hydrosilylation cycle.



Scheme 1.14. Proposed mechanism for hydrosilylation by Seitz and Wrighton in 1988.

To obtain evidence for the oxidative addition and reductive elimination steps, Seitz and Wrighton utilised $\text{Co}(\text{CO})_4\text{Me}$ as a model compound for $\text{Co}(\text{CO})_3\text{CH}_2\text{CH}_2\text{SiR}_3$ and assumed thermal loss of CO. The proposed intermediate, $\text{Co}(\text{CO})_3\text{Me}$, reacts with silane to give $\text{Co}(\text{CO})_3(\text{Me})(\text{SiMe}_3)\text{H}$ (**i-39**) and subsequent reductive elimination of the alkyl and hydrido ligands yields methane (**i-40**) and $\text{Co}(\text{CO})_3\text{SiMe}_3$ (**i-41**) (Scheme 1.15). If this reaction was

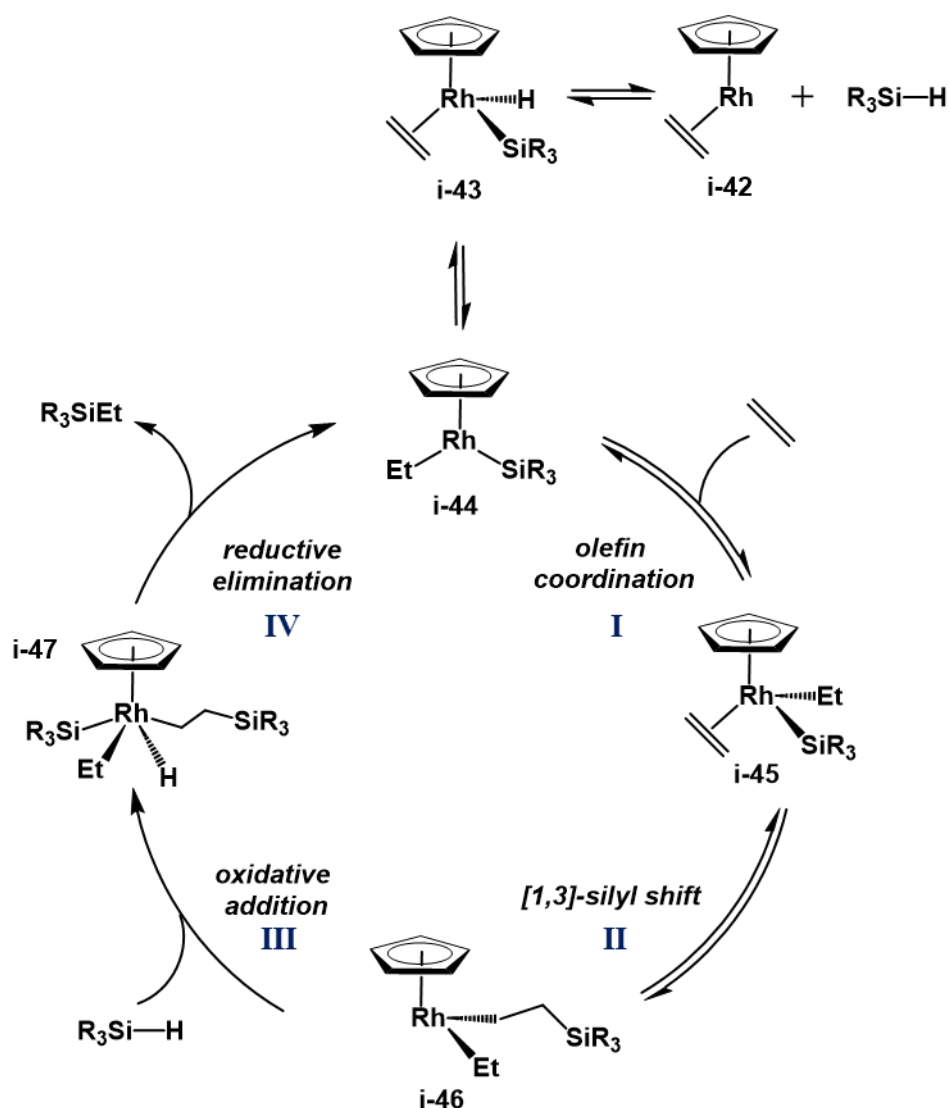
proceeding according to the Chalk–Harrod mechanism, there would be reductive elimination of the silyl and alkyl ligands to afford SiMe_4 and $\text{Co}(\text{CO})_3\text{H}$. That only CH_4 and $\text{Co}(\text{CO})_3\text{SiMe}_3$ were evident by ^1H NMR and FTIR spectroscopy respectively, is not consistent with the reaction operating *via* the Chalk–Harrod mechanism.



Scheme 1.15. Reductive elimination of the alkyl and hydrido ligands from $\text{Co}(\text{CO})_3\text{MeSiMe}_3\text{H}$ (**i-39**).

1.2.4 The Two-Silicon mechanism for hydrosilylation

Duckett and Perutz later demonstrated that silyl migration was operative in their rhodium catalysed hydrosilylation using $\{\text{RhCp}\}$ fragments.⁴⁸ Upon photolysis of the rhodium(I) complex $\text{CpRh}(\text{C}_2\text{H}_4)$ (**i-42**) in the presence of R_3SiH ($\text{R} = \text{Me}, \text{Et}$), the rhodium(III) complex $\text{CpRh}(\text{C}_2\text{H}_4)(\text{SiR}_3)(\text{H})$ (**i-43**) is formed (Scheme 1.16).⁴⁹ This complex bears all the necessary ligands to probe the intermediates postulated by the Chalk–Harrod mechanism, and it was also found to be catalytically active in hydrosilylation reactions.³³ However, the fact that **i-43** is observed renders it implausible as a key, on-cycle intermediate. Duckett and Perutz instead proposed that the active catalytic species in their system is $\text{CpRh}(\text{C}_2\text{H}_5)(\text{SiR}_3)$ (**i-44**), which forms by a [1,3]-H shift from **i-43**. Ethene attack on **i-44** yields $\text{CpRh}(\text{C}_2\text{H}_4)(\text{SiR}_3)\text{Et}$ (**i-45**) which then undergoes a [1,3]-silyl shift to form $\text{CpRh}(\text{CH}_2\text{CH}_2\text{SiEt}_3)\text{Et}$ (**i-46**). Addition of Et_3SiH to **i-46** yields a complex containing two silicon atoms, $\text{CpRh}(\text{CH}_2\text{CH}_3\text{SiEt}_3)\text{Et}(\text{SiEt}_3)\text{H}$ (**i-47**). This species, formally in oxidation state V, but possibly containing an RhSiH or RhCH 3-center bond could then undergo reductive elimination to form the hydrosilylation product and reform the original intermediate (**i-44**).



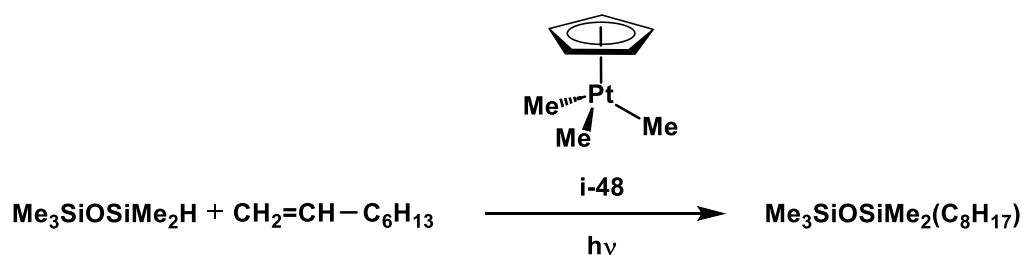
Scheme 1.16. Two silicon cycle for hydrosilylation, proposed by Duckett and Perutz in 1992.

The hydrosilylation of C_2D_4 with Et_3SiH using $\text{CpRh}(\text{C}_2\text{H}_4)(\text{SiEt}_3)\text{H}$ failed to produce significant quantities of $\text{CpRh}(\text{C}_2\text{D}_4)(\text{SiEt}_3)\text{H}$, which suggests that the ethyl group in the active species is a spectator ligand. The silyl group in $\text{CpRh}(\text{C}_2\text{H}_4)(\text{SiR}_3)\text{H}$ does however play a part in hydrosilylation as hydrosilylation of ethene with HSiR'_3 afforded $\text{CpRh}(\text{C}_2\text{H}_4)(\text{SiR}'_3)\text{H}$. To demonstrate that this does not proceed via reductive elimination of $\text{SiR}'_3\text{H}$ followed by oxidative addition of $\text{SiR}'_3\text{H}$ to the rhodium centre, a control experiment was conducted. In this experiment, it was shown that the hydrosilylation of ethene and $\text{HSi}[\text{CH}_2\text{CH}(\text{CH}_3)_2]_3$ with $\text{CpRh}(\text{C}_2\text{H}_4)(\text{SiMe}_3)\text{H}$ produced 30% $\text{CpRh}(\text{C}_2\text{H}_4)\{\text{Si}[\text{CH}_2\text{CH}(\text{CH}_3)_2]_3\}\text{H}$ after 7 days whereas a mixture of $\text{HSi}[\text{CH}_2\text{CH}(\text{CH}_3)_2]_3$ and $\text{CpRh}(\text{C}_2\text{H}_4)(\text{SiMe}_3)\text{H}$ produced only 10% $\text{CpRh}(\text{C}_2\text{H}_4)\{\text{Si}[\text{CH}_2\text{CH}(\text{CH}_3)_2]_3\}\text{H}$ after 9 days.

The formation of the rhodium (V) intermediate in this mechanism was deemed plausible as there have been many examples of rhodium complexes in different oxidation states that act as hydrosilylation catalysts, for example $\text{Cp}^*\text{Rh}(\text{SiEt}_3)_2(\text{H})_2$.⁵⁰ Overall, this study revealed that the Chalk–Harrod mechanism or its variant does not apply to the $\text{CpRh}(\text{C}_2\text{H}_4)(\text{SiR}_3)(\text{H})$ complex (**i-43**). In the Chalk–Harrod mechanism, the alkene and silane ligands are replaced once for every turnover, yet the isotope labelling experiments in this study show conclusive evidence that the ethene ligand is not replaced. Rather, this postulated mechanism is more akin to that proposed by Seitz and Wrighton that also involves two silicon atoms in one intermediate (**i-38**).⁴⁶ Various studies of rhodium⁵¹, iridium⁵², iron⁴⁴ and cobalt⁵³-catalysed hydrosilylation reactions have supported Duckett and Perutz's and Wrighton's mechanistic proposals.

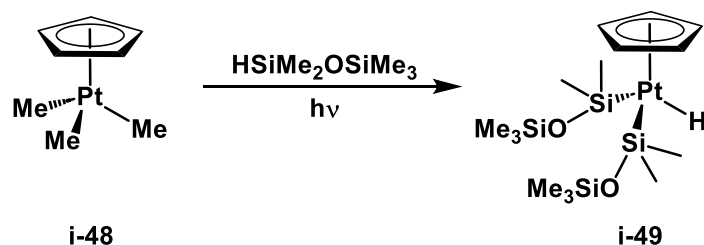
1.2.5 Hydrosilylation reactions involving colloidal platinum

Boardman demonstrated that upon photolysis of CpPtMe_3 (**i-48**), an active species was generated which rapidly catalysed the hydrosilylation reaction between 1-octene and $\text{HMe}_2\text{SiOSiMe}_3$ (Scheme 1.17).⁵⁴ The product was formed in essentially quantitative yield. No reaction was observed for the same sample held at room temperature for 20 days in the dark.

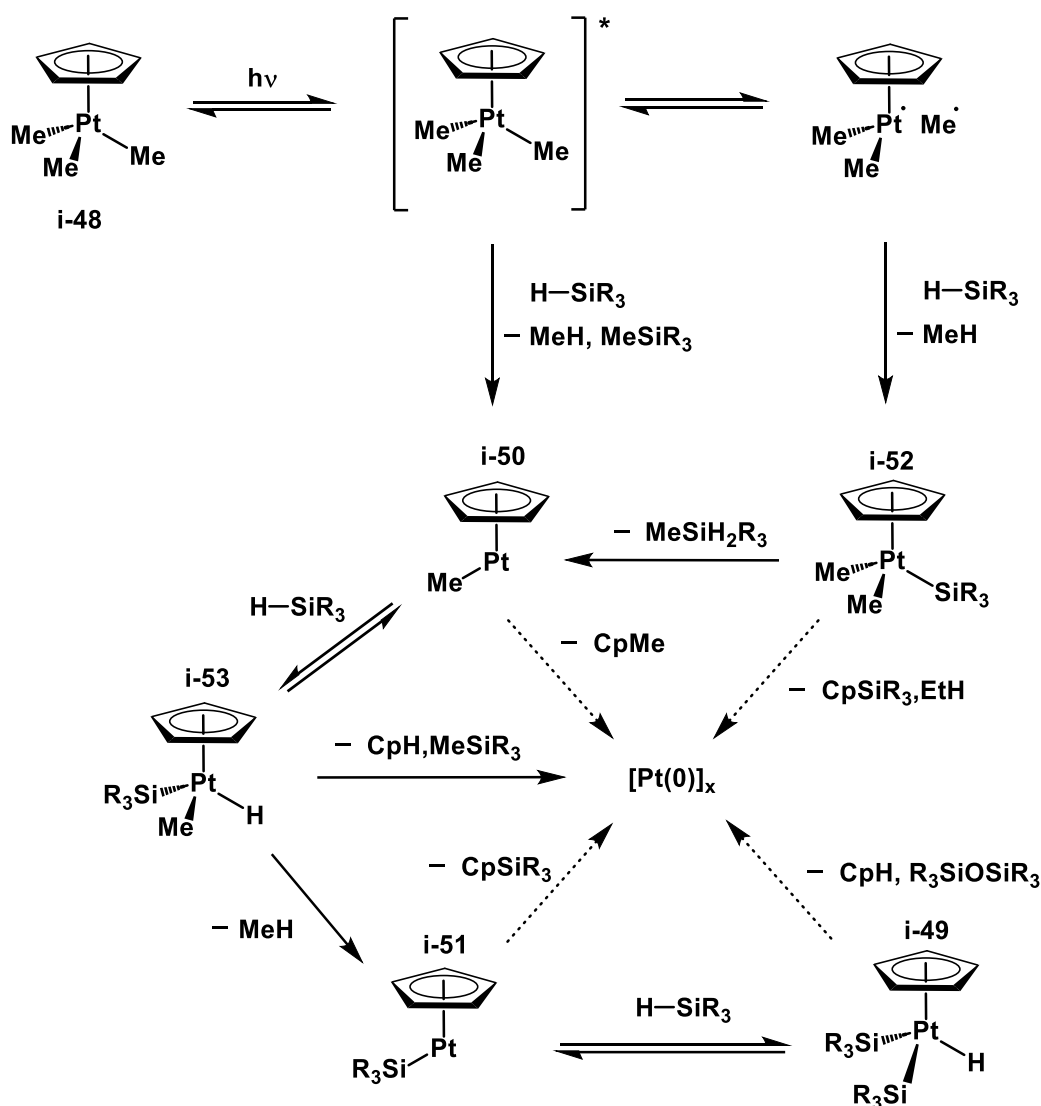


Scheme 1.17. The photoactivated hydrosilylation reaction catalysed by CpPtMe_3 (**i-48**).

The active catalyst was proposed to be a heterogenous platinum colloid as the mercury drop test showed a characteristic deactivation of the catalyst, whilst addition of DBCOT had no effect. Analysis of the reaction mixture post-photolysis by TEM confirmed the presence of platinum colloids that were 10–25 Å in size. Boardman also found that upon photolysis of **i-48** in the presence of a silane, $\text{HMe}_2\text{SiOSiMe}_3$, the bis(silyl) hydride species, $\text{CpPt}(\text{SiMe}_2\text{OSiMe}_3)_2\text{H}$ (**i-49**) was formed (Scheme 1.18). Under photolysis conditions, the activity of **i-49** was found to be significantly lower than **i-48** in the hydrosilylation reaction between 1-octene and $\text{HMe}_2\text{SiOSiMe}_2\text{OSiMe}_3$. In the dark, however, **i-49** initiated this same reaction and full conversion to the hydrosilylation product was achieved in 40 hours whereas no reaction was observed for **i-48** on the same time scale. Thus, Boardman concluded that **i-49** was not an intermediate in the conversion of **i-48** to the active species under photolysis conditions. Analysis of the reaction mixture by gas chromatography–mass spectrometry after irradiating **i-48** in the presence of $\text{HMe}_2\text{SiOSiMe}_3$ led to Boardman’s mechanistic proposal for platinum colloid formation (Scheme 1.19).



Scheme 1.18. Photolysis of CpPtMe_3 (**i-48**) in the presence of $\text{HMe}_2\text{SiOSiMe}_3$ to form the bis(silyl) hydride species (**i-49**).



Scheme 1.19. Boardman's mechanistic proposal for platinum colloid formation.⁵⁴

The absence of methylcyclopentadiene and any cyclopentadienylsiloxanes in the gas chromatography-mass spectrometry (GC-MS) analysis of the reaction mixture ruled out the platinum(II) intermediates CpPtMe (**i-50**) and CpPt(SiMe₂OSiMe₃) (**i-51**), as well as the possible platinum(IV) intermediate CpPtMe₂(SiMe₂OSiMe₃) (**i-52**) as direct colloid precursors. Overall Boardman concluded that the silyl methyl hydride complex CpPtMe(SiR₃)H (**i-53**) is the critical intermediate which is partitioned under the reaction conditions between colloidal platinum and a bis(silyl)platinum hydride such as **i-49**.

1.3 Silane activation

The activation of silanes by transition metal centres to form metal hydride silyl species has been widely studied since they have been postulated as key intermediates for hydrosilylation. The traditional pathway towards silane activation is oxidative addition of an Si–H bond from a hydrosilane to a metal centre. Examples have been shown for almost all of the transition metals since the seminal works of Schubert and Kubas.^{55,56,57}

1.3.1 Comparison between C–H and Si–H activation

The interaction of hydrosilanes with transition metals can occur under mild conditions for platinum species, especially when compared with C–H activation. This is attributed to the weaker sp^3 -Si–H bond compared with the stronger sp^3 -C–H bond, and the formation of a stronger Pt–Si bond compared with the Pt–C bond. Sakaki showed through *ab initio* calculations that Si–H oxidative addition of SiH_4 to $\text{Pt}(\text{PH}_3)_2$ is thermodynamically favourable compared to C–H oxidative addition of CH_4 to $\text{Pt}(\text{PH}_3)_2$, since the former process is exothermic whilst the latter is endothermic ($\Delta H = -110.5$ vs. 27.2 kJ mol^{-1}).⁵⁸ This process is also kinetically favoured as the calculated activation barrier for SiH_4 addition to $\text{Pt}(\text{PH}_3)_2$ is much smaller than that for CH_4 addition to $\text{Pt}(\text{PH}_3)_2$ ($\Delta H^\ddagger = 2.9$ vs. 120 kJ mol^{-1}). It is worth noting however, that Si–H bond strengths can vary substantially with substituents. To exemplify, the following values were reported for HSiR_3 : 74.6, 96.8 and 100 kcal/mol for $\text{R} = \text{Me}$, OEt and F , respectively. Sakaki concluded that ultimately, the driving force for Si–H activation arises from the formation of a Pt– SiH_3 bond, $D(\text{Pt–SiH}_3)_{\text{calc.}} = 257.3 \text{ kJ mol}^{-1}$, which is stronger than the Pt– CH_3 bond, $D(\text{Pt–CH}_3)_{\text{calc.}} = 166.1 \text{ kJ mol}^{-1}$.

Puddephatt utilised differential scanning calorimetry (DSC) to provide the first experimental estimation of Pt–Si bond energy.⁵⁹ For $\text{PtIme}_2(\text{SiMe}_3)(\text{bpy})$ ($\text{bpy} = 2,2'$ -bipyridine), the estimated

Pt–Si bond energy was found to be $D(\text{Pt–SiMe}_3)_{\text{calc.}} = 233 \pm 14 \text{ kJ mol}^{-1}$. Bond energies for Pt–Me bonds were also calculated by Puddephatt using DSC and values of 137 and 129 kJ mol^{-1} were found for *cis*-PtMe₄(MeCN)₂ and *cis*-PtMe₄(2,6-Me₂C₆H₃NC)₂, respectively.⁶⁰

Overall, the *ab initio* calculations by Sakaki and the experimental observations by Puddephatt revealed that the Pt–Si bond is roughly 100 kJ mol^{-1} stronger than the Pt–C bond, with a dependence on the substituent R.

1.3.2 Bonding in metal silyl hydride and η^2 -silane complexes

Classically, a hydrosilane will react with a metal centre via oxidative addition to give a complex with two-centre, two-electron, M–SiR₃ and M–H bonds. These likely proceed via a three-centre, two electron intermediate. Such interactions can be referred to as σ -complexes. Synergic bonding can take place in this pathway: the Si–H σ -bonding orbital can interact with the metal d-orbital, and the metal $d\pi$ -orbital can interact with the Si–H σ^* -antibonding orbital (Figure 1.4). Sufficient contribution from π -backbonding will result in a full oxidative addition. The σ donor and σ^* -acceptor ability of the Si–H bond can be modified by changing the substituents on the Si atom.

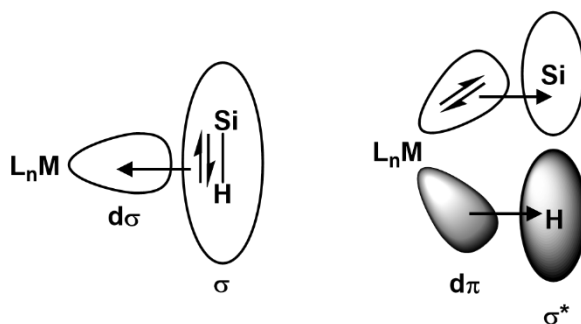


Figure 1.4. Bonding interaction of Si–H with metals.

An η^2 -Si–H bonded complex can be considered as an arrested state in the course of the oxidative addition pathway, and there are many examples of isolated silane σ -complexes. Schubert

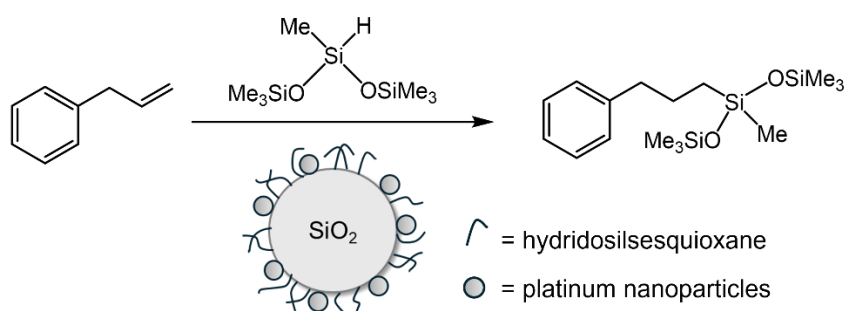
characterised a substantial series of complexes that showed a 3-centre 2-electron bonding interaction by neutron diffraction.^{61,62} He proposed that a Si–H bond length of 2.00 Å defines the limit of any appreciable interaction between silicon and hydrogen. The Si–H bond length is expected to be elongated relative to the free silane (~1.48 Å, sum of the van der Waals radii 3.10 Å) when the oxidative addition is incomplete. Schubert demonstrated through the $[(\eta^5\text{-C}_5\text{H}_4\text{Me})\text{Mn}(\text{CO})_2(\text{H-SiR}_3)]$ series that the coupling constant ($J(\text{Si,H})$) can be used as an indicator of the extent of Si–H activation. When the silicon is directly bonded to the hydride, $J(\text{Si,H})$ is expected to be around 200 Hz, but when there is no bonding between the silicon atom and the hydride, $^2J(\text{Si,H})$ is expected to be in the range of 3.5 – 20 Hz.⁶³ A weakening of the bond would mean that $J(\text{Si,H})$ lies somewhere between the two. For example, $J(\text{Si,H})$ for $[(\eta^5\text{-C}_5\text{H}_4\text{Me})\text{Mn}(\text{CO})_2(\text{H-SiHPh}_2)]$ is 63.5 Hz, whereas for $[(\eta^5\text{-C}_5\text{H}_4\text{Me})\text{Mn}(\text{CO})_2(\text{H-SiCl}_3)]$, $J(\text{Si,H})$ is 54.8 Hz. This difference can be attributed to the more electronegative chlorine substituent on the silicon promoting more back-donation from the metal into the Si–H σ^* orbital, thereby decreasing the Si–H bond order. Schubert also demonstrated that changing a substituent on the metal itself has much the same effect - $[(\eta^5\text{-C}_5\text{H}_4\text{Me})\text{Mn}(\text{CO})(\text{PMe}_3)(\text{H})\text{SiCl}_3]$ has an even lower $J(\text{SiMnH})$ value of 20 Hz. This can be explained by the more electron donating substituent imparting more electron density onto the metal centre and increasing the extent of back-donation to the Si–H σ^* antibonding orbital, thereby weakening the Si–H bond. It was concluded that oxidative addition in this complex must be very advanced or even complete. Data from molecular orbital calculations support this idea.⁶²

1.3.3 Si–H activation by metal nanoparticles

The role of platinum nanoparticles as active species for hydrosilylation catalysis has been a topic of controversy over the past 40 years.⁶⁴ For example, in their extensive study, Lewis and colleagues initially proposed that platinum nanoparticles were formed using Karstedt's catalyst

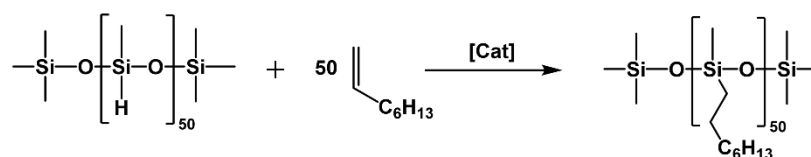
for the hydrosilylation of alkenes, and that they likely played an important role in the catalytic reaction.^{65,66} After a follow-up study however, Lewis proposed that mononuclear Pt(0) species were the real active species, and that the formation of platinum nanoparticles was the result of the aggregation of these unprotected species.¹⁹ A few years later, Finney and Finke discussed the controversial nature of the active species in hydrosilylation catalysed by Pt(COD)Cl₂, and concluded that further mechanistic studies were needed to confirm either a homogeneous or heterogeneous catalyst.⁶⁷

In spite of the controversy, evidence has shown that platinum nanoparticles can promote Si–H activation in hydrosilylation via a heterogenous process, where bond activation occurs at the surface of the nanoparticle.⁶⁴ One of the first examples of pre-formed platinum nanoparticles for hydrosilylation was presented by Brook and coworkers in 1997, who designed a heterogeneous platinum catalyst by reacting Karstedt's catalyst with silica particles modified with a hydridosilsesquioxane layer (Scheme 1.20).⁶⁸ Analysis by TEM showed that the platinum nanoparticles were uniformly distributed on the silica surface and had an average diameter of 2 nm. It was proposed that the hydridosilsesquioxane layer acts as an anchor for the platinum catalyst, as well as a protective steric barrier to prevent platinum aggregation. This supported catalyst successfully catalysed the hydrosilylation reaction of alkenes and alkynes and was also demonstrated to be rechargeable without significant loss of activity. Several other examples of platinum nanoparticles have been reported to be catalytically active for alkene hydrosilylation.^{69,70}



Scheme 1.20. The hydrosilylation reaction catalysed by a heterogeneous catalyst.

Overall, the development of catalysts based on metal nanoparticles has not been as extensively explored as homogeneous systems, because of their generally lower activity compared to the latter, which is often the consequence of clustering of nanoparticles to give catalytically less active bulk metal.¹ Industrially, the turnover number (TON) for hydrosilylation with homogeneous catalysts are on the order of 10^6 h^{-1} , and only recently have similar values been achieved by nanoparticles. Thieuleux and coworkers synthesised platinum nanoparticles by decomposing $\text{Pt}(\text{dba})_2$ (dba = dibenzylideneacetone), or Karstedt's catalyst in the presence of *n*-octylsilane or polymethylhydrosiloxane (PMHS) under 4 bars of hydrogen as a reducing agent.⁸ The platinum colloids were analysed by TEM and determined to have a mean diameter between 1.6 and 1.7 nm. In the hydrosilylation reaction between oct-1-ene and PMHS, the platinum colloids showed comparable activity to Karstedt's catalyst, as well as yielding a similar percentage of olefin isomerisation, as measured by ^1H NMR spectroscopy (Scheme 1.21).



Catalyst	Pt precursor	Stabiliser	Mean diameter (nm)	Si-H conv. (%) (TON) 7 ppm Pt	1-octene isomerisation (%)
Karstedt	-	-	-	96 (1.0×10^5)	12
$\text{Pt}(\text{dba})_2$	-	-	-	98 (1.1×10^5)	12
Pt NPs	$\text{Pt}(\text{dba})_2$	<i>n</i> -octylsilane	1.6	98 (1.1×10^5)	11
Pt NPs	Karstedt	PMHS	1.7	97 (1.0×10^5)	11
Pt NPs	Karstedt	<i>n</i> -octylsilane	1.7	99 (1.1×10^5)	11

Scheme 1.21. The hydrosilylation reaction between PMHS and oct-1-ene catalysed by platinum nanoparticles. The table shows the percentage conversion to the hydrosilylation product as well as the percentage of oct-1-ene isomerisation.

These results demonstrate that stabilised nanoparticles can achieve activities comparable to Karstedt's catalyst and are not simply a consequence of catalyst deactivation. Such systems may then offer a potential substitute for the homogeneous processes that take place industrially, as they show recyclability and often enhance the purity of final products when the nanoparticles

are immobilised on solid supports, and therefore do not end up in the final product. It is still not entirely clear however, whether Si–H bond activation takes place exclusively at the surface of the nanoparticles, or if platinum leached homogeneous species are the real active catalysts, so further mechanistic studies are needed.

1.4 Photoactivated catalysts for hydrosilylation

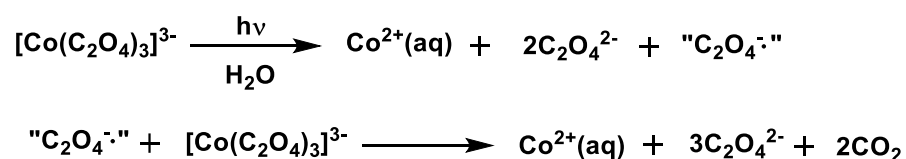
Despite a wealth of study on catalysis in the hydrosilylation reaction, the overwhelming bulk of published work has dealt with processes that occur without external activation, i.e. under so-called “thermal” conditions. Relatively few examples of UV-activated catalysts have been disclosed.^{3,5,46,48,71,72} One major challenge in making silicone polymers by hydrosilylation is the design of catalytic systems that exhibit near-zero rates under ambient conditions, but very fast rates during the curing step, otherwise known as latency.⁷³ This is useful for processes that require temporal and spatial control, such as the production of cross-linked silicones with complex shapes, as the catalyst and formulation can be preloaded into a mould and the cross-linking process is only initiated upon exposure to heat or UV-light.⁷³ The development of latent catalysts would also simplify the manufacturing process, since addition-curing silicone formulations are usually handled as two-component systems consisting of the polyvinylsiloxane plus catalyst and the separate hydrosiloxane.⁷⁴ The ability to store all the components together in a one-pot formulation that can then be externally activated would present a significant advantage to the whole process, from manufacturing and packaging to mixing. Several strategies have been employed to achieve these targets, including the use of catalyst inhibitors, catalyst encapsulants and dormant precatalysts that require heat or light triggering, and this is discussed in more detail in chapter three.^{1,5} All of these methods present their own drawbacks, but light-triggered catalysts hold promise as the required curing temperature for curing cross-linked silicones can often be quite low (<100 °C), so heat-triggered catalysts are not always suitable. This has prompted recent interest to design a new suite of platinum catalysts with tuneable

ligand sets that show essentially no hydrosilylation activity under ambient conditions and high curing rates upon UV-triggering.⁷⁵

Two general approaches have been exploited in the development of generating photoactivated hydrosilylation catalysts.⁷⁶ The first is via photodecomposition / photoreduction of platinum(II) and platinum(IV) precursors to give catalytically active platinum(0) species.^{77,78,79} The second is ligand photodissociation from a coordinatively saturated platinum(0) complex.⁷¹ The former route offers more promise in the way of exploiting a latency period, as ligand dissociation can also occur in the absence of irradiation, making it very challenging to design catalysts that have sufficient stability in the dark but also give prompt curing times. Some catalysts require continuous irradiation to promote turnover (photocatalysis), whilst others only require a short burst of irradiation and then proceed to promote turnover under thermal conditions (photoactivated catalysis).^{5,72}

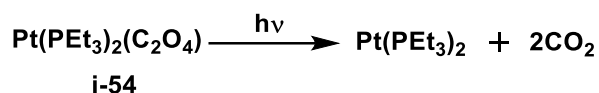
1.4.1 Oxalate complexes

It has been recognised that upon UV-irradiation of transition-metal oxalate complexes, irreversible fragmentation of the oxalate dianion occurs to give two molecules of carbon dioxide, with concomitant transfer of two electrons to two metal centers.⁸⁰ A well-studied and representative example is $[\text{Co}(\text{C}_2\text{O}_4)_3]^{3-}$, where photolysis leads to the reduction of two metal centres and the formation of Co(II) (Scheme 1.22).



Scheme 1.22. UV-irradiation of transition-metal oxalate complexes.

Trogler and co-workers proposed that photochemical reductive elimination of the oxalate ligand from $\text{Pt}(\text{C}_2\text{O}_4)\text{L}_2$ (L = triarylphosphine or trialkyl-) forms PtL_2 , a highly reactive Pt(0) 14-electron fragment, along with two molecules of carbon dioxide (Scheme 1.23).^{77,81}



Scheme 1.23. Photochemical reductive elimination of the oxalate ligand from $\text{Pt}(\text{PEt}_3)_2(\text{C}_2\text{O}_4)$ (**i-54**).

The 14-electron fragment was not observed directly, but its presence was inferred from the reaction of $\text{Pt}(\text{PEt}_3)_2(\text{C}_2\text{O}_4)$ (**i-54**) with ethene, to yield $\text{Pt}(\text{PEt}_3)_2(\text{C}_2\text{H}_4)$. Trogler postulated that upon photolysis of **i-54**, rapid transfer of two electrons from the oxalate ligand to the platinum occurs. Transfer of two electrons leads to the stable Pt(0) oxidation state, rather than the unstable Pt(I) oxidation state which would occur if only one electron was transferred to the metal.

Shortly after the initial report, Trogler covalently linked the photoactive **i-54** complex to a silica support (**i-55**) and demonstrated that it was effective as a hydrosilylation catalyst (Figure 1.5).⁷⁷

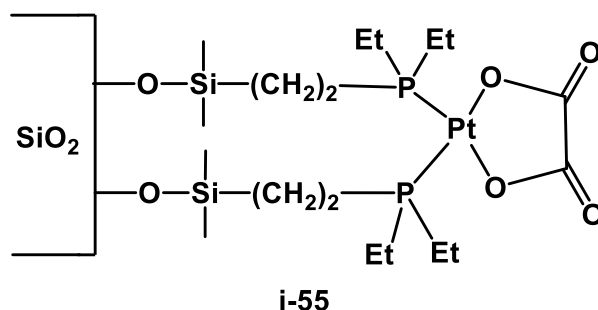


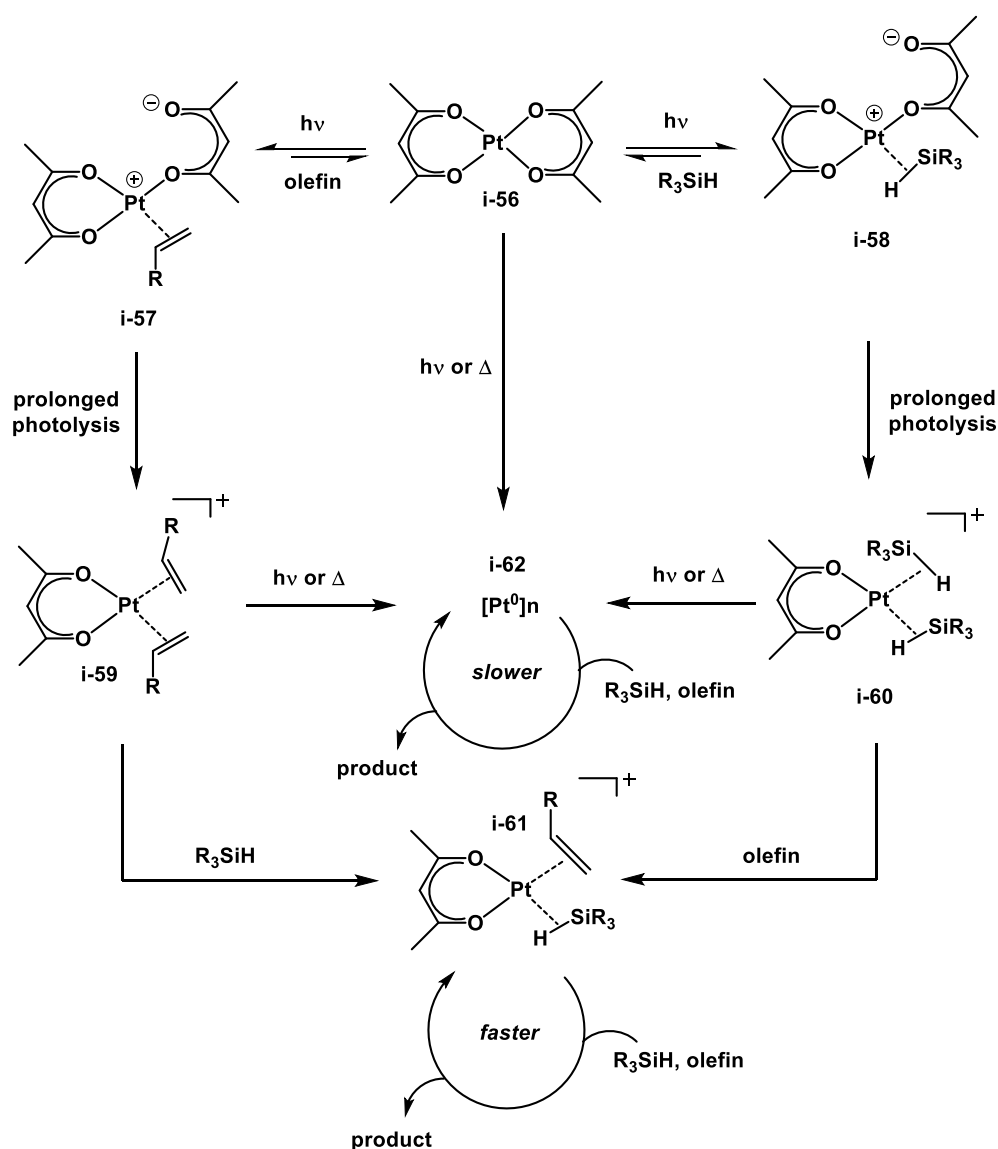
Figure 1.5. Complex **i-54** linked to a silica support to form **i-55**.

Unsurprisingly, Trogler found marked differences between the unsupported (**i-54**) and supported (**i-55**) bis(phosphine)platinum oxalates as hydrosilylation catalysts. In the photoactivated hydrosilylation reaction between $\text{MeCl}_2\text{Si-H}$ and hept-1-ene (irradiating the catalyst plus one substrate then adding the partner substrate post-irradiation), **i-55** showed no induction period, and a linear formation of product with time. In contrast, photoactivation of **i-54** in the same reaction showed a long induction period, followed by a rapid reaction. Moreover, addition of mercury to **i-55** had no effect on the catalytic activity, and an excess of olefin or the presence of a coordinating solvent was inhibitory for catalysis. The effect of mercury or coordinating solvent on **i-54** was unfortunately not disclosed. Trogler argued that the difference in kinetics for **i-54** could be attributed to the tendency of Pt(0) phosphine complexes to react with silanes and form catalytically inactive cluster compounds.⁸² According to Trogler, metal cluster formation was not possible with **i-55**, and hydrosilylation proceeds on monomeric active sites on the silica support.

1.4.2 Platinum bis(β -diketonates)

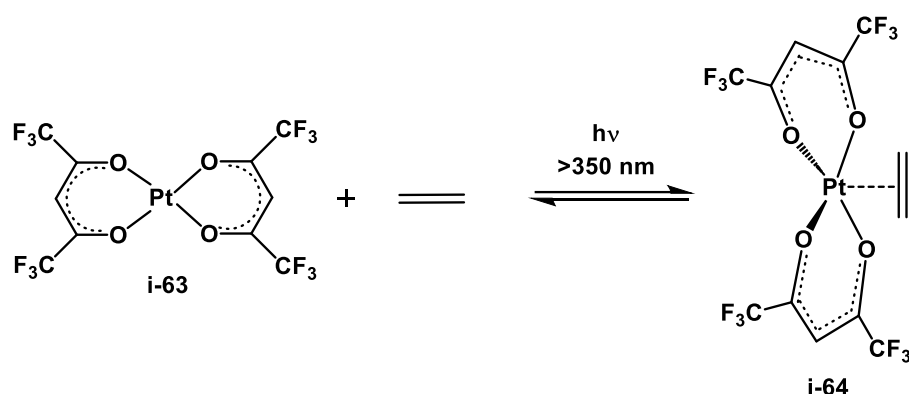
Lewis and Salvi were the first to investigate the mechanism of platinum bis(β -diketonates) as photoactivated hydrosilylation catalysts in 1995.⁷⁹ They postulated that short periods of irradiation of $\text{Pt}(\text{acac})_2$ (acac = acetylacetonate) (**i-56**) in the presence of either silane or olefin resulted in homolysis of the Pt–O bond to form a primary photoproduct (**i-57** or **i-58**), which was identified by ^1H NMR spectroscopy (Scheme 1.24). Upon termination of irradiation and addition of the complementary substrate, the primary photoproduct reverts back to **i-56** and no hydrosilylation product is formed. This suggests that the primary photoproduct is not the active catalyst. Continued irradiation of the primary photoproduct, however, leads to full dissociation of one of the acac ligands to give an unsaturated Pt(II) species (**i-59** or **i-60**), which can coordinate either two hydrosilanes or two olefins. Subsequent addition of the complementary substrate to this secondary photoproduct forms the active homogeneous catalyst (**i-61**), which in the

presence of excess silane or olefin, retains its catalytic activity for several hours. Lewis and Salvi found that upon irradiation of **i-56** in the absence of silane or olefin, or upon thermal decomposition of **i-56** in the presence or absence of silane and olefin, a less active heterogeneous catalyst is formed (**i-62**). The homogeneous nature of the active species was verified by showing that the catalyst formed upon irradiating **i-56** in the presence of silane or olefin was poisoned by DBCOT but only slightly inhibited by mercury, whereas the same solution but in the absence of irradiation and stirred in the dark overnight was completely inhibited by mercury, but unaffected by DBCOT.^{37,83}



Scheme 1.24. Formation of active catalysts using Pt(acac)₂ (**i-56**).

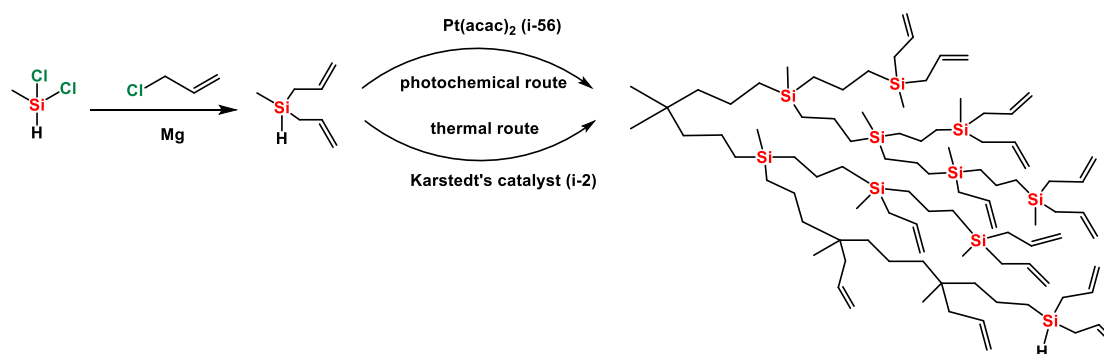
Subsequently, Neckers showed that upon irradiation of $\text{Pt}(\text{hfac})_2$ (hfac = hexafluoroacetylacetonate) (**i-63**) at 350 nm under an atmosphere of excess ethene, the isolable, trigonal bipyramidal complex, $\text{Pt}(\text{hfac})_2(\eta^2\text{-C}_2\text{H}_4)$ (**i-64**) was formed (Scheme 1.25).⁸⁴ Interestingly, Neckers reported that this complex could only be isolated if **i-63** was irradiated at 350 nm, as irradiation at the shorter wavelength of 300 nm led to initial formation of **i-64**, followed by rapid dissociation of the two hfac ligands. Neckers reported that no photoreaction occurred between **i-56** and ethene when the mixture was irradiated at 350 nm, and this was attributed to the inability of **i-56** to form a stable olefin adduct. This is consistent with the observation that **i-56** has higher thermal catalytic activity in the hydrosilylation process than does **i-63**, as the ability of **i-63** to form stable olefin adducts attenuates its activity.⁸⁵ When **i-64** was employed as a catalyst for the hydrosilylation reaction between triethylsilane and vinylsilane, full conversion to the hydrosilylation product was achieved after 2 hours, in the absence of irradiation.



Scheme 1.25. Reaction of $\text{Pt}(\text{hfac})_2$ (**i-63**) in the presence of ethene under UV-irradiation to form $\text{Pt}(\text{hfac})_2(\eta^2\text{-C}_2\text{H}_4)$ (**i-64**).

More recently, Huang and coworkers utilised **i-56** as a photocatalyst for the synthesis of hyperbranched polycarbosilanes and compared its activity with Karstedt's catalyst (**i-2**).⁸⁶ To compare the thermal and photochemical reaction times for the synthesis of polymer, **i-56** was continuously exposed to UV-light whilst Karstedt's catalyst was heated to 60 °C, since the latter is not amenable to photohydrosilylation (Scheme 1.26). By following the reaction by FT-IR spectroscopy, Huang showed that all of the Si-H groups were consumed in 40 min when **i-56** was

used as the photocatalyst, whereas consumption of the Si–H groups took 6 hours under thermal conditions using **i-2**. The highly branched polycarbosilane was characterised by ^1H , ^{13}C and ^{29}Si NMR spectroscopy, along with SEC/ MALLS (size exclusion chromatography/ multi angle laser light scattering), and Huang concluded that the same branching structure was formed irrespective of hydrosilylation *via* the thermal or photochemical route.



Scheme 1.26. Formation of hyperbranched polycarbosilanes using either Karstedt's catalyst (**i-2**) thermally or $\text{Pt}(\text{acac})_2$ (**i-56**) under photochemical conditions.

1.4.3 Trimethyl(β -dicarbonyl) platinum(IV) complexes

Fouassier and coworkers developed trimethyl(β -dicarbonyl) platinum(IV) (**i-65**) complexes as photocatalysts for the hydrosilylation of silicone polymers (Figure 1.6).⁷⁸ They were able to demonstrate that upon irradiation of these complexes with the substrates, active species were generated that rapidly catalysed the hydrosilylation reaction between pentamethyldisiloxane and oct-1-ene. Through simultaneous analysis by UV-visible and infrared spectroscopy, Fouassier proposed that the active species was homogeneous as during catalysis, two distinct bands appeared in the UV-vis spectrum at 272 and 335 nm which corresponded to the photoproduct. The disappearance of these bands coincided with the time taken to fully consume the alkene and silane substrate. After catalysis, there was evidence of new absorption bands at 400 and 420

nm, consistent with the formation of platinum colloids.⁸⁷ It was thus concluded that the colloidal platinum was not the active species.

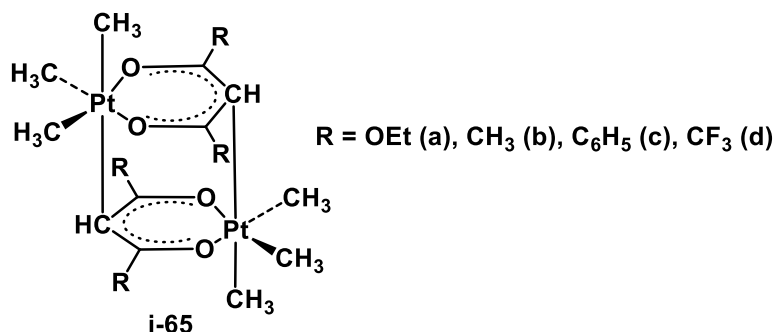


Figure 1.6. Dimeric structure of trimethyl(β -dicarbonyl) platinum(IV) (**i-65**) complexes found to be photocatalysts for the hydrosilylation of silicone polymers.

In addition to elucidating the nature of the active species when complexes based on **i-65** are employed as photocatalysts for hydrosilylation, Fouassier extended the study to demonstrate the practicality of these complexes in the hydrosilylation of industrial silicone polymers **i-66** and **i-67** (Figure 1.7). Using the initial rates method on the conversion–time profiles for various catalysts, it was elucidated that the hydrosilylation activity was enhanced by electron donating groups at the carbonyl C-atom of the β -dicarbonyl ligand. The order of reactivity was reported to be **i-65a** > **i-65b** > **i-65c**, **i-65d**. This was attributed to the increased stability of the light-promoted catalyst and increased resistance to thermal decomposition to platinum nanoparticles.

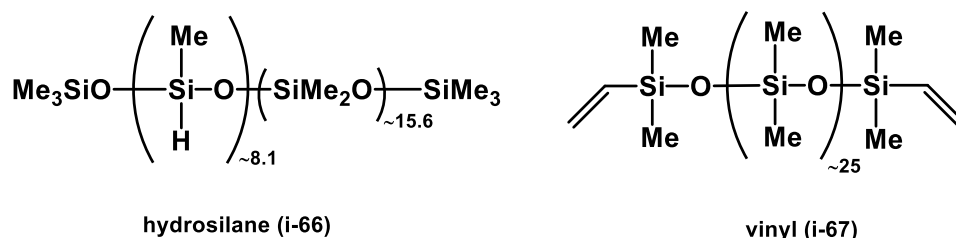


Figure 1.7. Industrial silicone polymers (**i-66** and **i-67**).

1.4.4 Cyclopentadienyl-platinum complexes

Cyclopentadienyl-platinum complexes (**i-48**) have already been discussed in this chapter as photoactivated catalysts for hydrosilylation (section 1.2.5).⁵⁴ Their highly efficient photochemical activity means that they are primed for photohydrosilylation and consequently, they have been employed extensively in industry as catalysts in light-curable silicone elastomer compounds for applications such as dental impressions and adhesives.^{5,88,89} It has been reported that the gel-time (time required to achieve a state in which the formulation no longer flows) under UV-light is between 16 and 40 s (Pt at 200 ppm), whilst without irradiation under ambient conditions, the gel-time is more than 1550 hours.⁹⁰ This renders this catalyst the benchmark system with regards to exploiting a latency period.

Marchi and coworkers recently studied $(\eta^5\text{-C}_5\text{H}_4\text{CH}_3)\text{Pt}^{\text{IV}}(\text{CH}_3)_3$ (**i-68**) as a photocatalyst for hydrosilylation in the presence of 2-chlorothioxanthen-9-one (CTX, **i-69**) as a photosensitizer (Figure 1.8).⁸⁹ Sensitisers are often employed to either increase the overall rate of the curing process at a given wavelength of initiating radiation, by absorbing light energy and transferring it to the initiator, or to shift the optimum effective wavelength of the initiating radiation to longer wavelengths, for example, into the visible region.⁹¹ The hydrosilylation reaction between poly(methylhydrogenosilane) (**i-70**) and vinyl dimethylsiloxane (**i-71**) was studied in the presence of 1000 ppm **i-68** / **i-69** under continuous visible light exposure (380 – 515 nm) and separately under continuous UV-light exposure for comparison. It was found that under visible light exposure in the absence of **i-69**, **i-68** (1000 ppm) would not activate and there was no hydrosilylation product, whereas in the presence of 4000 ppm **i-69**, 55% conversion to the hydrosilylation product was achieved in 400 seconds. By contrast, exposure of the same formulation to UV-light resulted in 80% conversion to the hydrosilylation product in 150 seconds.

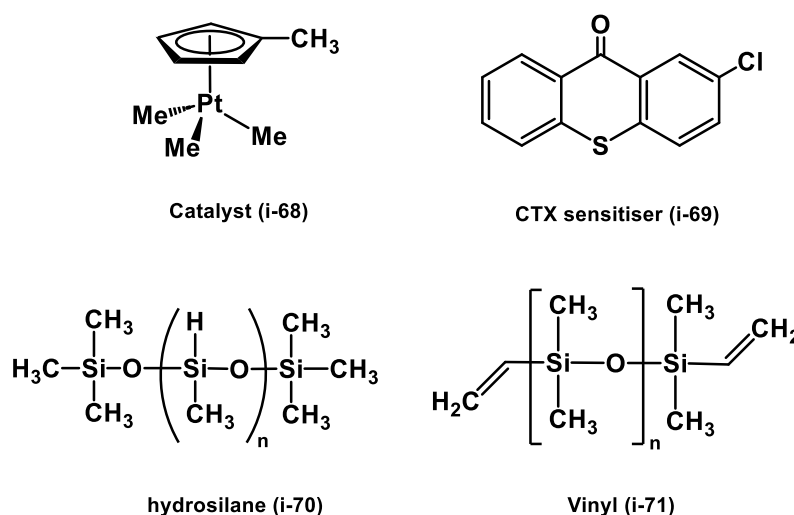


Figure 1.8. Structure of $(\eta^5\text{-C}_5\text{H}_4\text{CH}_3)\text{Pt}^{\text{IV}}(\text{CH}_3)_3$ (**i-68**) as a photoactivated hydrosilylation catalyst along with the structures of 2-chlorothioxanthen-9-one (**i-69**) photosensitiser and the industrial silicone polymers (**i-70** and **i-71**).

The presence of dark-curing, which is the occurrence of curing after the irradiation source is removed, was also evaluated by Marchi and coworkers after 10, 30 and 60 seconds of visible light exposure (1000 ppm **i-68** / 4000 ppm **i-69**). After 60 seconds of exposure, the conversion increased from 35% to 60% over the course of an hour, demonstrating that the catalyst remained active after long periods of time, i.e. a photoactivated catalyst. The thermal stability of the visible light cured material was shown by thermogravimetric analysis (TGA) to be comparable to that of the UV-cured material, with the main degradation starting at 300 °C and resulting in about 70% residue at 800 °C.

More recently, Xiang *et al.* investigated the influence of a variety of photosensitisers on photoactivated hydrosilylation in the presence of **i-68**, in an effort to reduce the required catalyst loading of platinum for industrial application (Figure 1.9).⁹² They first studied the reaction between **i-70** and **i-71** under 100 s UV-light exposure (365 nm LED) at different catalyst loadings (50 – 400 ppm), and discovered that 400 ppm of **i-68** was required to achieve full conversion to the hydrosilylation product in 300 seconds post-irradiation.⁵ At 50 ppm catalyst loading, conversion did not exceed 50% at 300 seconds post-irradiation. To study the effect of the

photosensitisers, Xiang and coworkers used **i-68** at 100 ppm, with 100 s UV-light exposure. The study revealed that introduction of naphthalene, fluorene, phenanthrene or pyrene increased the catalytic activity up to a point, but then became inhibitory. The incorporation of other photosensitisers, biphenyl, anthracene and perylene led to a decrease in catalytic activity. Xiang argued that a potential reason for some photosensitisers inhibiting catalysis is due to their insolubility in the monomers used for photopolymerisation, meaning that light energy cannot effectively be transferred to the catalyst and promote polymerisation.⁹¹ In addition, the cured samples were analysed in the presence and absence of photosensitiser by photo-differential scanning calorimetry (P-DSC), tensile tests and TGA. It was found that the presence of naphthalene in the formulation during curing led to an increased photopolymerisation rate (0.15 vs 0.09 mmol.g⁻¹.s⁻¹), higher tensile strength (0.23 vs 0.17 MPa) and a higher glass transition temperature (-115 vs -121 °C). The superior properties were attributed to the higher conversion and cross-linking density of the naphthalene-assisted reaction. Overall, this work demonstrated the opportunity to fabricate complicated architectures using photolithography in the presence of the photoactivated **i-68** / naphthalene system.

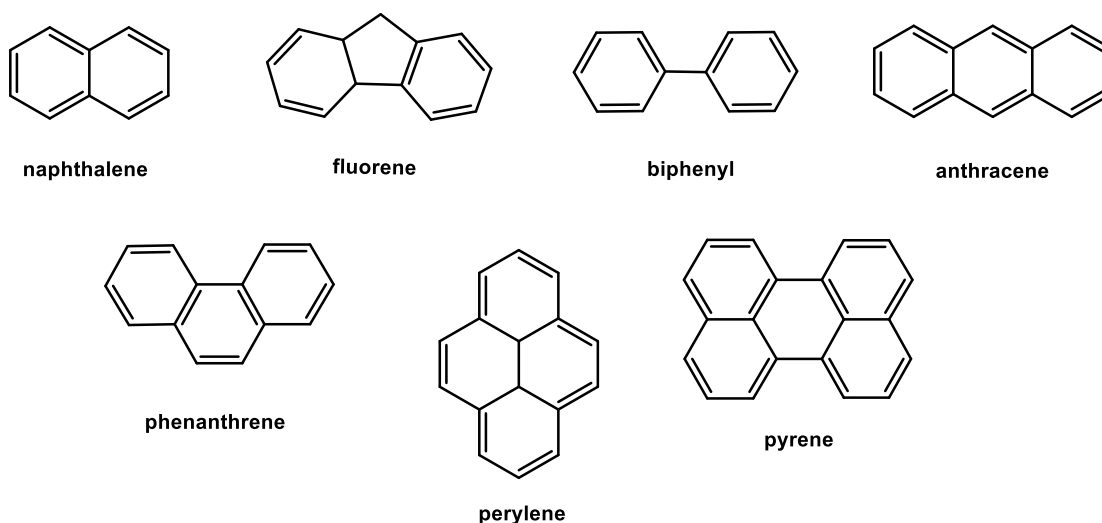


Figure 1.9. Photosensitisers used to facilitate hydrosilylation.

1.5 Summary and outlook

The preceding sections have provided a comprehensive overview of the hydrosilylation reaction and outlined its industrial importance for the production of organosilicon compounds. Despite a rich history of catalyst development, substrate scope exploration and practical application in industry, there are still serious concerns about the exact nature of the hydrosilylation mechanism.¹ This is largely due to the presence of highly active platinum intermediates in the catalytic cycle. Considerable attention has been devoted to understanding the mechanism of thermally activated catalysts, whilst kinetic and mechanistic studies of photoactivated hydrosilylation reactions have been relatively scarce. Photoactivated catalysts for the hydrosilylation of silicone polymers to produce cross-linked silicones are of particular interest as they offer spatial and temporal control, as well as the potential for increased shelf-life of pre-mixed catalyst / substrate mixtures.^{5,88} Important applications of such catalysts come from the production of fast-curing films, and in additive or continuous manufacturing processes. Ideally such systems combine high pre-catalyst stability in the silane/vinyl polymer formulation (latency) with rapid photoactivation, to afford a catalyst that works at low loadings with fast rates of turnover.⁵ There are currently very few known catalyst systems that harness these features, and those that do, i.e. CpPtMe₃ or Pt(acac)₂ based systems, are either highly toxic or suffer from poor solubility in the silicone substrates.^{85,89} Development of a new series of photoactivated catalysts, along with obtaining mechanistic insight, will enable the rational design of improved catalysts for photoactivated hydrosilylation, leading to improved catalytic activity and selectivity. This will ultimately lead to the development of a diverse array of organosilicon compounds with enhanced functionalities.

The aim of this work is to develop a new series of photoactivated hydrosilylation catalysts that overcome the current drawbacks of the existing catalysts. These catalysts will ideally show latent reaction kinetics under photohydrosilylation conditions, to make them suitable for the industrial requirements. A further aim is to conduct a detailed kinetic and mechanistic study on such

complexes to gain insight into the mechanism of photoactivated hydrosilylation reactions, as this is an area that has been relatively understudied. It is hoped that this study will shed light on the photoactivated hydrosilylation reaction and inspire future investigations that pave the way for new advancements in organosilicon chemistry.

Chapter 2 – Synthesis, Structure and Characterisation of Pt(II) Complexes for Hydrosilylation

2.1 Preamble

As discussed extensively in chapter one, the hydrosilylation reaction is one of the most useful catalytic transformations in homogeneous catalysis.¹ Organosilicon products derived from olefin hydrosilylation are usually added to a diverse range of consumer products, such as car tyres, contact lenses, and paints as performance enhancers.^{3,5,93} Since the first report of the hydrosilylation reaction in the academic literature, platinum-based catalysts have been the most widely used owing to their high activity, selectivity and tolerance to processing conditions.⁹⁴ Karstedt's catalyst remains the benchmark catalyst in industrial hydrosilylation, due to its excellent activity and solubility in many polysiloxane compositions.^{2,18} In the reaction between hexamethylsiloxymethylsilane and oct-1-ene using Karstedt's catalyst, the turnover frequency (TOF) was $5.2 \times 10^6 \text{ h}^{-1}$ and the turnover number (TON) was 0.9×10^6 .⁹⁵ There are, however, certain disadvantages associated with using platinum-based catalysts on such a large industrial-scale process. For example, due to the viscous properties of many organosilicon products, the platinum can easily become trapped in the final product and is challenging to recover.^{3,93} Combined with the low crustal abundance and high price of this noble metal, there has been a long endeavour to develop less expensive catalysts based on more earth abundant metals or using lower catalyst loadings of platinum-based systems.^{1,3} Despite intensive research on lower priced transition metals such as cobalt and iron as hydrosilylation catalysts, platinum-based catalysts remain unmatched in catalytic activity and are still therefore first-choice for industrial hydrosilylation.^{3,13,18,20}

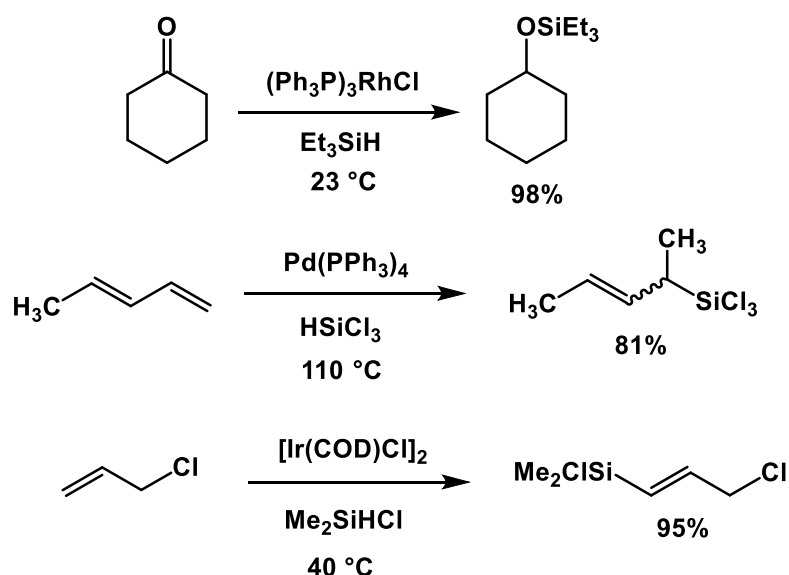
The development of a hydrosilylation catalyst that can be switched by external triggers presents a huge challenge since many hydrosilylation reactions will proceed spontaneously under ambient conditions in the presence of a catalyst.³ For some processes such as additive manufacturing

however, it is required to have the catalyst, vinylsiloxane and Si–H functionalised siloxane as a one component formulation that is shelf-stable for multiple months.¹ For specialised and growing demands of some organosilane products such as release liners and adhesives, there is a drive to develop systems that are unreactive under ambient conditions but proceed rapidly upon exposure to an external trigger. This concept is known as latency and will be explored in more detail in chapter three. Thermal triggering of catalysts has so far been the most common method employed in industry to exercise precise spatiotemporal control, and this has been achieved with the use of catalyst inhibitors and dormant precatalysts.¹ Light and UV-irradiation also present an attractive stimulus to achieve latency, especially when the required curing temperature of the organosilicon compounds is close to room temperature.⁷³ The importance of this methodology is shown by the significant number of examples of photo-triggerable hydrosilylation catalysts reported in the literature. Unfortunately however, many of these catalysts suffer from major drawbacks such as being highly toxic, having poor solubility in the polysiloxane substrates or showing low activity upon phototriggering.^{5,54,79,96,97}

This chapter details a brief overview of important catalysts which have been developed for hydrosilylation, with particular emphasis on those used in photoactivated hydrosilylation reactions. The rationale behind the use of Pt(II)-salicylaldimine-phenylpyridine complexes, Pt(sal)(ppy), the subject of this thesis, as photoactivated hydrosilylation precatalysts is discussed, along with details of their synthesis. Subsequently, the spectroscopic and structural properties obtained for the Pt(sal)(ppy) complexes are presented. In the following chapters, an in-depth kinetic and mechanistic study using the Pt(sal)(ppy) complexes as photoactivated hydrosilylation precatalysts will be detailed.

2.2 Platinum-based catalysts for hydrosilylation

Among all the metals active in hydrosilylation reactions, platinum is superior in terms of activity and selectivity.¹ Many catalysts based on other transition metals have been developed for hydrosilylation, and different catalysts are employed depending on the desired utilisation.¹ Platinum complexes are most commonly used for the hydrosilylation of alkenes, whilst rhodium is more efficient for carbonyl hydrosilylation (Scheme 2.1).^{1,98,99,100} Palladium complexes have been reported to efficiently catalyse the hydrosilylation of conjugated dienes, and iridium is most selective for the hydrosilylation of allyl electrophiles.^{1,7}



Scheme 2.1. Hydrosilylation of cyclohexanone with Wilkinson's catalyst (top), $\text{Pd}(\text{PPh}_3)_4$ catalysed hydrosilylation of 1,3-pentadiene (middle) and $[\text{Ir}(\text{COD})\text{Cl}]_2$ catalysed hydrosilylation of allyl chloride.

All of these metals are relatively expensive at an average price of \$962 (Pt), \$1,924 (Pd), \$11,366 (Rh), \$3488 (Ir) and \$421 (Ru) per troy oz (1 troy oz = 31.1 g) in the past 5 years (Figure 2.1).¹⁰¹ However, their efficiency is unmatched by more earth-abundant metals, so they are still first choice for industrial hydrosilylation.

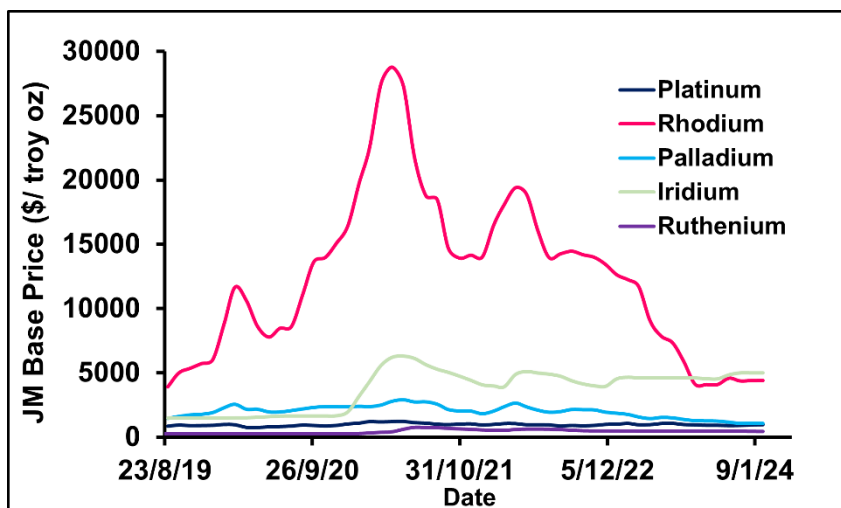


Figure 2.1. Monthly average metal prices between 2019 and 2024 in \$ / troy oz (1 troy oz = 31.1 g). Average prices: **Pt**, \$962.52, **Pd**, \$1,923.79, **Rh**, \$11,366.34, **Ir**, \$3,487.52, **Ru**, \$420.89.¹⁰¹

As discussed in chapter one, there has been significant research effort directed towards developing platinum-based hydrosilylation catalysts since Speier's report in 1957.⁹⁴ Selected examples of important platinum-based complexes that have received special attention for hydrosilylation reactions are shown in Figure 2.2. Whilst Speier's catalyst (**2.1**) exhibits extremely high catalytic activity at low loadings, it shows long induction periods and poor solubility in polysiloxane mixtures.⁹³ Furthermore, *in situ* reduction of hexachloroplatinic acid to the active platinum(0) species can be dangerous on a large scale, and effective heat dissipation is challenging in large reactors.¹⁶ This can lead to thermal degradation of the catalyst or potential explosions. Karstedt's catalyst (**2.2**) was developed in 1973 and remains the most widely used industrial catalyst for the hydrosilylation of alkenes.^{1,18} This is attributed to its extremely high catalytic activity and better solubility in siloxane substrates than **2.1**.⁶ Furthermore, **2.2** does not require *in situ* reduction. Despite **2.2** being the most well-established hydrosilylation catalyst, it presents several limitations. For instance, the divinylsiloxane ligand is labile which can lead to facile decomposition to platinum colloids upon prolonged storage, and this can lead to discolouration in the end products.^{102,103} These colloids also give rise to unwanted side reactions such as alkene hydrogenation and isomerisation, resulting in increased product cost and waste,

as distillations are required to achieve the desired purity of the final product.⁹³ Marko and colleagues prepared platinum(0) complexes bearing *N*-heterocyclic carbene (NHC) ligands (**2.3**) in 2002 to address the issue of colloid formation.²⁰ Although these complexes generally show lower catalytic activity than **2.2**, they offer the advantage of no colloid formation in addition to improved stability. The success of these complexes in hydrosilylation prompted the development of many metal-based catalysts bearing NHC ligands.^{20,104} More recently, Nolan reported that platinum(II)-thioether-based precatalysts (**2.4**) were effective in hydrosilylation.¹⁰⁵ These complexes are easily synthesised, show comparable selectivity to **2.3**, and can be used at very low catalyst loadings (0.00001 mol%; 100 ppb). Whilst all of these complexes represent significant milestones in the advancement of hydrosilylation catalysts, it should be highlighted that all complexes require heating, often to temperatures >80 °C, to achieve good conversions to the hydrosilylation products. Platinum-based catalysts that can be activated by irradiation at room temperature have been relatively understudied compared with thermally activated catalysts, and development of these types of catalysts are needed for new and emerging applications in polymer chemistry.³

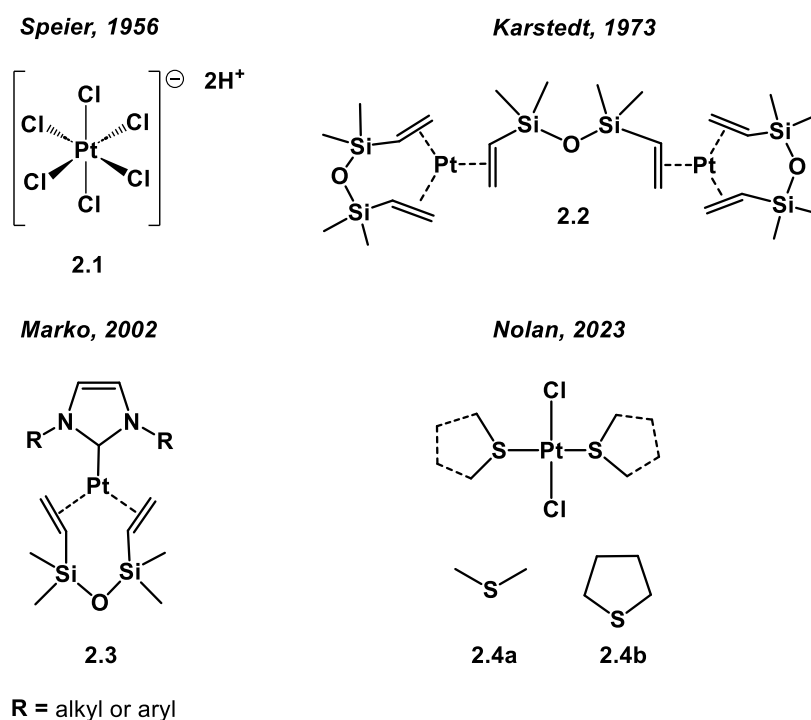


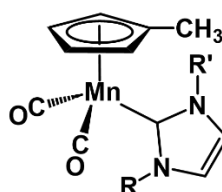
Figure 2.2. Selected platinum-based thermal hydrosilylation catalysts.^{13,18,20,105}

2.3 Light-initiated catalysts for hydrosilylation

The silicones industry consumes 5.6 metric tons of platinum per annum, so intensive research efforts have been devoted to developing low-cost transition metal catalysts for hydrosilylation.^{3,7} Other motivations to shift towards more earth abundant metals for hydrosilylation are the toxicity of heavy metals, and the environmental consequences associated with mining elements of scarce abundance in the Earth's crust.⁹³ One particular field of interest has been the development of earth-abundant metal catalysts that are switchable. This means that they should be unreactive under ambient conditions but show excellent catalytic activity upon exposure to irradiation.¹ This is a requirement for certain applications such as the manufacture of release coatings, that require the catalyst to be stored with the vinylsiloxane and Si-H functionalised siloxane for a number of months. Early approaches towards photoactivated hydrosilylation focused on various metal carbonyls such as Cr(CO)₆, Mo(CO)₆, Fe(CO)₅ and Ni(CO)₄.⁹⁶ Unfortunately however, using these complexes in hydrosilylation led to poor conversions, poor selectivity and in some cases, aggregation of the metal. This amounts to increase costs, as distillations are then required to purify the final product.⁹³ More recently, Sortais and colleagues prepared a series of manganese(I) NHC complexes that were shown to be successful precatalysts for the hydrosilylation of various carbonyl compounds under UV irradiation (Figure 2.3).¹⁰⁶ All complexes **2.5** to **2.10** at 1 mol% loading catalysed the hydrosilylation reaction between Ph₂SiH₂ and acetophenone at room temperature under constant UV irradiation (350 nm), and showed no activity in the absence of irradiation. There were marked structure / activity relationships observed for these complexes. After 2 hours, **2.7** promoted only 10% conversion, whereas **2.8** and **2.9** had catalysed 97% conversion, demonstrating that the *N*-mesityl group on the NHC ligand promotes higher catalytic activity. Precatalyst **2.9** was then taken forward for hydrosilylation reactions between Ph₂SiH₂ and a variety of aldehydes under constant UV irradiation. The reduction of benzaldehyde and its derivatives substituted in the *para*-position by either electron donating groups such as NMe₂ or electron withdrawing groups such as CN

proceeded within 1 h and very high conversions were achieved (>97%). However, it was found that the reduction of *meta*-fluorobenzaldehyde required 8 h of constant irradiation to achieve a similar level of conversion. The substrate scope was also expanded to include a variety of ketones, and **2.9** (1 mol%) was proven to successfully catalyse the hydrosilylation reaction between Ph_2SiH_2 and various acetophenone derivatives substituted in the *para*-position within 4 h under constant UV irradiation. Less reactive substrates such as acetylferrocene and cyclic ketones were included in the substrate scope, and these required 24 h of constant UV irradiation to achieve full conversion.

Sortais, 2014



	2.5	2.6	2.7	2.8	2.9	2.10
R	Me	<i>i</i> -Pr	Cy	Mes	Mes	Dipp
R'	Me	<i>i</i> -Pr	Cy	Me	Mes	Dipp

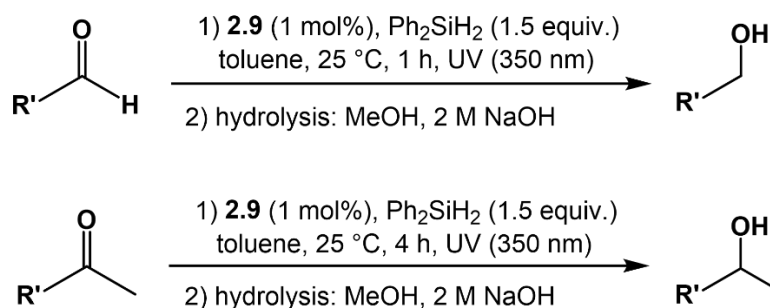


Figure 2.3. Manganese(I) NHC complexes as photoactivated hydrosilylation catalysts.¹⁰⁶

Kumar and colleagues also prepared a series of cationic iron(II) complexes bearing cyclopentadienyl (Cp) and NHC ligands that were shown to be effective catalysts for the

hydrosilylation reaction between PhSiH_3 and a variety of aldehydes and ketones (Figure 2.4).¹⁰⁷ All complexes (**2.11** to **2.15**) required activation by constant exposure to visible light ($\lambda = 400 - 700 \text{ nm}$). For the reaction between PhSiH_3 and benzaldehyde using the iron complexes (2 mol%) at 30°C , **2.11** yielded 68% conversion after 3 h of reaction time, whereas only 15% and 6% conversions were observed when using **2.12** and **2.13**. The reactions with the latter two catalysts under constant irradiation required 17 h to achieve full conversion. Using **2.14** under the same conditions led to 90% conversion within 3 h of reaction time, whereas **2.15** gave only 44% conversion. For the reaction between PhSiH_3 and acetophenone, it was found that the reaction mixtures also required heating to 70°C for 17 h to achieve good conversions (72 – 98%) in the presence of **2.11** – **2.15**.

Kumar, 2014

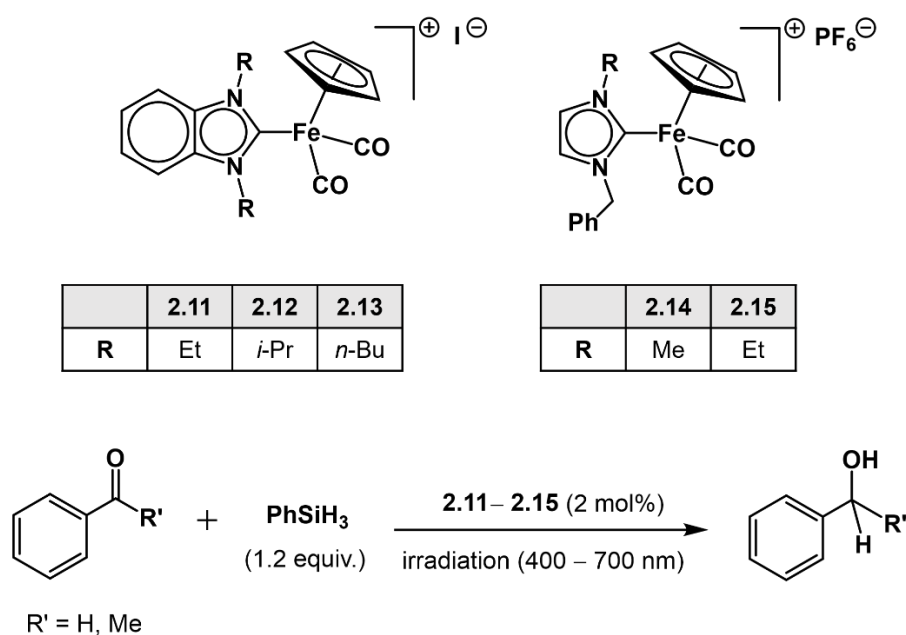


Figure 2.4. Iron(II) NHC complexes as photoactivated hydrosilylation catalysts.¹⁰⁷

Despite intensive research efforts to develop more earth-abundant metal catalysts for hydrosilylation, platinum-based complexes still dominate the field. The review by Radchenko and Ganachaud summarises a variety of light-induced platinum-based hydrosilylation catalysts and their applications in the silicone industry.⁵ As discussed in more detail in chapter one, Troglér

pioneered the first platinum-based photoactivated hydrosilylation catalyst, namely the platinum / oxalate complex, $\text{Pt}(\text{C}_2\text{O}_4)_2$ (**2.16**) (Figure 2.5).⁸¹ This was proposed to operate via photochemical reductive elimination of the oxalate ligand from **2.16** to form PtL_2 , a highly reactive 14-electron Pt(0) fragment, along with two molecules of carbon dioxide. Since then, platinum-based complexes bearing a variety of ligands have been prepared as photoactivated hydrosilylation catalysts, as shown in Figure 2.5. Lewis and Salvi studied Pt bis(β -diketonate) complexes (**2.17**) as photoactivated hydrosilylation catalysts in 1995 and reported that irradiation ($\lambda < 300$ nm) initially yields a highly active homogenous catalyst, which is thermally converted to a less active heterogeneous catalyst (see chapter one).⁷⁹ Boardman first investigated the $\text{Pt}(\text{CpMe})\text{Me}_3$ complex (**2.18**) in 1992 and proposed that the active species generated from this complex is a heterogeneous platinum colloid since the active catalyst was poisoned by mercury but not inhibited by dibenzo[a,e]cyclooctatetraene.⁵⁴ Compounds based on the **2.17** and **2.18** frameworks have been studied extensively in industry and academia alike for their ability to photocure silicone polymers.⁵ Both classes of complex have been used as catalysts to produce silicone products for applications such as silicone gaskets, optical devices and light-emitting-diode (LED) encapsulating materials. In 2021 alone, three patent applications were published for the use of complexes based on **2.18** in the production of transparent silicone resins under UV-triggering conditions.^{108,109,110} Although these complexes are highly active upon activation by UV-irradiation and can be used at very low catalyst loadings (5 ppm), they are very volatile and highly toxic. Another class of photoinitiators for hydrosilylation was introduced by Fouassier in 1996, where trimethyl(β -dicarbonyl) platinum(IV) complexes (**2.19**) were found to be effective homogeneous catalysts under UV-irradiation ($\lambda > 300$ nm) for the hydrosilylation reaction between pentamethyldisiloxane and oct-1-ene.⁷⁸ The practicality of these complexes was also assessed using industrial silicone polymers and it was reported that catalytic activity was enhanced by the presence of electron donating groups at the carbonyl C-atom of the β -dicarbonyl ligand. A few years later, Neckers showed that upon irradiation of $\text{Pt}(\text{hfac})_2$ (hfac = hexafluoroacetylacetonate) with 350 nm light under an atmosphere of excess ethene, the isolable

trigonal bipyramidal complex, $\text{Pt}(\text{hfac})_2(\eta^2\text{-C}_2\text{H}_4)$ (**2.20**), was formed.¹¹¹ This complex successfully catalysed the hydrosilylation reaction between triethylsilane and vinylsilane in 2 h, in the absence of irradiation.

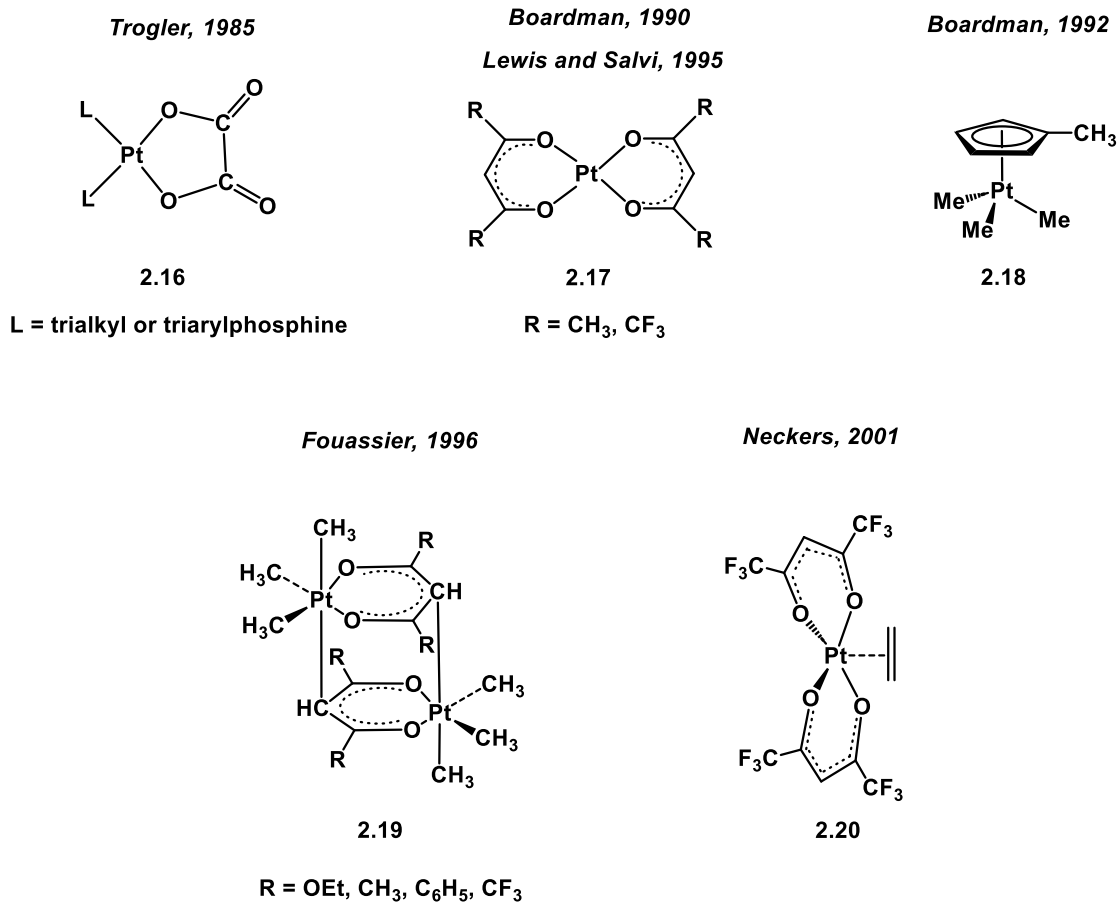
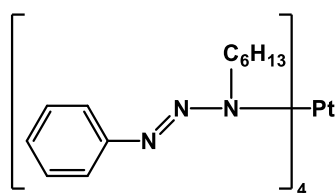


Figure 2.5. Selected platinum-based photoactivated hydrosilylation catalysts.^{54,78,79,81,84}

The past three decades have seen a further development of platinum-based photoactivated hydrosilylation catalysts bearing different ligand sets, as shown in Figure 2.6. Wokaun and colleagues studied the $\text{Pt}(\text{PhNNN}(\text{CH}_2)_5\text{Me})_4$ complex (**2.21**) in 1996 and showed that upon irradiation with 370 nm light, the photolabile ligands decompose which generates a highly reactive and coordinatively unsaturated platinum species.⁹⁷ This species could undergo the addition of Si–H fragments, leading to hydrosilylation in the presence of an alkene substrate. Skvortsov and colleagues later investigated $\text{Pt}(\text{L}_2)\text{Cl}_2$ complexes under thermal and photochemical conditions as hydrosilylation catalysts.¹¹² Under thermal conditions (55 °C), the

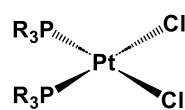
reaction rate decreased in the order *cis*-[Pt(P(CH₃)₂Ph)₂Cl₂] (**2.22a**) > *cis*-[Pt(PPh₃)₂Cl₂] (**2.22c**) > *cis*-[Pt(PBu₃)₂Cl₂] (**2.22b**) for the reaction between heptamethylvinyltrisiloxane and tetramethyldisiloxane. The reaction also had a significant induction period which increased in the following ligand order: Ph₃P < PhMe₂P < Bu₃P, in parallel with the σ -donor ability of the ligands. Under photochemical conditions ($\lambda < 280$ nm), significant accelerations in catalytic activity were observed. In the case of **2.22a**, the reaction took 205 min to reach completion under thermal conditions, whereas under photochemical conditions with 1 min irradiation, this time was reduced to 139 min. Another notable difference under photochemical conditions was that the induction period increased in the order: PhMe₂P < Bu₃P < Ph₃P. It was found that the optimal irradiation time was 1 min, as longer or shorter periods of irradiation resulted in longer induction periods. Prolonged irradiation times (80 min) were found to destroy the active catalyst, giving rise to inactive forms of the metal complex. In 2013, Ruhland and colleagues developed a novel platinum hydrosilylation catalyst that contained the photoactive moiety in the outer ligand sphere of the complex (**2.23**).⁷¹ Upon irradiation ($\lambda = 300$ nm), this moiety reacts irreversibly with a part of the inner ligand sphere, releasing a free coordination site and activating the precatalyst. This novel concept presented the opportunity to tune the catalytic activity based on the structure of the ligands in the outer ligand sphere, and different functional groups exhibited different catalytic activity upon irradiation.

Wokaun, 1996



2.21

Skvortsov, 2004

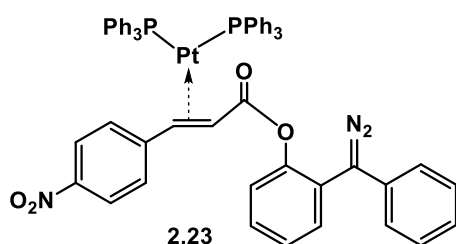


2.22

R = (CH₃)₂Ph, (CH₂)₃CH₃, Ph

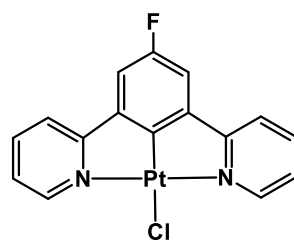
a b c

Ruhland, 2013

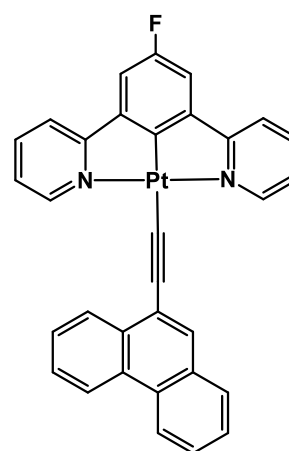


2.23

Mata, 2023



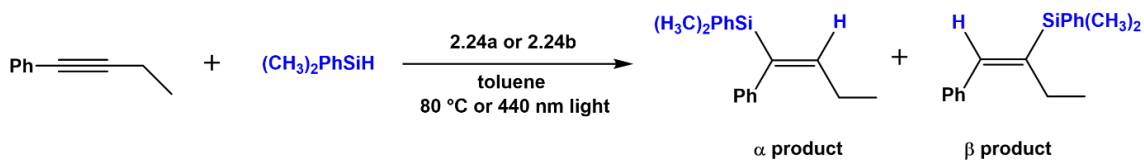
2.24a



2.24b

Figure 2.6. Further developments of platinum-based photoactivated hydrosilylation catalysts.^{71,72,97,112}

More recently, Mata and colleagues prepared two platinum pincer complexes that were found to be effective catalysts for the hydrosilylation of alkynes under thermal (80 °C) and photochemical (440 nm, blue light) conditions (see).⁷² For the thermal hydrosilylation reaction between 1-phenyl-1-butyne and dimethylphenylsilane, the α/β selectivity observed was 71/29 and 63/37 for **2.24a** and **2.24b**, respectively (Figure 2.7). The selectivity was enhanced when using visible light (440 nm) to promote catalysis under milder conditions ($\alpha/\beta = 81/19$ for **2.24a** and **2.24b**).



Cat (mol%)	Temp (°C)	hν λ (nm)	Time (h)	Yield (%)	Selectivity (%) (α/β)
2.24a (0.7)	80	-	7	97	71/29
2.24b (0.7)	80	-	7	98	63/37
2.24a (0.7)	r.t.	440	2	99	81/19
2.24b (0.7)	r.t.	440	2	98	81/19

Figure 2.7. Thermal and photochemical hydrosilylation results under various conditions using Mata's complexes, **2.24a** and **2.24b**.

Under thermal conditions, a normal isotope effect was observed ($k_{\text{H}}/k_{\text{D}} = 1.2$), whilst an inverse isotope effect was observed under photochemical conditions ($k_{\text{H}}/k_{\text{D}} = 0.9$).⁷² This led to the suggestion that different mechanisms are operating under the different conditions. For the thermal reaction, catalysis is proposed to proceed homogeneously via an organometallic silane complex, whilst a radical-mediated pathway is suggested for the reaction under photochemical conditions (Figure 2.8). First, $[(\text{NCN})\text{PtX}]$ (**2.25**) absorbs blue light to form the triplet state excited species, $[(\text{NCN})\text{PtX}]^*$ (**2.26**). Then, homolytic splitting of the Pt–X bond forms the radical (**2.27**), which abstracts a hydrogen atom from the Si–H bond to generate a silyl radical along with the formation of the hydride complex, $[(\text{NCN})\text{PtH}]$ (**2.28**), through a hydrogen atom transfer (HAT) process. Finally, addition of the silyl radical to the alkyne forms a radical vinyl species, which undergoes another HAT process to deliver the hydrosilylation products (**2.29**). Supporting evidence for this mechanism was obtained by the observation that trityl tetrafluoroborate, a hydride abstractor, completely inhibited the reaction. This provided indirect evidence that platinum hydrides were plausible intermediates. Interestingly, continuous irradiation of the catalytic reaction was required for productive catalysis under the photochemical conditions,

which confirms that light plays a crucial role in the activation step, and throughout the course of the reaction.

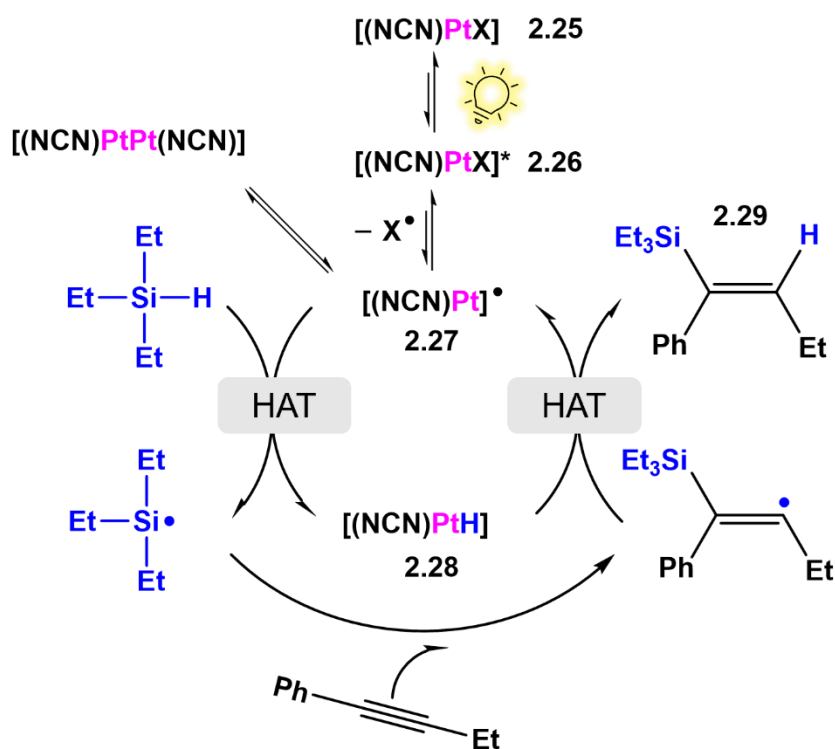


Figure 2.8. Proposed mechanism for photohydroosilylation using Mata's complexes.⁷²

As discussed above, there have been many examples of photoactivated catalysts and photocatalysis systems for hydrosilylation over the past few decades. The former refers to a situation where the photochemical reaction generates an active species that participates in a thermal catalytic reaction, whilst the latter refers to a system that requires continuous irradiation in order to promote productive catalysis. Despite a whole variety of complexes having been explored, there has been relatively limited attention paid to any latency periods prior to UV-irradiation or indeed a detailed kinetic analysis of the subsequent catalysis. Furthermore, there has been relatively little focus on square-planar Pt(II) complexes for the photoactivated hydrosilylation of alkenes. The very few studies that are available are often performed under conditions that are drastically different than those employed industrially and are also not consistent with one another. In the following sections of this chapter, the rationale behind the

use of Pt(sal)(ppy) complexes, shown in Figure 2.9, as hydrosilylation precatalysts will be discussed. The synthesis of these complexes will also be outlined, along with their spectroscopic and structural features. The subsequent chapters will investigate the use of these complexes as hydrosilylation precatalysts under thermal and photochemical conditions, and a detailed kinetic and mechanistic study will be presented. It is hoped that this study will provide valuable insight into platinum mediated photohydrosilylation, as detailed kinetic and mechanistic investigations in this area are scarce in the academic and patent literature.

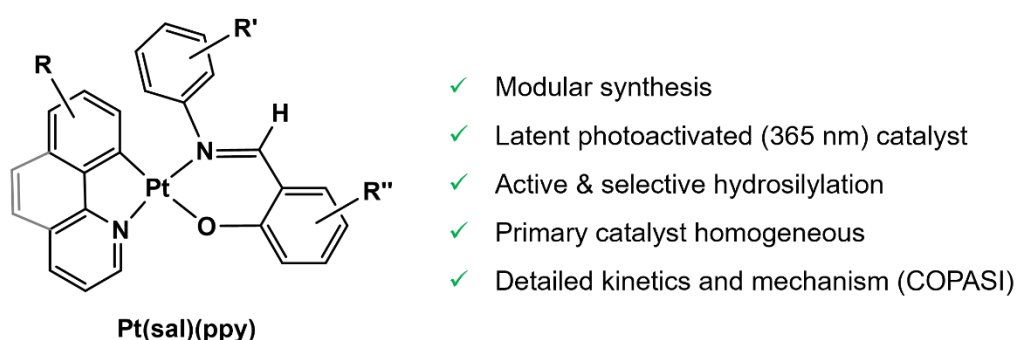


Figure 2.9. General structure and advantages of complexes synthesised herein.

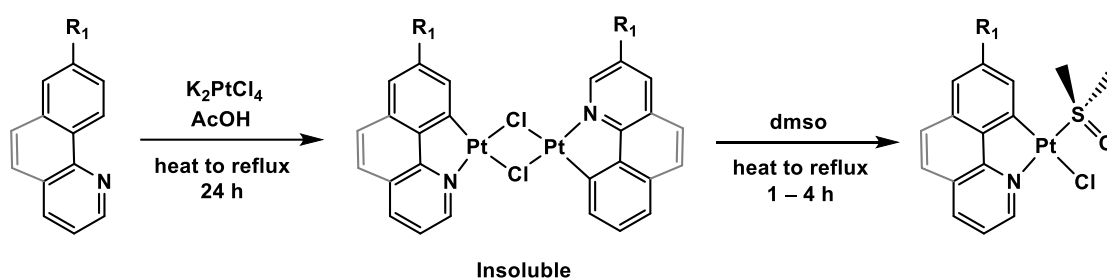
2.4 Preparation and characterisation of Pt(ppy)(dmsO)Cl complexes

The d^8 platinum(II) complexes containing phenylpyridine and Schiff base ligands are good starting points for photochemical activation as modulation of the photophysical properties can be fine-tuned by subtle changes in ligand design.^{113,114} Cyclometalated complexes based around Pt(sal)(ppy) have well established photophysical properties and have been shown to display aggregation-induced phosphorescent emission (AIPE).^{113,114} Furthermore, they are considered to have low cytotoxicity and offer potential for hemilabile reactivity profiles through decoordination of the imine group.^{113,115} This is important as the mode of activation for photohydrosilylation is anticipated to proceed via decoordination of the imine group in order to coordinate the alkene or silane substrate (see Scheme 1.24 in chapter one).⁷⁹ The Pt(sal)(ppy)

complexes are structurally related to the photoactivated hydrosilylation catalysts based on Pt bis(β -diketonate) complexes, in that they are Pt(II) complexes with LX-type ligands (Figure 2.9).⁵ Many Pt(II) complexes with cyclometalated 2-arylpyridine ligands are known and have been intensively studied because of their useful photophysical and photochemical properties, which makes them suitable for diverse applications in bioimaging, chemosensors, and photoredox catalysis.^{116,117,118} Despite their anticipated applications in luminescence and intracellular temperature imaging, Pt(sal)(ppy) complexes have not before been studied as photoactivated hydrosilylation catalysts. The study of these complexes in this field is expected to provide valuable insight into the mechanism for photoactivated hydrosilylation.

The first step in preparing the Pt(sal)(ppy) complexes, **1a–1g**, starts with the synthesis of the **dmsO** complexes (Scheme 2.2). These steps were carried out under an inert atmosphere despite the air stability of the complexes, the main concern being the oxidative and thermal stability of the reaction intermediates at elevated temperatures ($> 110\text{ }^{\circ}\text{C}$).¹¹⁹ The $N^{\wedge}C$ -cyclometalating ligand was reacted with $\text{K}_2[\text{PtCl}_4]$ in wet AcOH for 24 h to afford an insoluble orange precipitate, meaning unambiguous identification was not possible. However, based on the fact that $N^{\wedge}C$ -cyclometalating ligands such as 2-phenylpyridine invariably yield chloro-bridged dimers of the form $[\text{Pt}(N^{\wedge}C)(\mu\text{-Cl})_2]$, the dimer structure shown in Scheme 2.2 seems most likely.¹¹⁹ In fact, this low solubility proved to be a problem as subsequent direct reaction with the Schiff base proto ligands proceeded to give a complicated mixture of multiple unidentified products. Isolation of the desired product, Pt(sal)(ppy), then required purification by column chromatography. Nonetheless, this situation could be improved greatly if the dimers were first reacted with dmsO under reflux for 1–4 h, which led to bridge cleavage and to soluble mononuclear complexes bearing dmsO as one of the ligands, $\text{Pt}(N^{\wedge}C)(\text{dmsO})\text{Cl}$. Cleaving of the dimer to form **2-dmsO** required longer reaction times than the corresponding reactions to form **1-dmsO** and **3-dmsO** (4 h compared to 1 h), which could be attributed to the higher stability of the dimer containing benzo[*h*]quinoline provided by the additional electron delocalisation. All products, **1-dmsO**, **2-dmsO** and **3-dmsO**, were obtained in moderate to good yields (39–83%) after removal of dmsO

under reduced pressure and could be then reacted with the Schiff base ligands, **L-a-L-i**, to afford the target Pt(sal)(ppy) complexes cleanly. The details of this step are described in section 2.6. Previous studies by Bruce using nuclear Overhauser effect spectroscopy (NOESY) suggest that the **dmsO** complexes exist as the isomer where the coordinated dmsO is found trans to the pyridine nitrogen, as shown in Figure 2.10.¹²⁰ The molecular structures of **1-dmsO** and **2-dmsO** have already been reported by Ghedini, which also confirm this isomer and sulfur-coordination of dmsO.¹²¹



Scheme 2.2. Synthetic route towards **1-dmsO**, **2-dmsO** and **3-dmsO**.

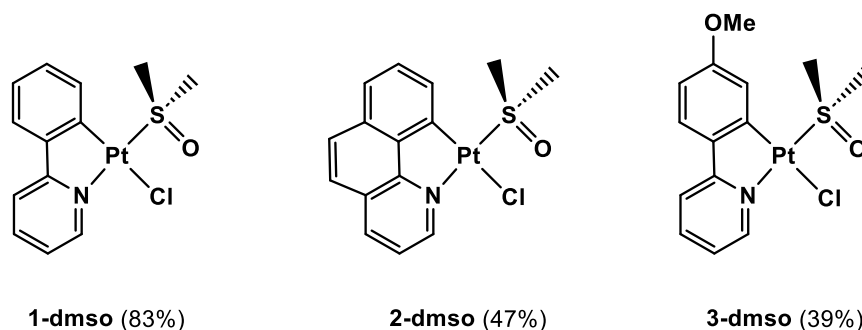


Figure 2.10. **dmsO** complexes synthesised herein (% yield).^{121,122}

2.4.1 NMR characterisation of Pt(ppy)(dmsO)Cl complexes

The three **dmsO** complexes were characterised by NMR / UV-vis spectroscopies and electrospray ionisation mass spectrometry, which is detailed in chapter six. The ¹H NMR spectrum of **1-dmsO** in *d*₂-dichloromethane is shown in Figure 2.11. A characteristic feature in the ¹H NMR spectra of

such complexes is very distinctive ^{195}Pt satellites ($I = \frac{1}{2}$, 33.8% natural abundance) associated with the proton *ortho* to nitrogen in the cyclometalated ligand, and also the methyl protons of the bound dmsO ligand. In the case of **1-dmsO**, the proton *ortho* to nitrogen in phenylpyridine appears as a doublet [δ 9.61 (d, 1H, $^3J_{\text{H-H}} = 5.9$ Hz, $^3J_{\text{H-Pt}} = 35.6$ Hz)]. The methyl protons of the bound dmsO ligand in **1-dmsO** appear as a distinctive singlet [δ 3.60 (s, 6H, $^3J_{\text{H-Pt}} = 23.4$ Hz)]. These data are in accordance with the values reported by Ghedini and coworkers for the ^1H NMR characterisation of **1-dmsO**.¹²¹ The corresponding ^1H NMR data for **2-dmsO** and **3-dmsO** are shown in Table 2.1. Compared to **1-dmsO**, a slightly downfield resonance is observed for the proton *ortho* to nitrogen in phenylpyridine [δ 9.83 (d, 1H, $^3J_{\text{H-H}} = 5.5$ Hz, $^3J_{\text{H-Pt}} = 32.9$ Hz)] and also for the methyl protons of the bound dmsO [δ 3.74 (s, 6H, $^3J_{\text{H-Pt}} = 21.5$ Hz)] in the case of **2-dmsO**. This trend is consistent with that reported by Ghedini for this complex.¹²¹ Regarding **3-dmsO**, the proton *ortho* to nitrogen shows a slightly upfield signal compared to **1-dmsO** [δ 9.56 (d, 1H, $^3J_{\text{H-H}} = 5.9$ Hz, $^3J_{\text{H-Pt}} = 31.3$ Hz)], whilst the methyl protons of bound dmsO in this compound are observed slightly downfield [δ 3.67 (s, 6H, $^3J_{\text{H-Pt}} = 21.3$ Hz)]. These data are consistent with that reported by Rourke.¹²² The minor differences in chemical shift can be attributed to the metal-chelated ring aromaticity and the extent of π back-bonding from the cyclometalated ligand.¹²²

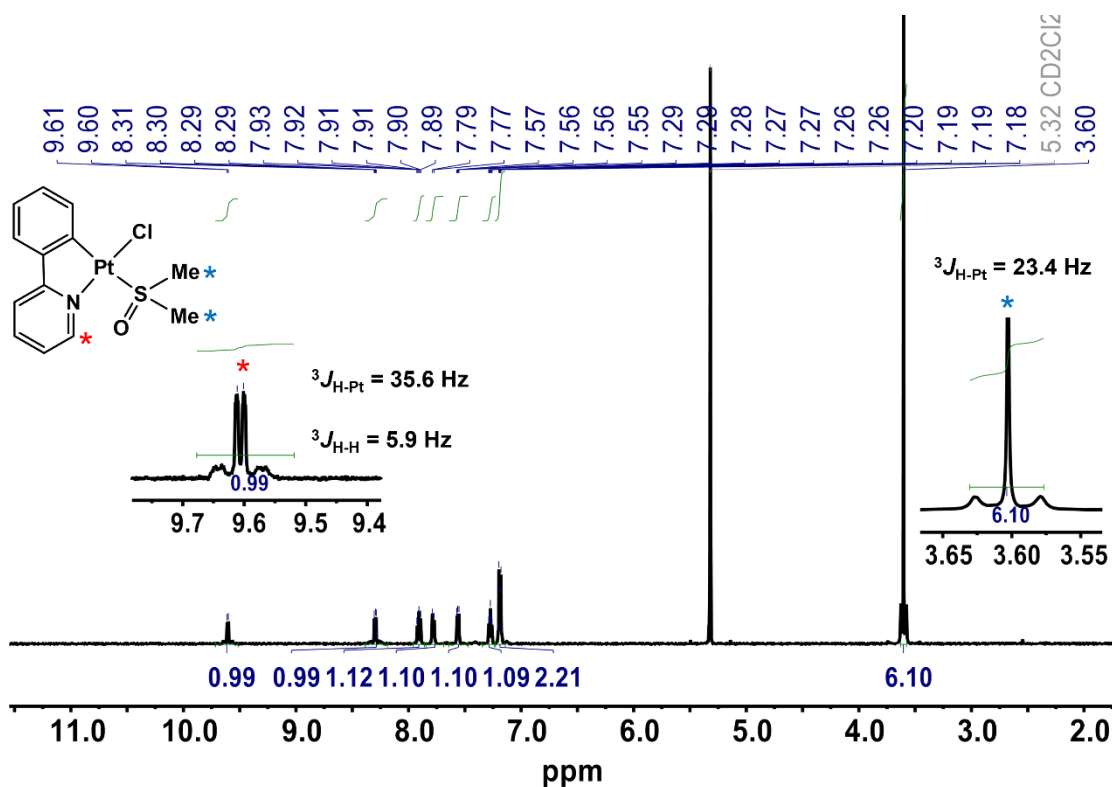


Figure 2.11. ^1H NMR spectrum of **1-dmsO** with insets to show platinum satellites (600 MHz, d_2 -dichloromethane, 298 K).

Table 2.1. Selected ^1H NMR shifts (ppm) with $|\text{}^1\text{H}-\text{}^1\text{H}|$ and $|\text{}^1\text{H}-\text{}^{195}\text{Pt}|$ coupling constants (Hz) of synthesised **dmsO** complexes measured in d_2 -dichloromethane at 600 MHz.

Precatalyst	δ^a	$^3J_{\text{H-H}}$	$^3J_{\text{H-Pt}}$	δ^b	$^3J_{\text{H-Pt}}$
1-dmsO	9.61	5.9	35.6	3.60	23.4
2-dmsO	9.83	5.5	32.9	3.74	21.5
3-dmsO	9.56	5.9	31.3	3.67	21.3

^a Proton ortho to nitrogen on phenylpyridine. ^b Methyl protons on dmsO.

2.4.2 UV-vis spectroscopic data of Pt(ppy)(dmsO)Cl complexes

The UV-Vis absorption spectra of the **dmsO** complexes recorded in CH_2Cl_2 solutions (1.6×10^{-5} M) are shown in Figure 2.12, and the relevant data are listed in Table 2.2. The absorption spectra of

all the complexes are similar in overall shape with a relatively wide absorption band. The intense absorption bands below 340 nm correspond to the $\pi \rightarrow \pi^*$ spin-allowed LC (ligand centred) transitions, and the weaker absorption bands at $\sim 340 - 400$ nm are attributed to the spin-allowed MLCT (metal-to-ligand charge transfer) and LLCT (ligand-to-ligand charge transfer) transitions.¹¹³ Compared to **1-dmso** where $\lambda_{\text{max}} = 282$ nm and 316 nm, there is a general red-shift in the absorption spectrum of **3-dmso**, where the corresponding values are $\lambda_{\text{max}} = 298$ nm and 336 nm. This is due to the presence of the electron donating $-\text{OMe}$ group on the phenylpyridine ligand of **3-dmso**. For the MLCT transitions, an obvious red-shift is observed in the absorption spectrum of **2-dmso** compared to the other two complexes. Indeed $\lambda_{\text{max}} = 395$ nm for **2-dmso**, whilst the corresponding values are $\lambda_{\text{max}} = 328$ nm and 381 nm for **1-dmso** and **3-dmso**, respectively. This can be attributed to the extended conjugation present in benzo[*h*]quinoline compared to phenylpyridine, as the former has a reduced energy gap between the ground and lowest excited states.¹²³

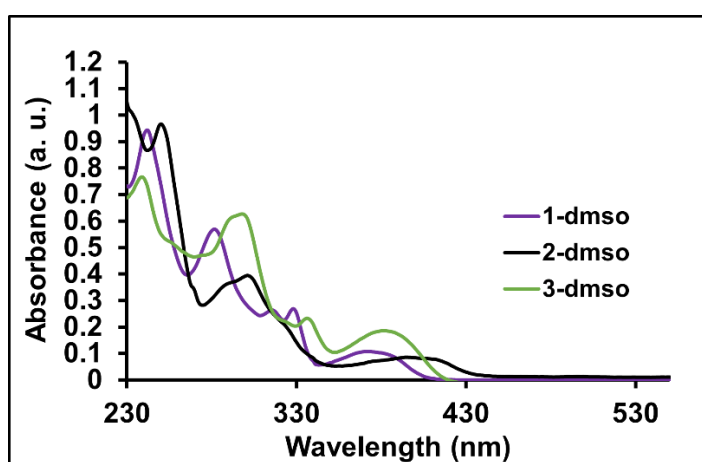


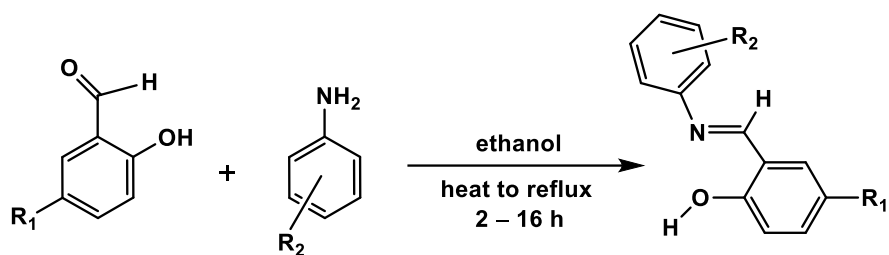
Figure 2.12. UV-vis absorption spectra of **1-dmso**, **2-dmso** and **3-dmso** in dichloromethane (1.6×10^{-5} M).

Table 2.2. Selected bands and absorption coefficients within the UV–vis spectra of **1-dmsso**, **2-dmsso** and **3-dmsso**.

Complex	Absorption, λ_{\max} , /nm [$\log(\epsilon \text{ dm}^3 \text{ mol}^{-1} \text{ cm}^{-1})$]
1-dmsso	242 (4.77), 282 (4.55), 316 (4.22), 328 (4.22)
2-dmsso	228 (4.83), 250 (4.78), 301 (4.39), 395 (3.73)
3-dmsso	239 (4.68), 298 (4.59), 336 (4.16), 381 (4.06)

2.5 Preparation and characterisation of Schiff base ligands

Schiff base ligands have long been studied in the field of coordination chemistry due to their facile synthesis, easy availability and tuneable electronic properties.¹²⁴ These versatile organic ligands and their metal complexes have enormous applications in areas such as biology^{113,114} materials chemistry¹²⁵ and the dye industry.¹²⁶ Coordination of the Schiff base ligands to platinum for this study provides a simple and robust method of correlating the structure of the ligands with their catalytic activity in hydrosilylation. All Schiff base ligands reported herein are known and were synthesised using a literature procedure shown in Scheme 2.3, where an ethanol solution of the salicylaldehyde derivative was added to an ethanol solution of the aniline derivative and stirred at room temperature for 1 h.¹²⁷ The mixture was then heated to reflux until complete consumption of the starting materials was observed. Subsequently, ethanol was removed under reduced pressure and the obtained Schiff bases were purified by dissolving in minimal dichloromethane and layering with hexane. These ligands were obtained as yellow or orange crystalline solids and were afforded in excellent yields ($\geq 90\%$) (Figure 2.13).



Scheme 2.3. General synthesis of Schiff base ligands (L-a–L-i).¹²⁷

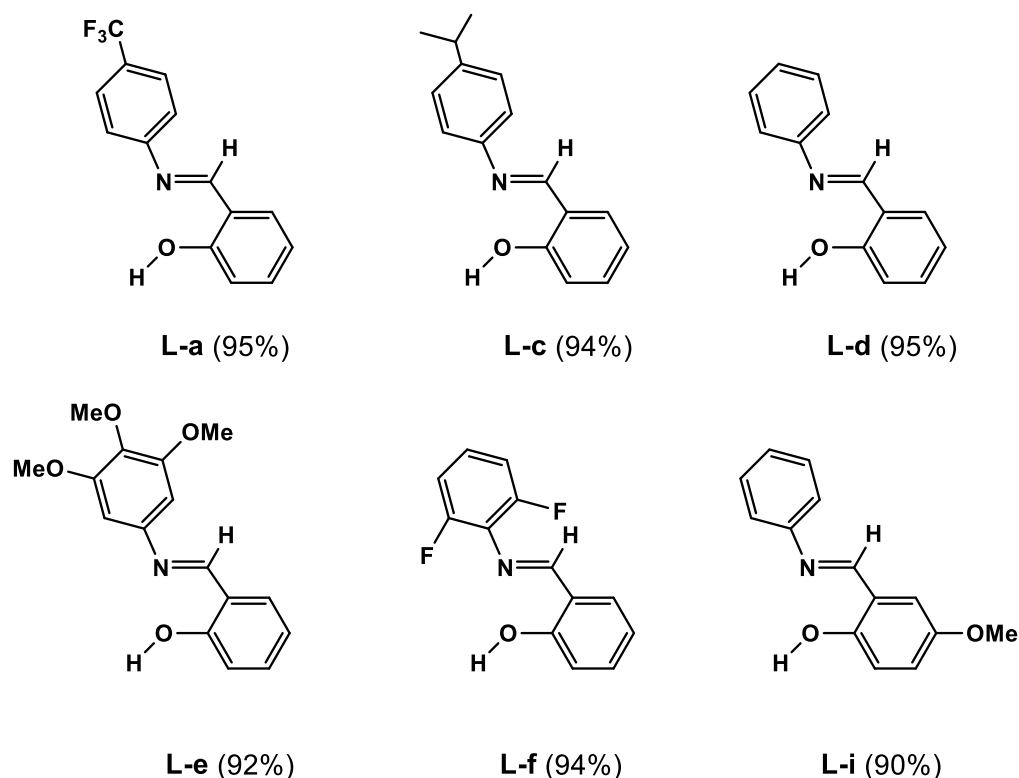


Figure 2.13. Schiff base ligands (L-a–L-i) synthesised herein (% yield).^{128,129,130,131,132}

2.5.1 NMR characterisation of Schiff base ligands

The ligands were characterised by NMR / UV-vis spectroscopies and electrospray ionization mass spectrometry, as detailed in chapter six. The ¹H NMR spectrum for L-a in *d*₂-dichloromethane is shown in Figure 2.14. One characteristic signal for L-a is the singlet at δ 12.77 ppm, which corresponds to the O–H proton. This chemical shift is typical for the resonance-assisted hydrogen bonded proton of O–H⋯N=C.¹³³ Another characteristic feature of the ¹H NMR spectrum obtained

for **L-a** is the singlet at δ 8.66 ppm, which is attributed to the C=N–H imino proton. The remaining aromatic protons for **L-a** appear in the range δ 7.71–6.97 ppm and the whole spectrum integrates to give the expected 10 protons. The characteristic O–H and C=N–H proton signals for ligands **L-a**–**L-i** are provided in Table 2.3. Overall, the variation in substituents on the Schiff base ligands has a negligible effect on the chemical shift of the C=N–H proton except for **L-f**, where the signal appears more downfield (δ 8.89 ppm) relative to the other ligands (δ 8.63–8.67 ppm). Regarding the chemical shift of the O–H proton, the variation in substituents has a more pronounced effect, and the signals for **L-c** (δ 13.29 ppm), **L-d** (δ 13.18 ppm) and **L-e** (δ 13.14 ppm) are observed further downfield compared to **L-a** (δ 12.77 ppm), **L-f** (δ 12.84 ppm) and **L-i** (δ 12.70 ppm).

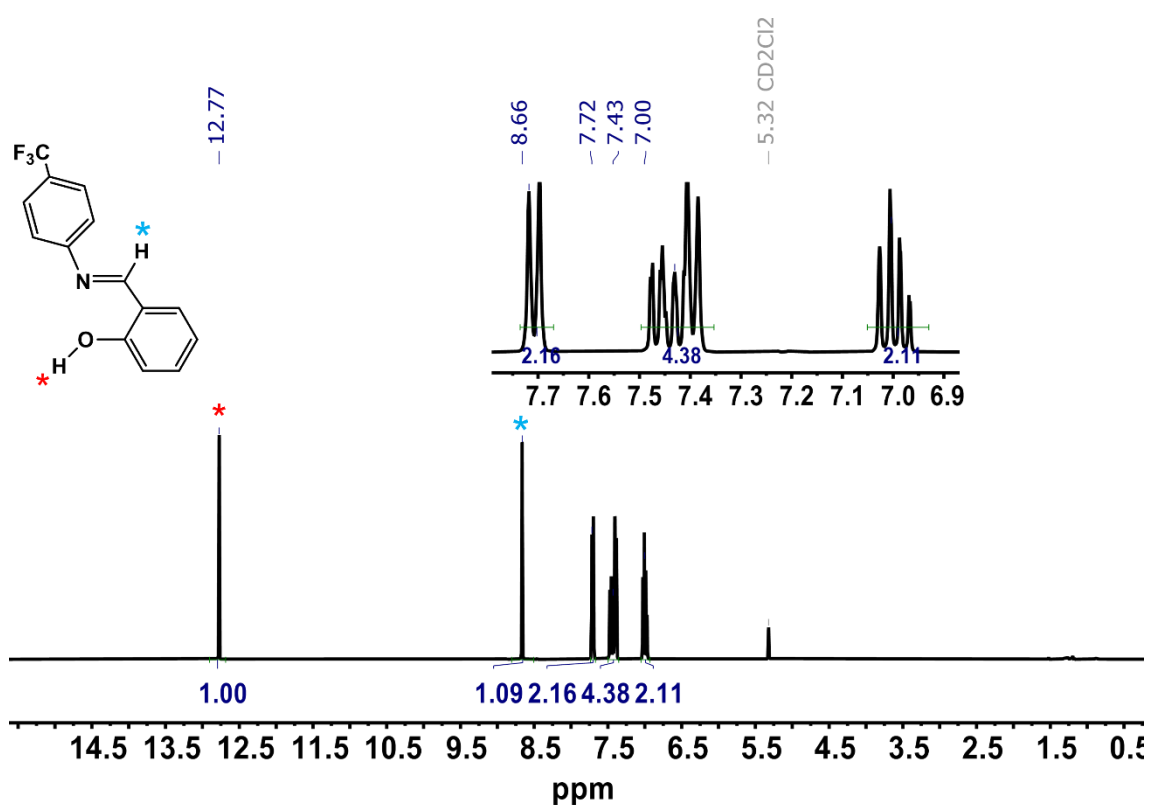


Figure 2.14. ^1H NMR spectrum of **L-a** (600 MHz, d_2 -dichloromethane, 298 K).

Table 2.3. Selected ^1H NMR shifts (ppm) of synthesised Schiff base ligands (**L-a**–**L-i**) measured in d_2 -dichloromethane at 600 MHz.

Ligand	δ (O–H)	δ (C=N–H)
L-a	12.77	8.66
L-c	13.29	8.67
L-d	13.18	8.67
L-e	13.14	8.66
L-f	12.84	8.89
L-i	12.70	8.63

2.5.2 UV-vis spectroscopic data of Schiff base ligands

The UV-vis absorption spectra for ligands **L-a**–**L-i** recorded in CH_2Cl_2 solutions (1.6×10^{-5} M) are shown in Figure 2.15, and the relevant data are listed in Table 2.4. All ligands exhibit UV-visible absorption peaks between 230 and 380 nm which are assigned to $\pi \rightarrow \pi^*$ transitions in the aromatic rings and $n \rightarrow \pi^*$ transitions in the $-\text{HC}=\text{N}-$ groups, as informed by previous studies.¹³³

The introduction of the *i*Pr group onto the aniline component of the Schiff base ligand (**L-c** compared to **L-a**) has a negligible effect on the absorption spectra of the ligands. However, the ligands bearing $-\text{CF}_3$ (**L-a**) and $-\text{F}$ (**L-f**) groups show a lower absorption than the unsubstituted ligand (**L-d**). Interestingly, the introduction of the $-\text{OMe}$ group onto the *o*-hydroxybenzaldehyde group of the Schiff base ligand caused an obvious red-shift of the absorption spectrum compared to that of **L-d**, where λ_{max} values for the $n \rightarrow \pi^*$ transitions were observed at 376 nm and 340 nm, respectively. A similar effect was observed for **L-e** where the presence of three $-\text{OMe}$ groups on the aniline group caused a red-shift in the absorption spectrum compared to **L-d** ($\lambda_{\text{max}} = 352$ and 340 nm for **L-e** and **L-d**, respectively).

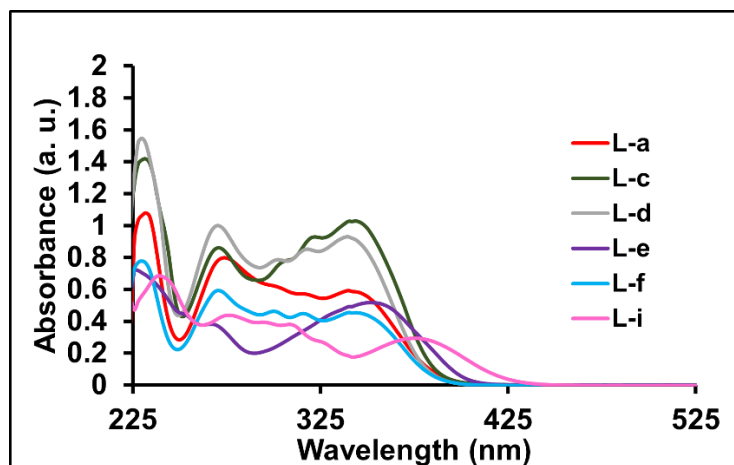


Figure 2.15. UV–Vis absorption spectra and absorption coefficients of Schiff base ligands (L-a–L-i) in dichloromethane (1.6×10^{-5} M).

Table 2.4. Selected absorption bands within the UV–vis spectra of Schiff base ligands (L-a–L-i).

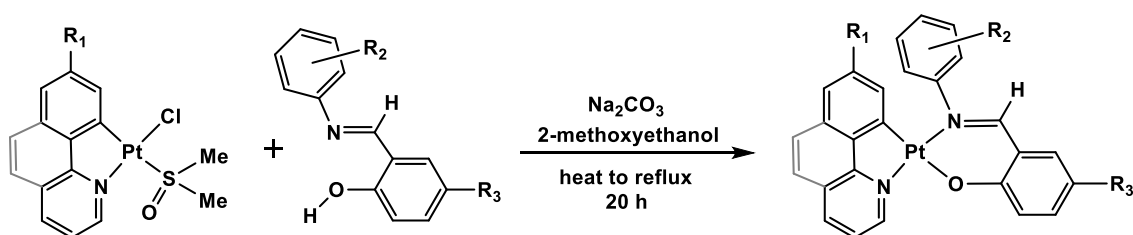
Ligand	Absorption, λ_{\max} , /nm [$\log(\epsilon \text{ dm}^3 \text{ mol}^{-1} \text{ cm}^{-1})$]
L-a	232 (4.83), 274 (4.70), 340 (4.57)
L-c	232 (4.95), 270 (4.73), 308 (4.69), 322 (4.76), 344 (4.81)
L-d	230 (4.99), 270 (4.80), 302 (4.69), 318 (4.73), 340 (4.76)
L-e	266 (4.38), 352 (4.51)
L-f	230 (4.69), 270 (4.57), 300 (4.46), 316 (4.45), 344 (4.45)
L-i	240 (4.63), 274 (4.43), 294 (4.39), 308 (4.38), 376 (4.26)

2.6 Preparation and Characterisation of Pt(sal)(ppy) complexes

As discussed in section 2.4, complexes based on the Pt(sal)(ppy) framework have well established photophysical properties and they have been used in previous studies for bioimaging.¹¹³ For this study, the introduction of various functional groups onto the Schiff base and phenylpyridine moieties is expected to give rise to different catalytic activities in hydrosilylation. This is because different photoactivation efficiencies are expected from different

complexes. The ability to correlate the structure of the ligands with the catalytic performance in photohydrosilylation may provide mechanistic insight – an area which has thus far been overlooked.

The synthesis of all the Pt(sal)(ppy) complexes, **1a–1i**, was performed according to the same procedure that was modified from the literature (Scheme 2.4).¹¹³ A solution of the Pt(*N*[^]C)(dmsO)Cl precursor, 3 equiv. of the Schiff base ligand and 10 equiv. of Na₂CO₃ in 2-methoxyethanol was heated to reflux overnight. The solvent was then removed under reduced pressure and hexane was added gradually to give an orange or red precipitate that was subsequently filtered and washed with water. Subsequent freeze-drying followed by recrystallisation by slow diffusion of hexane into a dichloromethane solution of the complexes resulted in the formation of **1a–1i** as orange solids in moderate yields (27–54%) (Figure 2.16). Complexes **1b**¹¹³ and **1d**¹¹⁴ have been previously reported, whilst **1a**, **1c**, **1e**, **1f**, **1g**, **1h** and **1i** are new. All complexes were synthesised from the Pt(*N*[^]C)(dmsO)Cl precursor rather than directly from the insoluble [Pt(*N*[^]C)(μ-Cl)]₂ dimer, as this afforded a cleaner product that could be purified by a simple recrystallisation. The product obtained from reacting [Pt(*N*[^]C)(μ-Cl)]₂ directly with the Schiff base proto ligand required purification by column chromatography.



Scheme 2.4. General synthesis of Pt(sal)(ppy) complexes (**1a–1i**).

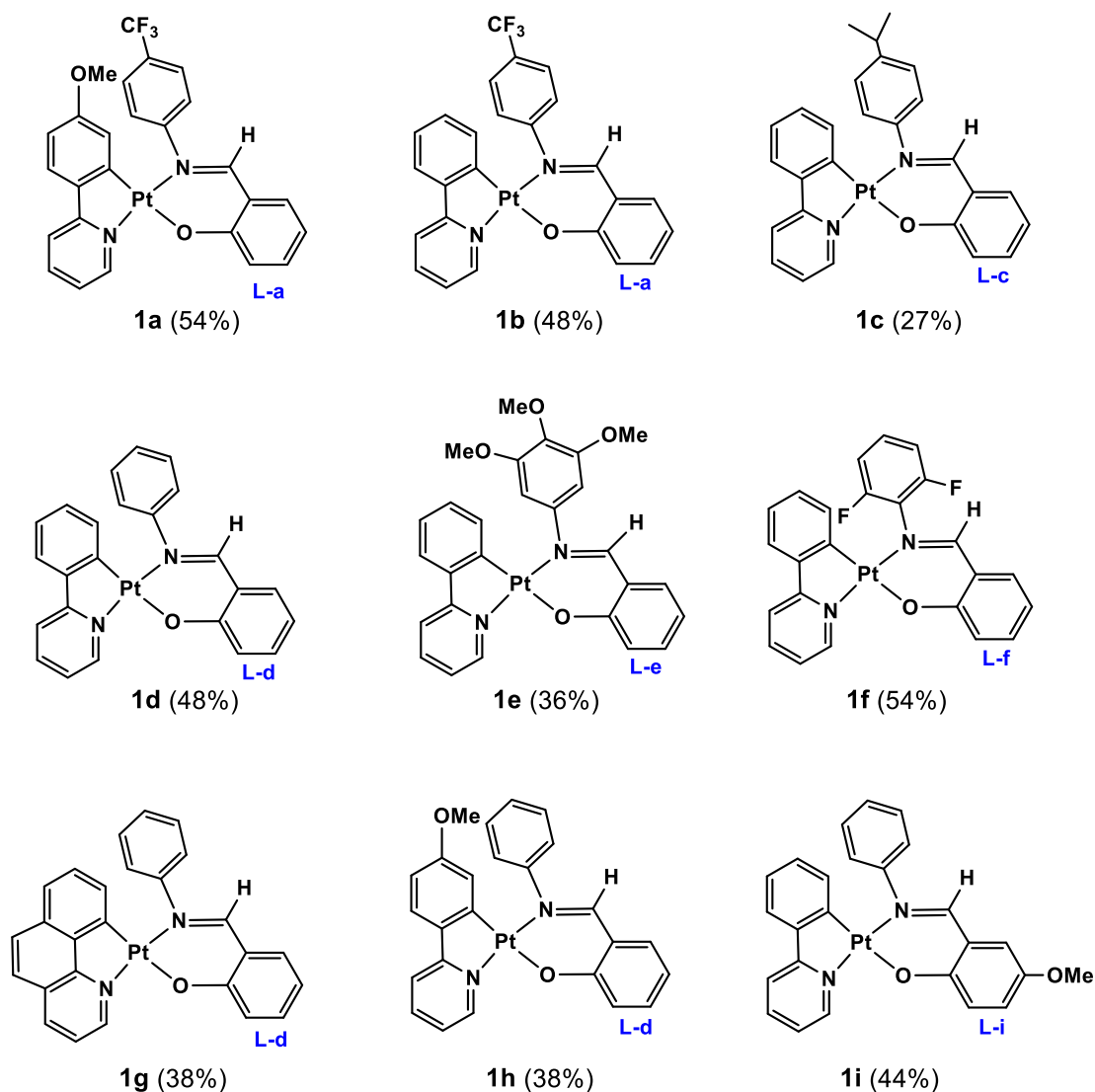


Figure 2.16. Pt(sal)(ppy) complexes (1a–1i) synthesised herein (% yield).^{113,114}

2.6.1 NMR characterisation of Pt(sal)(ppy) complexes

The Pt(sal)(ppy) complexes 1a–1i were characterised by NMR / UV-vis spectroscopies, elemental analysis, and electrospray ionization mass spectrometry, as detailed in chapter six. The ¹H NMR spectrum for complex 1a, stacked with the corresponding free Schiff base ligand, L-a, is shown in Figure 2.17. Confirmation that L-a has coordinated to platinum is evidenced by the disappearance of the –OH signal from the free ligand, and by the appearance of ¹⁹⁵Pt satellites (*I* = ½, 33.8% natural abundance) associated with the proton *ortho* to nitrogen in the cyclometalated ligand, and also with the imine proton. The proton *ortho* to nitrogen in 1a

appears as a doublet [δ 9.42 (d, 1H, $^3J_{\text{H-H}} = 5.8$ Hz, $^3J_{\text{H-Pt}} = 33.2$ Hz)], whilst the imine proton is observed as a sharp singlet [δ 8.25 (s, 1H, $^3J_{\text{H-Pt}} = 70.6$ Hz)]. This signal is shifted upfield relative to the free ligand [δ 8.66 (s, 1H)] upon coordination to platinum. The signal for the three protons of the –OMe group also appears as a sharp singlet [δ 3.23 (s, 3H)]. Overall, the spectrum integrates to give the expected 19 protons.

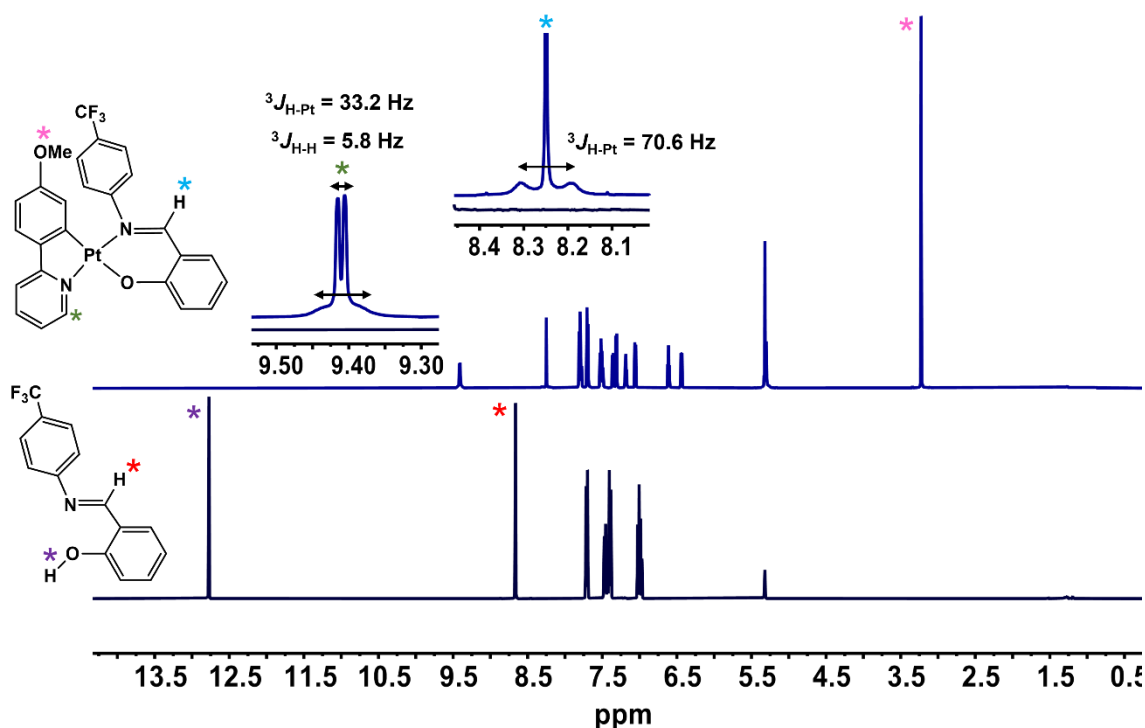


Figure 2.17. ^1H NMR spectra of **1a** (top) with insets to show platinum satellites and **L-a** (bottom) (600 MHz, d_2 -dichloromethane, 298 K).

The ^1H NMR spectra of all complexes show the signals from the bound Schiff base ligand frequently overlapped in the aromatic region with those of the phenylpyridine or benzo[*h*]quinoline backbone, which was also observed with the palladium analogues of these complexes.¹³⁴ However the distinctive signals due to the proton *ortho* to nitrogen in the cyclometalated ligand and the imine proton are present in all complexes and are listed in Table 2.5, along with their coupling constants. All protons *ortho* to nitrogen in the cyclometalated ligand are observed between δ 9.42 – 9.76, with $^3J_{\text{H-Pt}}$ varying slightly between 33.2 – 35.5 Hz, where the most upfield signal is observed in **1a**, and the most downfield signal is observed for

1g. This can be attributed to the metal-chelated ring aromaticity and the π backbonding of the cyclometalated ligand. The greater extent of electron delocalisation in benzo[*h*]quinoline compared to phenylpyridine and 4-methoxyphenylpyridine results in the signal being observed further downfield. Introducing various functional groups onto the complexes has a negligible effect on the chemical shift of the imine proton, as it is observed for all complexes between δ 8.19 – 8.35, with $^3J_{\text{H-Pt}}$ varying between 70.5 – 76.5 Hz. In complex **1g**, the signal for the imine proton overlaps with other proton signals in the aromatic region, so accurate measurement of the coupling constant for the platinum satellites is not possible.

Table 2.5. Selected ^1H NMR shifts (ppm) with $|\text{}^1\text{H}-\text{}^1\text{H}|$ and $|\text{}^1\text{H}-\text{}^{195}\text{Pt}|$ coupling constants (Hz) of synthesised Pt(sal)(ppy) complexes (**1a–1i**) measured in d_2 -dichloromethane at 600 MHz.

Precatalyst	δ^a	$^3J_{\text{H-H}}$	$^3J_{\text{H-Pt}}$	δ^b	$^3J_{\text{H-Pt}}$
1a	9.42	5.8	33.2	8.25	70.6
1b	9.51	5.7	33.5	8.27	70.5
1c	9.54	6.1	33.5	8.27	73.8
1d	9.54	6.0	34.9	8.27	76.5
1e	9.58	5.7	33.7	8.35	71.4
1f	9.55	5.8	35.5	8.19	73.1
1g	9.76	5.2	33.4	- ^c	- ^d
1h	9.50	5.7	33.2	8.28	70.7
1i	9.58	5.8	33.2	8.26	74.6

^aProton ortho to nitrogen on the phenylpyridine. ^bImine proton. ^cDistinct chemical shift not assigned due to signal overlap. ^dCoupling constant not measured due to signal overlap.

In the $^{13}\text{C}\{^1\text{H}\}$ NMR spectra of complexes **1a**, **1b** and **1f**, coupling to ^{19}F ($I = \frac{1}{2}$, 100% natural abundance) is observed. The $^{13}\text{C}\{^1\text{H}\}$ NMR spectrum for complex **1a** is shown in Figure 2.18, and

the corresponding data for **1b** and **1f** is detailed in chapter six. The carbon in position **1** is observed as a quartet due to coupling with the fluorines in the $-\text{CF}_3$ group [δ 129.9 (q, 1C, $^2J_{\text{C-F}} = 32.3$ Hz)], and the two carbons in position **2** are also observed as a quartet [δ 126.8 (q, 2C, $^3J_{\text{C-F}} = 3.8$ Hz)]. An additional quartet is observed for the carbon of the $-\text{CF}_3$ group [δ 121.8 (q, 1C, $^1J_{\text{C-F}} = 273.1$ Hz)], though this is not shown in Figure 2.18. The magnitude of the $J_{\text{C-F}}$ couplings is within the expected range for this complex, whilst coupling to ^{195}Pt was not observed in this spectrum due to noise in the baseline.¹²³

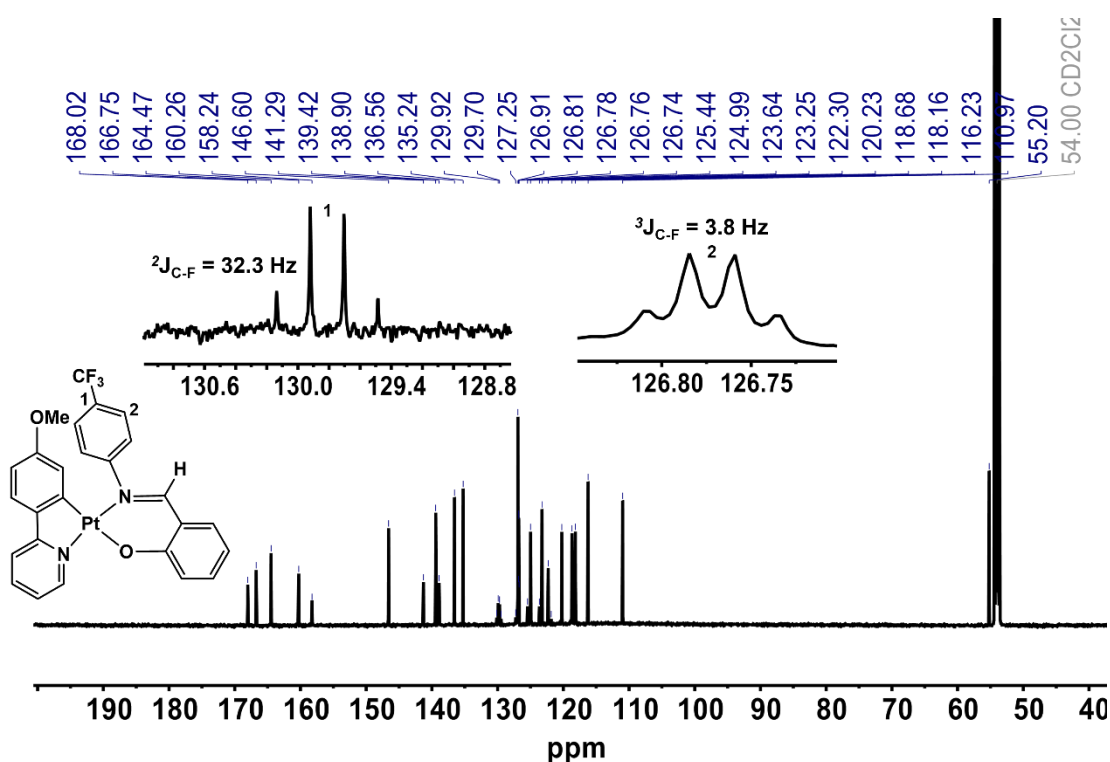


Figure 2.18. $^{13}\text{C}\{^1\text{H}\}$ NMR spectrum of **1a** with insets to show ^{13}C – ^{19}F coupling (151 MHz, d_2 -dichloromethane, 298 K).

2.6.2 UV-vis spectroscopic data of Pt(sal)(ppy) complexes

The UV-vis absorption spectra for complexes **1a–1i** recorded in CH_2Cl_2 solutions (1.6×10^{-5} M) are shown in Figure 2.19, and the detailed electronic absorption data are listed in Table 2.6. The absorption spectra of all the complexes are similar in shape with a relatively wide absorption band. Intense absorption bands below 300 nm correspond to the $\pi \rightarrow \pi^*$ spin-allowed LC (ligand

centred) transitions, as informed by previous studies.¹¹³ The weaker absorption bands at ~350–400 nm are assigned to the spin-allowed MLCT (metal-to-ligand charge transfer) and LLCT (ligand-to-ligand charge transfer) transitions, in accordance with previously reported data.¹¹³ The weak absorption peaks above 400 nm are assigned to MLCT and LC transitions. The introduction of the –OMe group on the phenylpyridine ligand (**1a** compared to **1b**) has a negligible effect on the absorption spectra of the complexes. However, replacement of the phenylpyridine ligand by benzo[*h*]quinoline shows an obvious red-shift in the absorption spectrum. Indeed, complex **1d** shows peaks at λ_{max} 228 nm and 266 nm for the LC transitions, whilst the corresponding values are λ_{max} 240 nm and 288 nm for complex **1g**. This can be attributed to the extended conjugation present in benzo[*h*]quinoline compared with phenylpyridine, as the former has a reduced energy gap between the ground and lowest excited states.¹²³ Compared to complexes **1e** and **1h**, **1i** shows an additional spin forbidden transition at λ_{max} 476 nm, which demonstrates that introducing the –OMe onto the *o*-hydroxybenzaldehyde group of the Schiff base ligand has a more pronounced effect on the absorption spectra than introducing this group on the aniline group or phenylpyridine ligand. The differences in the absorption spectra of complexes **1b**, **1c** and **1d** are negligible which demonstrates that electron-withdrawing (**1a**) or electron donating (**1c**) substituents do not exert a strong influence on the electronic transitions in these complexes.

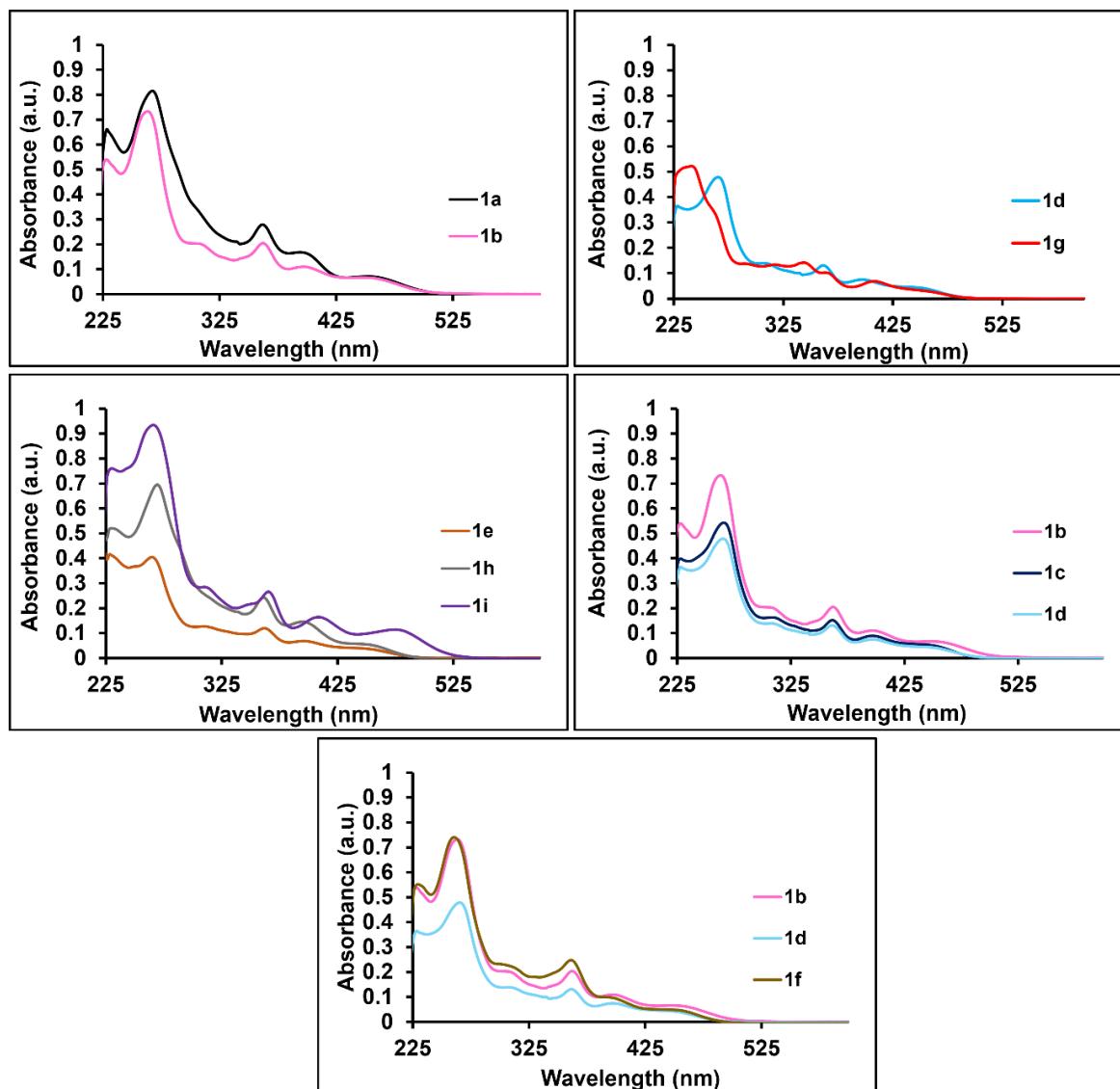


Figure 2.19. UV-Vis absorption spectra of Pt(sal)(ppy) complexes (**1a–1i**) in dichloromethane (1.6×10^{-5} M).

Table 2.6. Selected absorption bands and absorption coefficients within the UV–vis spectra of Pt(sal)(ppy) complexes (**1a–1i**).

Precatalyst	Absorption, λ_{\max} , /nm [$\log(\epsilon \text{ dm}^3 \text{ mol}^{-1} \text{ cm}^{-1})$]
1a	228 (4.66), 268 (4.75), 362 (4.29), 394 (4.07)
1b	228 (4.55), 264 (4.69), 362 (4.13), 396 (3.86)
1c	266 (4.54), 310 (4.02), 362 (3.99), 398 (3.76)
1d	228 (4.33), 266 (4.45), 308 (3.91), 362 (3.89), 398 (3.64)
1e	228 (4.45), 264 (4.44), 310 (3.94), 362 (3.92), 396 (3.67)
1f	230 (4.54), 260 (4.67), 300 (4.17), 362 (4.19)
1g	240 (4.51), 288 (3.93), 318 (3.92), 344 (3.94), 364 (3.80), 408 (3.62)
1h	230 (4.51), 270 (4.63), 360 (4.18), 394 (3.96)
1i	230 (4.68), 266 (4.77), 310 (4.25), 366 (4.22), 408 (4.01), 476 (3.86)

2.6.3 Crystal structures of Pt(sal)(ppy) complexes

Crystals suitable for diffraction were obtained for complexes **1a**, **1b**, **1f** and **1g** by slow diffusion of hexane into a dichloromethane solution of the complex. The collection and refinement of this data was performed by Joe Goodall. The structures are shown in Figure 2.20 and the relevant bond lengths and angles are reported in Table 2.7. Determination of the molecular structures by X-ray analysis revealed an *N,N-trans* arrangement of the ligands in all complexes. This arrangement has also been prevalent over the *N,N-cis* arrangement in related complexes reported in the literature.^{114,134} The NMR data are consistent with the obtained crystal structures.

The complexes adopt a slightly distorted square-planar structure, and this is indicated by the torsion angle between the arylpyridine and Schiff base ligand planes. The distortion is most pronounced in complex **1b** (16.64°) and is also quite significant in complex **1g** (14.95°). This twist

in the ligands may be due to a steric clash between the N–Ar group and the phenylpyridine ligand, and it is much less pronounced, but still significant, in complexes **1a** and **1f** where the torsion angles are 12.07° and 12.75°, respectively.

Compared to **1a**, **1b** and **1f**, complex **1g** has a larger N1–Pt–N2 angle of 177.0(2)°. The molecular structure of **1d**, which is the same complex except for benzo[*h*]quinoline being replaced by phenylpyridine, was reported by Huang.¹¹⁴ This work reports an N1–Pt–N2 bond angle of 174.81(19)° for **1d**. The N1–Pt–O1 bond angle is also smaller in **1g** (87.8(3)°) compared to **1b** (89.19(7)°), **1f** (89.29(11)°) and **1d** (89.92(18)°), which demonstrates the influence of additional ring strain.

Between complex **1a** and **1b**, there are no significant differences in the bond parameters which demonstrates that the –OMe group on phenylpyridine does not exert a strong influence on the ring conformation. The one notable difference is a slightly narrower N1–Pt–O1 bond angle of 88.01(8)° in **1a** compared to **1b**, where the corresponding angle in **1b** is 89.19(7)°.

Overall, the analysis of bond angles and lengths revealed no significant differences between the complexes. However, it is anticipated that a greater insight into the mode of activation of these complexes for photohydrosilylation may enable a link to be established between the structure of the complex and the catalytic performance. For example, if the catalyst is activated by decoordination of the imine group followed by coordination of the alkene or silane substrate, the extent of distortion from the square-planar geometry may prove to be significant.

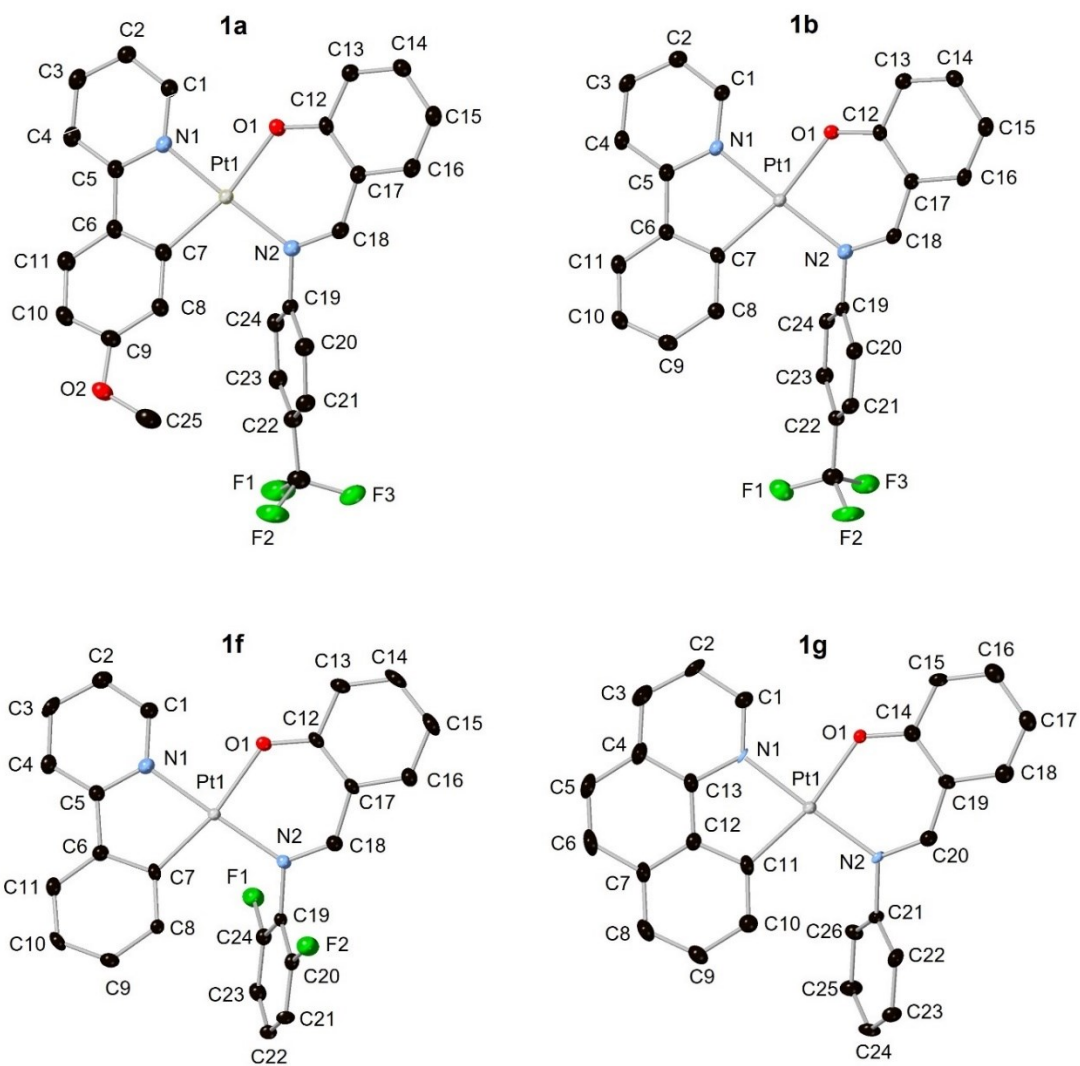


Figure 2.20. Crystallographically determined structures of **1a**, **1b**, **1f** and **1i**. Ellipsoids are shown at the 50% probability level and hydrogen atoms are omitted for clarity.

Table 2.7. Selected bond distances and bond angles for Pt(sal)(ppy) complexes **1a**, **1b**, **1f** and **1g**.

Bond Lengths (Å)/ Angles (°)	1a	1b	1f	1g
Pt1–C7	2.008(2)	2.006(2)	2.003(3)	2.009(15) ^a
Pt1–N1	2.017(2)	2.0205(19)	2.019(3)	2.018(6)
Pt1–N2	2.028(2)	2.025(2)	2.020(3)	2.018(6)
Pt1–O1	2.0653(17)	2.0731(16)	2.065(3)	2.062(11)
C7–Pt–N1	81.04(9)	80.99(9)	80.88(12)	81.4(3) ^a
C7–Pt–N2	100.89(9)	100.36(9)	101.14(12)	100.3(3) ^a
C7–Pt–O1	167.97(10)	168.17(9)	168.81(11)	168.4(3) ^a
N1–Pt1–N2	174.89(10)	174.70(8)	172.83(11)	177.0(2)
N1–Pt1–O1	88.01(8)	89.19(7)	89.29(11)	87.8(3)
N2–Pt1–O1	90.44(8)	90.01(7)	89.27(10)	90.7(2)
Torsion ^b	12.07	16.64	12.75	14.95

^aC7 is C11 in **1g**. ^bangle between phenylpyridine and Schiff base ligand planes.

2.7 Summary and Conclusions

In this chapter, a series of Pt(ppy)(dmsO)Cl complexes (**1–3-dmsO**) have been synthesised as precursors for the target Pt(sal)(ppy) (**1a–1i**) complexes. These complexes were characterised by NMR and UV-vis spectroscopies along with electrospray ionisation mass spectrometry, and the obtained data are in full accord with that reported in the literature (see chapter six).^{121,122} In line with the literature reported procedure, attempts were made to synthesise the Pt(sal)(ppy) (**1a–1i**) complexes directly from the [Pt(N[^]C)(μ-Cl)]₂ dimers, but it was found that this led to a complicated mix of products and required purification by column chromatography.^{113,114} The method developed herein affords **1a** to **1i** in similar yields (27–54%), and the complexes were

found to be analytically pure after recrystallisation by slow diffusion of hexane into a dichloromethane solution of the complex (see chapter six).

The library of Pt(sal)(ppy) complexes (**1a–1i**) were targeted and synthesised, owing to their well-established photophysical properties and modular nature, which allows for variation in the steric and electronic influence of the ligand.^{113,114} These complexes were characterised by NMR and UV-vis spectroscopies, elemental analysis, electrospray ionisation mass spectrometry and in some cases, X-ray diffraction (see chapter six). Analysis of the UV-vis spectroscopic data revealed that all the Pt(sal)(ppy) complexes (**1a–1i**) exhibit relatively wide absorption bands between 220–480 nm, which renders them primed for photoactivation. It was found that replacing the phenylpyridine ligand with benzo[*h*]quinoline (**1d** compared to **1g**) caused an obvious red-shift in the absorption spectrum, due to the extended conjugation present in the benzo[*h*]quinoline system. With the support of previous literature, it is anticipated that the mode of action of the Pt(sal)(ppy) complexes is through hemilabile reactivity profiles by decoordination of the imine.¹¹⁵ As such, it could be envisioned that **1g** would exhibit faster catalytic activity in hydrosilylation than complexes containing a phenylpyridine ligand, as the larger steric clash observed with benzo[*h*]quinoline as the cyclometalated ligand may facilitate more facile decoordination or loss of the salicylaldimine ligand. The extended conjugation present in **1g** relative to **1d** also manifests as a further downfield shift for the proton *ortho* to nitrogen in phenylpyridine (δ 9.54 and δ 9.76 for **1d** and **1g**, respectively), and a longer N1–Pt–N2 bond angle ($174.81(19)^\circ$ and $177.0(2)^\circ$ for **1d** and **1g**, respectively).¹¹⁴ Regarding complexes **1a** and **1b**, the differences in the NMR and UV-vis data are negligible. The slightly shorter N1–Pt–O1 bond angle of $88.01(8)^\circ$ in **1a** compared to **1b** ($89.19(7)^\circ$) may prove to impact on the catalytic performance in hydrosilylation.

For the reasons outlined above, the synthesised and characterised Pt(sal)(ppy) complexes (**1a–1i**) where the ligands contain a variety of functional groups are expected to exhibit a range of reactivity in the hydrosilylation of alkenes. Two major advantages of these complexes are that the ligands can be easily tuned in a modular way with commercially available starting materials, and they do not require handling in a glovebox. Chapter 3 discusses investigations into the

performance of **1a–1i** as precatalysts in the hydrosilylation reaction under thermal and photoactivated conditions, with the aim of correlating the structure of the complexes (**1a–1i**) with the catalytic activity. It is hoped that this study will reveal insight into the kinetics and mechanism of the photoactivated hydrosilylation reaction, as research in this area has been relatively scarce.

Chapter 3 – Reactivity of the Pt(sal)(ppy) Complexes in Thermal and Photoactivated Hydrosilylation Reactions

3.1 Preamble

In chapter two, the synthesis and characterisation of a series of Pt(sal)(ppy) complexes was reported. The modularity of these systems presents the opportunity to correlate the structure of the ligands with the activity and selectivity of these complexes in their use as precatalysts in hydrosilylation reactions. This chapter details the development of a model reaction which was then used to benchmark the efficacy of precatalysts **1a–1i** in thermal and photoactivated hydrosilylation reactions. As part of this process, the optimisation of a robust QNMR (Quantitative Nuclear Magnetic Resonance) set-up was developed, which was used to monitor the temporal evolution of catalysis in-situ. This method has allowed for a detailed kinetic study of precatalysts **1a–1i**, along with a comparison of their performance in hydrosilylation reactions under thermal and photoactivated conditions. In addition, the substrate scope is explored by employing a variety of alkene substrates. Lastly, the thermal stability of several precatalysts (**1a**, **1b**, **1d** and **1i**) is presented, along with their ability to photolytically promote the curing of commercially relevant substrate formulations.

3.2 Latent reaction kinetics

Whilst fast and immediate catalytic activity is preferable in many processes, hydrosilylation on an industrial scale often requires catalyst latency.^{1,73,135} In general, catalytic hydrosilylation is a fast reaction that proceeds rapidly at elevated temperatures in the presence of a catalyst, vinylsiloxane and Si–H functionalised siloxane.⁴ For example, Karstedt's catalyst proceeds without an observable induction period.^{1,18} Because of this, two-component mixtures are often prepared to prevent premature cross-linking, where one component contains the catalyst and

the vinylsiloxane, and the other contains the Si–H functionalised siloxane. These mixtures are ideally shelf-stable when separated from one another but cure rapidly upon mixing. However, for some cured silicone products such as release coatings, high production speeds are needed.^{6,93} To eliminate the extra time required for mixing, a one-component mixture consisting of the catalyst, vinylsiloxane and Si–H functionalised siloxane is ideal for such applications. The major problem with one-component systems is that they lead to premature cross-linking, where silicone polymers block machine parts and equipment has to be frequently shut down for cleaning. As such, the ability to fine-tune the activation kinetics for one-component systems would allow for control over the curing times, ideally where there should be no, or very little, catalytic activity under ambient conditions, but rapid curing upon energy input. Towards this purpose, switchable catalysts that are triggered by thermal activation or UV-irradiation have been developed.

One method that has been used to achieve latent reaction kinetics under thermal conditions is the use of catalyst inhibitors.¹³⁶ These act by inhibiting the low temperature activity of the (generally) platinum catalyst, whilst maintaining the high curing speed at elevated temperatures. In order to prevent premature cross-linking, the selected inhibitor needs to have a low vapour pressure to mitigate against deleterious evaporation at ambient temperature. The most frequently employed inhibitors are maleates, fumarates and β -alkynols (Figure 3.1).^{137,138,139}

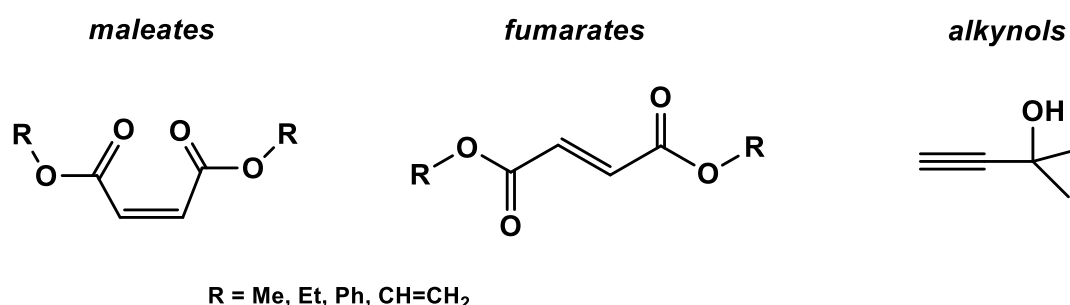


Figure 3.1. Commonly used inhibitors to achieve latent reaction kinetics in the hydrosilylation reaction.

It was initially accepted that inhibitors block the hydrosilylation reaction by binding to the metal centre, and then releasing the active catalyst under elevated temperatures.^{6,138} However, recent computational studies revealed that the commonly used inhibitors would not be soluble in polysiloxane substrates.¹³⁹ It was thus proposed that the presence of inhibitors causes the formation of a second micro-phase, where the platinum catalyst is physically separated from the substrates. Elevating the temperature results in vaporisation of the inhibitor, releasing the active catalyst to allow for rapid curing. This means that shelf-stability and curing rates are highly dependent on the inhibitor's vapor pressure. As such, low boiling maleates can be combined with higher boiling phosphites to extend the shelf-stability but still allow for rapid curing upon thermal triggering.^{1,140}

Dormant platinum complexes bearing relatively strong binding ligands have also been exploited to achieve latent reaction kinetics as they show no hydrosilylation activity under ambient conditions, but rapidly catalyse the reaction upon thermal triggering.¹ These complexes do not require an inhibitor. Dauth and colleagues reported that platinum complexes bearing triazene (**3.1**) and triazeneoxide (**3.2**) ligands allow for good shelf-stability and cure rapidly upon heating > 50 °C (Figure 3.2).¹⁴¹ Platinum bisalkynyl complexes reported by Fehn (**3.3** and **3.4**) have also proven to be catalytically inactive until thermal triggering at temperatures > 40 °C.¹⁴² Calculations using density functional theory (DFT) have shown that the key activation step for converting such platinum bisalkynyl precatalysts into the active catalyst is oxidative addition of the Si–H bond to form the platinum bisalkynyl silyl hydride.¹³⁵ The activation energy of this process can be fine-tuned by modifying the R substituent in the alkynyl groups, which means these systems are industrially applicable to a variety of siloxane substrate systems. More recently, Girolami reported a series of platinum di- ω -alkenyl complexes (**3.5** and **3.6**) that show no reactivity in hydrosilylation reactions for several hours under ambient conditions, but have rapid catalytic activity when heated to 50 °C.⁷³ As detailed in Scheme 3.1, the latent reaction kinetics are attributed to the slow dissociation of the bound COD ligand from **3.6a**, which forms the highly reactive Pt(II) ω -alkenyl intermediate, **3.7**. This species undergoes oxidative addition

of HSiR_3 to form **3.8**. Reductive elimination of the ligands from **3.8** forms the $\text{Pt}(0)$ species, **3.9**, which is converted to the active species **3.10**, following oxidative addition of HSiR_3 . Under ambient conditions, dissociation of COD is very slow, which gives the latent reaction kinetics, but the rate increases exponentially at higher temperatures. The $\text{Pt}(0)$ species **3.9** is suggested to be a molecular Karstedt-like species, and it was proposed that the exact resting state of the Pt^0 species depends on the nature of the substrates used, as different alkenes have different binding strengths.² This concept was introduced by Kühn who suggested that strongly binding alkenes such as norbornadiene forms $\text{Pt}(\text{alkene})_3$ as the active species, whilst weaker binding alkenes such as oct-1-ene form $\text{Pt}(\text{alkene})_2(\text{SiR}_3)\text{H}$ as the active species ($\text{Pt}(\text{II})$). This concept is explored in more detail in chapter four.

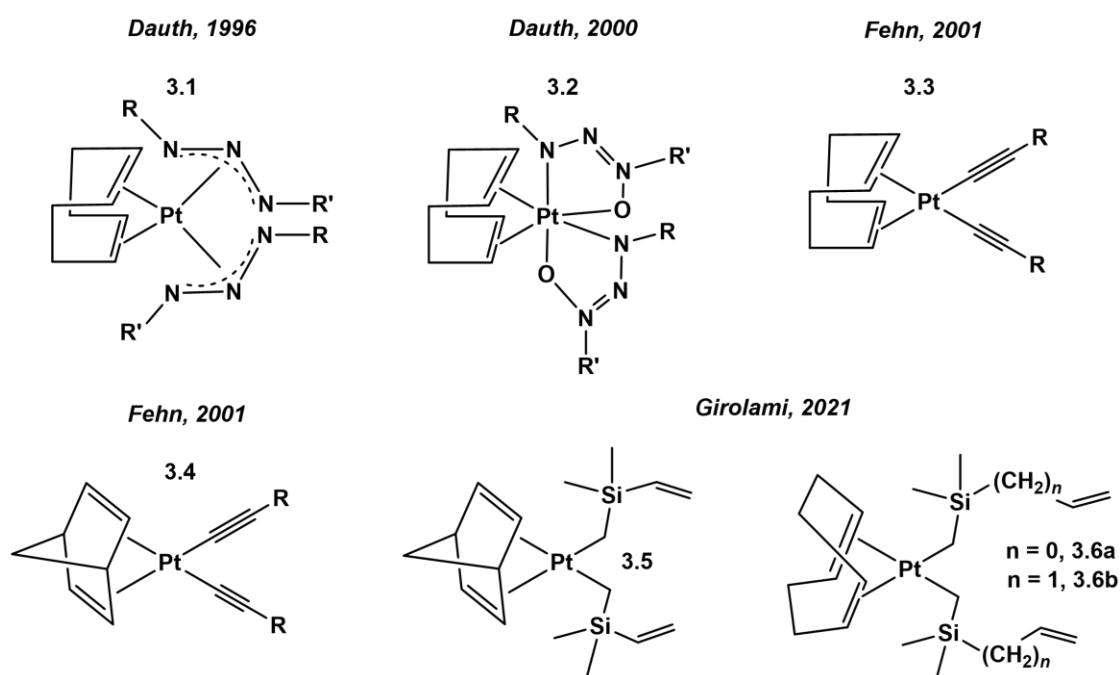
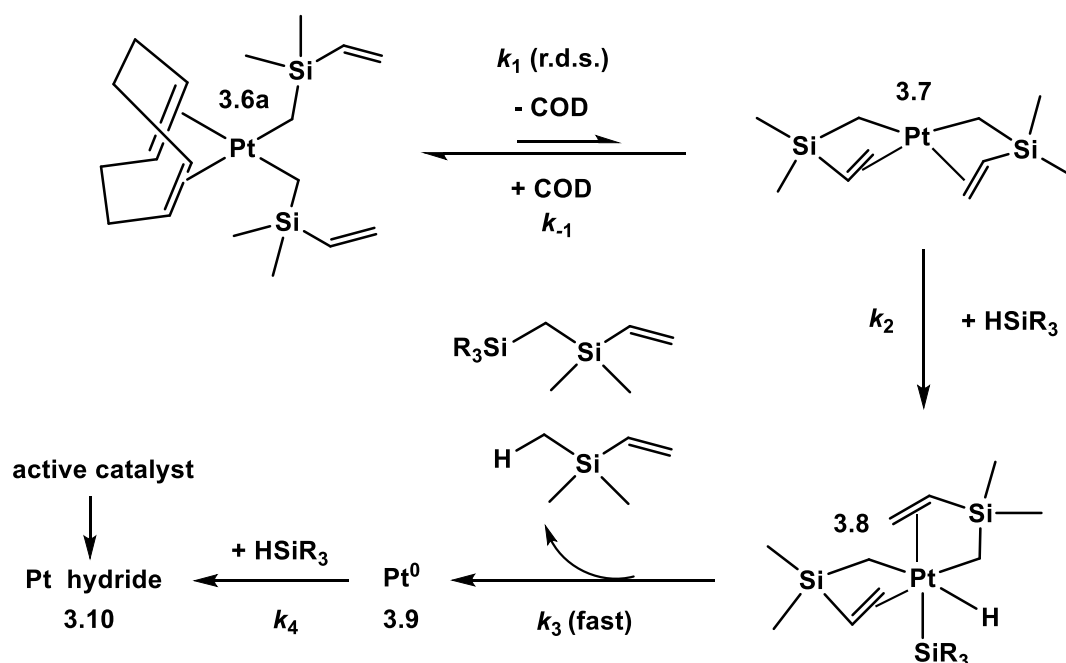


Figure 3.2. Selected examples of dormant platinum complexes used to exploit latent reaction kinetics.



Scheme 3.1. Proposed mechanism for conversion of the platinum di- ω -alkenyl complex into the active catalyst.⁷³

Photogenerated catalysts which are formed upon light triggering of a catalyst precursor have also been explored as a means of achieving latent reaction kinetics.^{1,5} The advantages of such systems are that they potentially have good shelf-stabilities as one-component systems under ambient conditions, and rapid curing can be achieved upon UV-triggering. This is an ideal method for mixtures containing heat-sensitive substrates. As discussed in detail in chapter one, photoactivatable hydrosilylation has been achieved by combining platinum complexes with photosensitisers such as naphthalene and pyrene.¹⁴³ The most well-studied photoactivated hydrosilylation catalysts are those based on the CpPtMe_3 framework, and they have been used extensively in industry for applications such as release liners, dental impressions and sealing compounds.^{78,88} Boardman proposed that the active species generated from this complex is a heterogeneous platinum colloid (see chapter one Scheme 1.19).⁵⁴ However, these complexes are very volatile and highly toxic, so they are being phased out from use.¹⁴⁴ Alternative classes of complexes that have been reported to have excellent catalytic activity upon triggering with UV-light have been discussed in depth in chapter two (Figure 2.5 and Figure 2.6).^{78,97,111,112}

Despite the reports of several platinum complexes finding use in photoactivated hydrosilylation reactions, there has been relatively little attention paid to any latency periods prior to UV-irradiation, or detailed kinetic analysis of the subsequent catalysis. However, given the potential of photoactivated catalysts to provide latent reaction kinetics for one-component formulations, it is paramount that further studies on photocatalysed hydrosilylation reactions are conducted. Furthermore, complexes that have significantly lower toxicity than the benchmark photoactivated hydrosilylation catalyst, CpPtMe₃, are needed. Developments in this area would simplify the manufacturing process and ensure high production speeds of high value silicone products such as release coatings, dental impressions, and adhesives.

The ideal kinetic profile for making cross-linked silicones by hydrosilylation is near-zero rates of catalysis under ambient conditions, but rapid reaction rates upon thermal or UV-triggering, as shown by diagram **1** in Figure 3.3. However, it is very challenging to design catalysts that behave in this way, as some complexes may show no activity under thermal conditions, but still react very slowly upon triggering with UV-light (**2**). Alternatively, some complexes are highly reactive thermally (**3** and **4**), which does not allow exploitation of a latency period.

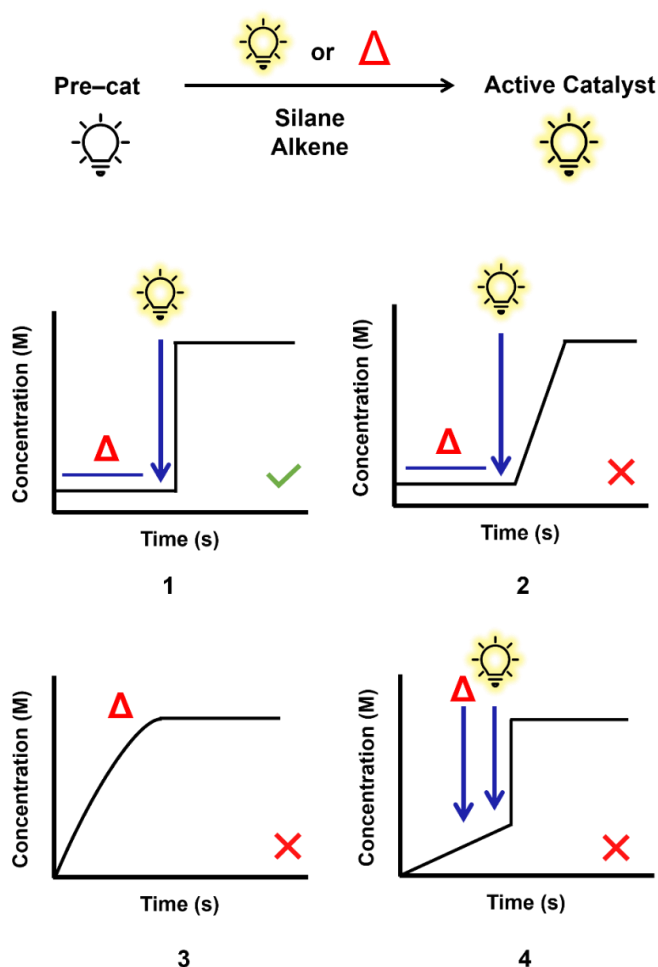


Figure 3.3. Characteristic concentration-time profiles showing ideal latent reaction kinetics upon UV-triggering (1) and non-ideal reaction kinetics (2 – 4).

3.3 Reaction monitoring by NMR spectroscopy

Solution phase NMR spectroscopy is a powerful technique which has long been used to monitor chemical reactions.¹⁴⁵ The quantitative capability of the technique provides a platform for interrogating reaction mechanisms, as selectivity, side products and reaction rates can be determined under suitable conditions. Moreover, the concentrations of substrates, intermediates and products during a reaction can be monitored over time. Whilst many other techniques offer advantages such as rapid data acquisition (UV-Vis or IR spectroscopy) and extremely high sensitivity and dynamic range (mass-spectrometry), often the acquired data are not representative of the 'normal' reaction conditions. Reaction monitoring by NMR

spectroscopy, however, is possible under conditions that replicate the real experimental conditions, and it is therefore a highly valuable tool for studying a wide range of organic and inorganic reaction mechanisms. In order to effectively monitor reactions and obtain mechanistic insight, a number of practicalities need to be considered and are discussed below.

I. Internal standard

It is common practice to employ an internal standard when relying on NMR to obtain accurate concentrations of substrates and products, to eliminate any instrumental variability.^{145,146,147} A suitable internal standard must have low volatility to prevent its loss over the course of the reaction, and similar or lower longitudinal relaxation (T_1) rates compared with the other analytes. For reaction mixtures containing multiple substrates, the delay needs to be 5 times the longest T_1 value so that all spins approach $\geq 99.3\%$ equilibrium before the next 90° pulse. If this condition is not met, it leads to significant integration errors. The internal standard must also have a well resolved peak that does not overlap with any signals from the substrates or products that grow in over the course of the reaction. Most importantly, the internal standard must be inert under the reaction conditions, to other species in the analyte mix and also to external stimuli such as heat or light. Commonly used internal standards are mesitylene, fluorobenzene and dibromomethane.^{148,149,150}

II. Continuous in-situ reaction monitoring

In-situ reaction monitoring describes an experiment that is conducted entirely within one NMR tube.^{151,152} This is in contrast to ex-situ monitoring, where the reaction is conducted as it would be under standard laboratory conditions, and aliquots of the reaction mixture are taken over suitable time points and analysed by NMR.¹⁵³ In both cases, there is a time delay between starting the reaction (t_0) and the acquisition of the first NMR spectrum, which is referred to as the 'dead time'. In-situ reaction monitoring for a kinetic study is only suitable if there is sufficient

access to an NMR spectrometer.¹⁴⁵ The most significant difference with in-situ monitoring compared to ex-situ monitoring is that reactions in NMR tubes cannot be stirred and thus rely on diffusion for mixing.¹⁵⁴ The major benefit of continuous in-situ reaction monitoring is that reactions can be monitored over minutes, hours, or days, with excellent control over the reaction temperature, and after the initial set-up, the experimentalist is not required. Most spectrometers can be programmed to automatically acquire a series of spectra at defined intervals so the NMR tube can be left in the spectrometer until the desired extent of completion is reached.

III. Acquisition parameters

Prior to the acquisition of a series of individual NMR spectra at varying time points over the course of a reaction, several acquisition parameters need to be considered to ensure accurate quantitative analysis.¹⁴⁵ The general workflow is: preparing the sample, inserting it into the spectrometer, allowing the sample to equilibrate to the set temperature, setting acquisition parameters, tuning the probe, locking to the solvent, shimming, and collecting data. Well-resolved peaks are important for accurate quantitation, and this can be achieved by good shimming. This process minimises field inhomogeneity by adjusting the current in shim coils around the probe and ensures that sharp signals are generated. It is also important that the spectral width is sufficiently wide that all species in the reaction mixture are captured. The acquisition time plays a key role in the acquirement of quantifiable data, and it should be set to maximise the signal to noise ratio. Setting an appropriate relaxation delay (i.e., 5 x the slowest T_1) leads to a suitable acquisition time.

IV. Quantitation by integration

In an NMR spectrum, chemically distinct spins give rise to signals whose area is directionally proportional to the number of nuclei.¹⁴⁵ This means that concentrations of substrates and products in the reaction mixture can be determined over time. It is important that the chosen

substrates have distinct chemical shifts from one another, as spectral congestion due to overlapping signals does not allow for accurate quantification of substrate and product concentration. Quantitative NMR can be conducted using relative or absolute methods.¹⁴⁷ In the relative quantitation method, the integrals of signals are compared with one another to determine the ratio of different compounds. The ratios are calculated using Equation 3.1, where M , I and N are molar ratio, integral and number of nuclei respectively.

$$\frac{M_x}{M_y} = \frac{I_x}{I_y} \cdot \frac{N_y}{N_x}$$

Equation 3.1. Calculation to determine relative ratios of analytes by NMR.

For absolute quantitation, a compound of known concentration is needed.¹⁴⁵ This is often the internal standard, as it is at fixed concentration and the number of nuclei contributing to each signal is known. The absolute values of concentration of the analytes can be determined using Equation 3.2, where C , I , and N are concentration, signal integral and number of nuclei respectively.

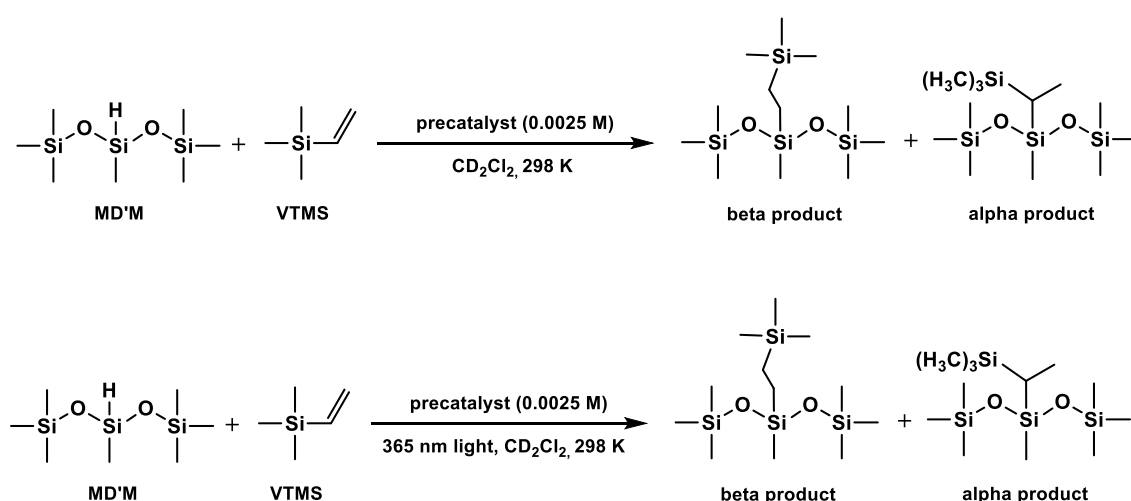
$$C_x = \frac{I_x}{I_{std}} \cdot \frac{N_{std}}{N_x} \cdot C_{std}$$

Equation 3.2. Calculation to determine absolute concentration of analytes by NMR.

When using NMR integrals to determine the concentration of analytes, it is imperative that the integral regions are consistent throughout the series of spectra. This means that satellite peaks are consistently included or excluded from the integration region, and that the same proportion of each peak of interest is covered.

3.4 Optimised model hydrosilylation reaction

At the onset of the kinetic studies reported in this thesis, a model reaction was chosen with a set of conditions that would allow for detailed and meaningful comparisons of the performance of precatalysts **1a–1i** in hydrosilylation reactions under thermal and photoactivated conditions. The hydrosilylation of vinyltrimethylsilane (**VTMS**) by hexamethylsiloxymethylsilane (**MD'M**) in d_2 -dichloromethane in the presence of 0.0025 M precatalyst at room temperature was optimised as the model reaction. All reactions performed under ‘thermal conditions’ were conducted at room temperature (298 K) under ambient conditions, in the absence of irradiation (Scheme 3.2, top). For the reactions under photoactivated conditions, the reaction mixture was monitored under thermal conditions for ~1 h to assess the latency period, before being irradiated outside of the NMR spectrometer for either 10, 60 or 120 s on a bespoke 365 nm LED array (Scheme 3.2, bottom). The sample was then returned to the spectrometer post-irradiation. Mesitylene was added as an internal standard to account for variation in the absolute integrals between individual spectra in the data set. This internal standard was found to be unreactive under the reaction conditions and the signal for the methyl groups (δ 2.29) is sufficiently distinct from the **MD'M**, **VTMS** and precatalyst signals.



Scheme 3.2. Model hydrosilylation reaction used for kinetic studies under thermal (top) and photoactivated (bottom) conditions.

The use of this reaction and specific conditions was motivated by the following reasons:

- I. After initial optimisation, the catalyst loading of 0.25 mol% (0.0025 M) was chosen to give a reaction time for all precatalysts on the order of 0.15 – 22.4 h, a timeframe which enables a sufficient number of data points for a satisfactory kinetic analysis by QNMR. As the precatalysts and hydrosilylation substrates are soluble in dichloromethane, this solvent was chosen for the model reaction. Furthermore, dichloromethane is used to dissolve the precatalysts before their addition to the commercial polymer substrates in the commercial set-up (see section 3.9), so this solvent was chosen to closely mimic the industrial process.

- II. **MD'M** was chosen as the silane substrate as it bears a structural resemblance to the commercially used hydrosiloxane polymer. In addition to this, there have been many reports of **MD'M** being used as the silane substrate in the academic and patent literature, which allows for comparison of the system developed here with previously reported systems.^{73,105} The ¹H NMR spectrum of **MD'M** is shown in Figure 3.4 and the three distinct resonances at δ 4.63, 0.13 and 0.11 correspond to the Si–H, Si(CH₃)₃ and Si–CH₃ protons, respectively. The peaks at δ 4.63 and 0.13 are accompanied by ²⁹Si satellites ($I = \frac{1}{2}$, 4.7% natural abundance) which measure $^1J_{\text{H-Si}} = 236.2$ and $^5J_{\text{H-Si}} = 6.9$ Hz, respectively. The coupling for the quartet observed at δ 4.63 measures $^3J_{\text{H-H}} = 1.5$ Hz. Another set of ²⁹Si satellites is observed around the peak at δ 0.11, which measures $^2J_{\text{H-Si}} = 117.9$ Hz.

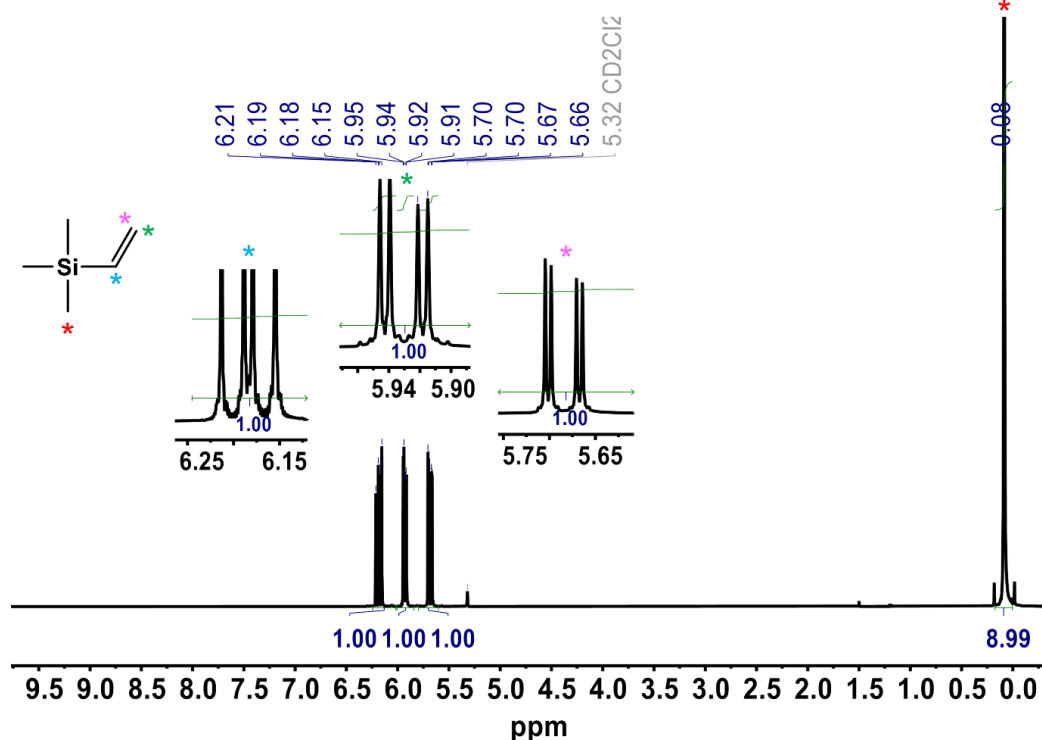


Figure 3.5. ^1H NMR spectrum of VTMS (600 MHz, d_2 -dichloromethane, 298 K).

IV. This reaction proceeds cleanly to afford the anti-Markovnikov (beta) hydrosilylation product, which can easily be distinguished in the ^1H and ^{29}Si NMR spectra. No difference in selectivity was observed between the thermal and photoactivated reaction conditions. Representative spectra from using precatalyst **1b** under photoactivated conditions are shown in Figure 3.6 and Figure 3.7. The signals centred at δ 0.42, 0.13, 0.04 and 0.01 in the ^1H NMR spectrum correspond to the $\text{Si}-\text{CH}_2-\text{CH}_2-\text{Si}$, $2 \times \text{Si}(\text{CH}_3)_3$, $\text{Si}-\text{CH}_3$ and $\text{Si}(\text{CH}_3)_3$ protons of the beta product, respectively. The signal observed at δ 2.28 corresponds to the $3 \times \text{CH}_3$ protons of mesitylene (internal standard). In the ^{29}Si NMR spectrum, the three signals are observed at δ 6.9, 3.1 and -20.7 , corresponding to the beta product. This assignment was facilitated by a $^{29}\text{Si}-^1\text{H}$ HMBC experiment (Figure 3.8). This spectrum shows the correlation between the ^{29}Si signal at δ 6.9 (**3**) with the 18 $\text{Si}-(\text{CH}_3)_3$ protons of the beta product. The ^{29}Si signal at δ 3.1 (**1**) correlates with the $\text{Si}-\text{CH}_2-\text{CH}_2-\text{Si}$ protons as well as the $\text{Si}(\text{CH}_3)_3$ protons of the beta product. Lastly the most

upfield ^{29}Si signal for the beta product at $\delta -20.7$ (**2**) correlates with the Si-CH₂-CH₂ and Si-CH₃ protons. No overlapping signals with the substrates at any time-point over the course of the reaction are observed. This allows for the clear and unambiguous determination, and quantification, of products and substrates.

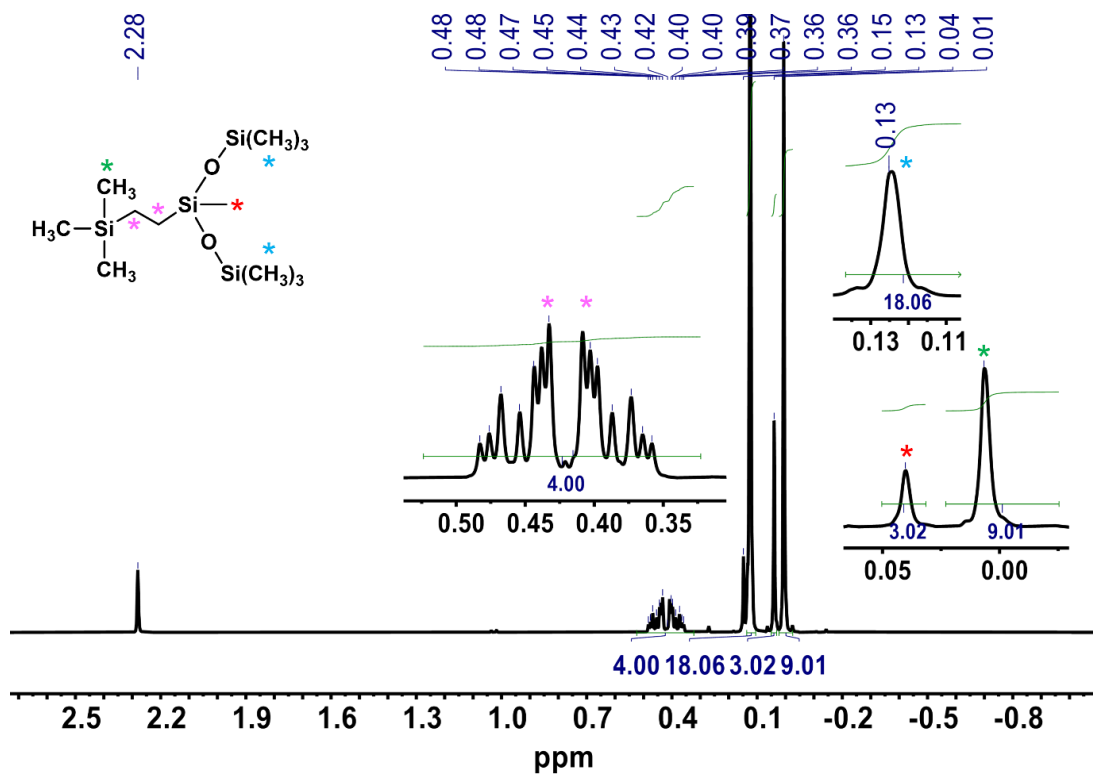


Figure 3.6. Representative ^1H NMR spectrum of the beta product formed in the photoactivated hydrosilylation reaction between **MD'M** and **VTMS** when using precatalyst **1b** (600 MHz, d_2 -dichloromethane, 298 K). Reaction conditions (0.93 M **MD'M** and 0.93 M **VTMS**, left for ~1 h thermally, then irradiated for 120 s).

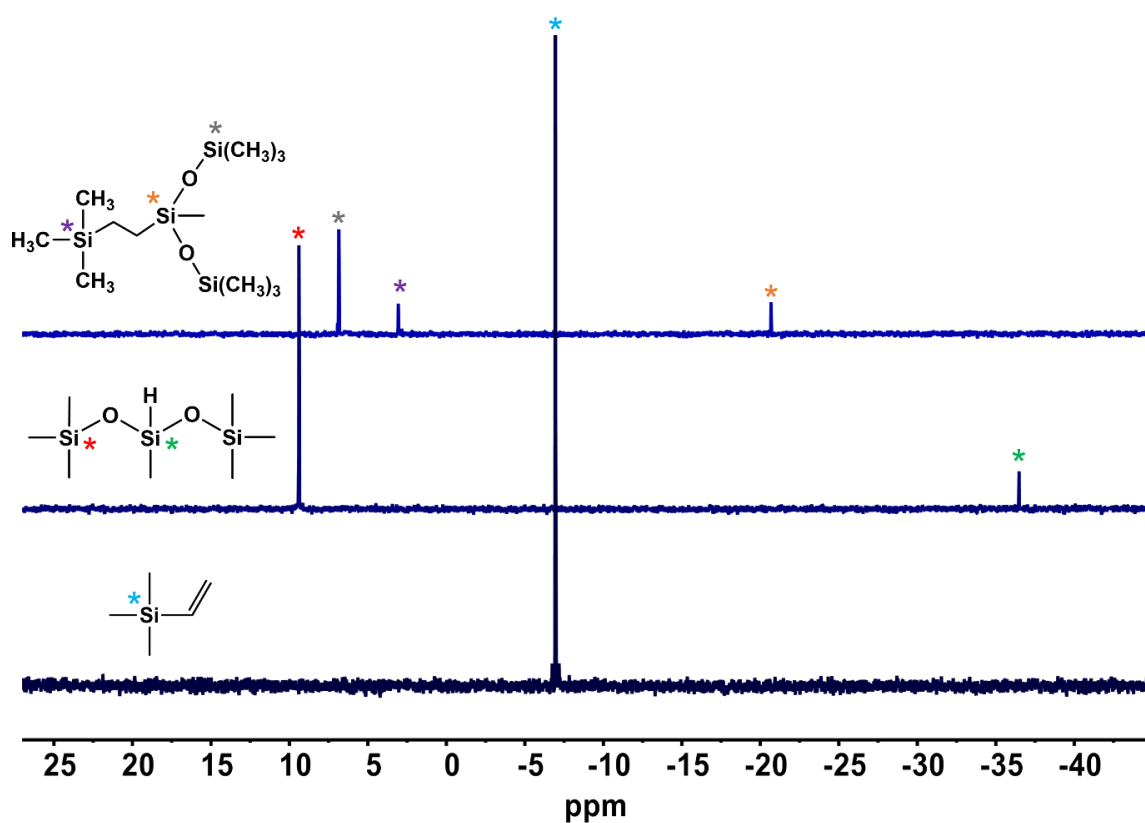


Figure 3.7. ^{29}Si NMR spectra of **VTMS** (bottom), **MD'M** (middle) and beta product (top) formed in the photoactivated hydrosilylation reaction between **MD'M** and **VTMS** when using precatalyst **1b** (119.2 MHz, d_2 -dichloromethane, 298 K). Reaction conditions (0.93 M **MD'M** and 0.93 M **VTMS**, left for ~1 h thermally, then irradiated for 120 s).

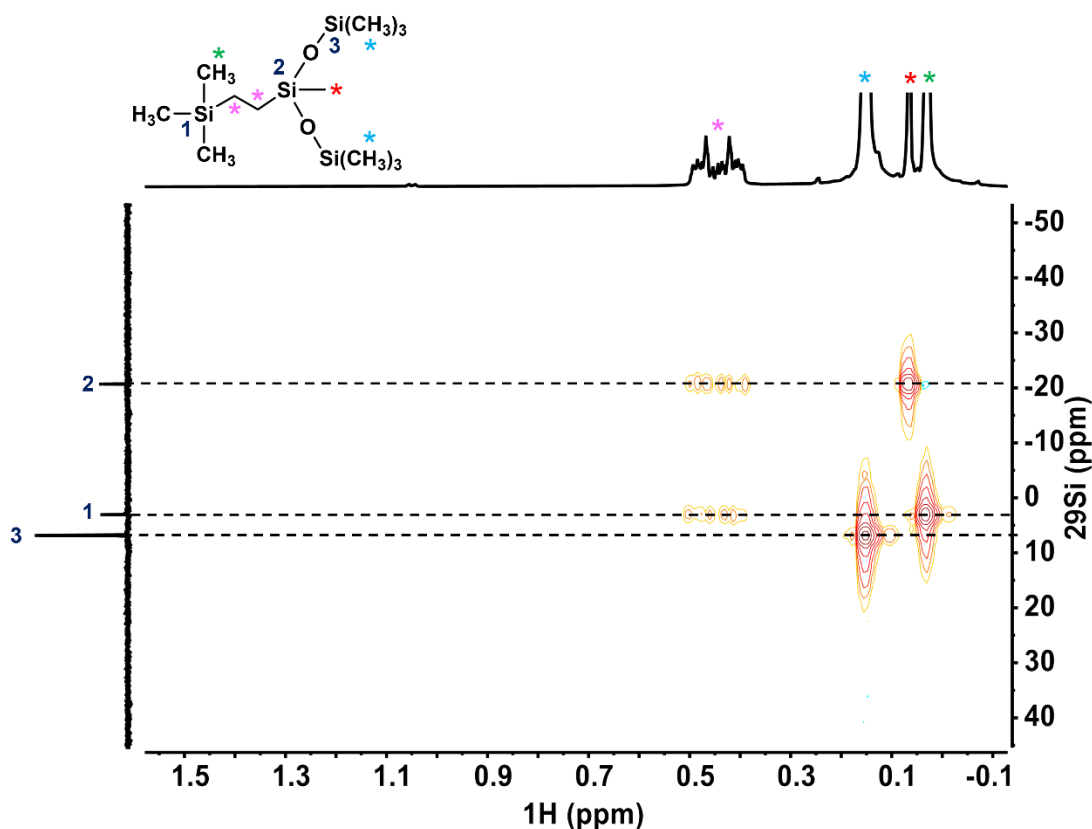


Figure 3.8. ^{29}Si - ^1H HMBC spectrum of the beta product formed in the photoactivated hydrosilylation reaction between **MD'M** and **VTMS** when using precatalyst **1b** (119.2, 600.1 MHz, d_2 -dichloromethane, 298 K). Reaction conditions (0.93 M **MD'M** and 0.93 M **VTMS**, left for ~1 h thermally, then irradiated for 120 s).

- V. For all experiments conducted under photoactivated conditions, an in-house designed and constructed 365 nm LED array was used (Figure 3.9). Four LEDs (each 1.36 W) are mounted in a cuboid made of aluminium and are arranged pointing towards one another so that the beams are orthogonal to the axis of the NMR tube. Four omnidirectional heatsinks are attached to the cuboid to facilitate the dissipation of heat. To ensure sufficient beam spread, the beam is centred 20 mm above the base of the NMR tube. A 3D-printed top cover has a hole drilled in of suitable size for the NMR tube (5 mm) and another hole to allow for tubing connected to the compressed air to dissipate extra heat and allow for temperature control. The benefits of this 365 nm LED array are that there is no ozone generation, no required warm up times and the power supply can be switched on and off with the associated timer unit. This allows for excellent control over

irradiation times and ensures accurate data collection. The absorption coefficients at 365 nm for precatalysts **1a** – **1i** are listed in Table 3.1.

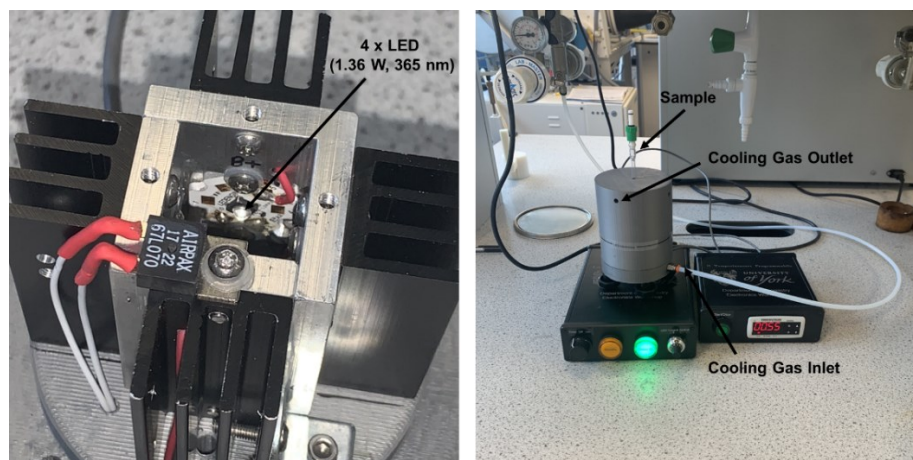


Figure 3.9. 365 nm LED array used in all photoactivated kinetic studies. Left – arrangement of LEDs. Right – NMR tube inserted into the LED array which is connected to the compressed air for temperature control, and a timer to set the irradiation time.

Table 3.1. Absorption coefficients at 365 nm in the UV-vis spectra of precatalysts **1a**–**1i**.

Precatalyst	Absorption coefficient at 365 nm [log(ϵ dm ³ mol ⁻¹ cm ⁻¹)]
1a	4.28
1b	4.12
1c	3.97
1d	3.87
1e	3.91
1f	4.18
1g	3.80
1h	4.16
1i	4.23

3.5 Optimised set-up for reaction monitoring by NMR spectroscopy

As shown in Figure 3.10, the chemical shifts of the mesitylene (CH_3)₃ (δ 2.29), Si–H (δ 4.63), olefinic CH (δ 6.18) and beta product Si–CH₂–CH₂–Si (δ 0.42) resonances are sufficiently distinct

from one another over the course of the reaction. This means that the same integral regions of each peak can be covered and ensures accurate quantitative analysis. Detailed optimisation of the NMR acquisition parameters resulted in using a long relaxation delay of 45 s, as ^{29}Si nuclei are characterised by very long T_1 relaxation times and therefore long delays between scans are required to allow for full relaxation.¹⁵⁶ Using a relaxation delay of 20 s resulted in the concentrations of **MD'M** and **VTMS** being underestimated.

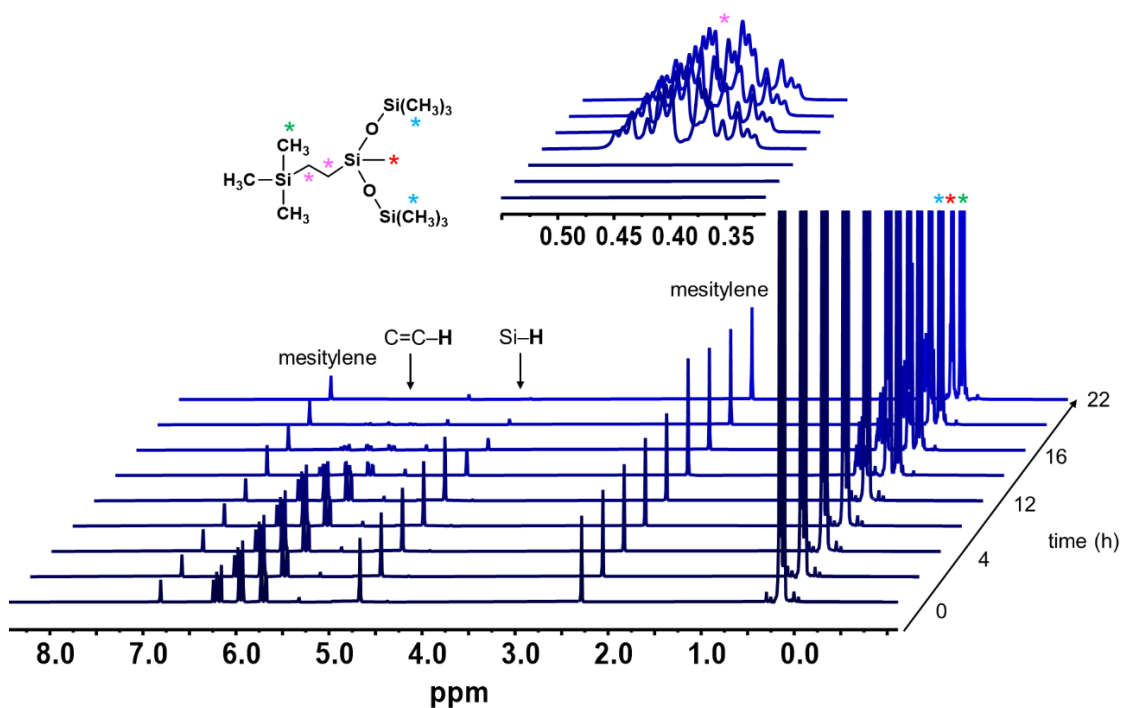


Figure 3.10. Representative stacked ^1H NMR spectra of the in-situ thermal hydrosilylation reaction between **MD'M** and **VTMS** over time to show distinctive signals of **MD'M**, **VTMS**, mesitylene and the beta product. The inset shows the ethylene signals of the beta product (600 MHz, d_2 -dichloromethane, 298 K). Reaction conditions (0.93 M **MD'M** and 0.93 M **VTMS**).

3.6 Performance of Pt(sal)(ppy) complexes in thermal and photoactivated hydrosilylation reactions

3.6.1 Precatalyst 1a

To assess and compare the catalytic activity of precatalysts **1a–1i** in the model hydrosilylation reaction, a series of NMR experiments were conducted. For each experiment, the precatalyst (0.0025 M) was loaded into a J. Young's NMR tube, and to it was added d_2 -dichloromethane, along with **MD'M** (0.8 – 1.0 M), **VTMS** (0.8 – 1.0 M) and mesitylene (0.10 M) from a stock solution. The sample was inserted into the NMR spectrometer and an array of ~ 20 ^1H NMR spectra was acquired to determine the thermal latency period over ~ 1 h. The sample was then removed from the spectrometer and irradiated using the bespoke 365 nm LED for either 10, 60 or 120 s before being returned to the spectrometer (note that this step is omitted for experiments conducted under thermal conditions). An array of 10 – 100 ^1H NMR spectra was acquired with appropriate delays between each acquisition (depending on the catalytic activity) and the concentrations of **MD'M**, **VTMS** and beta product were calculated using the absolute quantitation method (see Equation 3.2). The absolute NMR integrals of the Si–H (δ 4.63), olefinic CH (δ 6.18) and Si–CH₂–CH₂–Si (δ 0.42) resonances were compared with the (CH₃)₃ (δ 2.29) resonance of the internal standard. The kinetics were probed using the initial rates method, monitoring the rate of beta product formation over the first 3 – 5 data points after catalytic activity had been established. For the thermal profiles with an associated induction period, the initial rate was measured after the induction period, at the maximum rate of turnover. Errors were calculated using the linear regression model (LINEST) in Microsoft Excel. The reported errors are the estimated standard error from the model. For each figure in this section, silane refers to **MD'M**. The concentration-time profiles along with the table of initial rates for the model reactions conducted in the presence of precatalyst **1a** are shown in Figure 3.11.

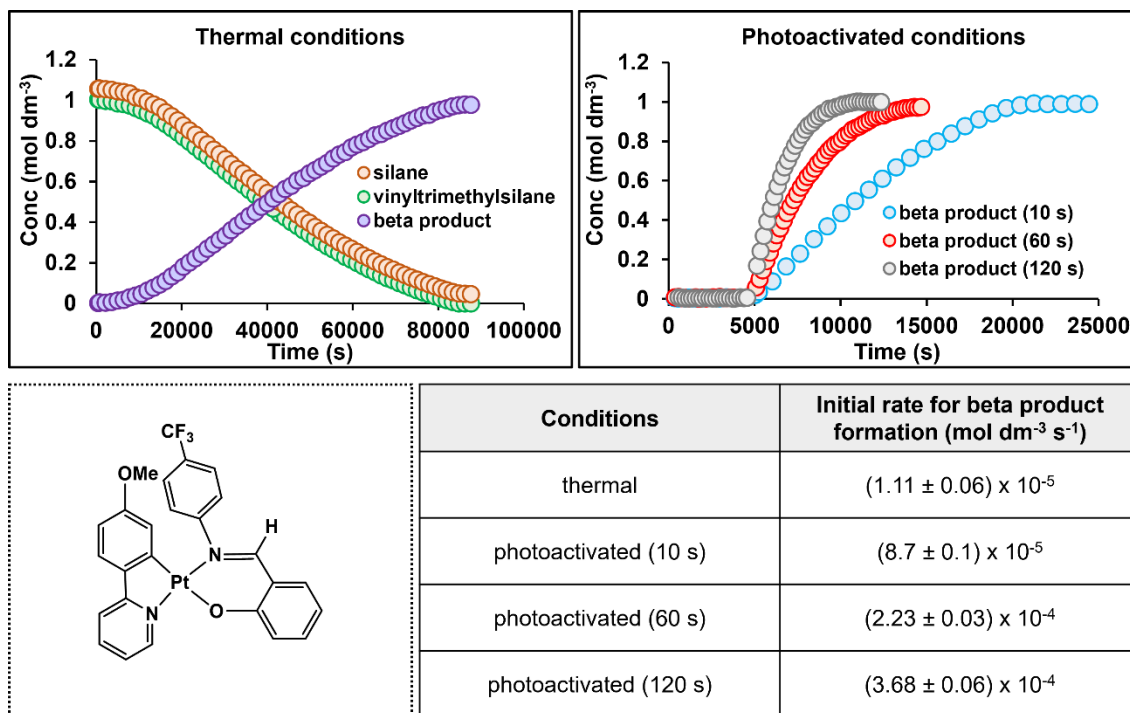


Figure 3.11. Left – concentration-time profile of **MD'M** and **VTMS** consumption and beta product formation during the thermal hydrosilylation reaction using **1a** as a precatalyst. Right – concentration-time profile of beta product formation during the photoactivated hydrosilylation reaction using **1a** as a precatalyst, with 10, 60 and 120 s irradiation. Reaction conditions as detailed in section 3.6. All photoactivated plots are time-shifted to 5000 s to show the same latency period. The table shows the initial rates extracted from the first five data points after catalytic activity has been established.

The thermal reaction is characterised by a sigmoidal profile, with a pseudo-zero order regime at maximum rate of turnover, which represents a process that converts the precatalyst into the active catalyst. The precatalyst has an associated induction period of 5.0×10^3 s (1.4 h). An expansion of the latent period for the thermal reaction is detailed in the appendix. Under the photoactivation regime, a latency period is confirmed followed by a burst of catalytic activity upon irradiation. That turnover continues after the irradiation is stopped identifies the active species generated from precatalyst **1a** as a photoactivated catalyst, as it does not require continuous irradiation to effect turnover (photocatalysis). Under thermal conditions, the reaction requires 8.06×10^4 s (22.4 h) to reach completion, compared with 1.7×10^4 s (4.7 h), 9.3×10^3 s (2.6 h) and 5.6×10^3 s (1.5 h) under photoactivated conditions at the 10, 60 and 120 s

irradiation times, respectively (excluding the ~1 h latency period). Correspondingly, compared with the initial rate measured under thermal conditions, the rates are 8, 20 and 33 x faster under the photoactivation conditions at the 10, 60 and 120 s irradiation times, respectively. Longer irradiation times are consistent with an augmented initial rate which suggests that more active catalyst is generated at the longer irradiation times. However, in the ^1H NMR spectrum at the end of catalysis, the distinctive signals due to the precatalyst at δ 9.42 (proton *ortho* to nitrogen in phenylpyridine) and 8.25 (imine proton) are still observed and integrate to show that the precatalyst is essentially unchanged (Figure 3.12). No new signals are observed in the ^1H NMR spectrum which would be indicative of a new species or decomposition. This suggests that only a very small amount (less than 5%) of the precatalyst is activated. This means that it is not possible to quantify how much active catalyst is generated from the precatalyst at the different irradiation times using NMR. Nonetheless, **1a** is a competent hydrosilylation precatalyst that is inactive under thermal conditions for ~1.4 h but promotes fast turnover upon irradiation.

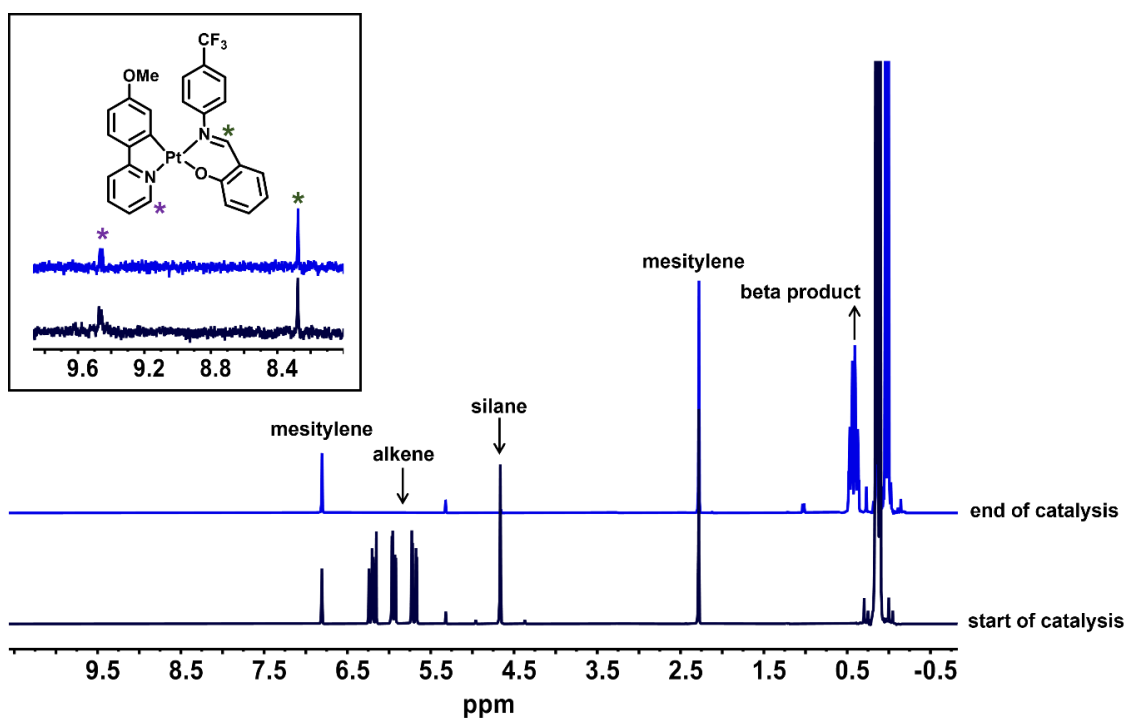


Figure 3.12. In-situ ^1H NMR spectra of the photoactivated hydrosilylation reaction between **MD'M** and **VTMS** using **1a** as a precatalyst (400 MHz). Reaction conditions (0.0025 M **1a**, 1.0 M **MD'M**, 1.0 M **VTMS** in d_2 -dichloromethane, 120 s irradiation with 365 nm LED, 298 K). The bottom spectrum is the reaction mixture at the start of catalysis and the top spectrum is at the end of catalysis. The inset shows that there is no observable change in the catalyst after hydrosilylation.

3.6.2 Precatalyst **1b**

In a similar series of experiments, precatalyst **1b** was employed in the model reaction to determine its efficacy as a latent, photoactivated hydrosilylation precatalyst. The concentration-time profiles for the experiments conducted under thermal and photoactivated conditions and the table of initial rates are shown in Figure 3.13.

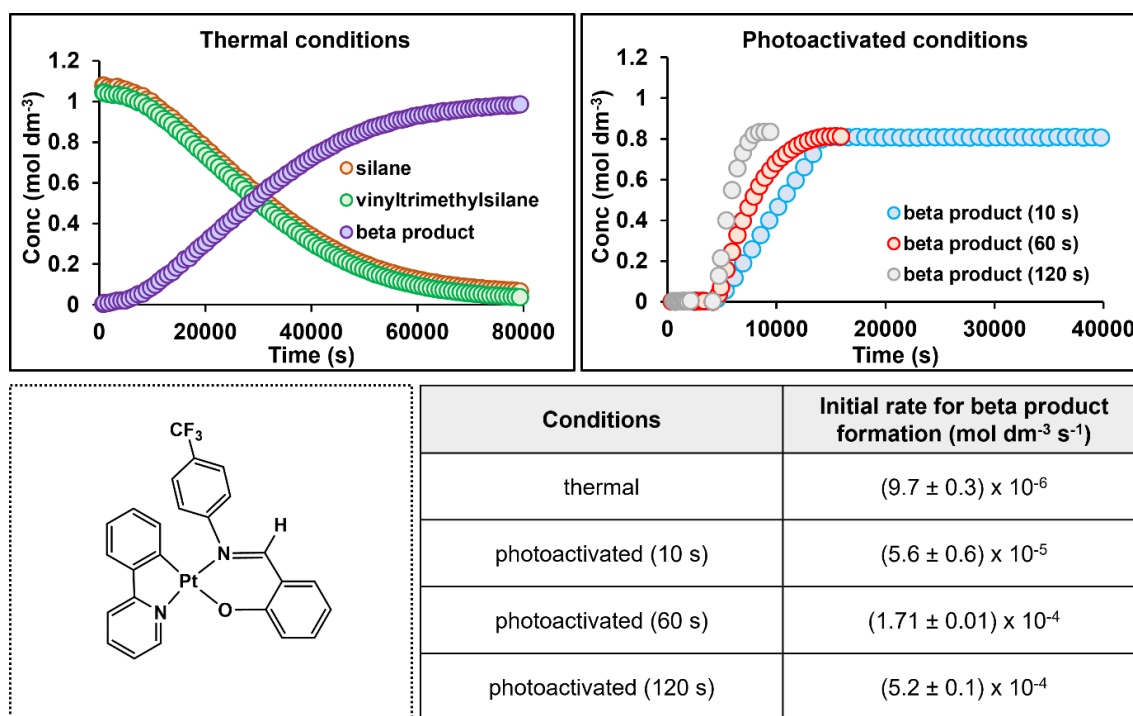


Figure 3.13. Left – concentration-time profile of **MD'M** and **VTMS** consumption and beta product formation during the thermal hydro-silylation reaction using **1b** as a precatalyst. Right – concentration-time profile of beta product formation during the photoactivated hydro-silylation reaction using **1b** as a precatalyst, with 10, 60 and 120 s irradiation. Reaction conditions as detailed in section 3.6. All photoactivated plots are time-shifted to 4000 s to show the same latency period. The table shows the initial rates extracted from the first five data points after catalytic activity has been established.

Concordant with that observed when **1a** was used as the precatalyst, **1b** successfully catalyses the model reaction under thermal and photoactivated conditions, and also shows latent reaction kinetics. The shape of the temporal profiles also resemble that observed for precatalyst **1a**, signalling a similar activation process for both precatalysts. The associated induction period for **1b** however is significantly longer than for **1a** (2.8 vs 1.4 h), which is conducive to good latent catalytic behaviour. The reaction takes 7.96×10^4 s (22.1 h) to reach completion under the thermal conditions, compared to 1.0×10^4 s (2.9 h), 9.3×10^3 s (2.6 h) and 4.4×10^3 s (1.2 h), at the 10, 60 and 120 s irradiation times, respectively (excluding the ~1 h latency period). Photoactivation at the 10, 60 and 120 s irradiation times concurs with a 6, 18 and 54-fold rate increase respectively, compared to the rate of the thermally activated precatalyst. Overall, the

reaction times are marginally faster for precatalyst **1b** than **1a** under the thermal and photoactivation conditions, which suggests a more efficient photoactivation mechanism for **1b**.

3.6.3 Precatalyst 1c

In order to elucidate the impact of the alkyl group on the Schiff base ligand, precatalyst **1c** was used in the model reaction under thermal conditions and at 10 and 120 s irradiation under photoactivation conditions (Figure 3.14).

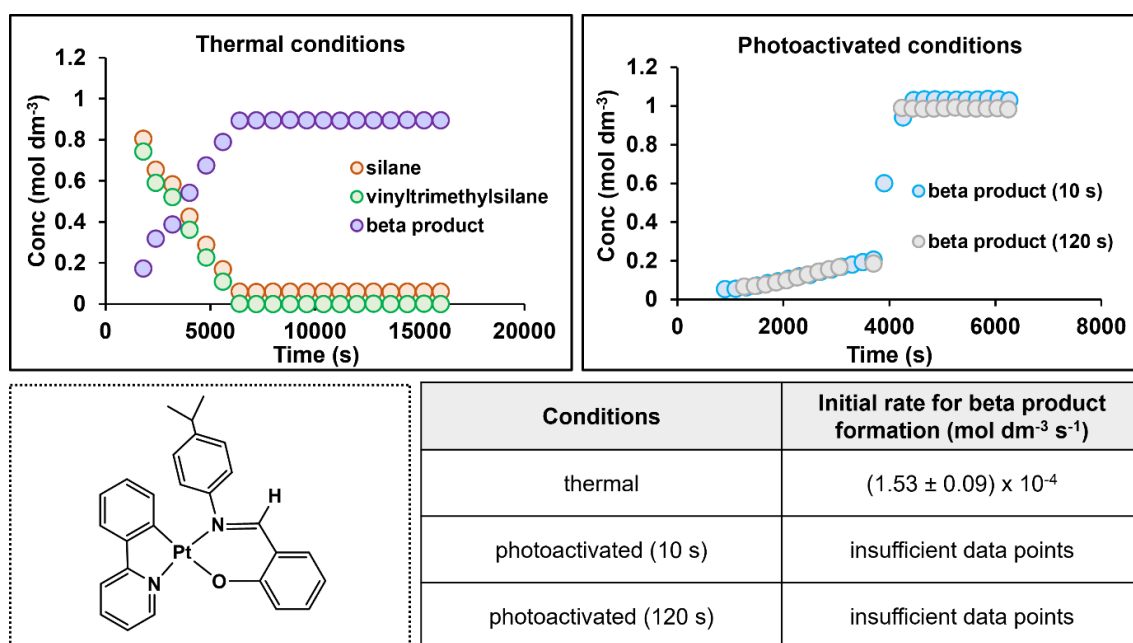


Figure 3.14. Left – concentration-time profile of MD'M and VTMS consumption and beta product formation during the thermal hydrosilylation reaction using **1c** as a precatalyst. Right – concentration-time profile of beta product formation during the photoactivated hydrosilylation reaction using **1c** as a precatalyst, with 10 and 120 s irradiation. Reaction conditions as detailed in section 3.6. Photoactivated plots are time-shifted to 3700 s to show the same latency period. The table shows the initial rates extracted from the first five data points after catalytic activity has been established.

In contrast to that observed when precatalysts **1a** and **1b** were used in the model reaction, precatalyst **1c** does not exhibit latent catalytic behaviour. The thermal profile follows an apparent zero-order regime over the course of the reaction, which requires 6.4×10^3 s (1.8 h) to reach

completion. After irradiating precatalyst **1c** for 10 and 120 s, the reaction is complete after 7.6×10^2 s (0.21 h) and 5.4×10^2 s (0.15 h) respectively, but ~18% conversion had already been reached pre-irradiation. Measurement of the initial rate was not possible due to the very high catalytic activity observed for precatalyst **1c** under the photoactivation conditions. Replacement of the $-\text{CF}_3$ functionality (**1a** and **1b**) by the $-\text{CH}(\text{CH}_3)_2$ group (**1c**) serves to accelerate the catalytic activity under thermal and photoactivation conditions, but the absence of a latency period for precatalyst **1c** is not conducive to the industrial requirements.

3.6.4 Precatalyst **1d**

After assessing the impact of the ligands bearing electron withdrawing ($-\text{CF}_3$) and electron donating ($-\text{CH}(\text{CH}_3)_2$) groups on catalysis, the effect of using an unsubstituted precatalyst was probed. The concentration-time profiles acquired for using precatalyst **1d** in the model thermal and photoactivated reactions are shown in Figure 3.15.

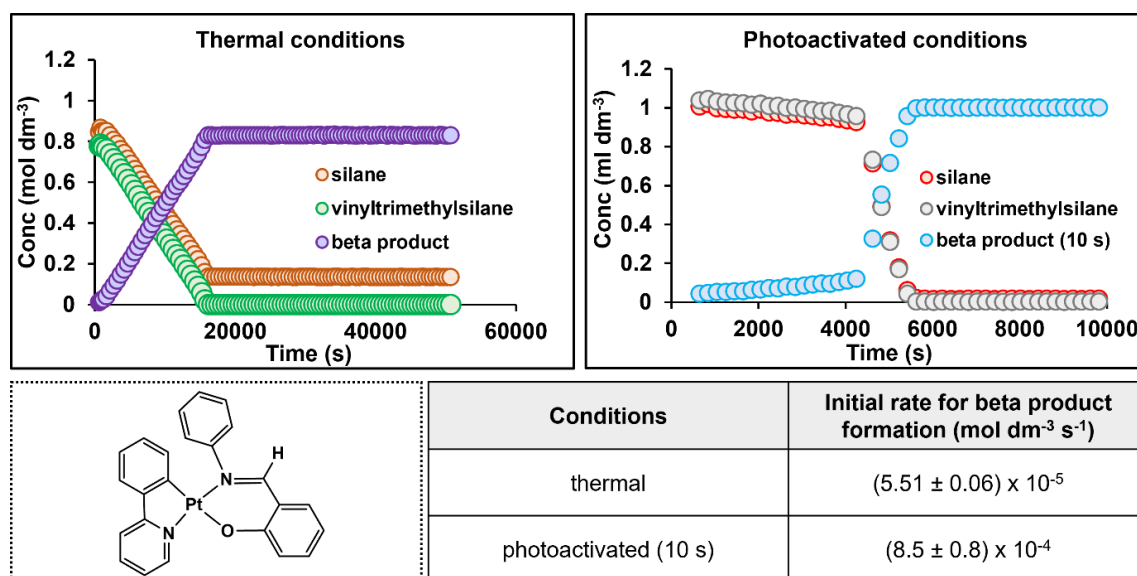


Figure 3.15. Left – concentration-time profile of **MD'M** and **VTMS** consumption and beta product formation during the thermal hydro-silylation reaction using **1d** as a precatalyst. Right – concentration-time profile of **MD'M** and **VTMS** consumption and beta product formation during the photoactivated hydro-silylation reaction using **1d** as a precatalyst, with 10 s irradiation. Reaction conditions as detailed in section 3.6. The table shows the initial rates extracted from the first five data points after catalytic activity has been established.

Under the thermal conditions, an apparent zero-order reaction profile is observed, where catalytic turnover is evident from the first measurement at 6.5×10^2 s. This translates to a very short induction period (5.8×10^2 s, 0.16 h) using the method of Morris (i.e. the time taken for 1% conversion to occur), and completion of the reaction requires 1.6×10^4 s (4.5 h).¹⁵⁷ Following the 10 s irradiation period in the photoactivated experiment, full conversion is achieved after 1.4×10^3 s (0.38 h), although the reaction had reached ~12% conversion before being irradiated. Nonetheless, a significant rate acceleration of 15 x that observed in the thermal reaction is obtained after only 10 s irradiation. This demonstrates that precatalyst **1d** is rapidly converted into the active species upon irradiation. Compared to precatalyst **1b** under thermal and photoactivated conditions (which has an induction period of 1.0×10^4 s (2.8 h)), much faster catalytic activity is observed when using the unsubstituted **1d**, but this precatalyst has a significantly reduced induction period, and therefore poor latency. Precatalyst **1c** reacts even faster than **1d** in the model reactions, but with an even shorter induction period (4.7×10^2 s, 0.13 h). This example serves to illustrate the challenges associated with designing precatalysts that show good thermal latency but fast catalytic activity upon irradiation with UV-light.

3.6.5 Precatalyst **1e**

To determine how the rate of hydrosilylation is influenced by the presence of three $-\text{OCH}_3$ groups on the Schiff base ligand of the precatalyst, **1e** was employed in the model reaction and monitored under thermal and photoactivated conditions (Figure 3.16).

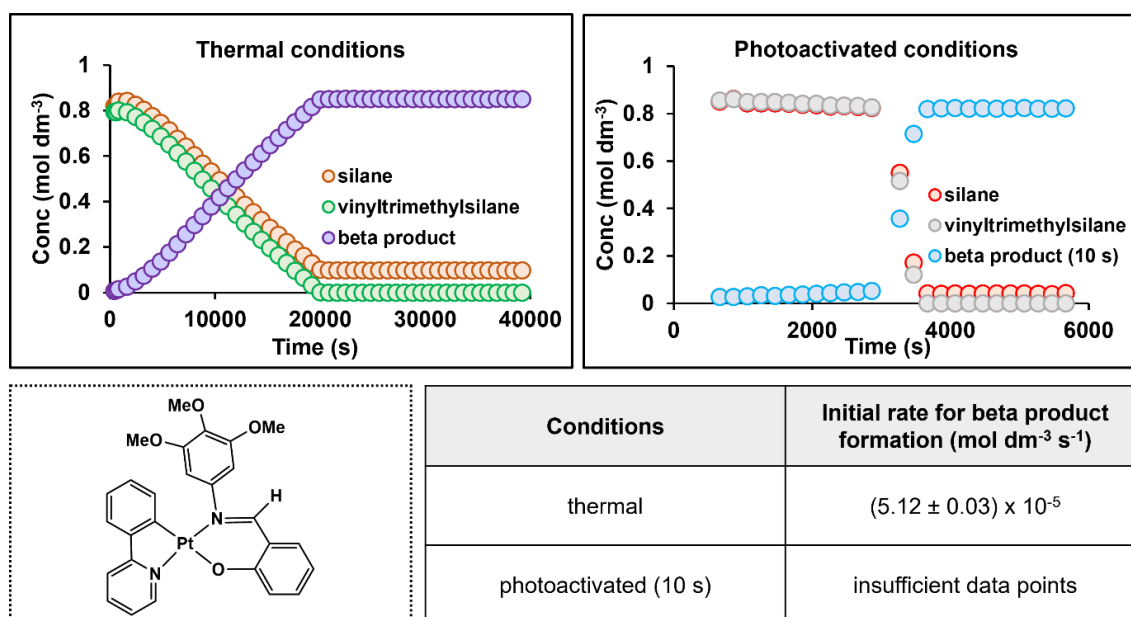


Figure 3.16. Left – concentration-time profile of **MD'M** and **VTMS** consumption and beta product formation during the thermal hydrosilylation reaction using **1e** as a precatalyst. Right – concentration-time profile of **MD'M** and **VTMS** consumption and beta product formation during the photoactivated hydrosilylation reaction using **1e** as a precatalyst, with 10 s irradiation. Reaction conditions as detailed in section 3.6. The table shows the initial rates extracted from the first five data points after catalytic activity has been established.

A short (1.6×10^3 s, 0.45 h) induction period is observed in the thermal reaction using precatalyst **1e**, presumably during which the precatalyst activates. This is preceded by a faster burst of catalytic activity which follows a zero-order regime and requires 2.0×10^4 s (5.6 h) to afford full conversion. Under photoactivated conditions, a very small amount of beta product is formed before irradiation (~5%), followed by rapid and full conversion (~to the beta product after only 10 s irradiation (initial rate not measured due to insufficient number of data points). This signals that the $-\text{OCH}_3$ groups facilitate the latent catalytic behaviour under thermal conditions, whilst promoting fast conversion to the active catalyst upon irradiation.

3.6.6 Precatalyst 1f

The impact of the Schiff base ligand on the precatalyst having two electron withdrawing –F groups was probed in the model reaction using precatalyst **1f**. The concentration-time profiles for the reactions under thermal and photoactivated conditions are shown in Figure 3.17. Note that the initial portion of the thermal experiment was not monitored due to technical issues with the spectrometer.

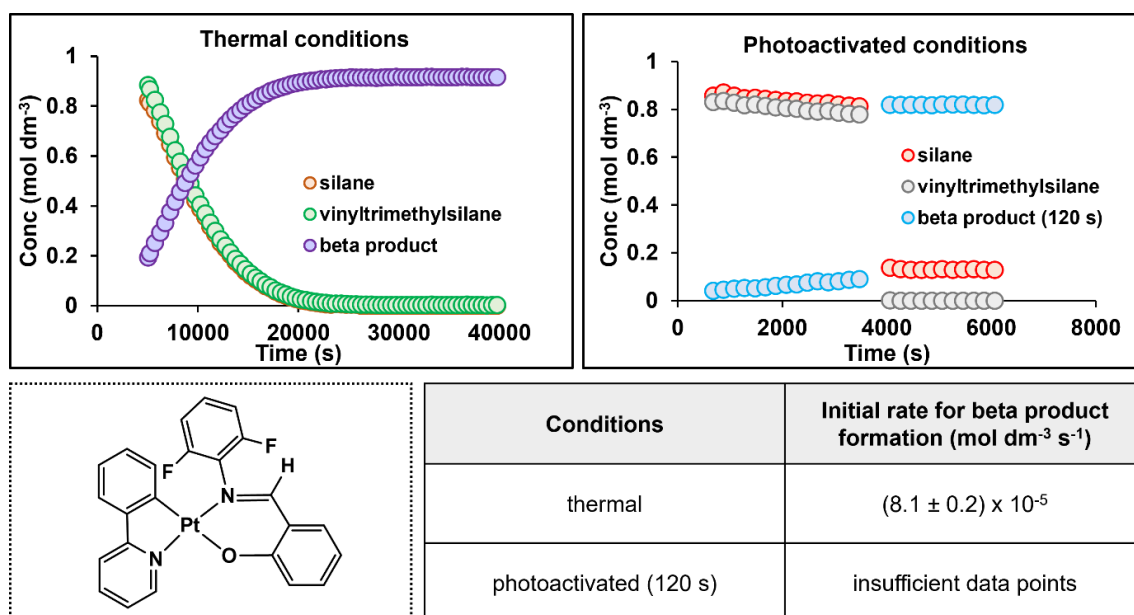


Figure 3.17. Left – concentration-time profile of **MD'M** and **VTMS** consumption and beta product formation during the thermal hydro-silylation reaction using **1f** as a precatalyst. Right – concentration-time profile of **MD'M** and **VTMS** consumption and beta product formation during the photoactivated hydro-silylation reaction using **1f** as a precatalyst, with 120 s irradiation. Reaction conditions as detailed in section 3.6. The table shows the initial rates extracted from the first five data points after catalytic activity has been established.

The reaction requires 2.0×10^4 s (5.5 h) to reach full conversion under thermal conditions, and catalytic activity is apparent from the first measurement. This manifests as 11% conversion after ~1 h in the thermal regime. Despite the non-ideal latent reaction kinetics, rapid and full conversion to the beta product is observed from the first measurement following the irradiation period under the photoactivation conditions. Compared to precatalyst **1b** which has the electron

withdrawing $-\text{CF}_3$ group on the Schiff base ligand, precatalyst **1f** exhibits faster catalytic activity under the thermal and photoactivation conditions. This demonstrates that the strong electron withdrawing group in the *para*- position of the aniline component of the Schiff base ligand exerts a more inhibitory effect on catalysis than $-\text{F}$ groups in the *ortho*- positions. This could also suggest that $-\text{F}$ groups promote catalysis.

3.6.7 Precatalyst **1g**

The phenylpyridine ligand in the precatalyst was replaced by the bulkier cyclometalated ligand, benzo[*h*]quinoline, and the effect of this ligand substitution on the model reaction was studied. The concentration-time profiles for the reactions conducted under the thermal and photoactivated regimes in the presence of precatalyst **1g** are detailed in Figure 3.18.

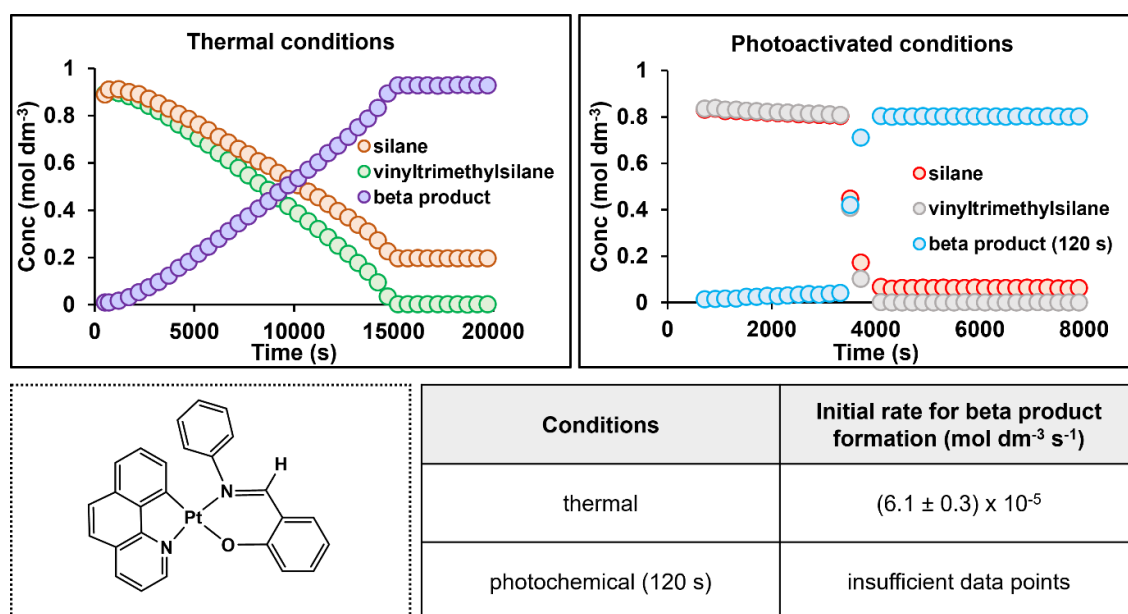


Figure 3.18. Left – concentration-time profile of **MD'M** and **VTMS** consumption and beta product formation during the thermal hydro-silylation reaction using **1g** as a precatalyst. Right – concentration-time profile of **MD'M** and **VTMS** consumption and beta product formation during the photoactivated hydro-silylation reaction using **1g** as a precatalyst, with 120 s irradiation. Reaction conditions as detailed in section 3.6. The table shows the initial rates extracted from the first five data points after catalytic activity has been established.

The thermal temporal profile is characterised by a short (1.2×10^3 s, 0.34 h) induction period during which the precatalyst activates, followed by an apparent zero-order regime at maximum turnover. Compared with precatalyst **1d**, the initial rate using **1g** is 1.1 x faster under the thermal conditions, demonstrating that the additional steric encumbrance introduced by the benzo[*h*]quinoline ligand is beneficial for catalysis. Precatalyst **1g** also offers a longer latency period than **1d** (0.34 vs 0.16 h). Overall, the reaction using precatalyst **1g** requires 1.5×10^4 (4.2 h) to achieve full conversion, compared with 1.6×10^4 s (4.5 h) using precatalyst **1d**. In the experiment conducted under photoactivation conditions, 5% conversion to the beta product has occurred prior to irradiation, but full conversion is realised 7.9×10^2 s after irradiation for 120 s.

3.6.8 Precatalyst 1h

As discussed above, the use of precatalyst **1a** in the model photoactivated reaction afforded a good latency period but did not promote the fastest turnover upon irradiation. To determine whether the $-\text{OCH}_3$ group on the phenylpyridine ligand or $-\text{CF}_3$ group on the Schiff base ligand exerted a more decisive effect on the reaction kinetics, **1h** was employed in the model reaction. This precatalyst has the $-\text{OCH}_3$ group on the phenylpyridine ligand but does not have the $-\text{CF}_3$ group on the Schiff base, thus facilitating a direct comparison of the catalytic activity to precatalyst **1a**. The concentration-time profiles for the thermal and photoactivated experiments, along with the table of initial rates are shown in Figure 3.19.

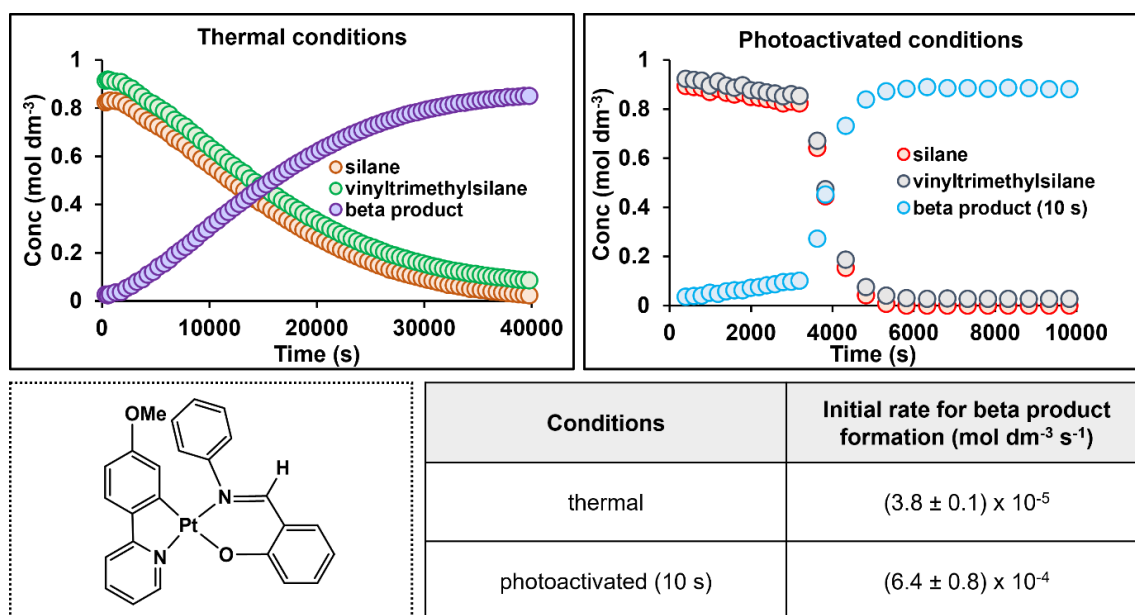


Figure 3.19. Left – concentration-time profile of **MD'M** and **VTMS** consumption and beta product formation during the thermal hydro-silylation reaction using **1h** as a precatalyst. Right – concentration-time profile of **MD'M** and **VTMS** consumption and beta product formation during the photoactivated hydro-silylation reaction using **1h** as a precatalyst, with 10 s irradiation. Reaction conditions as detailed in section 3.6. The table shows the initial rates extracted from the first five data points after catalytic activity has been established.

In a similar fashion to when precatalyst **1a** was employed in the model thermal reaction, a sigmoidal shape is observed for the temporal profile of beta product formation when **1h** is used as the precatalyst. There is an associated induction period (1.3×10^3 s, 0.35 h) followed by an apparent zero order regime at maximum rate of turnover. The reaction takes 3.78×10^4 s (10.5 h) to reach completion, which represents a 2-fold acceleration in rate compared to the same reaction conducted using precatalyst **1a**. A notable difference in the photoactivated experiment using **1h** is that 11% conversion to the beta product has occurred prior to irradiation, compared to no conversion at this time point using **1a**. This demonstrates that the $-\text{CF}_3$ group on the Schiff base ligand exerts a strong influence in making the precatalyst react very slowly under thermal conditions, thus providing good latency periods. Despite the poor latent behaviour observed for **1h**, photoactivation results in a significant rate acceleration (17-fold for 10 s irradiation)

compared with the thermally activated precatalyst. Full conversion to the beta product is achieved 2.1×10^3 s (0.6 h) after the irradiation period.

3.6.9 Precatalyst 1i

To probe the effect of introducing the $-\text{OCH}_3$ group on the salicylaldehyde component of the Schiff base ligand on catalytic performance, precatalyst **1i** was used in the model thermal and photoactivated hydrosilylation reactions. The concentration-time profiles for the thermal reaction, photoactivated reaction (with 10 s irradiation) and table of initial rates are shown in Figure 3.20.

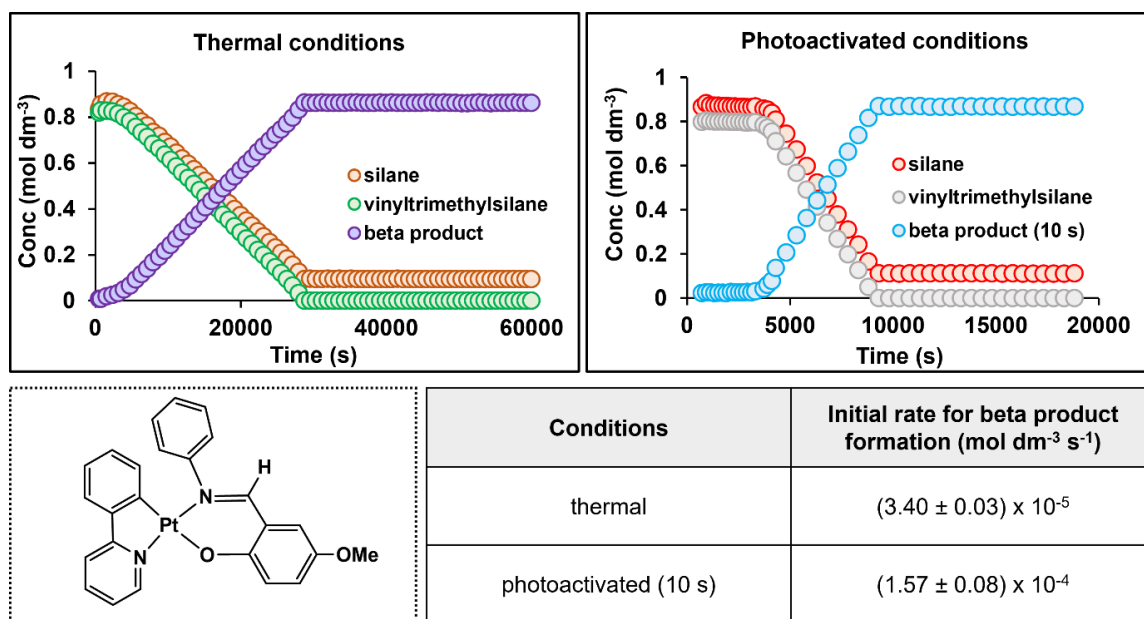


Figure 3.20. Left – concentration-time profile of **MD'M** and **VTMS** consumption and beta product formation during the thermal hydrosilylation reaction using **1i** as a precatalyst. Right – concentration-time profile of **MD'M** and **VTMS** consumption and beta product formation during the photoactivated hydrosilylation reaction using **1i** as a precatalyst, with 10 s irradiation. Reaction conditions as detailed in section 3.6. The table shows the initial rates extracted from the first five data points after catalytic activity has been established.

Under thermal conditions, the reaction has an associated induction period (3.71×10^3 s, 1.03 h) followed by an apparent zero order regime at maximum rate of turnover. Full conversion is

achieved after 2.9×10^4 s (8.0 h) in the thermal reaction, compared with 5.6×10^3 s (1.6 h) in the photoactivated reaction after 10 s irradiation. Irradiating the sample for 10 s results in a rate that is 5 x faster than that observed in the thermal regime, and this precatalyst also has a good latency period under the conditions studied. Compared to using precatalyst **1h** in the model reaction (where the $-\text{OCH}_3$ group is on the phenylpyridine ligand), **1i** offers better latent reaction kinetics, but the rate of conversion to the beta product following irradiation is 4 x slower than that when using **1h**.

3.6.10 Summary of precatalyst screening

All precatalysts (**1a–1i**) used in this study have proven to be photoactivated, as significant accelerations in rate are observed following the irradiation period and turnover continues after the irradiation source is removed. Furthermore, all precatalysts promote complete turnover for hydrosilylation, and furnish exclusively the product of anti-Markovnikov addition in the model reaction. No difference in selectivity is observed under thermal or photoactivated conditions. Consideration of the concentration-time profiles, however, shows very different rates of reaction and reaction profiles, as summarised in Table 3.2. Under thermal conditions, a sigmoidal profile, with an associated induction period and a pseudo-zero order regime at maximum rate of turnover, is observed for many of the precatalysts (e.g. **1a**, **1b**, **1e**, **1g**, **1h**, **1i**). However, other precatalysts (e.g. **1c** and **1d**) show much shorter induction periods and apparent zero-order reaction profiles that operate over nearly all of the reaction profile. The time measured to completion under thermal conditions varies from 1.8 h (**1c**) to 22.4 h (**1a**). Under photoactivated conditions, the time measured to completion varies from 0.15 h (**1c**) to 4.7 h (**1a**). While induction periods and sigmoidal profiles can signal the formation of a colloidal catalyst, they can also be consistent with a process that converts a homogenous precatalyst into an active

homogenous catalyst. The determination of the active species using precatalyst **1b** is discussed in Chapter 4.

Whilst a direct trend between the structures of the precatalyst and their activity in hydrosilylation cannot be established, there are some noteworthy observations. For example, in the model thermal reaction, **1d** has a shorter induction period than **1g** (5.8×10^2 s compared to 1.2×10^3 s), but **1g** promotes faster turnover overall (1.6×10^4 s for **1d** and 1.5×10^4 s for **1g**). This might suggest that the benzo[*h*]quinoline ligand is more suited than phenylpyridine for providing latent reaction kinetics, due to its higher stability. Comparing **1h** and **1i** in the thermal reaction, where the $-\text{OCH}_3$ group is on the phenylpyridine ligand and salicylaldimine ligand respectively, **1i** has a longer induction period (1.2×10^3 s for **1h** and 3.7×10^3 s for **1i**), and also promotes faster turnover overall (3.7×10^4 s for **1h** and 2.8×10^4 s for **1i**). In the photoactivated model reaction however, **1h** promotes turnover much faster than **1i** with 10 s irradiation (2.1×10^3 s for **1h** and 5.6×10^3 s for **1i**). This suggests that substitution of the $-\text{OCH}_3$ group on the salicylaldimine ligand offers better thermal stability, but introduction of this group on the phenylpyridine moiety gives rise to enhanced photoactivation efficiencies. Precatalyst **1c** promotes faster turnover than **1d** in both the thermal (6.4×10^3 s for **1c** compared to 1.6×10^4 s for **1d**) and photoactivated (7.6×10^2 s **1c** compared to 1.4×10^3 s **1d**) model reactions, which suggests that introduction of an alkyl group onto the salicylaldimine ligand is conducive to enhanced photoactivation efficiencies. Comparing **1a** and **1b**, the reaction times are overall faster under thermal and photoactivated conditions for **1b**, and **1b** offers a longer induction period (5.0×10^3 s for **1a** compared to 1.0×10^4 s for **1b**). As discussed in chapter 2, **1b** has a larger steric clash between the phenylpyridine and salicylaldimine ligand planes than **1a** (12.07° for **1a** and 16.64° for **1b**), so this arrangement may provide enhanced thermal stability and better photoactivation efficiencies. This is perhaps due to more facile loss of the salicylaldimine ligand in **1b** to coordinate a silane or alkene substrate.

Table 3.2. Comparison of precatalyst performance in the model hydrosilylation reaction between **MD'M** and **VTMS** under thermal and photoactivated conditions. Reaction conditions (0.0025 M precatalyst, 0.8 – 1.0 M **MD'M**, 0.8 – 1.0 M **VTMS** in *d*₂-dichloromethane).

Precatalyst ^a	Induction Period ^b / s (h)	Thermal Time / s (h)	Photochemical Time ^d / s (h) <i>irradiation time (s)</i>	
1a	5.0 x 10 ³ (1.40)	8.06 x 10 ⁴ (22.4)	10	1.7 x 10 ⁴ (4.7)
			60	9.3 x 10 ³ (2.6)
			120	5.6 x 10 ³ (1.5)
1b	1.0 x 10 ⁴ (2.80)	7.96 x 10 ⁴ (22.1)	10	1.0 x 10 ⁴ (2.9)
			60	9.3 x 10 ³ (2.6)
			120	4.4 x 10 ³ (1.2)
1c	4.7 x 10 ² (0.13) ^c	6.4 x 10 ³ (1.8)	10	7.6 x 10 ² (0.2) ^e
			120	5.4 x 10 ² (0.15) ^e
1d	5.8 x 10 ² (0.16)	1.6 x 10 ⁴ (4.5)	10	1.4 x 10 ³ (0.38) ^f
1e	1.6 x 10 ³ (0.45)	2.0 x 10 ⁴ (5.6)	10	8.1 x 10 ² (0.22) ^g
1f	2.5 x 10 ³ (0.70) ^c	2.0 x 10 ⁴ (5.5)	120	5.9 x 10 ² (0.16) ^h
1g	1.2 x 10 ³ (0.34)	1.5 x 10 ⁴ (4.2)	120	7.9 x 10 ² (0.22) ⁱ
1h	1.3 x 10 ³ (0.35)	3.8 x 10 ⁴ (10.5)	10	2.1 x 10 ³ (0.6) ^j
1i	3.7 x 10 ³ (1.03)	2.8 x 10 ⁴ (8.0)	10	5.6 x 10 ³ (1.6)

^a The precatalyst loading is 0.0025 M in all cases. ^b The induction period is estimated as the time taken for greater than 1% conversion, as an indication of the catalyst latency. ^c The method of Morris was used to estimate the induction period.¹⁵⁷ ^d Time to reach full conversion excludes the ~1 h latency period. ^e 18% conversion reached before the irradiation period. ^f 12% conversion reached before the irradiation period. ^g 5% conversion reached before the irradiation period. ^h 11 % conversion reached before the irradiation period. ⁱ 5% conversion reached before the irradiation period. ^j 11% conversion reached before the irradiation period.

3.7 Effect of varying the catalyst loading

One major challenge in making cross-linked silicones by hydrosilylation on an industrial scale is designing catalyst systems that show latent reaction kinetics at very low (< 50 ppm) catalyst loadings. This is a requirement to reduce the cost and also because the catalysts cannot generally be recovered after curing, so this helps to reduce the use of this precious metal and minimise discolouration in the end products. In 2007 alone, it was estimated that 5.6 tonnes of platinum

were used for silicone cross-linking.¹⁵⁸ To examine the efficacy of precatalyst **1b** under conditions more likely to be employed commercially, the model reaction was conducted at a variety of catalyst loadings (0.0025 – 0.25 mol%) under photoactivated conditions. This corresponds to 0.000025 M – 0.0025 M, or 14 – 1400 ppm. This precatalyst was chosen due to its good thermal latency. For each experiment, the reaction was monitored thermally for ~1 h to show the latency period, before being irradiated for 120 s. This irradiation time was chosen as it was anticipated that longer (> 24 h) reaction times would be required at such low loadings, so longer irradiation periods would increase the rate of conversion. The concentration-time profiles for the formation of the beta product are shown in Figure 3.21.

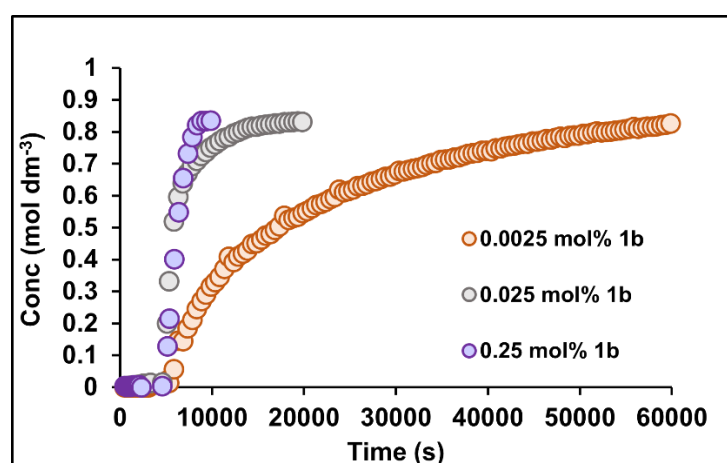


Figure 3.21. Concentration-time profiles of beta product formation during the photoactivated hydrosilylation reaction using **1b** as a precatalyst at varied loadings with 120 s irradiation. Reaction conditions (0.0025, 0.025 and 0.25 mol% **1b**, 0.93 M **MD'M** and 0.93 M **VTMS** in d_2 -dichloromethane). All plots are time-shifted to 4600 s to show the same latency period.

Dropping the catalyst loading had the expected effect of overall slower conversion to the hydrosilylation product. The times taken to achieve full conversion are 5.47×10^4 s (15.2 h), 1.1×10^4 s (3.1 h) and 4.4×10^3 s (1.2 h) at the 0.0025, 0.025 and 0.25 mol% catalyst loadings, respectively (excluding the ~1 h latency period). That photoactivated hydrosilylation still proceeds at the lowest catalyst loading (0.0025 mol%, 0.000025 M), and that there is a thermal latency period, suggests that precatalyst **1b** would be suitable for use in the commercial systems.

The kinetics of this series of experiments were probed using the initial rates method as detailed in Table 3.3.

Table 3.3. Initial rates extracted from the first five data points following irradiation in the photoactivated hydrosilylation reaction between **MD'M** and **VTMS** using precatalyst **1b** at varied loadings (0.0025 mol% – 0.25 mol%) with 120 s irradiation.

Catalyst loading (mol%)	Initial Rate (mol dm ⁻³ s ⁻¹)
0.0025	(7.1 ± 0.5) × 10 ⁻⁵
0.025	(2.0 ± 0.4) × 10 ⁻⁴
0.25	(5.2 ± 0.1) × 10 ⁻⁴

Compared with the initial rate measured at the 0.0025 mol% catalyst loading, the rates are 2.8 and 7.3 x faster at the 0.025 and 0.25 mol% loadings, respectively. This shows that an increase in catalyst loading does not result in a proportionally increased initial rate. This could be attributed to a light-path effect, where higher loadings result in more absorption of UV-light and less irradiation of the NMR tube. Using the Beer-Lambert law for a 1 mm pathlength and the molar absorption coefficient at 365 nm ($1.3 \times 10^4 \text{ dm}^3 \text{ mol}^{-1} \text{ cm}^{-1}$), the absorptions are 3.3×10^{-2} , 3.3×10^{-1} and 3.3 at the 0.000025, 0.00025 and 0.0025 mol% catalyst loadings, respectively.

As discussed previously, it is anticipated that less than 5% of the precatalyst is activated, as the distinctive signals due to the precatalyst are unchanged in the ¹H NMR spectrum at the end of catalysis (see Figure 3.12). This means that the precatalyst could potentially be used at much lower catalyst loadings, and still effect hydrosilylation. Irradiation for 600 s at 0.0025 mol% catalyst loading leads to a rate closer to that achieved at 0.25 mol% catalyst loading with 120 s irradiation ($(1.98 \pm 0.03) \times 10^{-4} \text{ mol dm}^{-3} \text{ s}^{-1}$), demonstrating that longer irradiation times could offset the need for higher catalyst loadings (Figure 3.22). Nolan and coworkers recently reported [Pt(DMS)₂Cl₂] as an effective hydrosilylation catalysts at 0.001 mol% (10 ppm), though this complex required heating to 80 °C to become active.¹⁵⁹ This catalyst was reported to achieve turnover numbers (ToN) of $6.4 - 6.6 \times 10^6$ and turnover frequencies (ToF) in the range of 2.7 –

$2.8 \times 10^5 \text{ h}^{-1}$. At the 600 s irradiation time using precatalyst **1b**, the $\text{ToN}_{\text{app}} = 4.0 \times 10^4$ and the $\text{ToF}_{\text{app}} = 2.7 \times 10^4 \text{ h}^{-1}$. While these ToN and ToF do not match some of the very best reported for other Pt-based hydrosilylation catalysts by at least an order of magnitude, the air stability, operation at room temperature, and photoactivated nature of precatalyst **1b** at low catalyst loadings represents a step forward in reducing the amount of platinum consumed in the silicone industry.

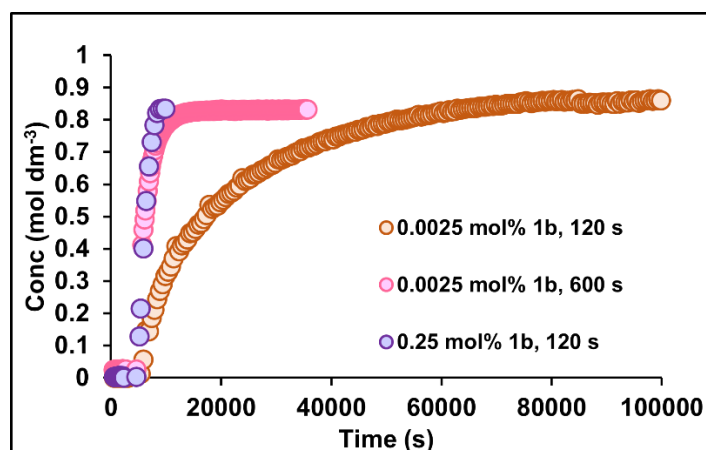


Figure 3.22. Concentration-time profiles of beta product formation during the photoactivated hydrosilylation reaction using **1b** as a precatalyst at 0.0025 mol% with 120 and 600 s irradiation, and at 0.25 mol% with 120 s irradiation. Reaction conditions (0.0025 and 0.25 mol% **1b**, 0.93 M **MD'M** and 0.93 M **VTMS** in d_2 -dichloromethane). All plots are time-shifted to show the same latency period.

Attempts were made to determine the order in catalyst at 120 s irradiation using the initial rates method in Microsoft Excel, but the rate-concentration profiles did not return a satisfactory fit. This attests to the complexity of the kinetics involved in hydrosilylation reactions, which has presented challenges to researchers in the field for decades. The order in substrates for the model reaction is discussed in detail in Chapter 4.

3.8 Substrate scope using precatalyst **1b**

After showing the successful hydrosilylation of **VTMS** by **MD'M** under the model reaction conditions using precatalyst **1b**, the substrate scope was expanded to include a variety of alkenes. Platinum based catalysts have been extensively used for the hydrosilylation of alkenes under thermal conditions but have far less been applied under photoactivated conditions.¹ For this study, the model photoactivated hydrosilylation reaction was replicated (as described in section 3.6) but **VTMS** was replaced by a variety of alkene substrates. In each case, the reaction was monitored thermally for ~1 h to determine the latency period, before being irradiated for 120 s. The results of this study, detailing the selectivity, reaction times and ToF_{app} are summarised in Table 3.4.

Table 3.4. Comparisons of selectivity and ToF_{app} using precatalyst **1b** in the photoactivated hydrosilylation reaction of **MD'M** with a variety of alkenes. Reaction conditions (0.0025 M **1b**, 0.8 – 1.2 M **MD'M** and 0.8 – 1.2 M **alkene** in d_2 -dichloromethane, left for ~1 h thermally, then irradiated for 120 s).

Alkene	Products ^a	Selectivity (%) ^b	Time / s (h) ^c	ToF_{app} / h^{-1}
		>99	4.4×10^3 (1.2)	3.3×10^2
		90	5.52×10^4 (15.3)	2.60×10^1
		10		
C_5H_{11}	C_5H_{11}	91 ^d	3.9×10^3 (1.1)	3.6×10^2
		7	1.3×10^4 (3.5)	1.1×10^2
		93		
		78	2.0×10^4 (5.6)	7.1×10^1
		22		
		87	$> 7.2 \times 10^4$ (20) ^e	$< 2.0 \times 10^1$
		13		

^a Products determined by signals in ^1H NMR spectra. ^b Selectivity determined by relative integrals in ^1H NMR spectra. ^c Time taken to achieve full conversion (excluding the latency period). ^d 9% isomerisation products also observed. ^e Reaction not monitored to completion.

Successful hydrosilylation was achieved for a wide variety of alkene substrates when using precatalyst **1b** under photoactivated conditions. For all alkene substrates except **3-Buten-2-one**, the main product conforms to the anti-Markonikov rule and yields the beta product. The **3-**

Buten-2-one substrate displays complete chemoselectivity in favour of the hydrosilylation of the terminal alkene, rather than the ketone, but is more selective towards the alpha (Markovnikov) product. As discussed previously, using **VTMS** as the alkene selectively yields the beta hydrosilylation product, whilst vinyltrimethoxysilane (**VTMOS**) also undergoes Markovnikov hydrosilylation to afford 10% alpha product. Both **styrene** substrates also furnish the alpha product when used in the model reaction. When **oct-1-ene** is employed as the alkene substrate, the beta product is formed as well as 9% isomerisation products. Compared with the model reaction using **VTMS**, the reaction proceeds slower in the presence of all the other studied alkenes, except **oct-1-ene**. The NMR spectra and concentration-time profiles for each substrate are discussed in more detail below.

3.8.1 Vinyltrimethoxysilane

In contrast to the model reaction between **MD'M** and **VTMS**, the reaction with **VTMOS** furnishes the Markovnikov (alpha) product as well as the anti-Markovnikov (beta) product, as detected by ^1H NMR spectroscopy. In the ^1H NMR spectrum at the end of catalysis, the three singlets at δ 3.54, 0.11 and 0.03 correspond to the $\text{Si}-(\text{OCH}_3)_3$, $2 \times \text{Si}-(\text{CH}_3)_3$ and $\text{Si}-\text{CH}_3$ protons of the beta product, respectively (Figure 3.23). These signals integrate to the expected ratios of 9:18:3. The complex multiplet centred at δ 0.51 is assigned to the $\text{Si}-\text{CH}_2-\text{CH}_2-\text{Si}$ protons of the beta product, which integrates to 4 protons. The doublet observed at δ 1.05 corresponds to the CH_3 protons of the alpha product, and it is not possible to distinguish any other resonances in the ^1H NMR spectrum that correspond to this product due to signal overlap with the beta product. This signal integrates to 0.34 (for 3 protons), compared to 4.00 (for four protons) in the beta product, meaning that the selectivity at full conversion is 90% beta and 10% alpha product. It is important to note that the calculated selectivity in this case is a close approximation, as all signals for the beta product are coincident with other signals of the alpha product (see discussion below).

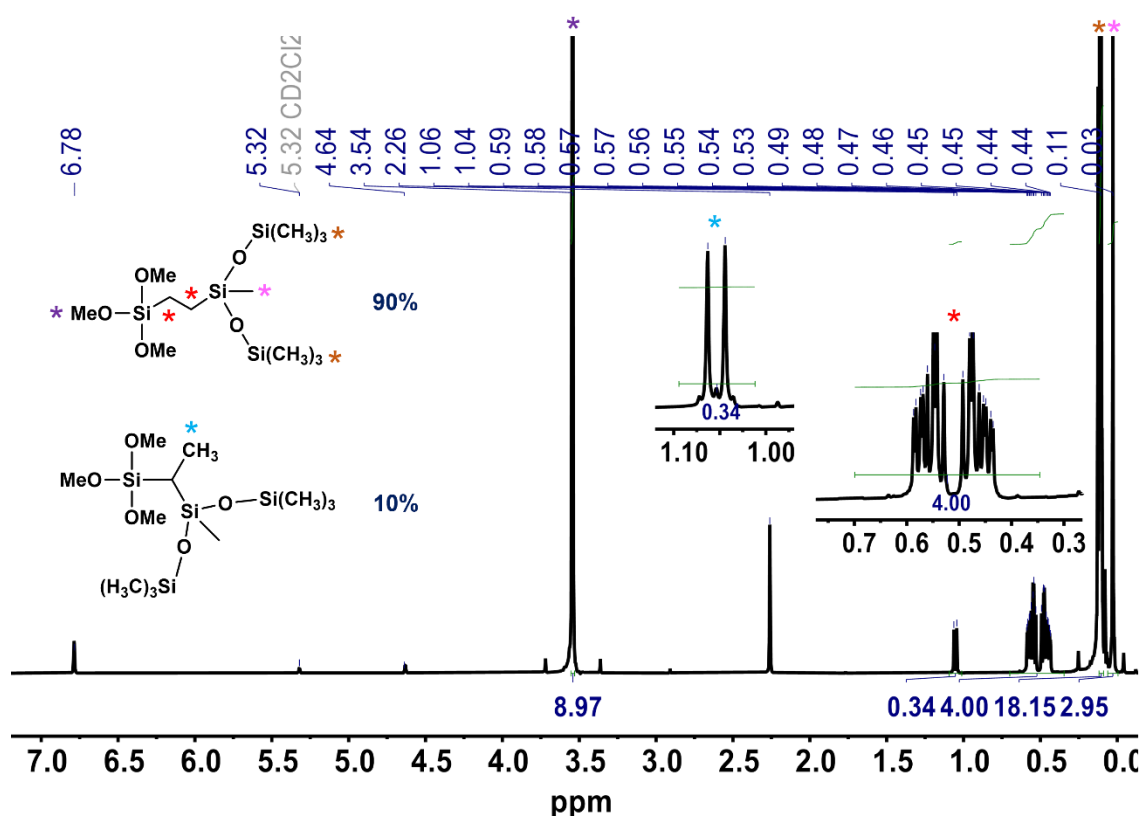


Figure 3.23. ^1H NMR spectrum of the alpha and beta products formed in the photoactivated hydrosilylation reaction of **MD'M** and **VTMOS** using precatalyst **1b** (400 MHz, d_2 -dichloromethane, 298 K). Reaction conditions (0.0025 M **1b**, 1.0 M **MD'M**, 1.0 M **VTMOS**, left for \sim 1 h thermally then irradiated for 120 s).

The corresponding ^{29}Si NMR spectrum at the end of catalysis shows three distinct resonances for the beta product at δ 7.2, -21.5 and -41.5 , all of which are singlets (Figure 3.24). For the alpha product, there are two distinct resonances at δ -23.1 and -42.5 , but the other expected resonance is masked by the signal of the beta product at δ 7.2. All of the new signals are at distinct chemical shifts from the starting materials (δ 9.4 and -36.5 for **MD'M**, and -55.4 for **VTMOS**). The assignment of the hydrosilylation products was facilitated by the acquirement of the ^{29}Si - ^1H HMBC spectrum (Figure 3.25). This spectrum shows the correlation between the ^{29}Si signal at δ 7.2 (**3**) with the 18 Si-(CH_3) $_3$ protons of the beta product. The ^{29}Si signal at δ -21.5 (**2**) correlates with the Si- CH_2 - CH_2 -Si protons, as well as the Si- CH_3 protons of the beta product. The most upfield ^{29}Si signal for the beta product at δ -41.5 (**1**) correlates with the Si- CH_2 - CH_2 -Si and Si-(OCH_3) $_3$ protons. For the alpha product, the ^{29}Si resonance at δ 7.2 (**C**) correlates with

the 18 Si-(CH₃)₃ protons, and this signal overlaps with the corresponding resonance of the beta product. The ²⁹Si resonance at δ -23.1 (B) correlates with the CH₃ and Si-CH₃ protons of the alpha product. Lastly, the most upfield ²⁹Si resonance at δ -42.5 (A) correlates with the Si-(OCH₃)₃ and CH₃ protons.

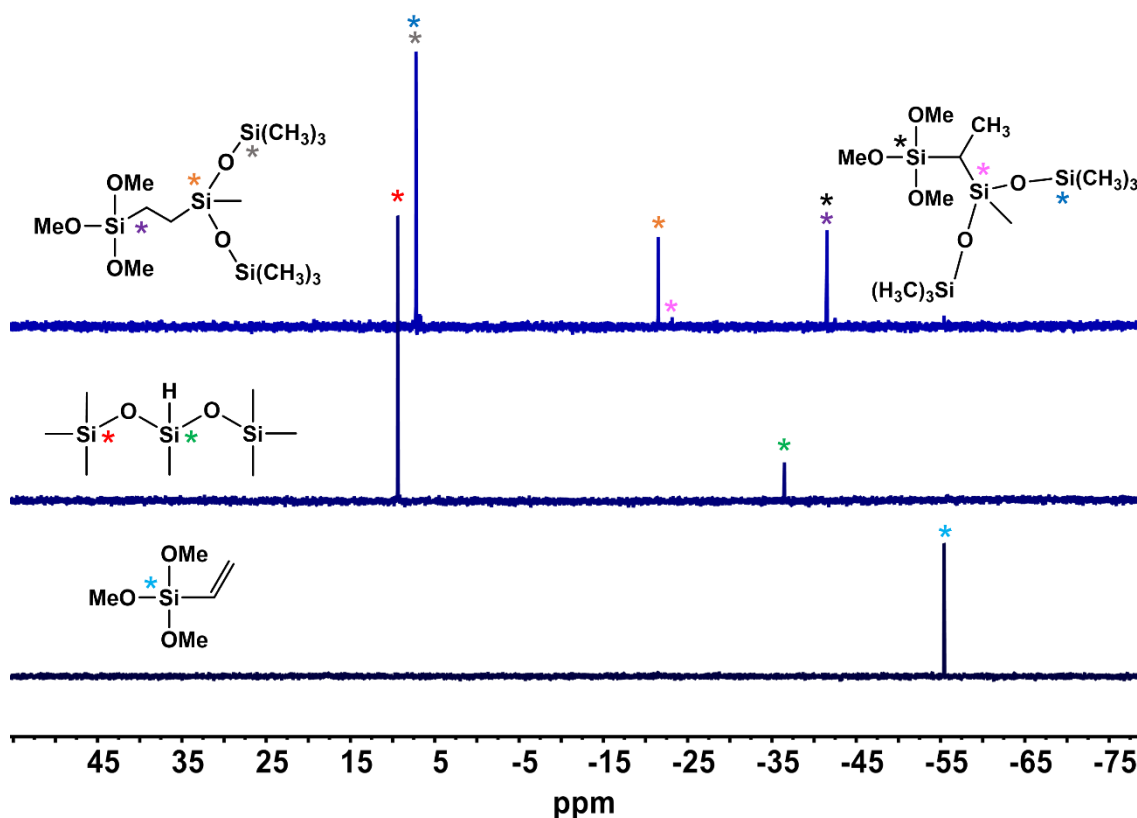


Figure 3.24. ²⁹Si NMR spectra of VTMOs (bottom), MD'M (middle) and alpha and beta products (top) formed in the photoactivated hydrosilylation reaction between MD'M and VTMOs using precatalyst **1b** (119.2 MHz, *d*₂-dichloromethane, 298 K). Reaction conditions (0.0025 M **1b**, 1.0 M MD'M and 1.0 M VTMOs, left for ~1 h thermally, then irradiated for 120 s).

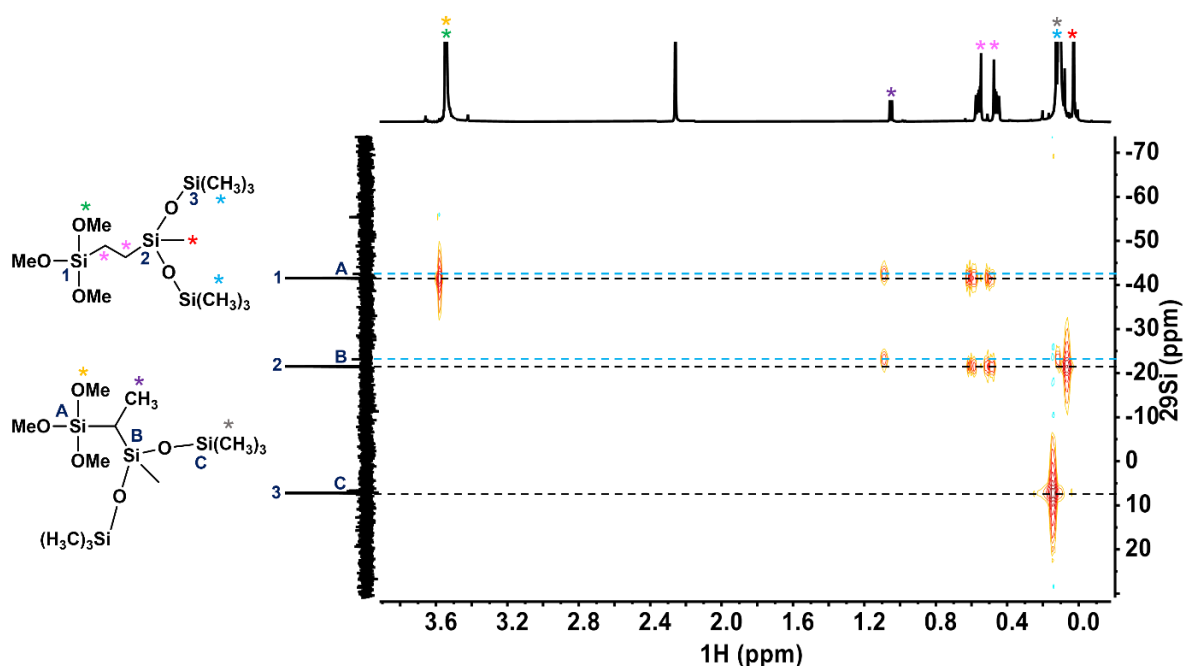


Figure 3.25. ^{29}Si - ^1H HMBC spectrum of the alpha and beta products formed in the photoactivated hydrosilylation reaction between **MD'M** and **VTMOS** using precatalyst **1b** (119.2, 600.1 MHz, d_2 -dichloromethane, 298 K). Reaction conditions (0.0025 M **1b**, 1.0 M **MD'M** and 1.0 M **VTMOS**, left for \sim 1 h thermally, then irradiated for 120 s).

With **VTMOS** as the alkene substrate, the concentration-time profile for the formation of the beta product has a sigmoidal shape (Figure 3.26). The sample was monitored for *ca.* 1 h to show the thermal latency, and then irradiated for 120 s. The initial rate measured after the irradiation period (8.8 ± 0.3) $\times 10^{-6}$ mol dm^{-3} s^{-1}) is slower than the rate measured after 3.0×10^4 s (2.09 ± 0.06) $\times 10^{-5}$ mol dm^{-3} s^{-1}). Compared to the rate of beta product formation, the alpha product forms at a rate that is 3.5 and 6.2 \times slower before and after 3.0×10^4 s, respectively. Using **VTMOS** as the alkene substrate also leads to an initial rate that is 59.4 \times slower compared to using **VTMS**, and the reaction requires 5.52×10^4 s (15.3 h) to reach completion. With **VTMS**, the reaction requires 4.4×10^3 s (1.2 h) to reach completion, which demonstrates that the $-\text{OCH}_3$ groups are inhibitory for catalysis in the model reaction.

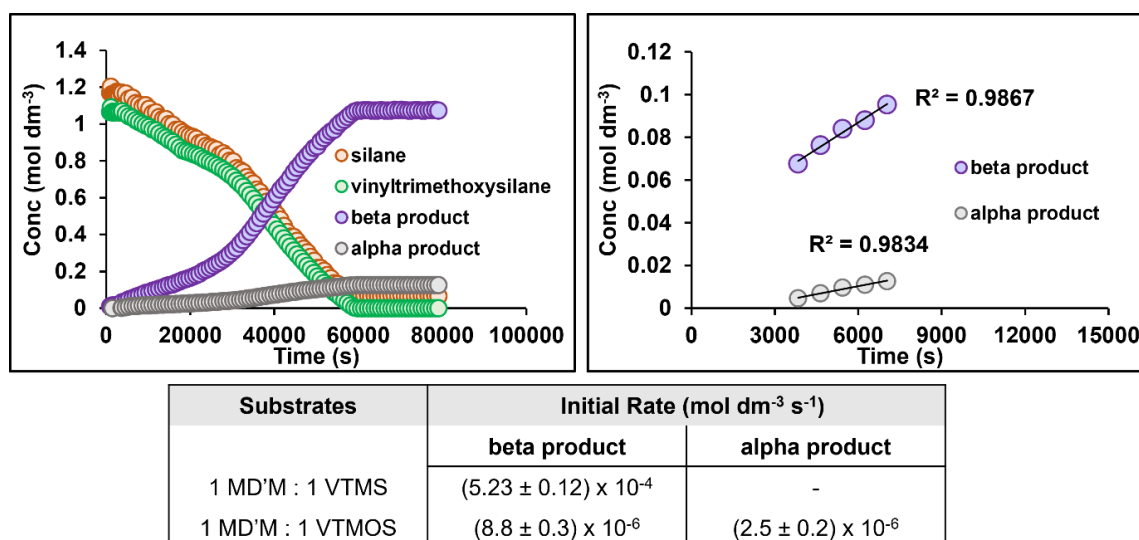


Figure 3.26. Left – concentration-time profile of **MD'M** and **VTMOs** consumption and alpha and beta product formation during the photoactivated hydrosilylation reaction using **1b** as a precatalyst. Right – linear fits for the alpha and beta products for the first 5 data points following irradiation to determine the initial rates. Reaction conditions (0.0025 M **1b**, 1.1 M **MD'M** and 1.1 M **VTMOs** in *d*₂-dichloromethane, left for ~1 h thermally then irradiated for 120 s). The table shows the initial rates for alpha and beta product formation.

3.8.2 3-Buten-2-one

To determine whether hydrosilylation of the alkene or ketone functionality was favoured, **3-Buten-2-one** was employed in the model reaction. Interestingly, a reverse in selectivity was observed for this substrate as the predominant reaction is the formation of the alpha product, as shown in the ¹H NMR spectrum at the end of catalysis (Figure 3.27). Also noteworthy is that complete chemoselectivity in favour of hydrosilylation of the alkene rather than the ketone is observed for this substrate. The alpha product was identified by the ¹H NMR resonances at δ 4.77, 1.74, 1.54 and 0.13, which correspond to the C–H, CH₃–C=O, CH₃ and Si(CH₃)₃ protons, respectively. These protons also integrate to the expected 1:3:3:18 ratio. The beta product was identified by the ¹H NMR resonances at δ 2.43, 1.80, 1.03 and 0.10, which correspond to the CH₂, CH₃, Si–CH₂ and Si(CH₃)₃ protons, respectively. It is worth noting that the integral of the Si(CH₃)₃ protons is an overestimate due to signal overlap with the starting materials.

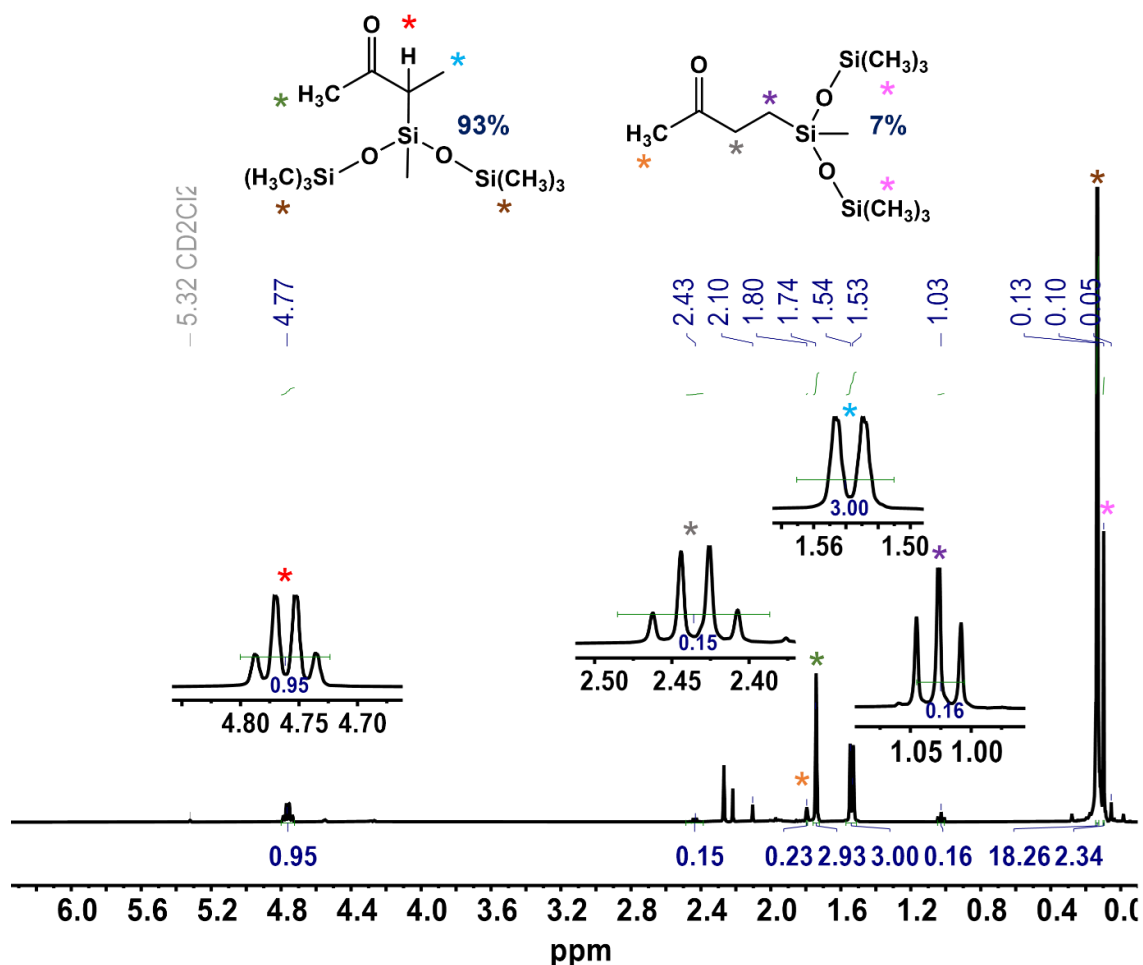


Figure 3.27. ¹H NMR spectrum of the alpha and beta products formed in the photoactivated hydrosilylation reaction of **MD'M** and **3-Buten-2-one** using precatalyst **1b** (400 MHz, *d*₂-dichloromethane, 298 K). Reaction conditions (0.0025 M **1b**, 1.2 M **MD'M**, 1.2 M **3-Buten-2-one**, left for ~1 h thermally then irradiated for 120 s).

With **3-Buten-2-one** as the substrate, latent reaction kinetics are observed over the monitored period (~1 h), as shown in the concentration-time profile (Figure 3.28). Following the irradiation period, the reaction requires 1.3×10^4 s (3.5 h) to achieve full conversion. The initial rate measured for the formation of the alpha product is $8.8 \times$ faster than that for the beta product, and overall, this reaction proceeds much slower than when **VTMS** is used as the alkene substrate in the model reaction.

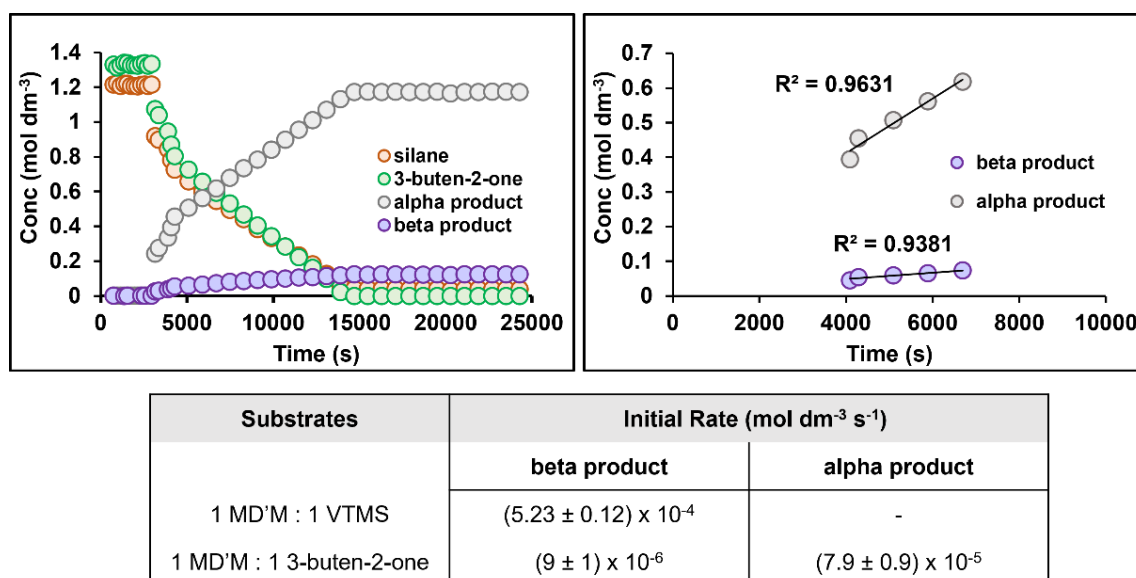


Figure 3.28. Left – concentration-time profile of **MD'M** and **3-Buten-2-one** consumption and alpha and beta product formation during the photoactivated hydrosilylation reaction using **1b** as a precatalyst. Right – linear fits for the alpha and beta products for the first 5 data points following irradiation to determine the initial rates. Reaction conditions (0.0025 M **1b**, 1.2 M **MD'M** and 1.2 M **3-Buten-2-one** in *d*₂-dichloromethane, left for ~1 h thermally then irradiated for 120 s). The table shows the initial rates for alpha and beta product formation.

3.8.3 Styrene

The hydrosilylation of **styrene** by **MD'M** using precatalyst **1b** was also successful under the model reaction conditions, affording both the alpha and beta products. The predominant reaction is the formation of the beta product, which was identified by the ¹H NMR resonances at δ 2.74, 0.93 and 0.22, and correspond to the CH₂, CH₂ and Si(CH₃)₃ protons, respectively (Figure 3.29). These peaks also integrate to the expected ratio of protons (2:2:18). Assignment of the aromatic and Si-CH₃ protons was not possible due to signal overlap with the starting materials. The alpha product was identified by the ¹H NMR resonances at δ 2.18, 1.43 and 0.23, which correspond to the C-H, CH₃ and Si(CH₃)₃ protons, respectively. These analytical data match the values reported in the literature.¹⁶⁰

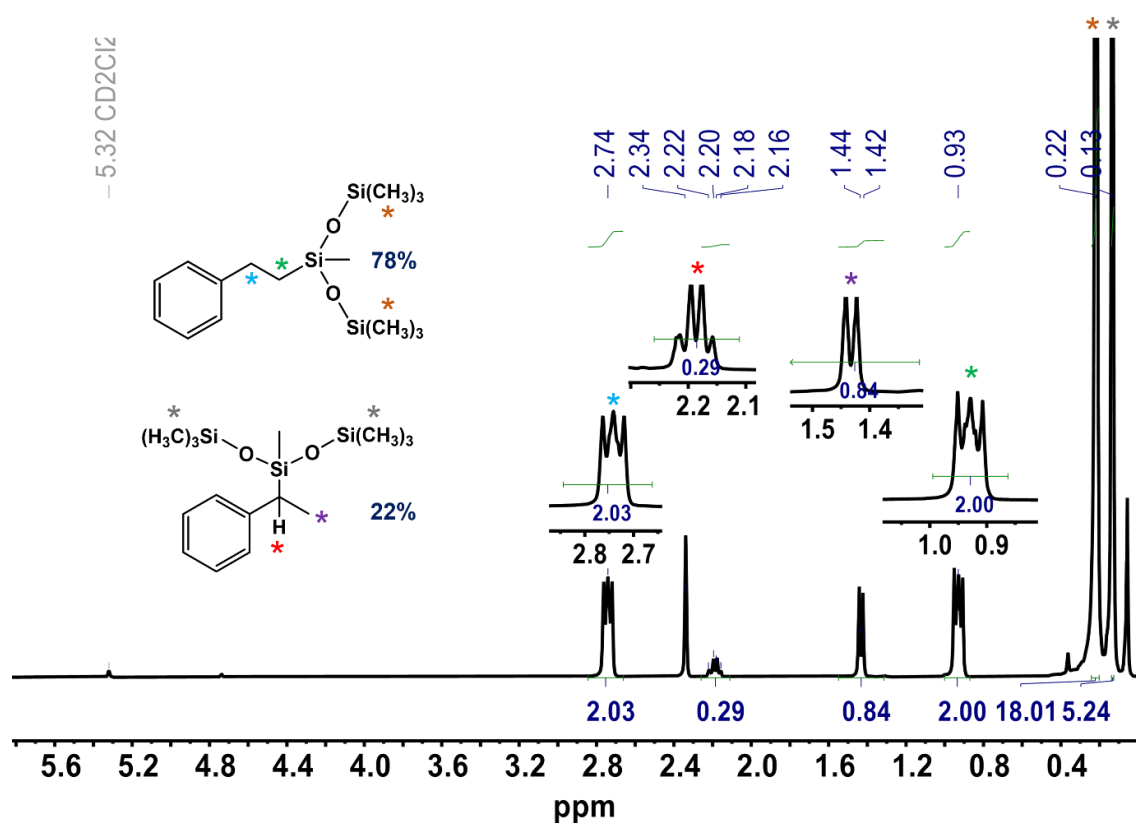


Figure 3.29. ^1H NMR spectrum of the alpha and beta products formed in the photoactivated hydrosilylation reaction of **MD'M** and **styrene** using precatalyst **1b** (400 MHz, d_2 -dichloromethane, 298 K). Reaction conditions (0.0025 M **1b**, 1.2 M **MD'M**, 1.2 M **styrene**, left for ~ 1 h thermally then irradiated for 120 s).

Nolan reported that using $[\text{Pt}(\text{DMS})_2\text{Cl}_2]$ (50 ppm) as the catalyst for the hydrosilylation of styrene by **MD'M** afforded 85% beta product and 16% alpha product.¹⁵⁹ The reaction required 4.8×10^3 s (1.3 h) to reach completion when conducted neat (no solvent) at 80 °C. When using precatalyst **1b** for the hydrosilylation of **styrene** by **MD'M**, there is no reaction under thermal conditions in the monitored latency period (~ 1 h), and full conversion to the hydrosilylation products is observed 2.0×10^4 s (5.6 h) after irradiation (Figure 3.30). The beta product forms at a rate that is $3.9 \times$ faster than that observed for forming the alpha product, which results in 78% beta and 22% alpha product after full conversion. Compared to when **VTMS** is used as the alkene substrate under the same conditions, the reaction using **styrene** proceeds at a rate that is 9 x slower. This could be due to styrene binding more strongly to the Pt centre, in line with Kühn's

observations that if the alkene binds too strongly, the reactivity suffers.² This concept is explored in more detail in chapter four. Despite the higher catalyst loading and longer reaction times compared to the system reported by Nolan, the photoactivated nature of precatalyst **1b** at room temperature may render it suitable for use in the commercial systems.

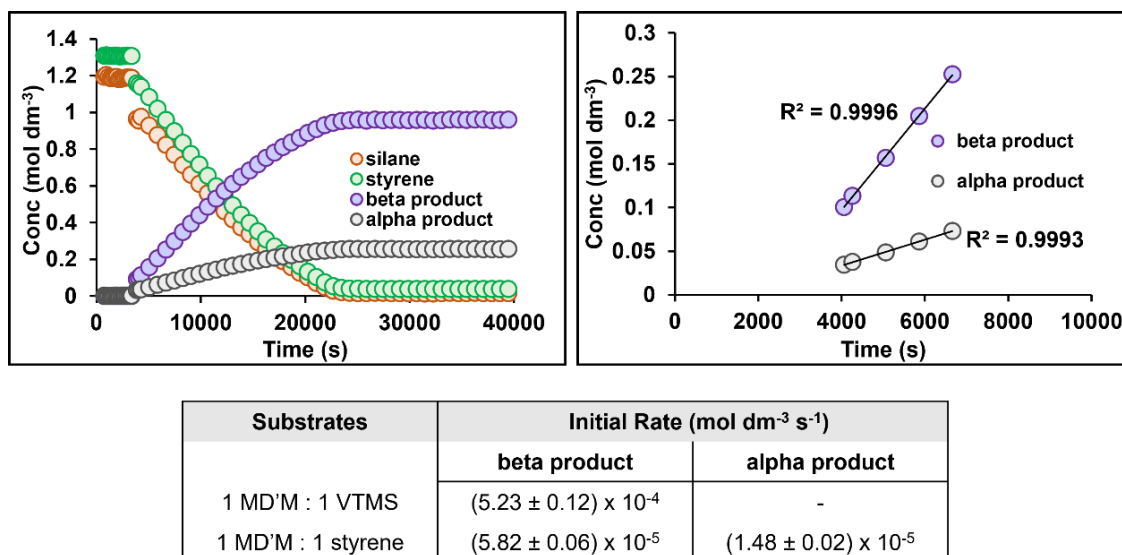


Figure 3.30. Left – concentration-time profile of MD'M and styrene consumption and alpha and beta product formation during the photoactivated hydrosilylation reaction using **1b** as a precatalyst. Right – linear fits for the alpha and beta products for the first 5 data points following irradiation to determine the initial rates. Reaction conditions (0.0025 M **1b**, 1.2 M MD'M and 1.2 M styrene in *d*₂-dichloromethane, left for ~1 h thermally then irradiated for 120 s). The table shows the initial rates for alpha and beta product formation.

3.8.4 4-methoxystyrene

4-methoxystyrene was next employed as the alkene substrate in the model reaction, to probe how the introduction of the –OCH₃ group onto styrene effects catalytic activity and selectivity. As shown by the ¹H NMR spectrum at the end of catalysis (Figure 3.31), the reaction furnishes a mix of the alpha and beta products. The beta product was identified by the ¹H NMR resonances at δ 3.80, 2.65, 0.86 and 0.18 which correspond to the OCH₃, CH₂, CH₂ and Si(CH₃)₃ protons, respectively. These peaks also integrate to the expected ratios of 3:2:2:18. Assignment of the aromatic and Si–CH₃ protons was not possible due to signal overlap with the starting materials.

The alpha product was identified by the ^1H NMR resonances at δ 3.83, 2.09, 1.36 and 0.11 which correspond to the OCH_3 , C-H , CH_3 and $\text{Si}(\text{CH}_3)_3$ protons, respectively. These analytical data match the values reported in the literature.¹⁶⁰

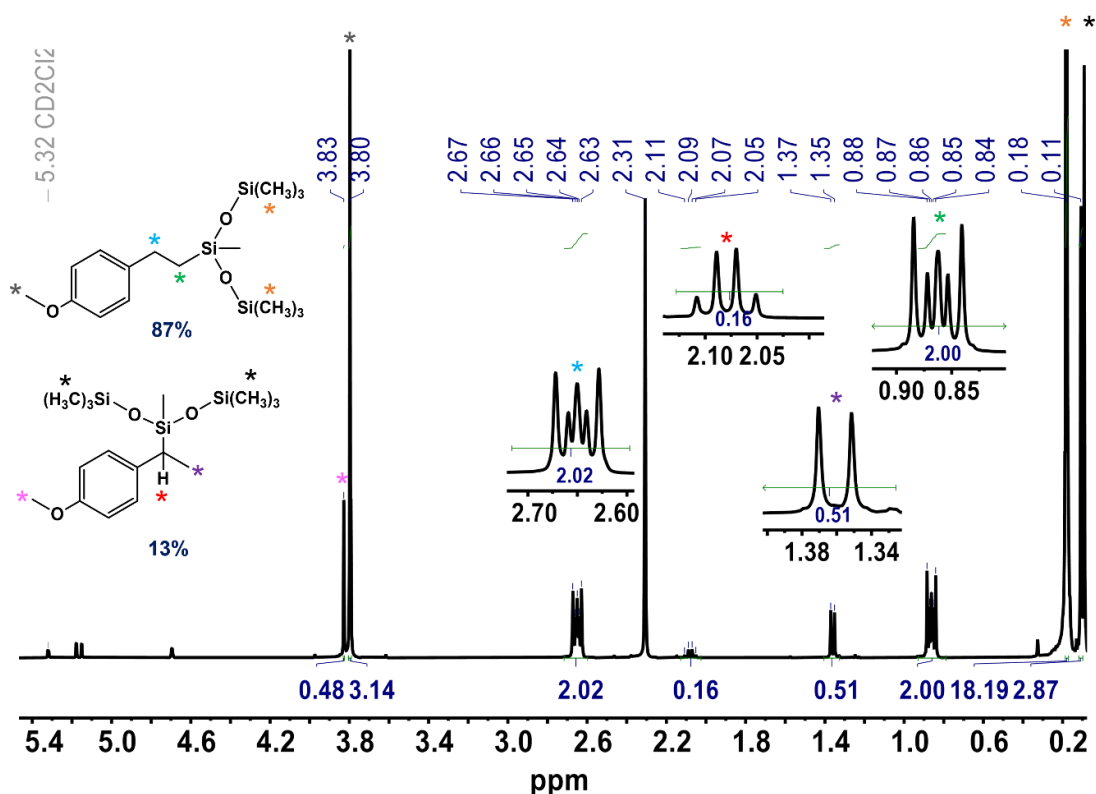


Figure 3.31. ^1H NMR spectrum of the alpha and beta products formed in the photoactivated hydrosilylation reaction of **MD'M** and **4-methoxystyrene** using precatalyst **1b** (400 MHz, d_2 -dichloromethane, 298 K). Reaction conditions (0.0025 M **1b**, 0.93 M **MD'M**, 0.93 M **4-methoxystyrene**, left for ~ 1 h thermally then irradiated for 120 s).

As shown in the concentration-time profile in Figure 3.32, the reaction was stopped at 7.2×10^4 s (20 h), before complete conversion was achieved. Latent reaction kinetics were observed in the presence of this substrate, but the catalytic activity is significantly attenuated compared with the corresponding reactions using **VTMS** or **styrene** as the alkene substrate. Indeed, the measured initial rate for beta product formation is $9.2 \times$ slower when **4-methoxystyrene** is used, compared to that measured for **styrene**. The beta product forms at a rate that is $2.6 \times$ faster than the alpha

product, and a higher selectivity for the beta product is observed compared to when **styrene** is used as the alkene substrate (87% vs 78%).

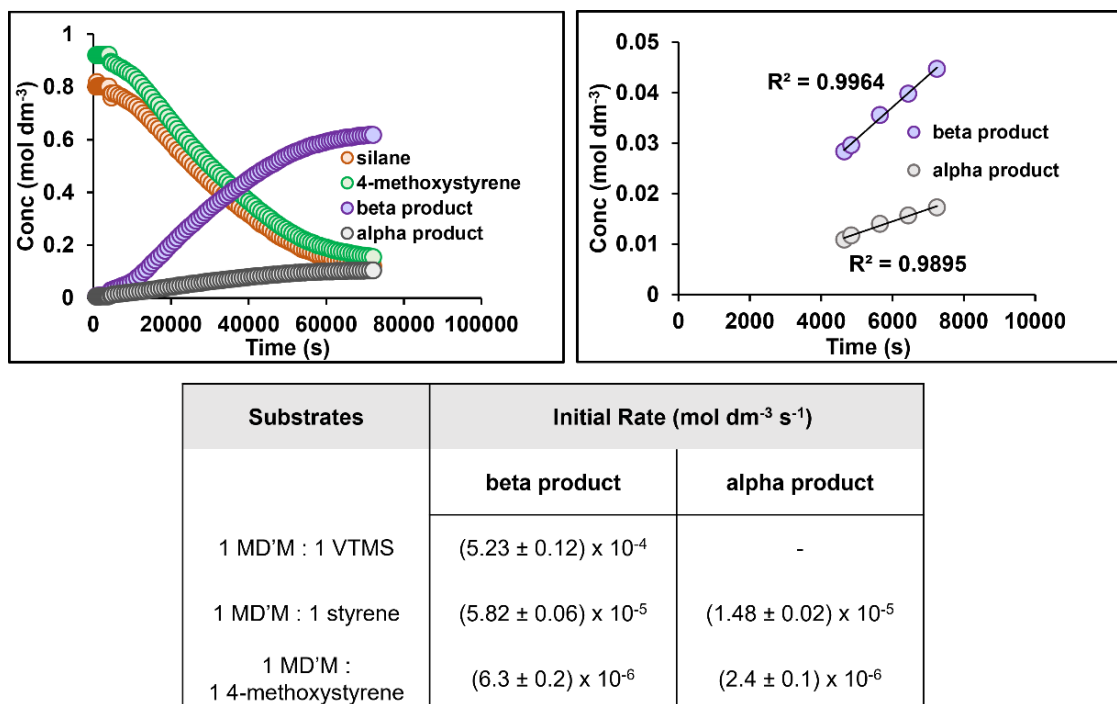


Figure 3.32. Left – concentration-time profile of **MD'M** and **4-methoxystyrene** consumption and alpha and beta product formation during the photoactivated hydrosilylation reaction using **1b** as a precatalyst. Right – linear fits for the alpha and beta products for the first 5 data points following irradiation to determine the initial rates. Reaction conditions (0.0025 M **1b**, 0.93 M **MD'M** and 0.93 M **4-methoxystyrene** in *d*₂-dichloromethane, left for ~1 h thermally then irradiated for 120 s). The table shows the initial rates for alpha and beta product formation.

3.8.5 Oct-1-ene

Oct-1-ene has been employed as a model alkene substrate for many hydrosilylation reactions conducted under thermal conditions.^{2,20,105} To assess its catalytic performance and proneness to isomerisation under photoactivation conditions, **oct-1-ene** was employed in the model reaction using precatalyst **1b**. As shown in the ¹H NMR spectrum taken at the end of catalysis (Figure 3.33), this reaction affords 91% beta product as well as 9% isomeric alkenes. The beta product was identified by the ¹H NMR resonances at δ 1.31, 0.91, 0.49, 0.12 and 0.03 which correspond to the CH₂, CH₃, Si-CH₂, Si-(CH₃)₃ and Si-CH₃ protons, respectively. These signals integrate to the

expected ratios of 12:3:2:18:3 and match the values reported in the literature.^{105, 159} The isomeric alkene or mixture of isomers could not be identified due to similar chemical shifts observed for *cis*- and *trans*-oct-2-ene.²⁰

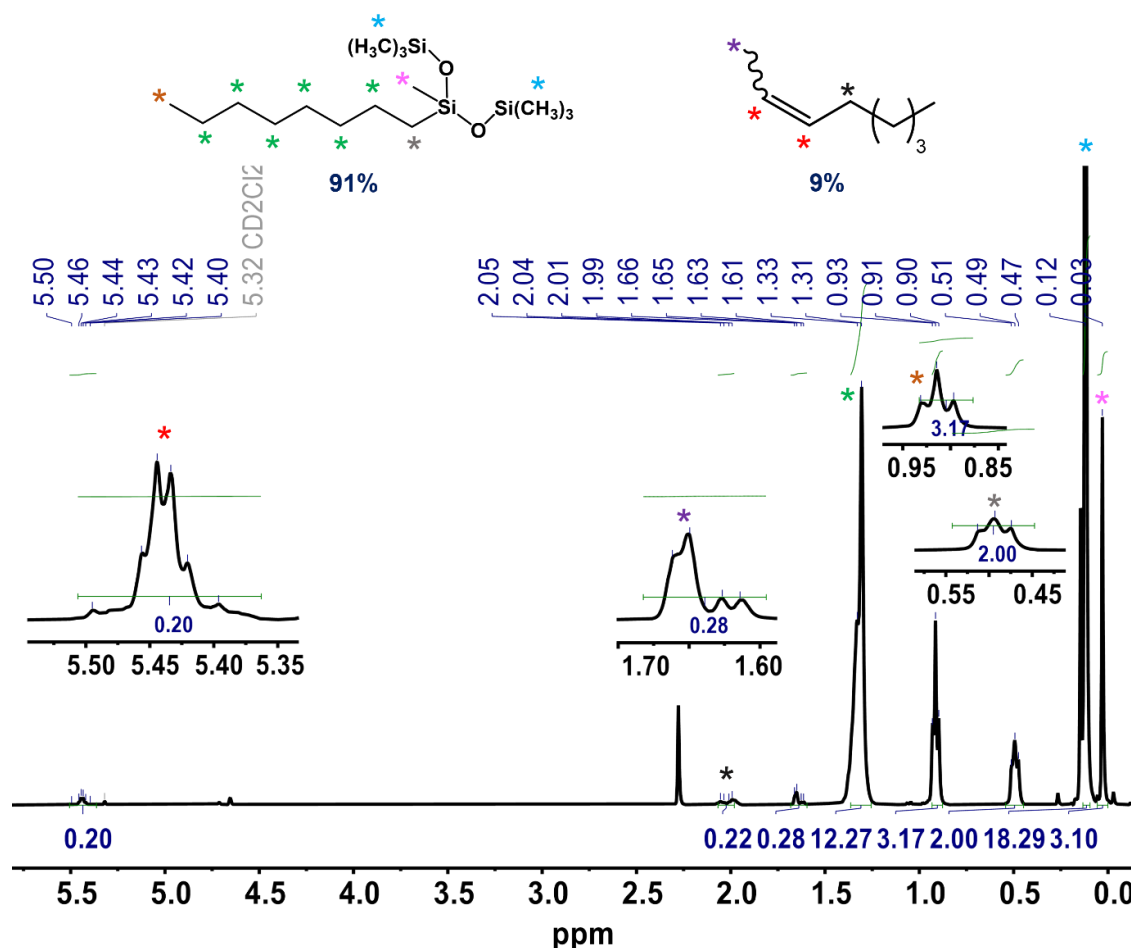


Figure 3.33. ^1H NMR spectrum of the beta and isomerisation products formed in the in-situ hydrosilylation reaction of **MD'M** and **oct-1-ene** using precatalyst **1b** (400 MHz, d_2 -dichloromethane, 298 K). Reaction conditions (0.0025 M **1b**, 1.1 M **MD'M**, 1.1 M **oct-1-ene**, left for ~ 1 h thermally then irradiated for 120 s).

The corresponding ^{29}Si NMR spectrum at the end of catalysis verifies that the reaction between **MD'M** and **oct-1-ene** only affords the beta product (δ 6.8 and -21.2) and isomeric alkenes, as there is no evidence of the alpha product or dehydrocondensation adduct (Figure 3.34). Marko and colleagues found that the hydrosilylation reaction between **MD'M** and **oct-1-ene** using

Karstedt's catalyst (30 ppm) at 72°C required 30 minutes to reach 80% yield of beta product.²⁰ This was, however, accompanied by the formation of isomeric alkenes, the hydrogenated alkene and the dehydrocondensation adduct (up to 20%). More recently, Nolan and colleagues found that the $[\text{Pt}(\text{DMS})_2\text{Cl}_2]$ complex (0.0001 mol%) could be used to catalyse the hydrosilylation reaction between **MD'M** and **oct-1-ene**, and 96% yield of beta product was obtained in 90 minutes.¹⁵⁹ Although this system could be used at very low catalyst loadings, it required heating to 80 °C. Precatalyst **1b** offers the advantage that it can be photoactivated to effect hydrosilylation, with relatively good selectivity towards the beta product.

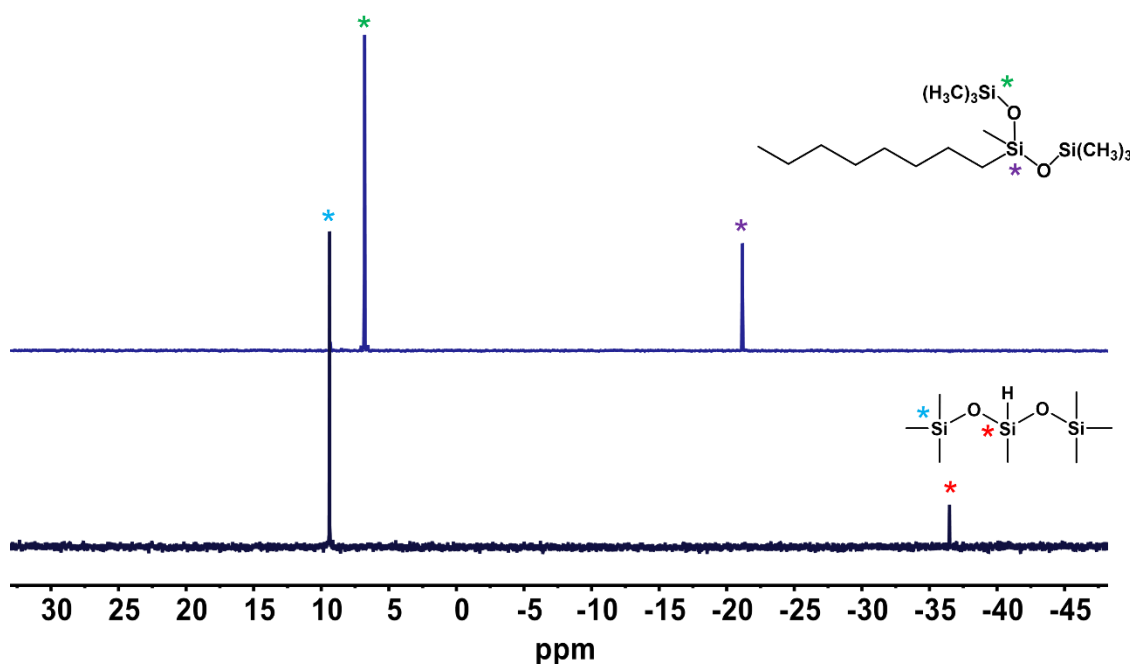


Figure 3.34. ^{29}Si NMR spectra of **MD'M** (bottom) and beta product (top) formed in the hydrosilylation reaction between **MD'M** and **oct-1-ene** using precatalyst **1b** (119.2 MHz, d_2 -dichloromethane, 298 K).

A further advantage of using precatalyst **1b** is that it shows good latent reaction kinetics under the model reaction conditions, as shown in Figure 3.35. The concentration-time profile for beta product formation (after irradiation) is characterised by a significant induction period, followed by an acceleration in catalytic activity. This profile is similar to that observed by Marko, where

platinum(0)–carbene catalysts (30 ppm) were employed in the hydrosilylation reaction between **MD'M** and **oct-1-ene**.¹⁰⁴ Marko reported that this reaction, conducted in xylene at 72 °C, required ~2 h to achieve full conversion to the beta product, and <2% of isomerisation products were detected. When using precatalyst **1b** under photoactivated conditions, this reaction requires 3.9×10^3 s (1.1 h) to reach completion (excluding the ~1 h latency period). Consideration of the initial rates shows that this reaction proceeds at a rate that is 1.5 x slower than when **VTMS** is used as the alkene substrate under the same conditions. The temporal profile also shows that isomerisation occurs at the same time as the formation of beta product. That the isomerisation products are still present at the end of catalysis suggests that they do not undergo the reverse isomerisation reaction to the terminal alkene, which means that they also do not undergo hydrosilylation.

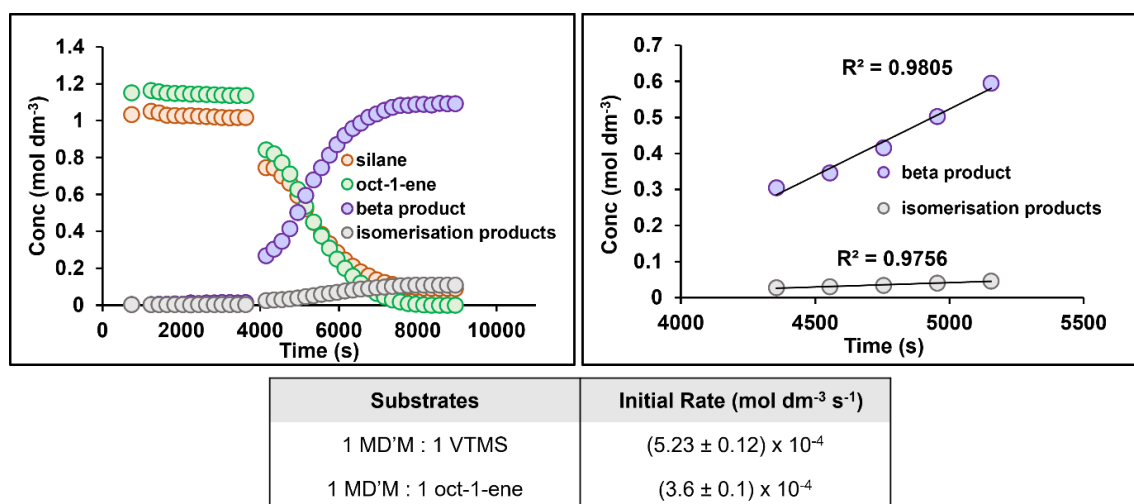


Figure 3.35. Left – concentration-time profile of **MD'M** and **oct-1-ene** consumption and beta and isomerisation product formation during the photoactivated hydrosilylation reaction using **1b** as a precatalyst. Right – linear fits for the beta and isomerisation products for the first 4 data points following irradiation to determine the initial rates. Reaction conditions (0.0025 M **1b**, 1.1 M **MD'M** and 1.1 M **oct-1-ene** in *d*₂-dichloromethane, left for ~1 h thermally then irradiated for 120 s). The table shows the initial rates for beta and isomerisation product formation.

3.8.6 Substrates inert to hydrosilylation in the model system

The scope of the catalytic system was also expanded to include internal alkenes and acetone, as these substrates are generally known to be far less reactive toward hydrosilylation than terminal alkenes under thermal conditions.¹ The in-situ ¹H NMR experiment was conducted under the same conditions as described in section 3.6 (0.0025 M **1b**, 0.8 – 1.4 M **MD'M**, 0.8 – 1.4 M **alkene** in *d*₂-dichloromethane, 120 s irradiation), but **VTMS** was substituted for either **cyclohexene**, **norbornadiene**, **trans-2-octene** or **acetone**. As shown in Figure 3.36, **cyclohexene**, **norbornadiene**, **trans-2-octene** and **acetone** are inert to hydrosilylation under the conditions employed in the model reaction.

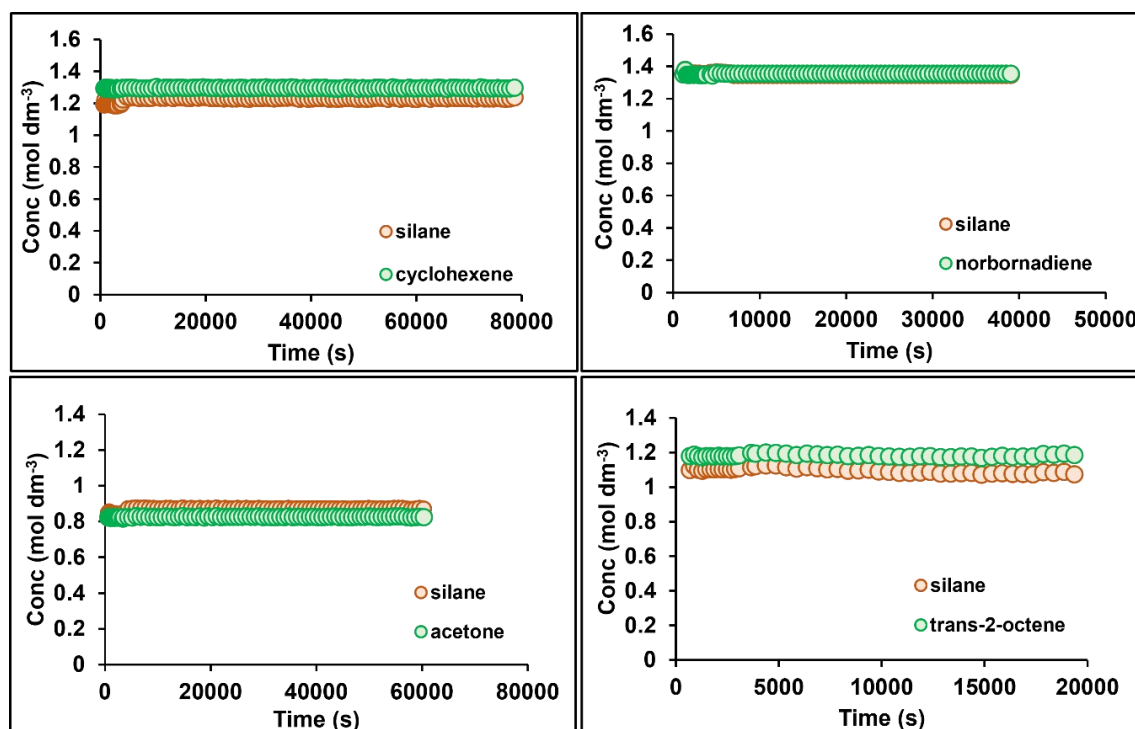


Figure 3.36. Concentration-time profiles of **MD'M** and inert alkenes in the photoactivated hydrosilylation reaction. Reaction conditions (0.0025 M **1b**, 0.8 – 1.4 M **MD'M** and 0.8 – 1.4 M **alkene** in *d*₂-dichloromethane, left for ~1 h thermally then irradiated for 120 s).

Kühn and colleagues also reported that **cyclohexene** was unreactive in the hydrosilylation reaction with HSiCl₃, using Karstedt's catalyst (125 ppm) at 60°C.² Hydrosilylation has been reported to depend on the ability of the alkene to coordinate to the Pt centre, and Kühn showed

that **cyclohexene** coordinated weakly compared to more reactive alkene substrates such as **oct-1-ene**. These results might imply that precatalyst **1b** does not bind **cyclohexene** strongly enough to effect hydrosilylation activity. Other studies have shown that hydrosilylation of **cyclohexene** is possible using Speier's catalyst under much more drastic conditions such as in sealed ampoules or autoclaves, with long reaction times (>20 h).¹⁶¹

Marko and colleagues found **trans-2-octene** to be inert in the hydrosilylation reaction with **MD'M** using a platinum-carbene catalyst at 30 ppm.¹⁰⁴ This system was heated to 72 °C in xylene and still afforded no hydrosilylation products, which highlights the reluctance of this substrate to undergo hydrosilylation.

To date, little is known about the hydrosilylation of **norbornadiene**, and a mixture of products is often observed when it is used as the alkene substrate.¹⁶² Bermeshev and colleagues recently reported the successful hydrosilylation of **norbornadiene** with **MD'M** using Karstedt's catalyst (0.05 mol%) at 25 °C.¹⁶³ This reaction required 48 h to achieve full conversion and formed a mix of the *exo* and *endo*-isomers of mono-silyl-substituted norbornene, as well as the mono-silyl-substituted nortricyclane (Figure 3.37). The ratio of these products was 32, 48 and 20%, respectively. It is anticipated that **norbornadiene**, an excellent chelating ligand, binds very strongly to the metal centre of precatalyst **1b** and impedes its catalytic activity.

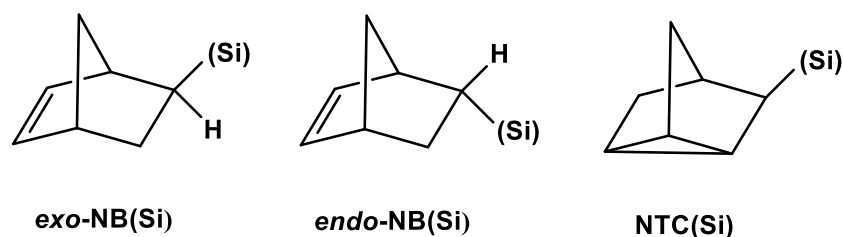


Figure 3.37. Products formed in the hydrosilylation reaction between **MD'M** and **norbornadiene** using Karstedt's catalyst (0.05 mol%).¹⁶³

For the hydrosilylation of ketones, rhodium-based complexes have been reported to be the most successful catalysts.¹⁶⁴ The mechanism for ketone hydrosilylation differs from alkene

hydrosilylation in the initial stages, due to the different polarities of the double bond. Proposed mechanisms suggest that the ketone is bound to the silyl group through the carbonyl oxygen atom.¹⁶⁵ This is in contrast to alkenes, which are coordinated to the metal centre through a π -interaction. This difference in mechanism may account for why precatalyst **1b** is able to successfully catalyse the hydrosilylation of alkenes, but not ketones.

3.8.7 Recharges with inert substrates

In an effort to effect hydrosilylation activity with the inert alkene substrates, a series of recharge experiments were conducted. The in-situ ^1H NMR experiment was repeated using the same conditions as described in section 3.6 (0.0025 M **1b**, 0.9 – 1.2 M **MD'M**, 0.9 – 1.2 M **VTMS** in d_2 -dichloromethane, 120 s irradiation) but stopped after complete conversion of **MD'M** and **VTMS** was observed. A batch of 1 **MD'M** : 1 **inert alkene** was then added into the reaction mixture. The logic behind this series of experiments was that the activation of the precatalyst via a reactive substrate could facilitate the hydrosilylation reaction of an otherwise unreactive alkene. The concentration-time profile for the model reaction recharged with 1 **MD'M** : 1 **cyclohexene** is shown in Figure 3.38.

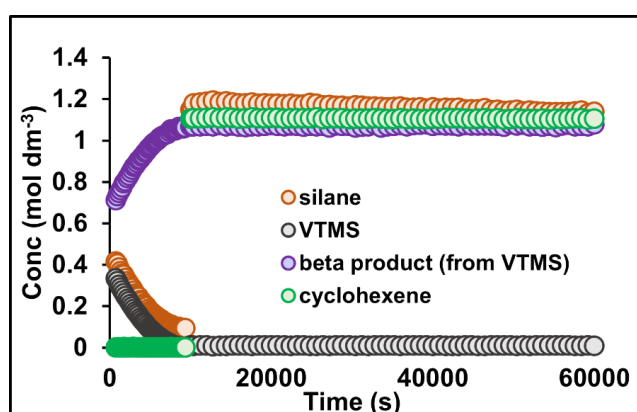


Figure 3.38. Concentration-time profile of **MD'M** and **VTMS** consumption and beta product formation during the photoactivated hydrosilylation reaction between **MD'M** and **VTMS**, recharged with **MD'M** and **cyclohexene** upon completion. Reaction conditions (0.0025 M **1b**, 0.93 M **MD'M**, 0.93 M **VTMS**, irradiated 120 s then recharged with 1.2 M **MD'M** and 1.2 M **cyclohexene** upon completion.

Addition of **MD'M** and **cyclohexene** to the catalysis solution post hydrosilylation did not afford any hydrosilylation products from cyclohexene. This substrate remains inert, even after activating the precatalyst. Based on Kühn's observations, this implies that the active species generated from precatalyst **1b** is saturated with **VTMS**, and **cyclohexene** cannot displace **VTMS** due to its poorer binding strength.²

To determine if **trans-2-octene** could undergo hydrosilylation after the precatalyst was activated, the model reaction was conducted and then recharged with 1 **MD'M**:1 **trans-2-octene**. The concentration-time profile for this experiment is shown in Figure 3.39.

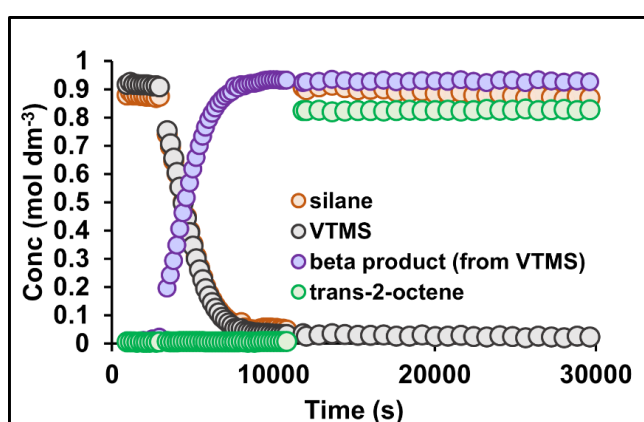


Figure 3.39. Concentration-time profile of **MD'M** and **VTMS** consumption and beta product formation during the photoactivated hydrosilylation reaction between **MD'M** and **VTMS**, recharged with **MD'M** and **trans-2-octene** upon completion. Reaction conditions (0.0025 M **1b**, 0.93 M **MD'M**, 0.93 M **VTMS**, left for ~1 h thermally then irradiated 120 s. Recharged with 0.93 M **MD'M** and 0.93 M **trans-2-octene** upon completion.

Similarly to what was observed when the model reaction was recharged with 1 **MD'M** : 1 **cyclohexene**, no reaction is observed when 1 **MD'M**:1 **trans-2-octene** are added to the reaction mixture. This shows that the active catalyst generated from **1b** in the model reaction using **VTMS** as the alkene substrate is not effective in catalysing the hydrosilylation of **trans-2-octene**. This could be attributed to **trans-2-octene** having a weaker binding strength than **VTMS**.

In an effort to effect the hydrosilylation of **norbornadiene**, the model reaction was recharged with 1 **MD'M**:1 **norbornadiene** after full conversion was achieved. The concentration-time profile for this experiment is shown in Figure 3.40.

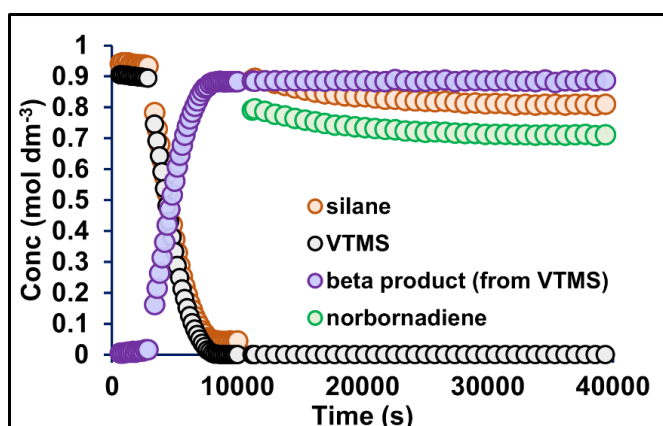


Figure 3.40. Concentration-time profile of **MD'M** and **VTMS** consumption and beta product formation during the photoactivated hydrosilylation reaction between **MD'M** and **VTMS**, recharged with **MD'M** and **norbornadiene** upon completion. Reaction conditions (0.0025 M **1b**, 0.93 M **MD'M**, 0.93 M **VTMS**, left for ~1 h thermally then irradiated 120 s. Recharged with 0.93 M **MD'M** and 0.93 M **norbornadiene** upon completion.

Unsurprisingly, the recharge experiment did not produce any hydrosilylation products from the **norbornadiene** substrate. However, a slight reduction in the concentrations of **MD'M** and **norbornadiene** was observed, concomitant with the formation of a distinguishable new signal at δ 2.93 in the ^1H NMR spectrum. This could be attributed to the formation of either a decomposition product, or quadricyclane, which has been reported as a photoisomerisation product of **norbornadiene**.¹⁶⁶ However, due to significant signal overlap with the other substrates, it is not possible to identify this product.

The recharge of 1 **MD'M**:1 **VTMS** with a batch of the same solution was successful, and this will be discussed in chapter four.

3.9 Comparison to the commercial catalyst

After verifying the suitability of the precatalysts for photoactivated hydrosilylation in the model reaction, they were taken forward for studies using the commercial substrates. All experiments discussed below were conducted as part of a placement at Johnson Matthey Technology Centre, with the assistance of Dr Samuel Douglas. The commercially used methylhydrosiloxane / dimethylsiloxane co-polymer (**HMS**) and vinyl-terminated polydimethylsiloxane (**DMS**) substrates are shown in Figure 3.41, and were used at a ratio of 6.8 **HMS** : 100 **DMS**, in line with the established industrial protocol.

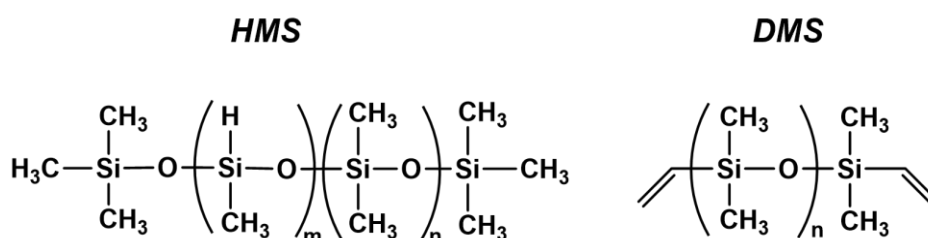


Figure 3.41. Structures of commercially used methylhydrosiloxane / dimethylsiloxane co-polymer (**HMS**) and vinyl-terminated polydimethylsiloxane (**DMS**) substrates.

3.9.1 Curing times in commercial substrates

To assess the curing times of precatalysts **1a**, **1b**, **1d** and **1i** in the commercial substrates, a series of cuvette tests were conducted. In this proof-of-concept study, the precatalyst (50 ppm) was dissolved in dichloromethane (100 μL) and added to the **HMS** / **DMS** formulation (2 g). The mixture was vigorously shaken in a sample vial and then transferred to a cuvette. A stirrer bar was added to the cuvette and then the cuvette was positioned on a stirrer set 110 mm away from a commercial 300 W Xe arc lamp with a water-cooled chamber, as shown in Figure 3.42. The same revolutions per minute were used for all experiments. The lamp was then switched on and a timer was started. The curing time was determined by the time needed for the stirrer bar to stop stirring, due to increased viscosity of the formulation once cured.



Figure 3.42. 300 W Xe arc lamp with water cooled chamber 110 mm away from the cuvette. The cuvette contains the catalyst solution and **HMS / DMS** polymers.

Stirring the solution resulted in the formation of a solid polymeric material, as shown in Figure 3.43, verifying that the precatalysts are suitable for curing the commercial substrates. The curing times and experimental conditions for each precatalyst are detailed in Table 3.5.



Figure 3.43. Inverted cuvette after curing the precatalyst in the **HMS / DMS** formulation.

Table 3.5. Comparisons of the cure times using a variety of precatalysts in the photoactivated hydrosilylation reaction of **HMS** and **DMS**.

Catalyst	Concentration (ppm)	Water bath temperature initial (°C)	Water bath temperature end (°C)	Time needed to cure (s)
1a	50	24	51	2.1×10^3
1b	50	22	52	2.5×10^3
1d	50	22	42	1.1×10^3
1i	50	23	34	4.8×10^2
i-68	50	23	28	1.5×10^2

Unfortunately, the water-cooled chamber did not provide sufficient cooling to maintain an ambient temperature over the course of the reaction, so significant increases in temperature were observed in the cuvette (up to 52 °C). This means that the precatalysts were thermally and photochemically activated, so the curing times cannot exclusively be attributed to the photoactivated nature of the precatalysts. Nonetheless, the 50 ppm precatalyst loading gives curing times for all precatalysts on the order of 4.8×10^2 s (0.13 h) – 2.5×10^3 s (0.69 h). Although these curing times are significantly longer than that required for the industry standard MeCpPtMe₃ (**i-68**) which only required 1.5×10^2 s to cure, the precatalysts used in this study offer advantages such as having a simpler synthetic route and potentially being less toxic.^{167,168,114}

Precatalysts **1d** and **1i** cure the **HMS** / **DMS** formulation faster than precatalysts **1a** and **1b**, which is in accordance with what was observed in the model reaction in the in-situ ¹H NMR studies (see Table 3.2). This demonstrates that the model reaction is a suitable system for benchmarking the precatalysts and determining their efficacy for industrial applications. The ability of the precatalysts to cure the siloxane polymers in a reasonable timeframe, at low catalyst loadings, demonstrates their potential to replace the currently used highly toxic commercial catalyst.^{144,169}

3.9.2 Thermal stability studies

Differential scanning calorimetry (DSC) was used to assess the thermal stability of the precatalysts (50 ppm) in the curable formulation composed of 6.8 **HMS**:100 **DMS**. As discussed in section 3.2, if the exotherm due to hydrosilylation (cure) occurs at low temperatures, this means that the formulation would gel prematurely and the precatalysts would not be suitable for industrial processes requiring a latency period. To determine the cure temperatures in the presence of precatalysts **1a**, **1b**, **1d** and **1i**, a stock solution of the precatalyst (50 ppm) in the **HMS** / **DMS** (2 g) formulation was prepared and 10 μL of this solution was pipetted onto an aluminium sample pan for analysis. The DSC measurement curves for all precatalysts are shown in Figure 3.44.

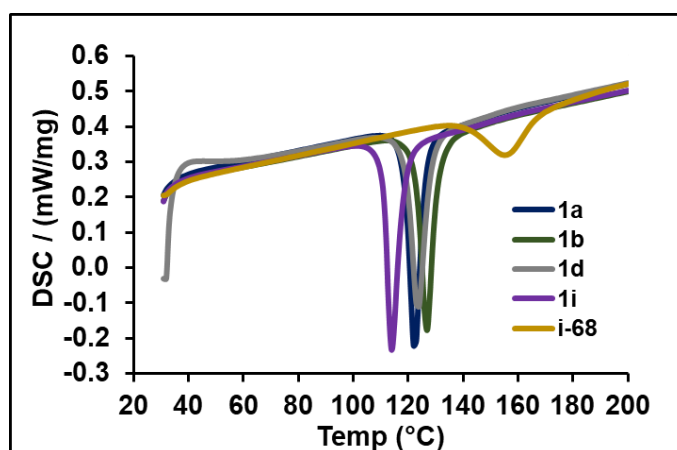


Figure 3.44. Thermal DSC analysis of the cure temperature of 6.8 **HMS** : 100 **DMS** in the presence of selected precatalysts.

The exotherm is observed as the hydrosilylation (curing) reaction takes place, and in all cases, the cure temperature is above 110 °C. The industry standard catalyst (**i-68**) cures at 156 °C, whilst the curing temperatures are 123, 127, 124 and 114 °C for precatalysts **1a**, **1b**, **1d** and **1i**, respectively. This shows that the curing temperature has a dependence on the nature of the catalyst and the structure of the ligands. Precatalyst **1i** has the lowest curing temperature, whereas **1a**, **1b** and **1d** have slightly higher curing temperatures, which demonstrates that the –

OCH₃ group on the salicylaldehyde component of the Schiff base ligand leads to a system that is slightly less thermally stable. This is in accordance with the reaction times required in the model thermal reaction in the in-situ ¹H NMR studies (see Table 3.2), where the reaction time is much faster for **1i** (2.8×10^4 s) than for **1a** or **1b** (ca. 8.0×10^4 s). This might imply that lower thermal stability is conducive to faster catalysis, but this trend does not hold for precatalyst **1d**, which takes only 1.6×10^4 s to promote full conversion in the model thermal reaction. Despite the precatalysts in this study showing slightly lower curing temperatures than **i-68**, they all cure at temperatures much higher than ambient conditions, which is an important characteristic of a latent, photoactivated catalyst.

3.10 Conclusions

This chapter has presented the development of a model hydrosilylation reaction between **MD'M** and **VTMS**, which has been used to assess the efficacy of precatalysts **1a–1i** in thermal and photoactivated hydrosilylation reactions. All precatalysts were found to effect hydrosilylation and afforded the anti-Markovnikov (beta) product exclusively, under thermal and photoactivated conditions. For all precatalysts, significant accelerations in rate were observed upon a burst of irradiation (10 – 120 s). That continuous irradiation was not required to effect hydrosilylation demonstrates the use of **1a–1i** as photoactivated hydrosilylation precatalysts. Under thermal conditions, a sigmoidal profile, with an associated induction period and a pseudo-zero order regime at maximum rate of turnover, is observed for all precatalysts except **1c** and **1d**. Precatalysts **1c** and **1d** show much shorter induction periods and apparent zero-order reaction profiles that operate over nearly all of the reaction profile. The time measured to completion under thermal conditions varies from 1.8 h (**1c**) to 22.4 h (**1a**). Under photoactivated conditions, the time measured to completion varies from 0.15 h (**1c**) to 4.7 h (**1a**). Whilst a direct trend has not been established, as a bigger library of complexes is required, some key structural features of these precatalysts can be related to their catalytic activity. For instance, in the model thermal

reaction, **1d** has a shorter induction period than **1g** (5.8×10^2 s compared to 1.2×10^3 s), but **1g** promotes faster turnover overall (1.6×10^4 s for **1d** and 1.5×10^4 s for **1g**). This might suggest that the benzo[*h*]quinoline ligand is more suited than phenylpyridine for providing latent reaction kinetics, due to its higher stability. Precatalyst **1c** promotes faster turnover than **1d** in both the thermal (6.4×10^3 s for **1c** compared to 1.6×10^4 s for **1d**) and photoactivated (7.6×10^2 s for **1c** compared to 1.4×10^3 s for **1d**) model reactions, which suggests that introduction of an alkyl group onto the salicylaldimine ligand is conducive to enhanced photoactivation efficiencies. Precatalysts **1a** and **1b** show the best latent reaction kinetics and have induction periods of 5.0×10^3 s and 1.0×10^4 s respectively, and after 120 s irradiation, full conversion to the beta product is realised after 5.6×10^3 s and 4.4×10^3 s, respectively. To demonstrate its suitability under commercially relevant conditions, precatalyst **1b** was also shown to catalyse the model reaction at a catalyst loading of 0.0025 mol% (0.000025 M / 14 ppm).

Owing to its excellent latency and ability to promote hydrosilylation photochemically, precatalyst **1b** was used to expand the alkene substrate scope in the model photoactivated (120 s) reaction. This precatalyst successfully catalysed the hydrosilylation reaction between **MD'M** and **VTMOS**, **oct-1-ene**, **3-Buten-2-one**, **styrene** and **4-methoxystyrene**. For all alkene substrates except 3-Buten-2-one, the main product conforms to the anti-Markovnikov rule and yields the beta product. The 3-Buten-2-one substrate displays complete chemoselectivity in favour of the hydrosilylation of the terminal alkene, rather than the ketone, but is more selective towards the alpha (Markovnikov) product (93%). Whilst using **VTMS** as the alkene selectively yields the beta hydrosilylation product, **VTMOS** also undergoes Markovnikov hydrosilylation to afford 10% alpha product. Both **styrene** substrates also furnish the alpha product when used in the model reaction (78% for styrene and 87% for **4-methoxystyrene**). The observed selectivities are similar to those when using $[\text{Pt}(\text{DMS})_2\text{Cl}_2]$ as a thermally activated hydrosilylation catalyst.¹⁵⁹ When **oct-1-ene** is employed as the alkene substrate, the beta product is formed as well as 9% isomerisation products. Compared with the model reaction using **VTMS**, the reaction proceeds more slowly in the presence of all the other studied alkenes except **oct-1-ene**, and **4-methoxystyrene** was

identified as the slowest reacting substrate ($ToF_{app} < 2.0 \times 10^1 \text{ h}^{-1}$ compared to $ToF_{app} = 3.3 \times 10^2 \text{ h}^{-1}$ for **VTMS**). Kühn suggested that the binding strength of alkenes dictates their reactivity in hydrosilylation, where substrates that bind too weakly will not undergo hydrosilylation, and the reactivity of substrates that bind too strongly will suffer.² This concept will be explored in more detail in chapter four. The hydrosilylation of **cyclohexene**, **norbornadiene**, **acetone** and **trans-2-octene** was attempted using precatalyst **1b**, but this was unsuccessful in all cases. It was found that these substrates would not undergo hydrosilylation even upon the recharge of a catalysis run using **MD'M** and **VTMS**.

The final section of this chapter has presented the ability of precatalysts **1a**, **1b**, **1d** and **1i** to cure the commercially used polysiloxane substrates (**HMS** and **DMS**) at commercially relevant catalyst loadings (50 ppm). All precatalysts photocured the substrates in a timeframe of $4.8 \times 10^2 - 2.5 \times 10^3 \text{ s}$. Precatalysts **1d** and **1i** cured the formulation faster than precatalysts **1a** and **1b**, which is in accordance with that observed in the in-situ ^1H NMR studies using the model reaction. The thermal stability of these precatalysts in the **HMS** / **DMS** formulations was also examined, and the cure temperatures were found to be in the range of $114 \text{ }^\circ\text{C} - 127 \text{ }^\circ\text{C}$. This is similar to that observed for the industry standard catalyst **i-68**, which has a cure temperature of $156 \text{ }^\circ\text{C}$.

Having established that precatalyst **1a** and **1b** show excellent latency and good photoactivation efficiencies, they were taken forward for mechanistic studies. The model reaction detailed in this chapter serves as a platform from which further mechanistic studies are conducted. Chapter four presents a detailed mechanistic study, where the order in substrates is determined and isotope labelling experiments are conducted to pinpoint the mechanistic steps. The experimental data is also modelled using COPASI, and a mechanism for photoactivated hydrosilylation using precatalyst **1b** is proposed. This chapter will also detail a series of experiments that were conducted to elucidate the nature of the active species formed from precatalyst **1b**. It is hoped that this study will shed light on photoactivated hydrosilylation reactions and pave the way for the development of new catalyst systems that combine the advantages of low toxicity, good

solubility in polysiloxane substrates, good latent reaction kinetics and excellent catalytic activity upon exposure to UV-light.

Chapter 4 – Mechanistic Studies on the Hydrosilylation Reaction

4.1 Preamble

In the previous chapter, the results obtained using the Pt(sal)(ppy) complexes **1a** to **1i** as hydrosilylation precatalysts were outlined. The high selectivity observed in the hydrosilylation reaction under thermal and photoactivated conditions between **MD'M** and **VTMS**, along with the latent reaction kinetics and extremely low levels of side reactions compared to other platinum catalysts warranted an in-depth mechanistic study on the mode of action of this unique class of platinum(II) complexes. In this chapter, our current understanding of the hydrosilylation reaction catalysed by Pt(sal)(ppy) complexes is developed through the use of poisoning experiments, reaction kinetics, isotope effects and kinetic modelling. For all of these studies, precatalysts **1a** and **1b** were chosen as exemplars. Despite not promoting the fastest turnover of all the precatalysts, their reaction times are slow enough to allow a sufficient number of data points for a satisfactory kinetic analysis. Furthermore, **1a** and **1b** offer the best latent reaction kinetics under thermal conditions, which is a desirable characteristic of a photoactivated hydrosilylation catalyst in industrial processes such as additive manufacturing.⁵ As outlined in Chapter three, the hydrosilylation reaction between **MD'M** and **VTMS** in *d*₂-dichloromethane using the precatalyst at 0.0025 M was optimised as the model reaction (Figure 4.1). In the photoactivated reactions, the sample was irradiated using 365 nm light, whilst this step was omitted in the thermal reactions.

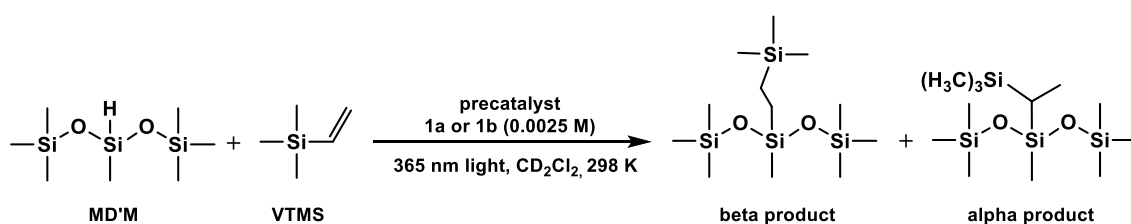


Figure 4.1. Model hydrosilylation reaction chosen for the mechanistic study.

Distinguishing between metal-complex homogeneous catalysis and metal-particle heterogeneous catalysis is not trivial and has attracted much attention in the literature.¹⁷⁰ There is no single technique that can provide an unambiguous answer as to whether homogeneous or heterogeneous catalysis is taking place, so a series of complementary experiments need to be conducted when attempting to identify the true nature of the active species. Finke and coworkers developed a general approach to address this problem by using a series of physical methods and tests involving reaction kinetics, transmission electron microscopy (TEM) imaging, light scattering, UV-visible spectroscopy, poisoning experiments, filtration experiments and catalyst isolation.^{170,171} The most relevant tests are discussed in more detail below.

I. Analysis of the reaction kinetics.

It has been suggested that homogenous catalysis yields reproducible kinetics whereas heterogeneous catalysis yields irreproducible kinetics.¹⁷² However, there have been cases where systems involving nanocluster catalysts have shown highly reproducible kinetics, which shows that such a distinction does not apply in all cases.¹⁷³ Therefore, the observation of reproducible reaction kinetics cannot be used to rule out heterogeneous catalysis. The observation of a sigmoidal kinetic curve however, has been shown to be compelling evidence for the in-situ formation of a heterogeneous catalyst, assuming that the reaction products have already been identified as nanoclusters (for example, by TEM), or by visual observation of bulk-metal precipitate.¹⁷⁴

II. Analysis by TEM.

Transmission electron microscopy is an incredibly powerful technique for detecting the presence of nanoclusters which have either been produced in reaction solutions, or deliberately synthesised. This technique is able to detect concentrations of colloidal metal as low as $\geq 10^{-12}$ M.¹⁷⁰ There is an abundance of literature on TEM being used to

characterise the size, shape and interface structure of platinum nanoparticles in the hydrosilylation reaction.^{8,66,175} The major drawback of TEM is that despite its sensitivity, it does not provide evidence that the observed nanoclusters are the actual species responsible for the catalysis. Separation of the nanoclusters from reaction solutions can be very challenging so it is imperative that TEM is used in combination with other tests, such as poisoning experiments, when attempting to identify the nature of the active species.

III. Analysis by light scattering.

The presence of metal particles in catalytic solutions can be detected by light scattering.^{176,177,178} This technique can detect particles > 1 nm in diameter and the analysis is performed in solution which means metal particles can be detected in-situ.¹⁷⁶ In the same way as TEM however, light scattering cannot ascertain that the detected metal particles are the catalytically active species, so this technique must be used in combination with poisoning experiments, for example, to determine the true nature of the active species. Another issue with this technique is that the presence of dust or particles from abrasion of the reactor can lead to “false positives”.¹⁷²

IV. Mercury poisoning experiments.

The use of elemental mercury to poison metal-particle heterogeneous catalysts is a well-practised technique.^{179,180} The catalytic activity of bulk platinum metal is suppressed by Hg(0) amalgamating the metal or adsorbing on the metal surface. Crabtree and Whitesides showed that whilst Hg(0) can be used as a selective poison for heterogeneous catalysts, homogeneous catalysts are unaffected.^{37,83,178} Lewis and coworkers studied the effect of Hg(0) in the hydrosilylation reaction between triethoxysilane and **VTMS**, using either Speier’s catalyst or Pt(COD)Cl₂.¹⁷⁶ It was shown

that pre-reaction of the catalysts with Hg(0) led to complete poisoning and therefore inhibition of catalysis, whilst in the absence of Hg(0), the reaction proceeded to give hydrosilylation products. These results suggest, in combination with complementary TEM images, that the active species for the hydrosilylation reaction in the presence of either Speier's catalyst or Pt(COD)Cl₂, is heterogeneous. It is important to note however, that pre-reaction of the catalyst with Hg(0) is not the same as adding Hg(0) during productive turnover, as Hg(0) may inhibit catalyst formation, rather than suppressing the actual catalyst. Inhibition by Hg(0) in the photoactivated hydrosilylation reaction using CpPtMe₃ as the catalyst has also been demonstrated by Boardman (see Chapter One, Scheme 1.19).⁵⁴

V. Fractional poisoning experiments by strongly coordinating ligands.

Poisoning experiments using strongly coordinating ligands such as CS₂, PMe₃ and thiophene can facilitate the process of distinguishing between homogeneous and heterogeneous catalysis.^{170,173,181} These poisons operate by binding strongly to metal centres and blocking access of substrate to the active site. If catalysis is inhibited when < 1.0 eq. of selective poison is added per metal centre, then this is good evidence for a heterogeneous catalyst. On the contrary, typically > 1.0 eq. of selective poison is required to completely halt a reaction that is catalysed by a homogeneous, monometallic complex. The rationale behind this is that in a heterogeneous catalyst, only a fraction of the metal atoms is on the surface, so < 1.0 eq. of selective poison would be sufficient to poison all active surface atoms.

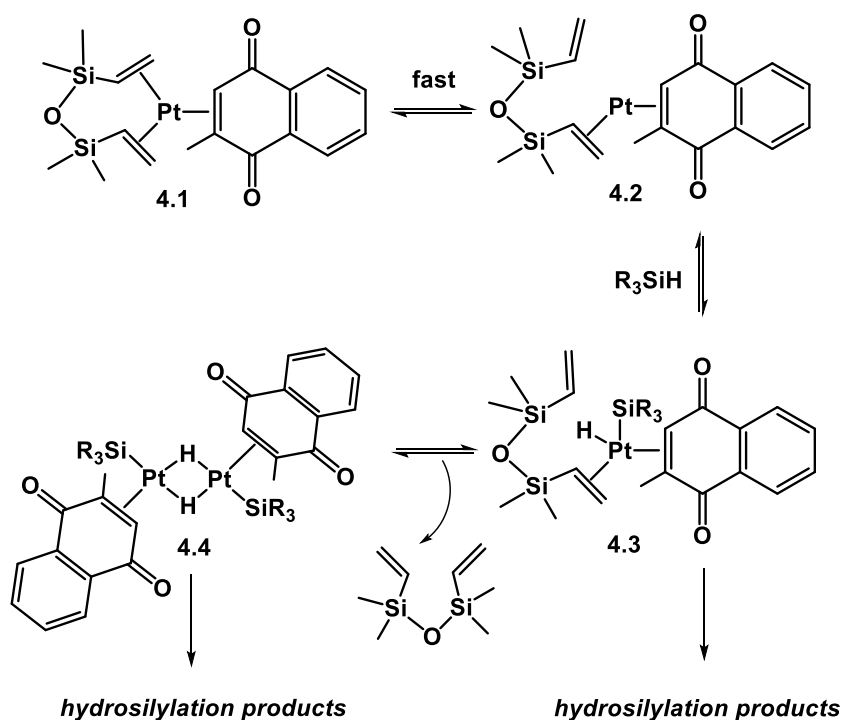
Crabtree and Anton introduced another homogeneous catalyst poisoning experiment, which is the addition of dibenzo[*a,e*]cyclooctatetraene (DBCOT) to catalytically active solutions.^{37,178} The conformational constraints of this molecule make it an excellent chelating ligand for transition metals but severely limit the interactions with metal

surfaces. Consequently, the presence of DBCOT should have an inhibitory effect on the catalytic activity of a homogenous complex but little effect on a heterogeneous platinum colloid. Boardman showed that DBCOT did not act to attenuate catalytic activity in the photoactivated hydrosilylation reaction using CpPtMe_3 as a precatalyst, which served as further evidence of a heterogeneous colloidal catalyst.⁵⁴

The ability to distinguish homogenous from heterogeneous catalysis is important because the nature of the catalyst directly influences the catalytic properties such as the catalytic activity, selectivity, lifetime, and recovery. For platinum catalysed hydrosilylation, the line between homogeneous and heterogeneous catalysis has long been blurred, and some precatalysts have been reported to facilitate reactions homogeneously in one case and heterogeneously in another.^{54,182,183,184}

There have been several studies that have explored how the coordination strength of the alkene exerts a decisive effect on the kinetics of the hydrosilylation reaction in a homogenous process. Following Lewis' conclusions that Karstedt's catalyst operates via a homogeneous mechanism, beginning with the decoordination of the surrounding 1,3-divinyl-1,1,3,3-tetramethyldisiloxane (dvtms) ligands prior to reaction of the substrate alkene, Osborn *et al.* reported an extremely active modification of Karstedt's catalyst by replacing one dvtms ligand with the electron-withdrawing alkene, methylnaphthoquinone.^{6,19,38} The presence of this electron deficient alkene on platinum is proposed to facilitate the decoordination of the remaining dvtms ligand and therefore greatly accelerate the pathway towards the active species. A detailed mechanism was not provided but it was proposed that **4.1** is formed from Karstedt's catalyst by displacement of the labile dvtms ligand under catalytic conditions, followed by dissociation of one alkene ligand to form the 14 e⁻ Pt⁰ species **4.2** (Scheme 4.1). This undergoes oxidative addition of silane to form **4.3**, which upon further loss of alkene and dimerisation forms **4.4**. Osborn suggested that both monomeric and dimeric species are involved in the catalytic cycle so **4.3** and **4.4** may then

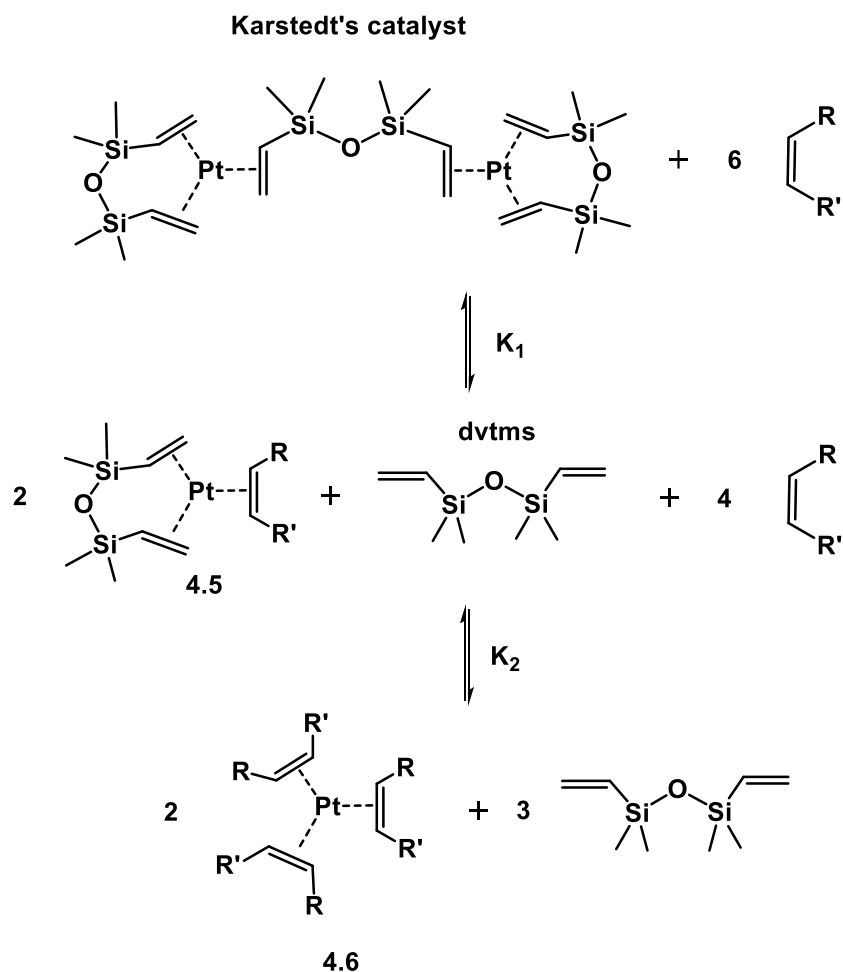
lead to hydrosilylation products. Since then, there have been several contributions with these types of platinum catalysts.^{185,186}



Scheme 4.1. Proposed mechanism for the observed rate acceleration of Osborn's catalysts compared to Karstedt's catalyst.

More recently, Kühn and colleagues conducted an in-depth study on how the binding strengths of a variety of alkenes impact on the hydrosilylation activity when using Karstedt's catalyst.² They found that the highest reaction rates were observed when the substrates used prompted ligand exchange of dvtms for the respective alkene (Scheme 4.2). Using ^{195}Pt NMR spectroscopy to monitor the extent of ligand exchange at 1.0, 5.0 and 50 equiv. of alkene per platinum, it was found that no ligand exchange was observed with substrates that exhibited no hydrosilylation activity such as cyclohexene and *trans*-oct-2-ene. On the contrary, the highly reactive oct-1-ene was found to replace the bridging dvtms ligand to form **4.5**, whilst norbornene was found to replace both the bridging and chelating dvtms ligand to form **4.6**. It was concluded that norbornene binds to Pt several orders of magnitude stronger than oct-1-ene. Despite a certain degree of alkene binding affinity to the Pt centre being beneficial for rapid hydrosilylation, Kühn

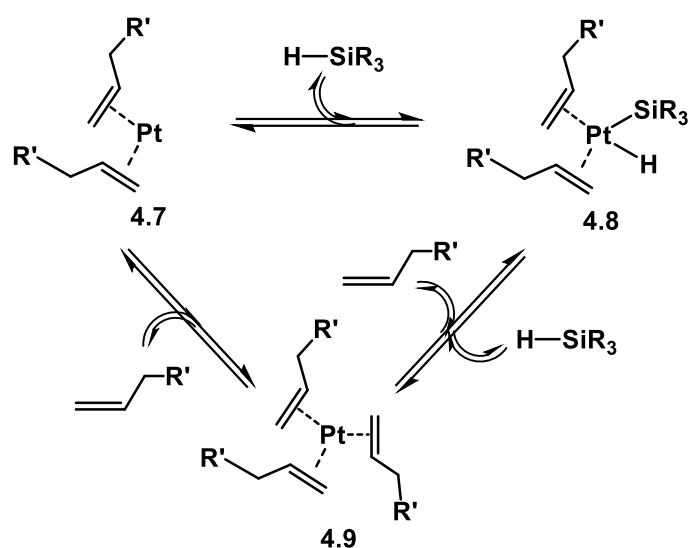
suggested that if the alkene binds too strongly, the reactivity suffers. This was exemplified with the use of maleic anhydride as the alkene substrate, which demonstrated full replacement of the dtvms ligands at the Pt:alkene ratio of 1:5 yet was not converted at all to hydrosilylation products in the catalytic reaction. This builds on the initial studies by Lewis, Osborn and others and demonstrates how stabilising the metal centre with ancillary ligands of just the right coordination strength is conducive to forming a highly active homogeneous catalyst.^{6,19,38}



Scheme 4.2. Ligand exchange of Karstedt's catalyst when exposed to olefin substrates.²

Kühn also suggested that the coordination strength of the alkene in question directly determines the nature of the active species (Scheme 4.3). At very low alkene concentrations, **4.7** is proposed to be the most dominant species, but typically Pt(0) is coordinated by three alkenes (i.e. **4.9**). For a relatively weakly coordinating alkene such as oct-1-ene, the identity of the active species is

thought to resemble **4.8**, whereas a strongly coordinating alkene is thought to be more akin to **4.9** (Scheme 4.3). This is attributed to the fact that if the interaction between the alkene and the platinum centre is weak, oxidative addition of $\text{SiR}_3\text{-H}$ with loss of one alkene ligand is more likely. The proposed coordination geometries about the platinum centre are typical for $\text{Pt}(0)$ complexes ($\text{Pt}(\text{II})$ for **4.8**) and have been previously suggested.¹⁹



Scheme 4.3. Different proposed active species depending on the binding strength of the alkene. The depicted alkene represents dtvms on Karstedt's catalyst and the alkene substrate for hydrosilylation.²

Mechanistic studies on the platinum catalysed hydrosilylation reaction have suffered on two accounts. Firstly, the complexity of the kinetics in this reaction has meant that there is an absence of reliable information in this regard.^{2,41,73,187} Secondly, identification of the nature of the active species for a mechanism based on mononuclear species has been incredibly challenging, due to the highly reactive and fleeting nature of platinum intermediates at low concentrations. Obtaining in-situ evidence of platinum colloids during the catalytically active portion of the hydrosilylation reaction also presents challenges. Due to these factors, there has been very few detailed kinetic studies where the concentration of substrates and products have been monitored over time.^{2,72,73} This chapter will present a study on the elucidation of the nature of

the active catalyst generated from precatalyst **1b**, along with a detailed kinetic and mechanistic study on the hydrosilylation reaction catalysed by **1a** and **1b**.

4.2 Identifying the nature of the active species

In order to explore the nature of the active catalyst derived from using **1b** as a precatalyst (0.0025 M) in the model hydrosilylation reaction between **MD'M** (0.8 – 1.0 M) and **VTMS** (0.8 – 1.0 M), a series of poisoning experiments was conducted. For each experiment, precatalyst **1b** was loaded into a J. Young's NMR tube and to it was added d_2 -dichloromethane, along with **MD'M**, **VTMS** and mesitylene as an integration standard from a stock solution. For the photoactivated experiments, the sample was inserted into the NMR spectrometer and an array of ~ 20 ^1H NMR spectra was acquired to show the thermal latency period for ~ 1 h. The sample was then irradiated using the bespoke 365 nm LED for either 10 or 120 s before being inserted back into the spectrometer. An array of ~ 10 ^1H NMR spectra was acquired, before the relevant poison (Hg(0) or DBCOT) was doped in after catalytic activity had been established. The sample was returned to the spectrometer and a further array of ~ 50 ^1H NMR spectra was acquired. The concentration of the beta product was calculated from the concentration of mesitylene and the NMR integral of the Si-CH₂-CH₂-Si (δ 0.42) resonance. The thermal experiments were conducted in the same way, with the irradiation step omitted. The kinetics were probed using the initial rates method, monitoring the rate of beta product formation over the first 3-5 data points after catalytic activity had been established. Errors were calculated using the linear regression model (LINEST) in Microsoft Excel. The reported errors are the estimated standard error from the model.

The effect of Hg(0) on the active catalyst under thermal conditions was determined by allowing the reaction to reach $\sim 40\%$ completion, then doping in a drop of Hg(0) and continuing to monitor

the progress of the reaction by ^1H NMR spectroscopy (Figure 4.2). Importantly, the NMR tube was shaken vigorously when $\text{Hg}(0)$ was added, to ensure good mixing.

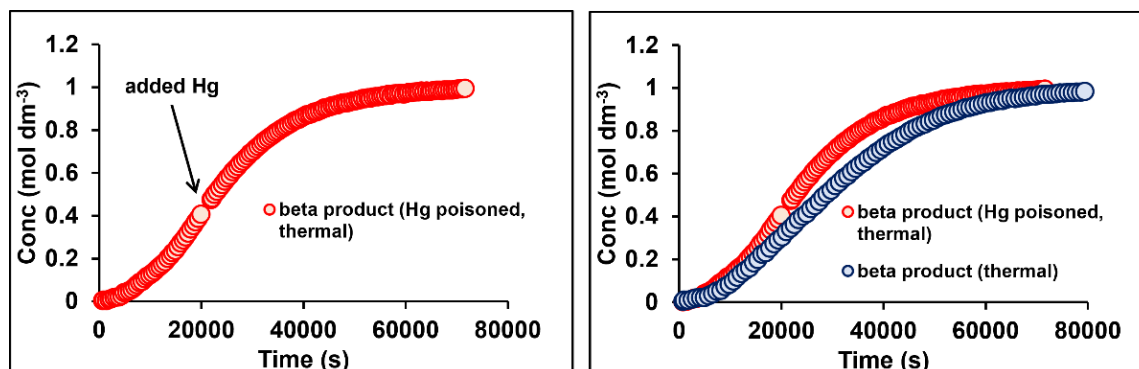


Figure 4.2. Left – concentration-time profile of beta product formation during the thermal hydrosilylation reaction between **MD'M** and **VTMS** using **1b** as a precatalyst with a drop of $\text{Hg}(0)$ added after $\sim 20,000$ seconds. Right – concentration-time profile of beta product formation in the corresponding non-poisoned thermal hydrosilylation reaction overlaid with the poisoned experiment. Reaction conditions as detailed in section 4.2.

Evidently, addition of $\text{Hg}(0)$ to the reaction mixture at $\sim 20,000$ s did not act to modify the active catalyst. The rate extracted from the 5 data points prior to the addition of $\text{Hg}(0)$ is $2.20 \pm 0.08 \times 10^{-5} \text{ mol dm}^{-3} \text{ s}^{-1}$, whilst the rate after the addition is $2.57 \pm 0.04 \text{ mol dm}^{-3} \text{ s}^{-1}$, which shows essentially no change. In the corresponding experiment with no addition of $\text{Hg}(0)$ and at the same concentration (after $\sim 40\%$ conversion), the rates from the 5 data points before and after 40% conversion are $2.4 \pm 0.1 \times 10^{-5} \text{ mol dm}^{-3} \text{ s}^{-1}$ and $2.3 \pm 0.2 \text{ mol dm}^{-3} \text{ s}^{-1}$, respectively. That there is no appreciable change in the rate after the addition of $\text{Hg}(0)$ shows that catalytic activity is not suppressed, which serves as strong evidence for an active catalyst that is homogeneous in nature.

In a similar fashion, the effect of $\text{Hg}(0)$ on the photoactivated catalyst was studied. After addition of **MD'M** and **VTMS** to precatalyst **1b** in d_2 -dichloromethane, the sample was monitored for 1 h thermally to show the latency period, then irradiated for 10 s to generate the photoactive catalyst. Once turnover was established and the reaction reached $\sim 40\%$ conversion, a drop of $\text{Hg}(0)$ was added to the reaction mixture, and the NMR tube was shaken vigorously. The sample

was not exposed to any further irradiation following the addition of Hg(0) and was monitored by ^1H NMR spectroscopy until full conversion was achieved (Figure 4.3).

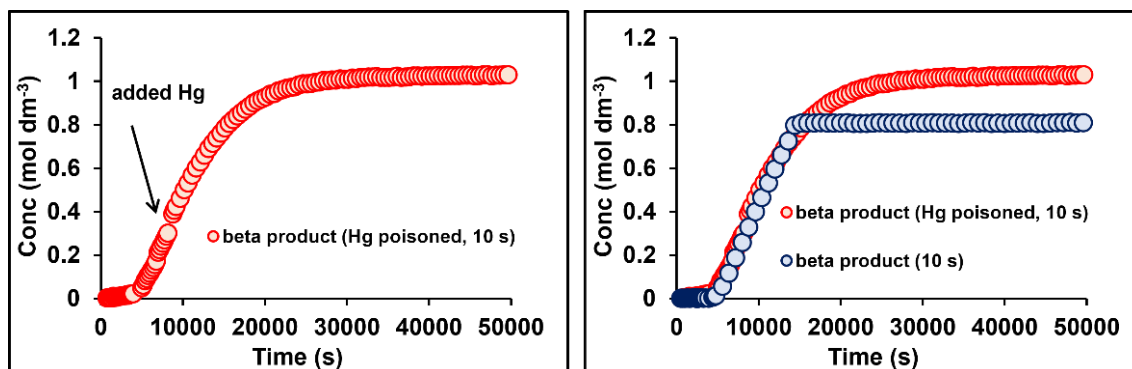


Figure 4.3. Left – concentration-time profile of beta product formation during the photoactivated hydrosilylation reaction between **MD'M** and **VTMS** using **1b** as a precatalyst with a drop of Hg(0) added after 40% conversion. Right – concentration-time profile of beta product formation in the corresponding non-poisoned photoactivated hydrosilylation reaction overlaid with the poisoned experiment. Substrate concentrations for non-poisoned experiment: 0.86 M **MD'M** and 0.86 M **VTMS**. Substrate concentrations for poisoned experiment: 0.86 M **MD'M** and 0.93 M **VTMS**. Plots are time-shifted to 6000 s to show the same latency period. Reaction conditions as detailed in section 4.2, with 10 s irradiation.

Concordant with the same experiment conducted under thermal conditions, the addition of Hg(0) did not attenuate catalytic activity for the active catalyst generated under photoactivated conditions. The rates extracted from the 5 data points before and after the addition of Hg(0) (40% conversion) are $5.9 \pm 0.1 \times 10^{-5}$ and $6.0 \pm 0.2 \times 10^{-5}$ mol dm $^{-3}$ s $^{-1}$, respectively. These rates are consistent with those in the corresponding non-poisoned experiment ($5.5 \pm 0.2 \times 10^{-5}$ mol dm $^{-3}$ s $^{-1}$ and $5.36 \pm 0.08 \times 10^{-5}$ mol dm $^{-3}$ s $^{-1}$ before and after 40% conversion, respectively) which shows that the photoactivated catalyst is essentially unaffected by Hg(0) and is therefore likely to be homogeneous.

As a complementary selective poisoning experiment to the Hg(0) drop test to confirm the homogeneous nature of precatalyst **1b** under thermal conditions, 0.3 equiv. of DBCOT relative to **1b** was added to the reaction mixture after productive catalysis had started ($\sim 20,000$ s, $\sim 30\%$ conversion) (Figure 4.4).

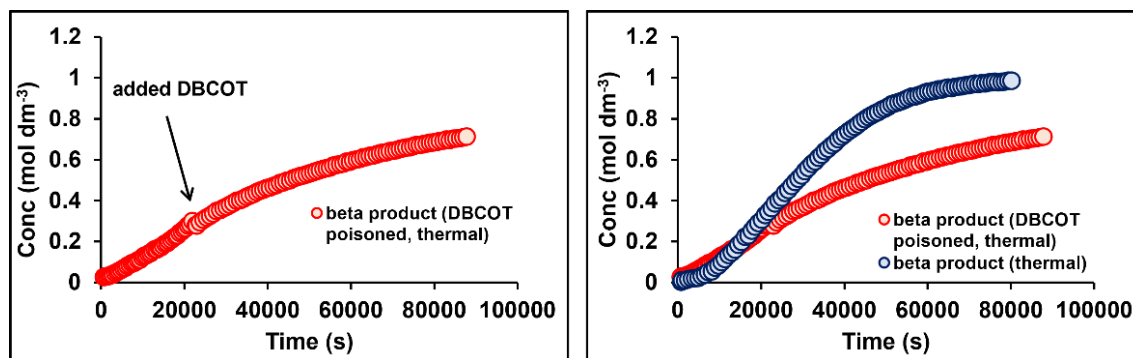


Figure 4.4. Left – concentration-time profile of beta product formation during the thermal hydrosilylation reaction between **MD'M** and **VTMS** using **1b** as a precatalyst with DBCOT added after 20,000 seconds. Right – concentration-time profile of beta product formation in the corresponding non-poisoned thermal hydrosilylation reaction overlaid with the poisoned experiment. Reaction conditions as detailed in section 4.2.

As was expected, the strongly chelating DBCOT ligand had an inhibitory effect on catalysis. The rates extracted from the 5 data points before and after the addition of DBCOT are $2.1 \pm 0.1 \times 10^{-5}$ and $1.55 \pm 0.06 \times 10^{-5} \text{ mol dm}^{-3} \text{ s}^{-1}$, respectively. That the rate after adding DBCOT is 1.3 x slower than the rate before the addition demonstrates that DBCOT has effectively chelated to the active homogeneous catalyst. This results in the reaction not reaching completion in the monitored time period. This result further substantiates the fact that the active catalyst generated under thermal conditions was unaffected by Hg(0).

The effect of DBCOT on the active catalyst generated under photoactivated conditions was also examined by first monitoring the reaction for 1 h thermally, then irradiating the sample for 10 s to generate the active catalyst, followed by addition of 0.3 equiv. of DBCOT after catalytic activity had been established ($\sim 10,000 \text{ s}$, $\sim 25\%$ conversion) (Figure 4.5).

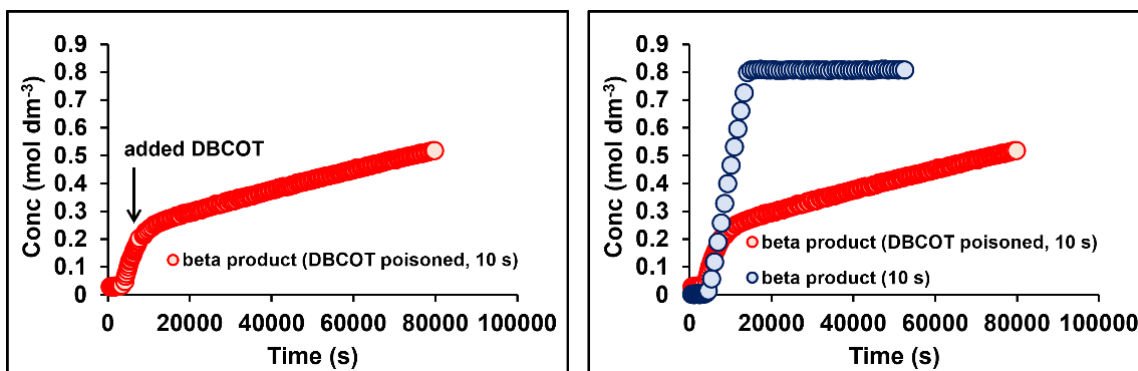


Figure 4.5. Left – concentration-time profile of beta product formation during the photoactivated hydrosilylation reaction between **MD'M** and **VTMS** using **1b** as a precatalyst with DBCOT added after 10,000 seconds. Right – concentration-time profile of beta product formation in the corresponding non-poisoned photoactivated hydrosilylation reaction overlaid with the poisoned experiment. Substrate concentrations for non-poisoned experiment: 0.86 M **MD'M** and 0.86 M **VTMS**. Substrate concentrations for poisoned experiment: 0.86 M **MD'M** and 0.93 M **VTMS**. Reaction conditions as detailed in section 4.2, with 10 s irradiation.

The rates before and after the addition of DBCOT are $5.1 \pm 0.1 \times 10^{-5}$ and $1.7 \pm 0.3 \times 10^{-5}$ mol dm⁻³ s⁻¹ respectively, which demonstrates a significant reduction in catalytic activity. That the rate after the DBCOT addition is 3 x slower than the rate before shows that it has a more pronounced effect on the active catalyst generated under photoactivated conditions than that under the thermal conditions. The reaction with DBCOT added did not reach completion in the monitored time period.

As discussed in chapter 3 but for precatalyst **1a**, though the same principle holds for precatalyst **1b** under thermal and photoactivated conditions, less than 5% of the precatalyst is likely converted to the active form. Therefore, 0.3 equiv. of DBCOT relative to the catalyst represents a considerable excess of this poison. That DBCOT only strongly attenuates, rather than halts catalysis, suggests that DBCOT undergoes reversible exchange at the thermally generated precatalyst. Exchange of DBCOT in Pt-complexes has been reported, as has partial suppression by DBCOT in Pt-catalysed hydrosilylation.^{73,79}

The post-catalysis mixture after the sample had been aged (2 h) was analysed by transmission electron microscopy (TEM) and dynamic light scattering (DLS). The sample for TEM was prepared

by adding a drop of the completed reaction mixture to a TEM grid and then removing the solvent under vacuum. The DLS sample was prepared by directly pouring the post-catalysis mixture into a cuvette. A bimodal distribution of platinum nanoparticles between 20 – 30 nm and < 2 nm was observed from the TEM and DLS data (Figure 4.6 and Figure 4.7). The formation of inactive, or less active platinum nanoparticles with molecular precatalysts has been previously suggested to be a result of catalyst deactivation.^{2,19,79}

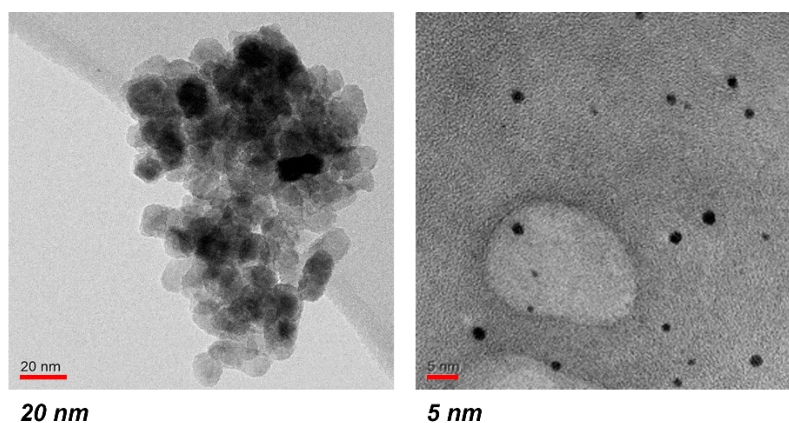


Figure 4.6. TEM images of the post-catalysis mixture (2 h). Reaction conditions as detailed in section 4.2, with 10 s irradiation.

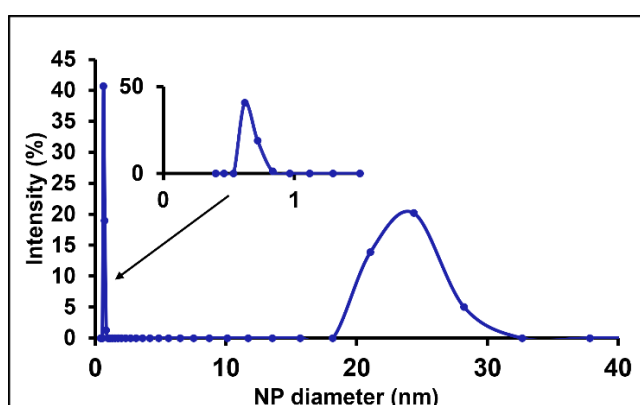


Figure 4.7. DLS data of the post-catalysis mixture (2 h). Reaction conditions as detailed in section 4.2, with 10 s irradiation.

Taken together, the effects of Hg(0) and DBCOT on the catalytic activity when using **1b** as a precatalyst are consistent with homogeneous rather than heterogeneous behaviour under the

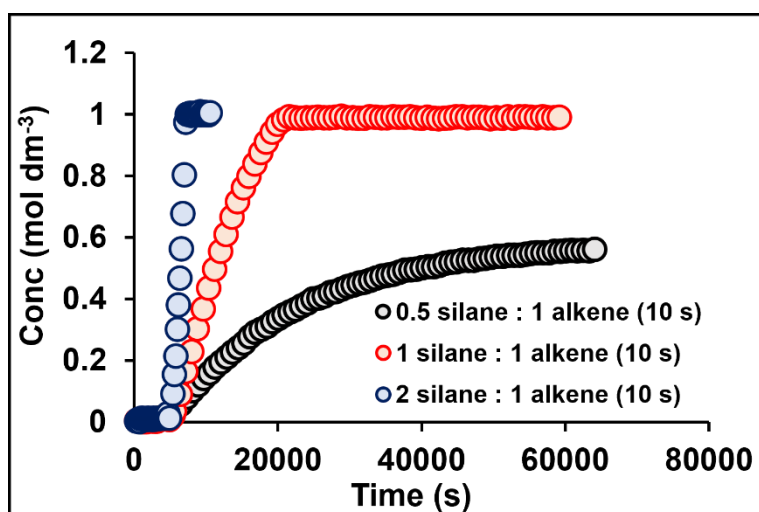
thermal and photoactivated conditions, despite nanoparticles being observed. This can be further supported by the fact that no discolouration of the reaction mixture is observed after catalysis. When combined, the observations on catalyst latency, photoactivation and homogeneity provide a platform to explore the mechanism of the active catalyst, and this is discussed below.

4.3 Determining order in silane

4.3.1 Using precatalyst **1a**

To probe the effect of the concentration of **MD'M** on catalysis, photoactivated hydrosilylation was conducted using precatalyst **1a** (0.0025 M) and varied **MD'M** concentrations of 0.5 M, 1.0 M and 2.0 M at three different irradiation times. The **VTMS** concentration was fixed at 1.0 M. For each experiment, **1a** was loaded into a J. Young's NMR tube and to it was added d_2 -dichloromethane, along with **MD'M**, **VTMS** and mesitylene as an integration standard from a stock solution. The sample was inserted into the NMR spectrometer and an array of ~ 20 ^1H NMR spectra was acquired to show the thermal latency period for ~ 1 h. The sample was then irradiated using the bespoke 365 nm LED for either 10, 60 or 120 s before being inserted back into the spectrometer. An array of ~ 100 ^1H NMR spectra was acquired and the concentrations of **MD'M**, **VTMS** and the beta product were calculated from the concentration of the integration standard and the NMR integrals of the Si-H (δ 4.63), olefinic CH (δ 6.18) and Si-CH₂-CH₂-Si (δ 0.42) resonances. The kinetics were probed using the initial rates method, monitoring the rate of beta product formation over the first 3-5 data points following irradiation. Errors were calculated using the linear regression model (LINEST) in Microsoft Excel. The reported errors are the estimated standard error from the model. For each figure in this section, silane refers to **MD'M** and [sil] and alkene refers to **VTMS** and [alk]. The times taken to achieve full conversion

exclude the latency period. The concentration-time profile along with a table of initial rates for the 10 s irradiation time is shown in Figure 4.8.



Ratio	Initial Rate (mol dm ⁻³ s ⁻¹)
0.5 silane : 1 alkene	$(2.53 \pm 0.05) \times 10^{-5}$
1 silane : 1 alkene	$(8.7 \pm 0.1) \times 10^{-5}$
2 silane : 1 alkene	$(3.6 \pm 0.2) \times 10^{-4}$

Figure 4.8. Concentration-time profiles of beta product formation during the photoactivated hydrosilylation reaction between **MD'M** and **VTMS** using **1a** as a precatalyst. Reaction conditions as detailed in section 4.3.1, with 10 s irradiation. All plots are time-shifted to 4300 s to show the same latency period. The table shows the initial rates extracted from the first 5 data points following irradiation.

As shown in the table in Figure 4.8, compared with the initial rate measured at the 0.5 **MD'M**:1 **VTMS** ratio, the rates are 3.4 x and 14.2 x faster at the 1 and 2 **MD'M**:**VTMS** ratios, respectively. This demonstrates that there is a positive order in silane under photoactivated conditions. Correspondingly, the times measured to achieve full conversion are 4.14×10^4 s (11.5 h), 1.7×10^4 s (4.7 h) and 3.1×10^3 s (0.9 h) for the 0.5, 1 and 2 **MD'M**:1 **VTMS** ratios, respectively. Using the rates for beta product formation, rate-concentration profiles were plotted for half, first and second order in silane (Figure 4.9).

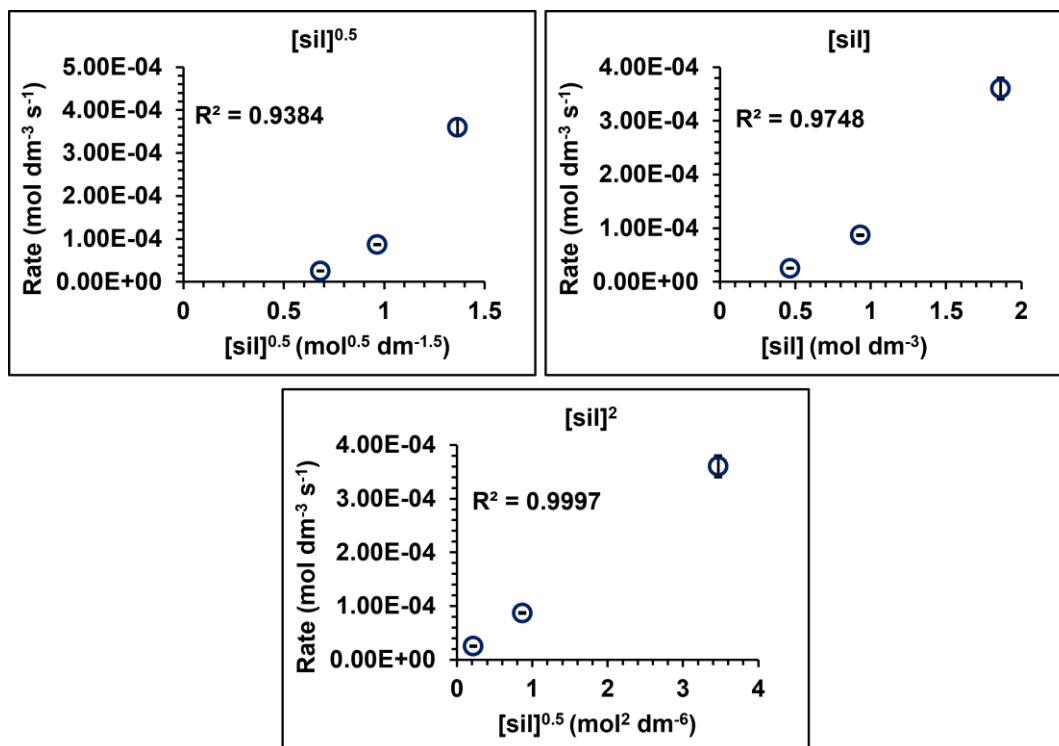
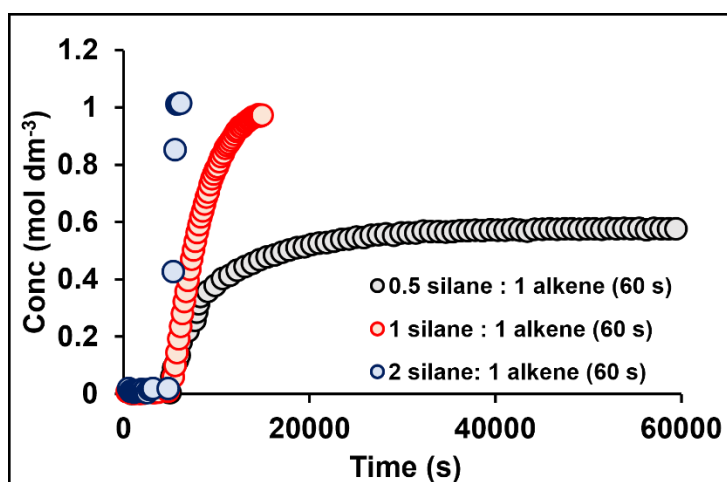


Figure 4.9. Rate-concentration profiles for half, first and second order in **MD'M** using the rates for beta product formation in the photoactivated hydrosilylation reaction between **MD'M** and **VTMS** with precatalyst **1a**. Reaction conditions as detailed in section 4.3.1, with 10 s irradiation.

It transpires that the reaction is approximately second order in **MD'M** with a linear fit ($R^2 = 0.9997$), implying that two **MD'M**'s are involved during, or prior to the rate determining step. This is consistent with the observations of Kühn and colleagues, who noted a second order in silane when using Karstedt's catalyst in the hydrosilylation reaction between HSiCl_3 and oct-1-ene.²

To determine if this same trend was observed upon exposure to longer irradiation times, the same experiment was conducted but the sample was irradiated for 60 s. The concentration-time profile along with the table of initial rates is shown in Figure 4.10.



Ratio	Initial Rate (mol dm ⁻³ s ⁻¹)
0.5 silane : 1 alkene	$(9 \pm 1) \times 10^{-5}$
1 silane : 1 alkene	$(2.23 \pm 0.03) \times 10^{-4}$
2 silane : 1 alkene	$(1.5 \pm 0.4) \times 10^{-3}$

Figure 4.10. Concentration-time profiles of beta product formation during the photoactivated hydrosilylation reaction between **MD'M** and **VTMS** using **1a** as a precatalyst. Reaction conditions as detailed in section 4.3.1, with 60 s irradiation. All plots are time-shifted to 4000 s to show the same latency period. The table shows the initial rates extracted from the first 3 data points following irradiation.

Consistent with the trends observed at the 10 s irradiation time, an excess of **MD'M** serves to rapidly increase catalytic activity. The rates measured at the 1 and 2 **MD'M**:1 **VTMS** ratios are 2.5 x and 16.7 x faster respectively, than that measured at the 0.5 **MD'M**:1 **VTMS** ratio. Importantly, the rate at the 2 **MD'M**:1 **VTMS** ratio had already reached 40% conversion by the first measurement, and the significant error is due to there being insufficient data points to yield a linear fit. The times taken to achieve full conversion to the beta product are 2.1×10^4 s (5.8 h), 9.3×10^3 s (2.6 h) and 1.7×10^3 s (0.5 h) for the 0.5, 1 and 2 **MD'M**:**VTMS** ratios, respectively. These times are significantly shorter relative to those in the corresponding experiments at 10 s irradiation (see Figure 4.8), which suggests that longer irradiation times promote the generation of more of the active catalyst. Concordant with the observations at 10 s irradiation, the rate-concentration profiles yield an approximate second order relationship with a linear fit with respect to the **MD'M** concentration ($R^2 = 0.9891$) (Figure 4.11). This is supportive evidence of the

same active species being generated at both 10 and 60 s irradiation, where the latter produces more of it.

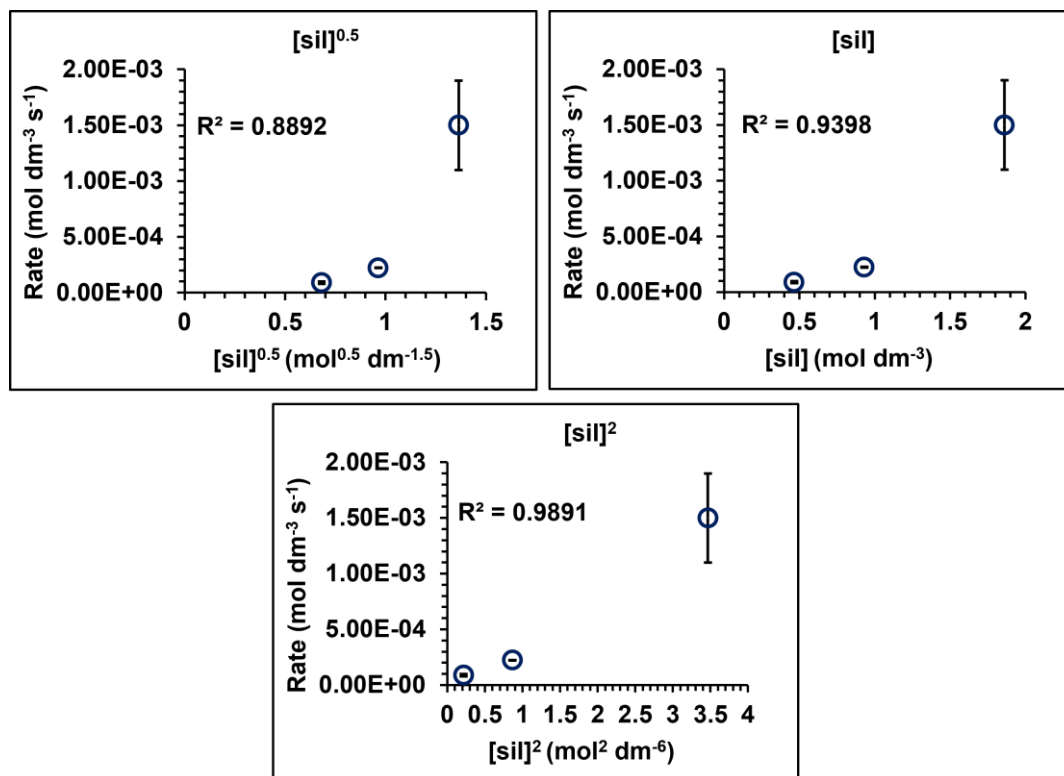
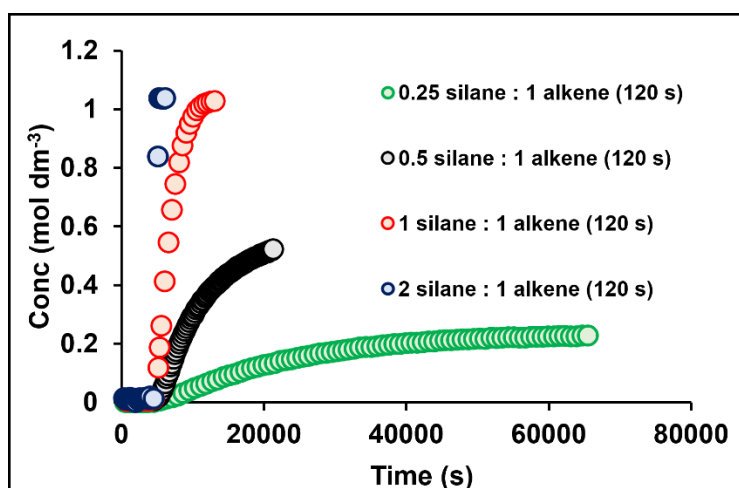


Figure 4.11. Rate-concentration profiles for half, first and second order in **MD'M** using the rates for beta product formation in the hydrosilylation reaction between **MD'M** and **VTMS** with precatalyst **1a**. Reaction conditions as detailed in section 4.3.1, with 60 s irradiation.

To assess whether the positive order in silane was also apparent upon even longer exposure to UV-light, the corresponding experiments were conducted in the same way but irradiated for 120 s. In this case, an additional ratio of 0.25 **MD'M**:1 **VTMS** was used, as it was anticipated that this longer irradiation time would promote faster conversion at the higher **MD'M**:**VTMS** ratios, and this would not provide a sufficient number of data points from which the initial rates could be extracted. The concentration-time profiles and table of initial rates are shown in Figure 4.12.



Ratio	Initial Rate (mol dm ⁻³ s ⁻¹)
0.25 silane : 1 alkene	$(7.4 \pm 0.2) \times 10^{-6}$
0.5 silane : 1 alkene	$(9.3 \pm 0.3) \times 10^{-5}$
1 silane : 1 alkene	$(3.68 \pm 0.06) \times 10^{-4}$
2 silane : 1 alkene	-

Figure 4.12. Concentration-time profiles of beta product formation during the photoactivated hydrosilylation reaction between **MD'M** and **VTMS** using **1a** as a precatalyst. Reaction conditions as detailed in section 4.3.1, with 120 s irradiation. All plots are time-shifted to 4500 s to show the same latency period. The table shows the initial rates extracted from the first 3 data points following irradiation.

As was observed at the 10 and 60 s irradiation times, an excess of **MD'M** promotes faster catalysis. The rates measured at the 0.5 and 1 **MD'M**:1 **VTMS** ratios are 12.6 and 49.7 x faster respectively, than that measured at the 0.25 **MD'M**:1 **VTMS** ratio. The times taken to achieve full conversion are 3.5×10^4 s (9.8 h), 1.7×10^4 s (4.6 h), 5.6×10^3 s (1.5 h) and 7.7×10^2 s (0.2 h) at the 0.25, 0.5, 1 and 2 **MD'M**:1 **VTMS** ratios, respectively. Due to the extremely high catalytic activity at the 2:1 ratio, it was not possible to measure the initial rate. Nonetheless, it follows that a second order relationship with respect to **MD'M** is observed from the 0.25, 0.5 and 1 **MD'M**:1 **VTMS** ratios ($R^2 = 0.9985$) (Figure 4.13). These data imply that the same active species is generated for all three irradiation times.

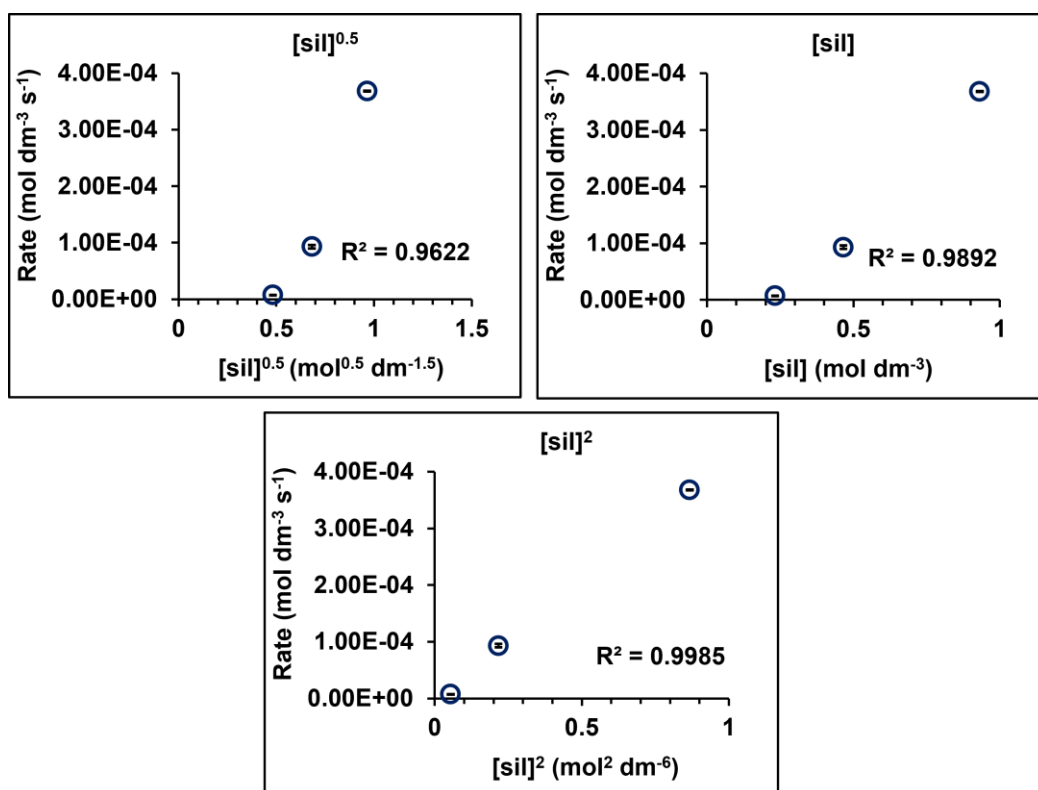


Figure 4.13. Rate-concentration profiles for half, first and second order in **MD'M** using the rates for beta product formation in the hydrosilylation reaction between **MD'M** and **VTMS** with precatalyst **1a**. Reaction conditions as detailed in section 4.3.1, with 120 s irradiation.

4.3.2 Using precatalyst **1b**

To determine whether precatalyst **1b** follows the same reaction kinetics as **1a**, the order in **MD'M** was determined in the same way as described in section 4.3.1, using **1b** as the precatalyst (0.0025 M). The concentration-time profile along with the table of initial rates for the 10 s irradiation time is shown in Figure 4.14.

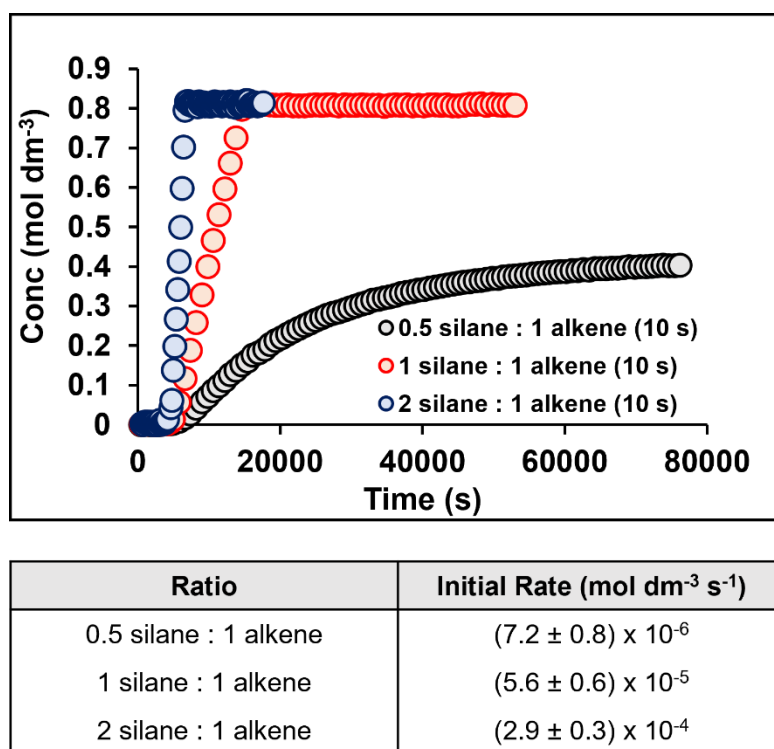


Figure 4.14. Concentration-time profiles of beta product formation during the photoactivated hydrosilylation reaction between **MD'M** and **VTMS** using **1b** as a precatalyst. Reaction conditions as detailed in section 4.3.1, with 10 s irradiation. All plots are time-shifted to 3300 s to show the same latency period. The table shows the initial rates extracted from the first 5 data points following irradiation.

As was demonstrated in the parallel experiments using precatalyst **1a**, it is evident that an increase in **MD'M** concentration concurs with an increase in initial rate for beta product formation when using precatalyst **1b**. The measured initial rate for the 1 and 2 **MD'M**:1 **VTMS** ratios are 7.8 x and 40.3 x faster than that observed at the 0.5 **MD'M**:1 **VTMS** ratio. Concordantly, the times taken to achieve full conversion for the 0.5, 1 and 2 **MD'M** : 1 **VTMS** ratios are 4.36 x 10⁴ s (12.1 h), 1.0 x 10⁴ s (2.9 h) and 3.3 x 10³ s (0.9 h), respectively. The rate-concentration profile illustrates that there is second order with respect to **MD'M** for a linear fit ($R^2 = 0.9992$), which is in good agreement with the results observed using precatalyst **1a** under the same conditions (Figure 4.15). For the concentration-time profile and table of initial rates for the 60 s irradiation time, the reader is referred to the appendix.

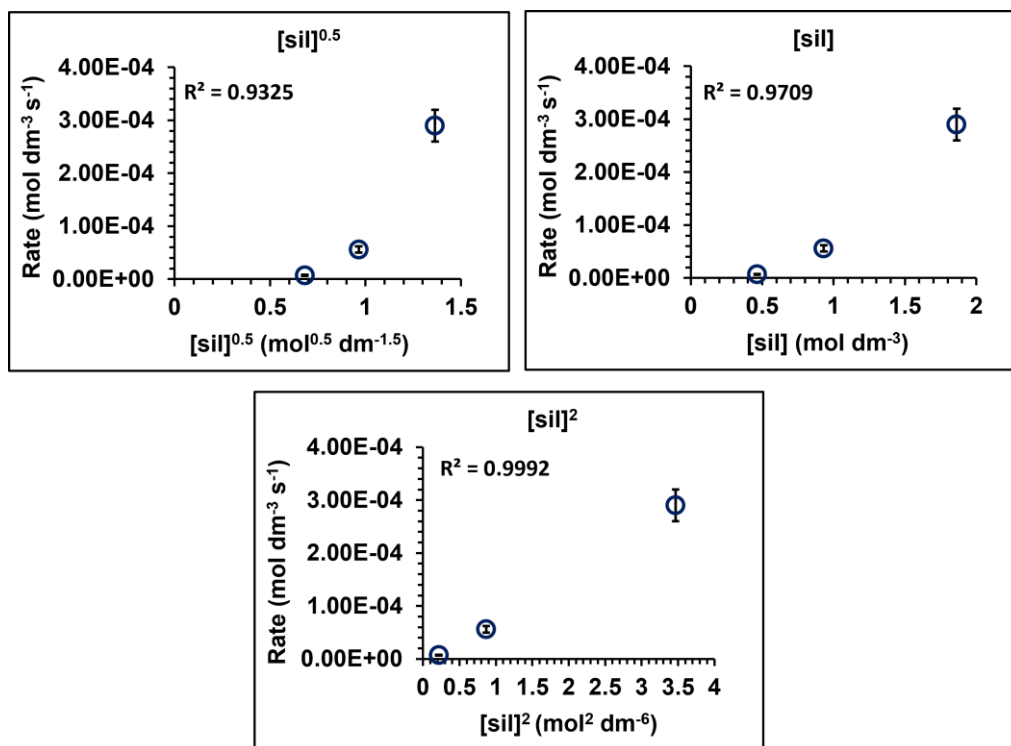
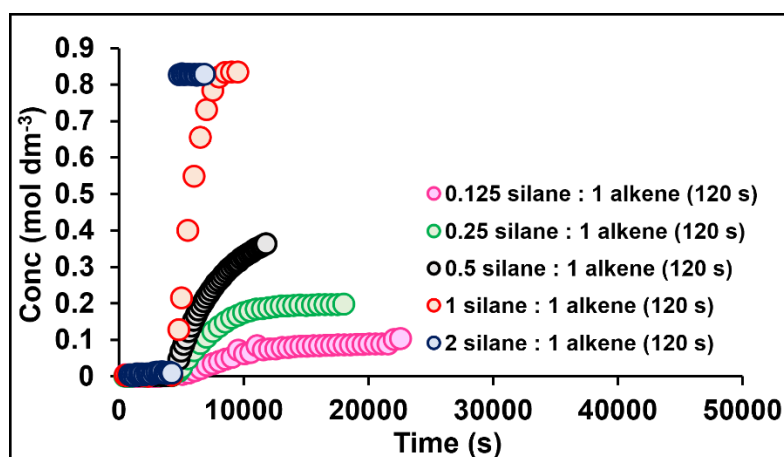


Figure 4.15. Rate-concentration profiles for half, first and second order in **MD'M** using the rates for beta product formation in the hydrosilylation reaction between **MD'M** and **VTMS** with precatalyst **1b**. Reaction conditions as detailed in section 4.3.1, with 10 s irradiation.

To account for the rapid reaction kinetics observed at excess **MD'M** to **VTMS** ratios using 120 s irradiation with **1a**, the range of concentrations was expanded to provide better data density for **1b**. Examining the effect of initial concentration of **MD'M** versus initial rate over a 5-fold range (0.11 M, 0.22 M, 0.44 M, 0.88 M and 1.76 M) whilst keeping the concentration of **VTMS** constant (0.88 M) led to the concentration-time profiles and table of initial rates detailed in Figure 4.16.



Ratio	Initial Rate (mol dm ⁻³ s ⁻¹)
0.125 silane : 1 alkene	$(1.17 \pm 0.1) \times 10^{-5}$
0.25 silane : 1 alkene	$(4.5 \pm 0.1) \times 10^{-5}$
0.5 silane : 1 alkene	$(9.4 \pm 0.2) \times 10^{-5}$
1 silane : 1 alkene	$(5.2 \pm 0.1) \times 10^{-4}$
2 silane : 1 alkene	-

Figure 4.16. Concentration-time profiles of beta product formation during the photoactivated hydrosilylation reaction between **MD'M** and **VTMS** using **1b** as a precatalyst. Reaction conditions (0.0025 M **1b**, 0.11, 0.22, 0.44, 0.88 and 1.76 M **MD'M**, 0.88 M **VTMS** in *d*₂-dichloromethane, left for ~1 h thermally then irradiated 120 s with 365 nm LED, 298 K). All plots are time-shifted to 4200 s to show the same latency period. The table shows the initial rates extracted from the first 5 data points following irradiation.

Compared with the 0.125 **MD'M**:1 **VTMS** ratio, the measured rates are 3.8, 8.0 and 44.7 x faster at the 0.25, 0.5 and 1 **MD'M**:1 **VTMS** ratios, respectively. As was observed when using precatalyst **1a** and irradiating for 120 s, the rapid conversion to the beta product following the latency period does not allow sufficient data points from which the initial rate can be measured. The times taken for full conversion to be achieved are 1.4×10^4 s (3.9 h), 1.0×10^4 s (2.8 h), 6.1×10^3 s (1.7 h), 4.4×10^3 s (1.2 h) and 6.4×10^2 s (0.2 h) for the 0.125, 0.25, 0.5, 1 and 2 **MD'M**:1 **VTMS** ratios, respectively. Consistent with that observed when precatalyst **1a** was used and at the shorter irradiation times for both precatalysts, the rate-concentration profiles yield a good linear fit to second order in **MD'M** ($R^2 = 0.9911$) (Figure 4.17). These results indicate that precatalysts **1a** and **1b** follow the same reaction kinetics. They also provide reassurance of linearity in the $[\mathbf{MD'M}]^2$ plots at low concentrations – especially the 0.125 **MD'M**:1 **VTMS** concentration regime.

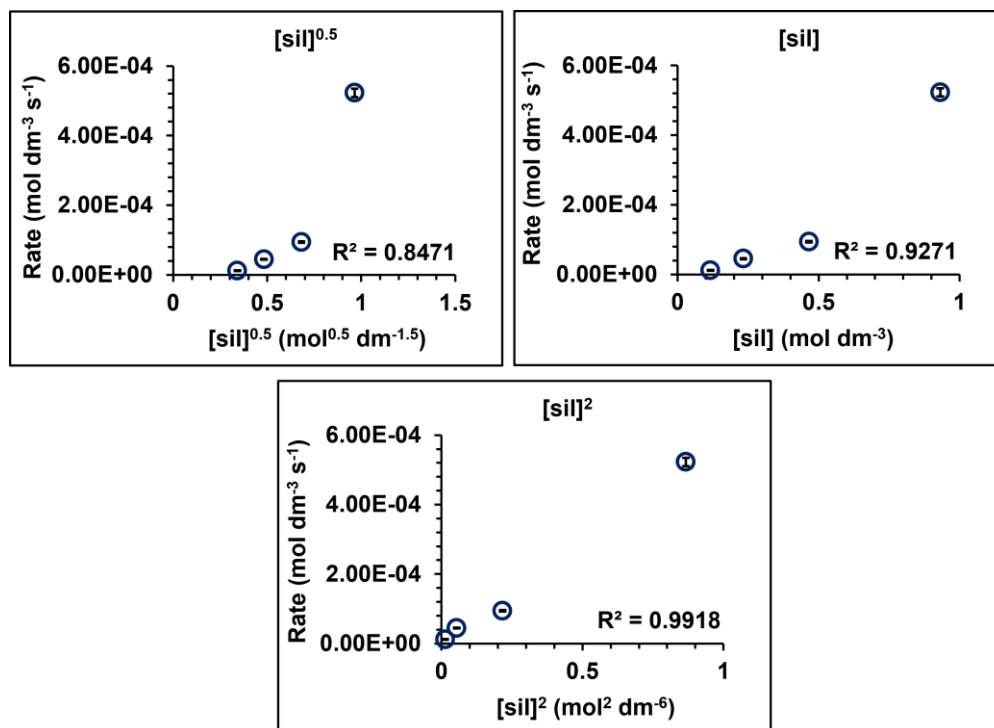


Figure 4.17. Rate-concentration profiles for half, first and second order in **MD'M** using the rates for beta product formation in the hydrosilylation reaction between **MD'M** and **VTMS** with precatalyst **1b**. Reaction conditions (0.0025 M **1b**, 0.11, 0.22, 0.44, 0.88 and 1.76 M **MD'M**, 0.88 M **VTMS** in *d*₂-dichloromethane, left for ~1 h thermally then irradiated 120 s with 365 nm LED, 298 K).

4.3.3 Using precatalyst **1b** at 0.000025 M

To ascertain that the same reaction kinetics were followed at lower catalyst loadings, the effects of varying the initial **MD'M** concentration over a 3-fold range (0.22 M, 0.44 M and 0.88 M) were examined using precatalyst **1b** (0.000025 M). As longer reaction times were anticipated due to the low loadings, the 120 s irradiation time was selected. The concentration-time profiles and table of initial rates are detailed in Figure 4.18.

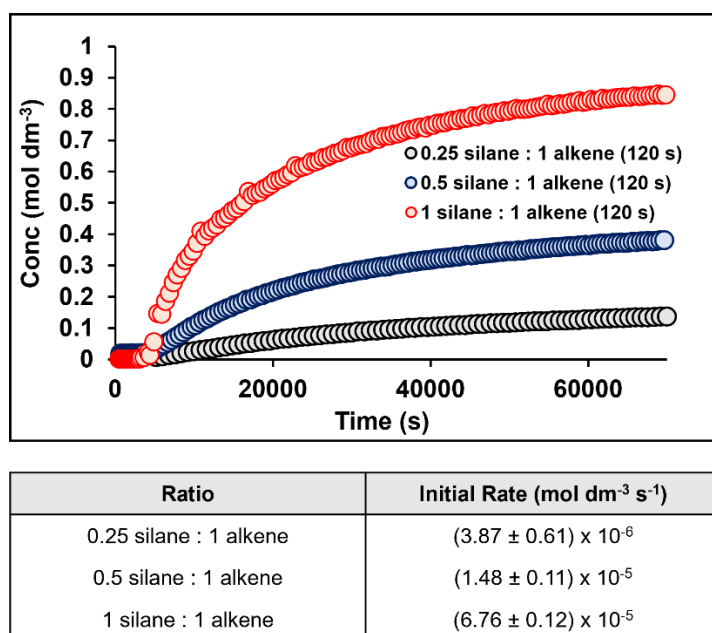


Figure 4.18. Concentration-time profiles of beta product formation during the photoactivated hydrosilylation reaction between **MD'M** and **VTMS** using **1b** as a precatalyst. Reaction conditions as detailed in section 4.3.3. All plots are time-shifted to 3600 s to show the same latency period. The table shows the initial rates extracted from the first 5 data points following irradiation.

In line with the observations when the precatalyst was used at 0.0025 M, an excess of silane results in an augmented initial rate. The measured rates at the 0.5 and 1 **MD'M**:1 **VTMS** ratios are 3.8 x and 17.5 x faster respectively, than that observed for the 0.25 **MD'M**:1 **VTMS** ratio. The times taken to achieve full conversion to the beta product are 5.16×10^4 s (14.3 h), 4.72×10^4 s (13.1 h) and 4.59×10^4 s (12.8 h) for the 0.25, 0.5 and 1 **MD'M**:1 **VTMS** ratios, respectively. It is noteworthy that the ratios with excess **VTMS**, i.e. 0.25 and 0.5 **MD'M**:1 **VTMS**, lead to the slowest turnover, and these rates could be accelerated using an excess of **MD'M**. Notably, using catalyst loadings 100 x less than the experiments reported above does not concur with a measured initial rate that is proportionally lower. Indeed using 0.0025 M precatalyst **1b** with 120 s irradiation, the measured initial rates are $4.5 \pm 0.1 \times 10^{-5}$ mol dm⁻³ s⁻¹, $9.4 \pm 0.2 \times 10^{-5}$ mol dm⁻³ s⁻¹, and $5.2 \pm 0.1 \times 10^{-4}$ mol dm⁻³ s⁻¹, for the 0.25, 0.5 and 1 **MD'M**:1 **VTMS** ratios, respectively (see Figure 4.16). This corresponds to rates that are approximately only 10 x slower at the respective ratios when using **1b** at 0.000025M. Importantly, the rate-concentration profiles depicted in Figure 4.19 demonstrate that there is still apparent second order in **MD'M** with a

linear fit ($R^2 = 0.9992$), which suggests no substantive change in the mechanism. Thus, the $[\text{MD}'\text{M}]^2$ relationship holds over two orders of magnitude precatalyst concentration.

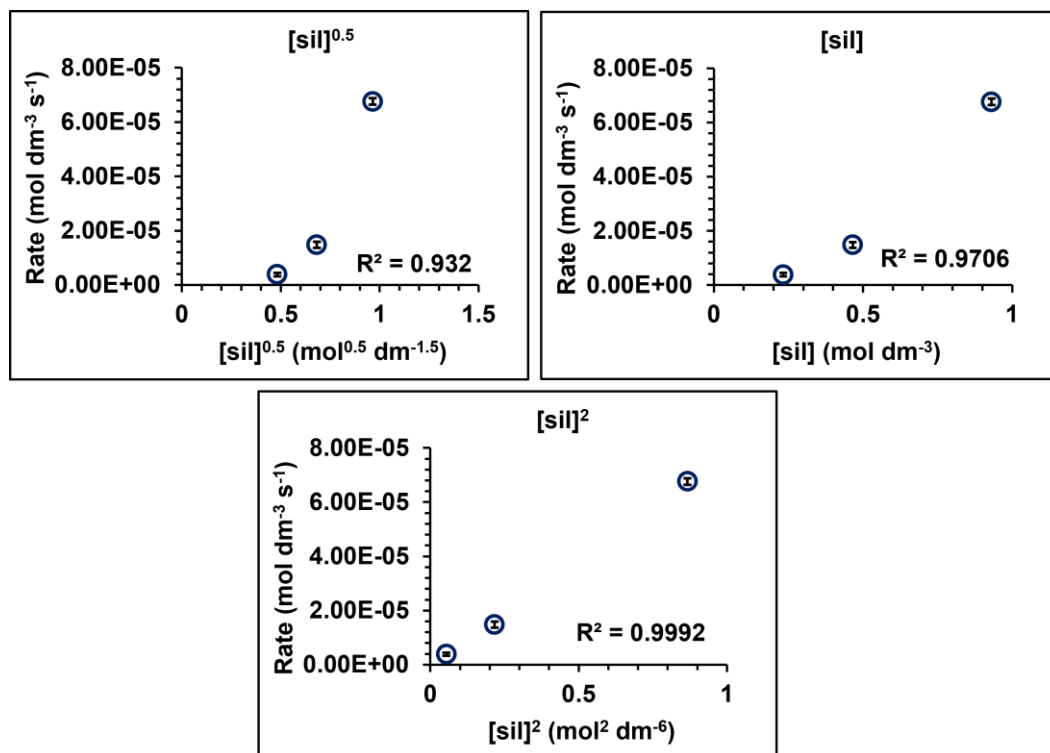
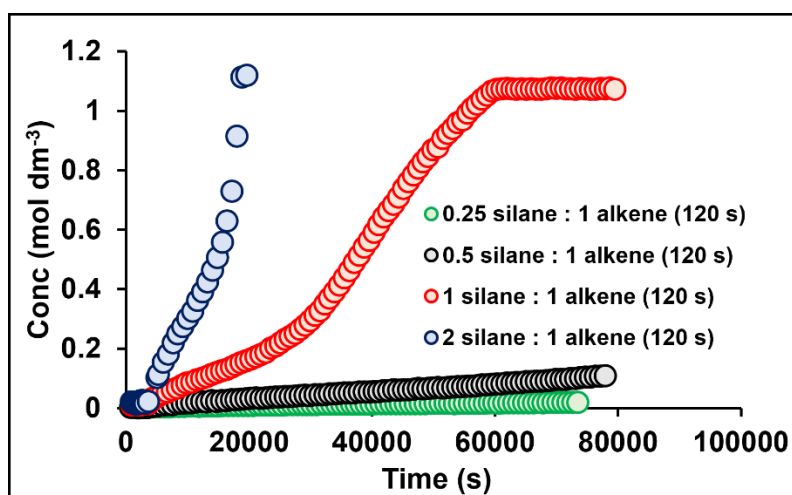


Figure 4.19. Rate-concentration profiles for half, first and second order in **MD'M** using the rates for beta product formation in the hydrosilylation reaction between **MD'M** and **VTMS** with precatalyst **1b**. Reaction conditions as detailed in section 4.3.3.

4.3.4 Using precatalyst **1b** with vinyltrimethoxysilane as the alkene substrate

In an effort to determine whether the observed reaction kinetics regarding the order with respect to **MD'M** were also observed with different alkene substrates, the effects of varying the **MD'M** concentration over a 4-fold range (0.25 M, 0.5 M, 1.1 M and 2.2 M) with a fixed concentration of vinyltrimethoxysilane (**VTMOS**) (1.1 M) were examined. For all experiments, precatalyst **1b** was used at 0.0025 M. The concentration-time profiles along with the table of initial rates are detailed in Figure 4.20.



Ratio	Initial Rate (mol dm ⁻³ s ⁻¹)
0.25 silane : 1 alkene	$(3.9 \pm 0.3) \times 10^{-7}$
0.5 silane : 1 alkene	$(2.2 \pm 0.4) \times 10^{-6}$
1 silane : 1 alkene	$(8.8 \pm 0.3) \times 10^{-6}$
2 silane : 1 alkene	$(4.4 \pm 0.1) \times 10^{-5}$

Figure 4.20. Concentration-time profiles of beta product formation during the photoactivated hydrosilylation reaction between **MD'M** and **VTMOS** using **1b** as a precatalyst. Reaction conditions as detailed in section 4.3.4, with 120 s irradiation. All plots are time-shifted to 3000 s to show the same latency period. The table shows the initial rates extracted from the first 5 data points following irradiation.

Following suit with that observed when **VTMS** was employed as the alkene substrate, an excess of **MD'M** also effects faster catalytic activity in the presence of **VTMOS**. Compared with the 0.25 **MD'M**:1 **VTMOS** ratio, the measured initial rates are 5.6 x, 22.7 x and 113.7 x faster at the 0.5, 1 and 2 **MD'M**:1 **VTMOS** ratios, respectively. Notably, at the 1 and 2 **MD'M**:1 **VTMS** ratios, the profile is characterised by slower catalytic activity up to ~50% conversion, followed by a marked burst of high catalytic activity. For the 2 **MD'M**:1 **VTMS** ratio, the measured rate of the final 3 data points is $2.40 \pm 0.05 \times 10^{-4} \text{ mol dm}^{-3} \text{ s}^{-1}$. This represents an increase in the rate by 5.5 x compared to the initial rate, which could be attributed to the very low concentrations of **VTMOS** available at this point in the reaction, since high concentrations of alkene have been reported to be inhibitory for hydrosilylation catalysis (see later in this chapter).^{2,188} This also reflects that the rate of catalysis increases as the substates become enriched in silane with each turnover.

Compared to the corresponding experiments using **VTMS**, the initial rates show that catalytic activity is 116.6 x, 43.3 x and 59.8 x slower when **VTMOS** is used as the alkene substrate at the respective 0.25, 0.5 and 1 **MD'M**:1 **VTMS** / **VTMOS** ratios (see Figure 4.16). Concordantly, the times taken to achieve full conversion with the **VTMOS** substrate are 5.73×10^4 s (15.9 h) and 1.6×10^4 s (4.4 h), compared with 4.4×10^3 s (1.2 h) and 6.4×10^2 s (0.2 h) when **VTMS** is used at the 1 and 2 **MD'M**:1 **VTMS** / **VTMOS** ratios, respectively. Due to very low activity, the experiments at the 0.25 and 0.5 **MD'M**:1 **VTMS** ratios were stopped before full conversion was achieved. In spite of the slower reaction kinetics, the rate-concentration profiles still return the best linear fit for second order with respect to **MD'M** ($R^2 = 0.9979$), consistent with that observed when **VTMS** is used as the alkene substrate (Figure 4.21).

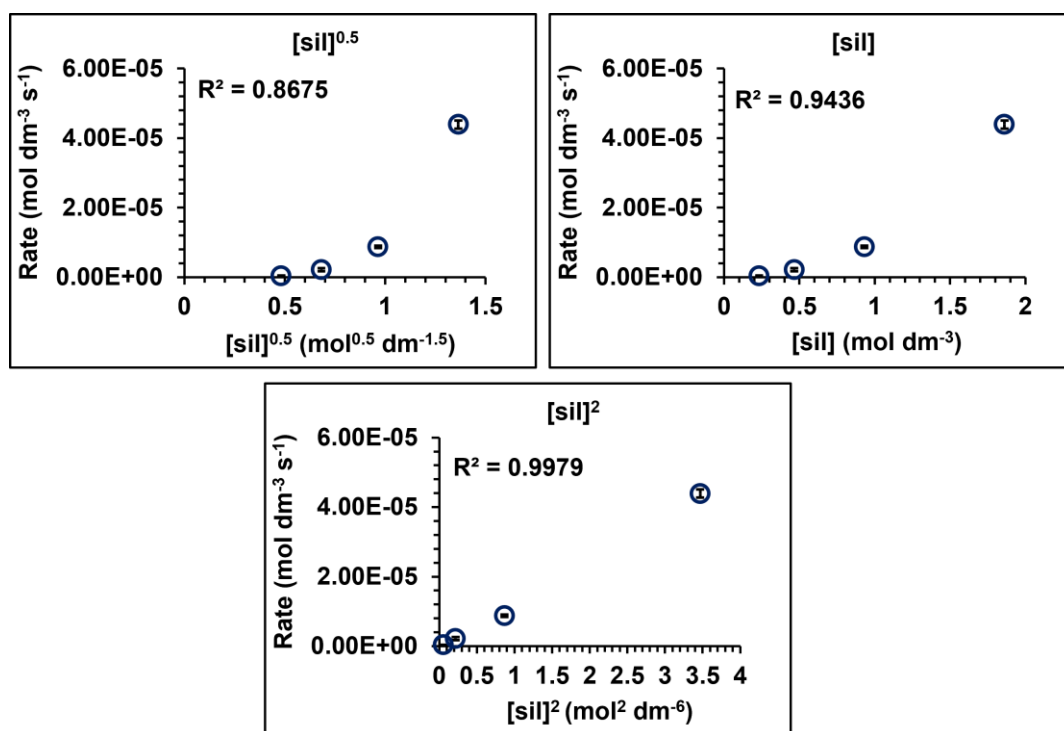


Figure 4.21. Rate-concentration profiles for half, first and second order in **MD'M** using the rates for beta product formation in the hydrosilylation reaction between **MD'M** and **VTMOS** with precatalyst **1b**. Reaction conditions as detailed in section 4.3.4, with 120 s irradiation.

Results from Kühn, Osborn and Elsevier have shown that the nature of the alkene substrate is a key factor in determining the stability and the hydrosilylation activity of a variety of Pt(0) complexes, including Karstedt's catalyst.^{2,38,189} It has become widely accepted from these studies that decoordination of an alkene moiety is key for generating the active catalyst. If the same principle applies for the active catalyst generated from precatalyst **1b**, it would be expected that **VTMOS** has an enhanced coordination ability to the metal centre compared to **VTMS**. This is due to **VTMS** providing more electron density to the Pt centre than **VTMOS**, which in turn means that **VTMS** is a poorer π -backbonder than **VTMOS** (Figure 4.22). Analysis of CO stretches in $\text{Fe}(\text{CO}_4)(\text{vinylsilane})$ complexes support this idea.¹⁹⁰ The enhanced binding strength of **VTMOS** could account for the lower hydrosilylation activity observed when **VTMOS** is used as the alkene substrate.

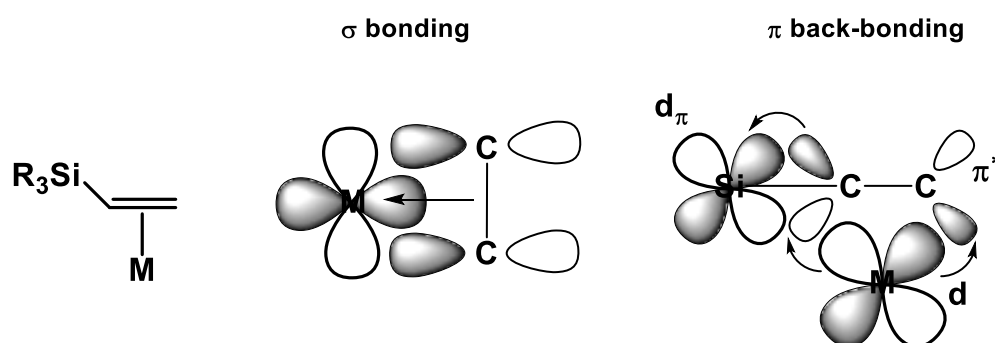


Figure 4.22. Bonding of vinylsilanes to metal centres.

4.3.5 Recharging using precatalyst **1a**

To ascertain whether the catalyst decomposes during the reaction, and to determine whether the photoactivated catalyst remains active without further irradiation, a series of recharge experiments were conducted. The in-situ ^1H NMR experiment was repeated using the same conditions as described in section 4.3.1 (0.0025 M **1a**, 0.25 M, 0.5 M, and 1.0 M **MD'M**, 1.0 M **VTMS** in d_2 -dichloromethane) but stopped after complete conversion of **MD'M** and **VTMS** was observed and then a fresh batch of the same stock solution was added in to the reaction mixture.

Importantly, the 120 s irradiation time was selected so that the recharge could be conducted on the same day as the first charge (to prevent possible change / decomposition of the catalyst overnight) and the sample was only irradiated after the ~1 h latency period with no further irradiation upon recharging. The concentration of beta product was monitored by in-situ ^1H NMR spectroscopy during the entire experiment and the initial rate of the recharge was calculated using the first 5 data points following the re-charge (Figure 4.23).

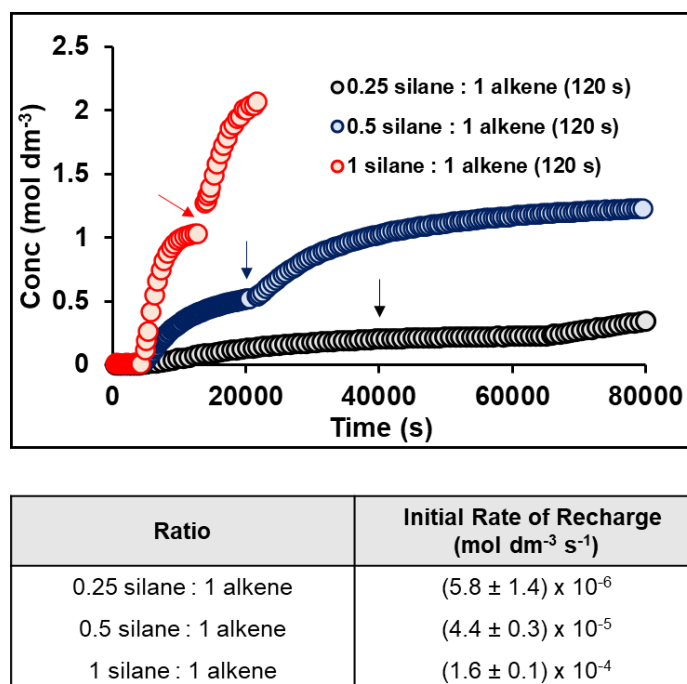


Figure 4.23. Concentration-time profiles of beta product formation during the photoactivated hydrosilylation reaction using **1a** between **MD'M** and **VTMS** with a recharge of the same amount of **MD'M** and **VTMS** after completion. Reaction conditions as detailed in section 4.3.5. All plots are time-shifted to 4200 s to show the same latency period. The table shows the initial rates extracted from the first 5 data points following the recharge.

Addition of a successive batch of **MD'M** (0.25 M 0.5 M or 1.0 M) and **VTMS** (1.0 M) to the catalysis solution post hydrosilylation resulted in full consumption of substrates and conversion to the beta product, demonstrating that the catalyst remains active. The initial rates of the recharge are 1.3, 2.1 and 2.3 x slower than the first charge at the 0.25, 0.5 and 1 **MD'M:VTMS** ratios, respectively (see Figure 4.12). This could be attributed to the slight dilution of the active

catalyst upon recharging with the stock solution. The formation of catalytically active nanoparticles may also become significant upon catalyst aging.

Attempts were made to plot the initial rate of the recharge against the concentration of the beta product, but this did not return an acceptable fit for half, first or second order in **MD'M**. This could be due to a contribution of catalytic activity from nanoparticles, which were observed in the post-catalysis mixture by TEM (see Figure 4.6).

4.3.6 Recharging using precatalyst **1b**

The series of recharge experiments were also conducted using precatalyst **1b** under the same conditions detailed in section 4.3.5, but over a 4-fold concentration range (0.0025 M **1b**, 0.125 M, 0.25 M, 0.5 M and 1.0 M **MD'M**, 1.0 M **VTMS** in d_2 -dichloromethane). Figure 4.24 depicts the concentration-time profiles along with the table of initial rates from the recharge.

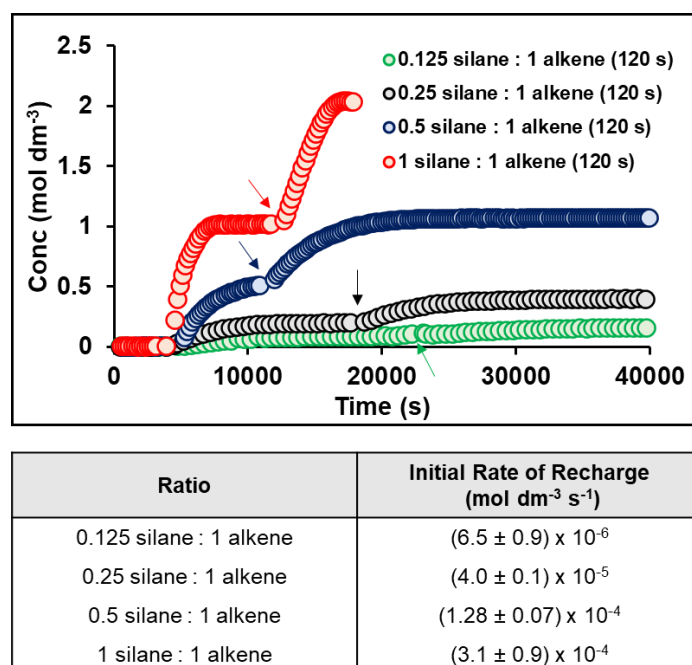


Figure 4.24. Concentration-time profiles of beta product formation during the photoactivated hydrosilylation reaction using **1b** between **MD'M** and **VTMS** with a recharge of the same amount of **MD'M** and **VTMS** after completion. Reaction conditions as detailed in section 4.3.6. All plots are time-shifted to 3900 s to show the same latency period. The table shows the initial rates extracted from the first 5 data points following the recharge.

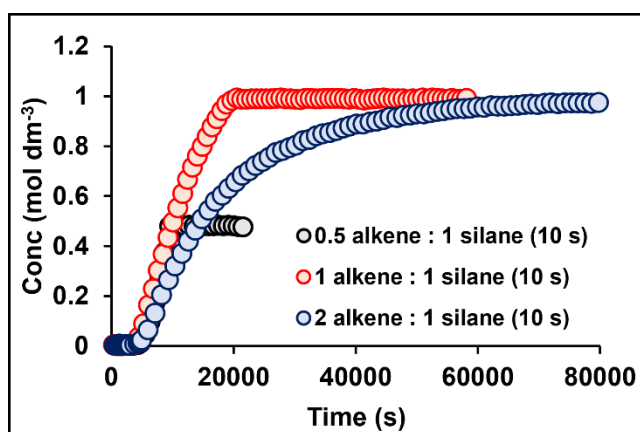
Evidently, the catalyst generated from precatalyst **1b** upon irradiation remains active after the first batch of **MD'M** and **VTMS** have been consumed. The initial rates of the recharges are 1.8, 1.1 and 1.7 x slower compared to the first charges at the 0.125, 0.25 and 1 **MD'M**:1 **VTMS** ratios, respectively (see Figure 4.16). For the 0.5 **MD'M**:1 **VTMS** ratio, the initial rate of the recharge is 1.4 x faster than that which was observed upon the first charge.

Similar attempts were made to plot the initial rate of the recharge against the concentration of the beta product, but this again, did not return an acceptable fit for half, first or second order in **MD'M**. This could be attributed to nanoparticles contributing to the catalytic activity.

4.4 Determining order in alkene

4.4.1 Using precatalyst **1a**

To analyse the effect of the concentration of **VTMS** on the model reaction, parallel experiments to those described in section 4.3 were carried out but at a fixed concentration of **MD'M** (1.0 M) and a 3-fold range of **VTMS** concentrations (0.5 M 1.0 M and 2.0 M) using precatalyst **1a** (0.0025 M). The concentration-time profiles along with the table of initial rates for the 10 s irradiation time are detailed in Figure 4.25.



Ratio	Initial Rate (mol dm ⁻³ s ⁻¹)
0.5 alkene : 1 silane	$(1.03 \pm 0.08) \times 10^{-4}$
1 alkene : 1 silane	$(8.7 \pm 0.1) \times 10^{-5}$
2 alkene : 1 silane	$(5.9 \pm 0.2) \times 10^{-5}$

Figure 4.25. Concentration-time profiles of beta product formation during the photoactivated hydrosilylation reaction between **MD'M** and **VTMS** using **1a** as a precatalyst. Reaction conditions as detailed in section 4.4.1, with 10 s irradiation. All plots are time-shifted to 4500 s to show the same latency period. The table shows the initial rates extracted from the first 5 data points following irradiation.

It transpires that there is a negative order with respect to **VTMS** since an excess of this substrate returns an inhibitory effect on catalysis. This is the opposite of what was observed when an excess of **MD'M** to **VTMS** was used. Indeed, the measured rates at the 1 and 2 **VTMS**:1 **MD'M** ratios are 1.2 and 1.7 x slower respectively, than that observed at the 0.5 **VTMS**:1 **MD'M** ratio. The effect is, however, much less pronounced than when catalysis is performed in the presence of an excess of **MD'M**. The rate-concentration profiles depicted in Figure 4.26 show that the best linear fit is obtained for a first order decay with respect to **VTMS** ($R^2 = 0.9988$).

The notion that alkene substrates have an inhibitory effect on hydrosilylation has been recently reported by Kühn and colleagues, who demonstrated a negative order with respect to oct-1-ene in the hydrosilylation reaction with HSiCl_3 using Karstedt's catalyst.² Earlier work using Karstedt's catalyst by Stein et al., has also shown that having excess silane accelerates the reaction compared to the reaction having equimolar or excess alkene.¹⁸⁸ They reported that reaction

between **MD'M** and vinylsilane was conducted at 2:1, 1:1 and 1:2 ratios, and the slowest rate was observed for the latter ratio.

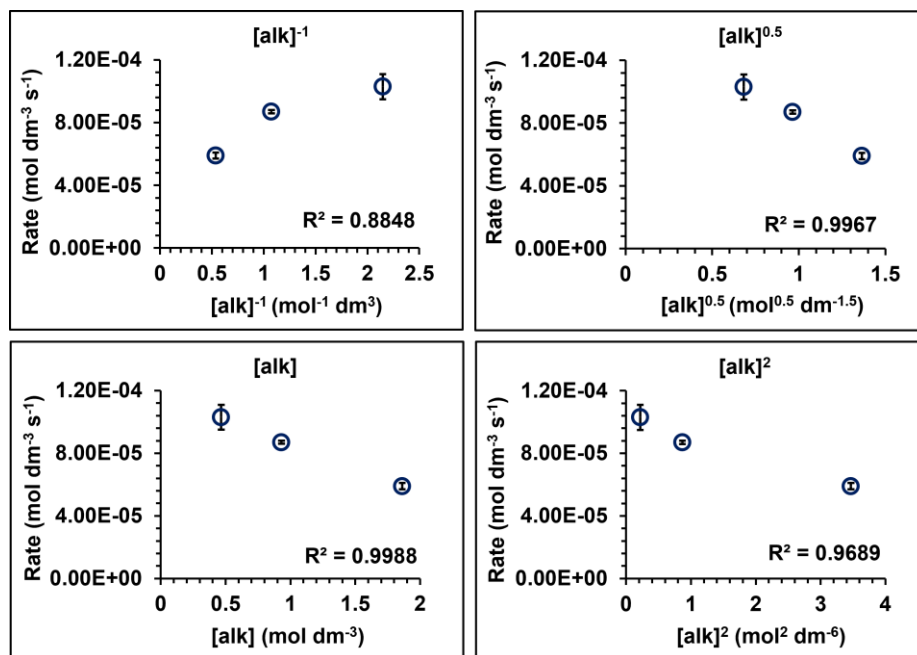
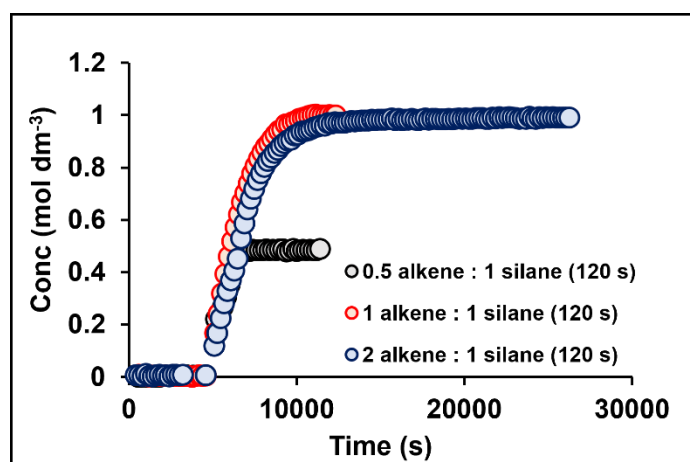


Figure 4.26. Rate-concentration profiles for negative first, half, first and second order in **VTMS** using the rates for beta product formation in the hydrosilylation reaction between **MD'M** and **VTMS** with precatalyst **1a**. Reaction conditions as detailed in section 4.4.1, with 10 s irradiation.

To ascertain that an inhibitory effect of **VTMS** was observed at longer irradiation times, the corresponding experiments were conducted under the same conditions, but irradiated for either 60 or 120 s. The concentration-time profile for the 120 s irradiation time is detailed in Figure 4.27. For the profiles obtained at 60 s irradiation, the reader is referred to the appendix.



Ratio	Initial Rate (mol dm ⁻³ s ⁻¹)
0.5 alkene : 1 silane	$(5.5 \pm 0.2) \times 10^{-4}$
1 alkene : 1 silane	$(3.68 \pm 0.06) \times 10^{-4}$
2 alkene : 1 silane	$(2.66 \pm 0.05) \times 10^{-4}$

Figure 4.27. Concentration-time profiles of beta product formation during the photoactivated hydrosilylation reaction between **MD'M** and **VTMS** using **1a** as a precatalyst. Reaction conditions as detailed in section 4.4.1, with 120 s irradiation. All plots are time-shifted to 4500 s to show the same latency period. The table shows the initial rates extracted from the first 5 data points following irradiation.

In accordance with the trend observed at the 10 s irradiation time, excess **VTMS** results in attenuation of catalytic activity at the 120 s irradiation time. Compared with the initial rate measured at the 0.5 **MD'M**:1 **VTMS** ratio, the rates are 1.5 and 2.1 x slower at the 1 and 2 **VTMS**:1 **MD'M** ratios, respectively. The rate-concentration profiles deliver the best linear fit for negative first order with respect to **VTMS** ($R^2 = 0.9992$) (Figure 4.28).

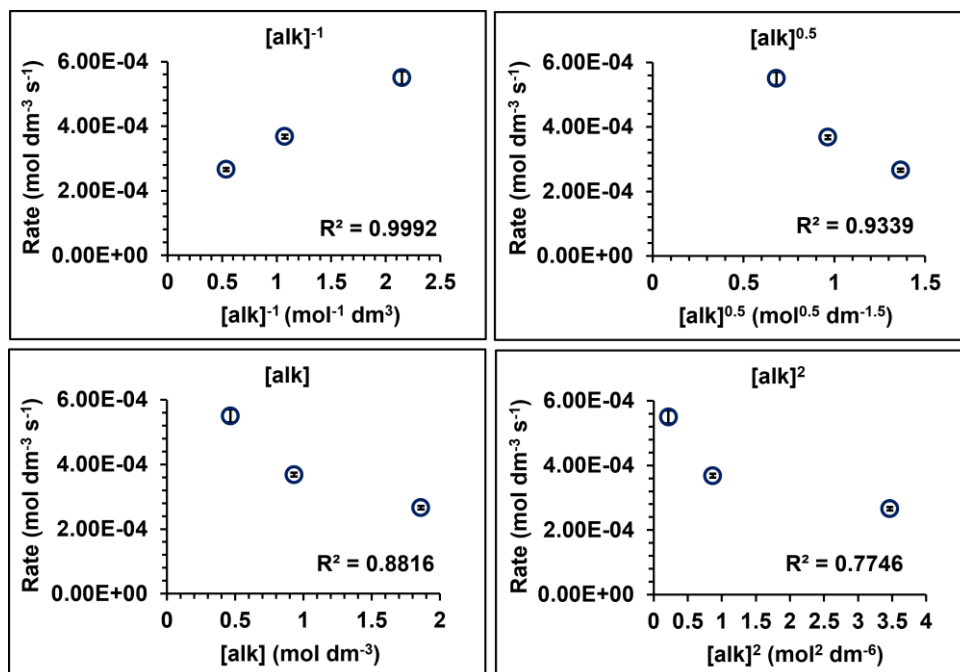
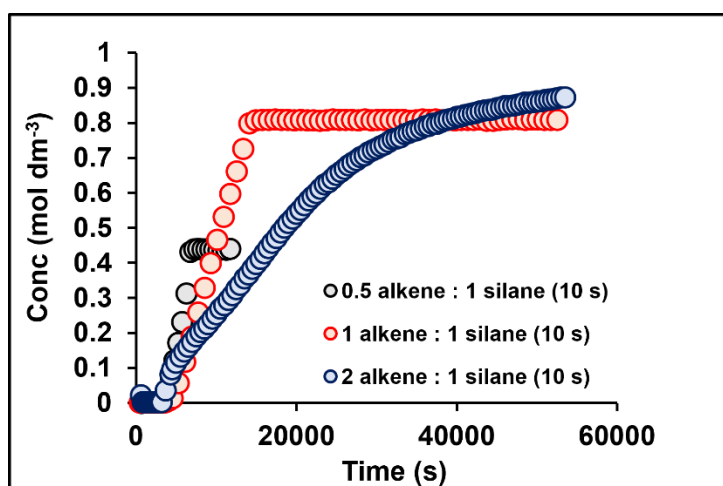


Figure 4.28. Rate-concentration profiles for negative first, half, first and second order in **VTMS** using the rates for beta product formation in the hydrosilylation reaction between **MD'M** and **VTMS** with precatalyst **1a**. Reaction conditions as detailed in section 4.4.1, with 120 s irradiation.

4.4.2 Using precatalyst **1b**

To confirm that **VTMS** also exerted an inhibitory effect on the active catalyst generated upon irradiation of precatalyst **1b**, the same experiments as described in section 4.4.1 were performed using precatalyst **1b** (0.0025 M) with 10 and 120 s irradiation, over a 3-fold concentration range (0.44 M, 0.88 M and 1.76 M **VTMS**). A fixed concentration of **MD'M** was used (0.88 M). The concentration-time profiles for the 10 s irradiation time are shown in Figure 4.29.



Ratio	Initial Rate (mol dm ⁻³ s ⁻¹)
0.5 alkene : 1 silane	$(1.1 \pm 0.2) \times 10^{-4}$
1 alkene : 1 silane	$(5.6 \pm 0.6) \times 10^{-5}$
2 alkene : 1 silane	$(3.5 \pm 0.3) \times 10^{-5}$

Figure 4.29. Concentration-time profiles of beta product formation during the photoactivated hydrosilylation reaction between **MD'M** and **VTMS** using **1b** as a precatalyst. Reaction conditions as detailed in section 4.4.2, with 10 s irradiation. All plots are time-shifted to 3200 s to show the same latency period. The table shows the initial rates extracted from the first 5 data points following irradiation.

Evidently the inhibitory effect of **VTMS** persists with the use of precatalyst **1b**. In comparison to the 0.5 **VTMS**:1 **MD'M** ratio, the rates are 2.0 and 3.2 x slower at the 1 and 2 **VTMS**:1 **MD'M** ratios, respectively. The best linear fit in the rate-concentration profile concurs with negative first order with respect to **VTMS** ($R^2 = 0.9929$) (Figure 4.30). For the corresponding concentration-time profile at 120 s irradiation, the reader is referred to the appendix, but a negative order in **VTMS** is also observed at this irradiation time.

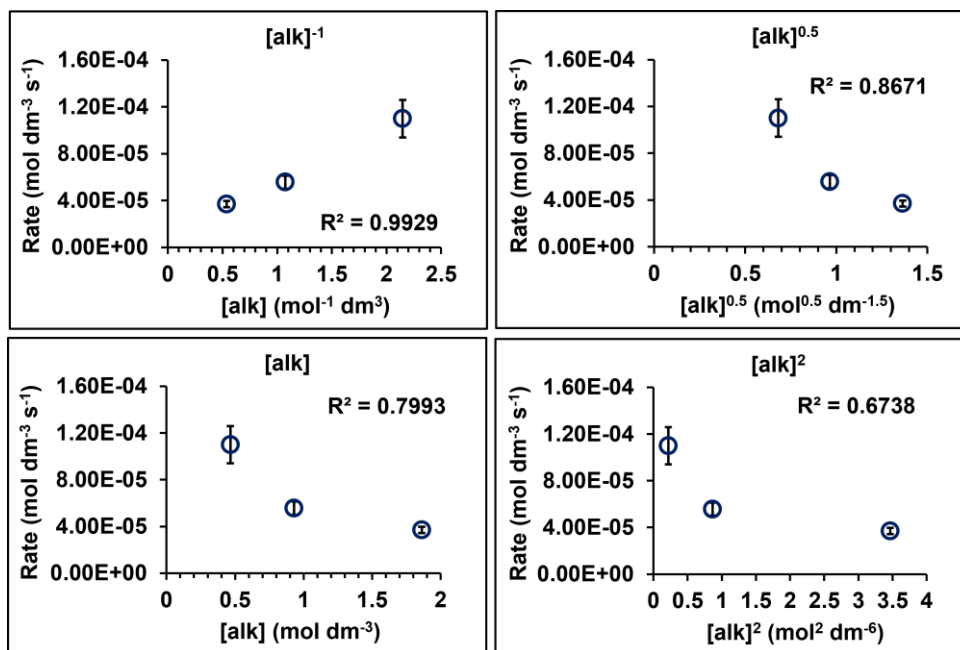


Figure 4.30. Rate-concentration profiles for negative first, half, first and second order in **VTMS** using the rates for beta product formation in the hydrosilylation reaction between **MD'M** and **VTMS** with precatalyst **1b**. Reaction conditions as detailed in section 4.4.2, with 10 s irradiation.

4.5 Adding substrates before and after irradiation

To probe whether the active catalyst released from precatalyst **1a** upon irradiation is formed in the absence of the **MD'M** and **VTMS** substrates, a simple experiment was conducted where the precatalyst was irradiated for 10 s in the absence of **MD'M** and **VTMS**, which were then added to the reaction mixture post-irradiation. A second aim was to determine which substrate, if any, plays a more important role in forming the active catalyst. This was examined by irradiating the precatalyst plus one substrate for 10 s with the 365 nm LED, followed by addition of the partner substrate post-irradiation. For all experiments in this series, precatalyst **1a** was used (0.0025 M) and the initial concentrations of **MD'M** and **VTMS** were 0.95 – 1.0 M. The concentration of the beta product forming over time was monitored by in-situ ¹H NMR spectroscopy as depicted in Figure 4.31 and the kinetics were probed using the initial rates method, monitoring the rate of beta product formation for the first 5 data points after catalytic activity had been established

(Table 4.1). Errors were calculated using the linear regression model (LINEST) in Microsoft Excel.

The reported errors are the estimated standard error from the model.

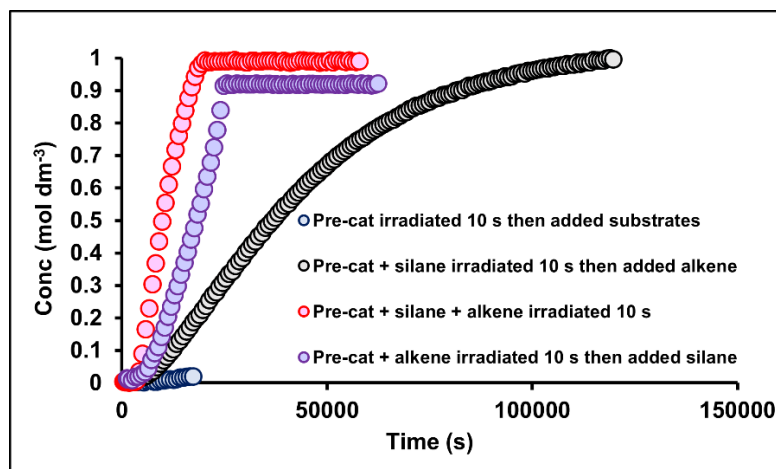


Figure 4.31. Concentration-time profiles of beta product formation during the photoactivated hydrosilylation reaction between **MD'M** and **VTMS** using precatalyst **1a**. Reaction conditions as detailed in section 4.5. Blue: precatalyst **1a** irradiated 10 s then added **MD'M** and **VTMS**, black: precatalyst **1a** and **MD'M** irradiated 10 s then added **VTMS**, pink: precatalyst **1a**, **MD'M** and **VTMS** irradiated 10 s, purple: precatalyst **1a** and **VTMS** irradiated 10 s then added **MD'M**.

This series of experiments revealed two very significant findings: 1) both **MD'M** and **VTMS** are required to form the active catalyst from precatalyst **1a**, hence the lack of activity observed after $\sim 1.7 \times 10^4$ s (4.7 h) when the precatalyst is irradiated in the absence of both substrates. 2) Despite both being required, **VTMS** plays a more significant role in forming the active catalyst than **MD'M**. Remarkably, when the precatalyst and **VTMS** are irradiated together prior to the addition of **MD'M**, the rate is 2.3 x faster than in the complementary experiment where the precatalyst and **MD'M** are irradiated together prior to the addition of **VTMS**. The significance of having the precatalyst irradiated in the presence of both **MD'M** and **VTMS** is evidenced by the 3-fold increase in rate compared to when only the precatalyst and **VTMS** are involved in the irradiation step.

Table 4.1. Initial rates extracted from the first 5 data points following irradiation in the hydrosilylation reaction between **MD'M** and **VTMS** using **1a** as a precatalyst. Reaction conditions as detailed in section 4.5.

Order of addition	Initial Rate (mol dm ⁻³ s ⁻¹)
Pre-cat irradiated 10 s then added substrates	-
Pre-cat and silane irradiated 10 s then added alkene	(1.25 ± 0.05) × 10 ⁻⁵
Pre-cat, silane and alkene irradiated 10 s	(8.7 ± 0.1) × 10 ⁻⁵
Pre-cat and alkene irradiated 10 s then added silane	(2.9 ± 0.12) × 10 ⁻⁵

In spite of **VTMS** exerting an overall inhibitory effect on catalytic activity, it clearly plays a very active role in the conversion of the precatalyst to the active catalyst. As discussed in chapter one, the complexity of the kinetics of the hydrosilylation reaction coupled with the elusive nature of the intermediates has made identification of the active species incredibly difficult for almost sixty years. The conclusions reached by Stein, Lewis et al.¹⁹, and Roy et al.¹⁸³, were that the active species contained Pt–Si and Pt–alkene bonds (Figure 4.32). More recently, Kühn expanded on the principles evoked by this earlier work and suggested that the identity of the active species is dependent on the binding strength of the alkene (see Scheme 4.3).² The results presented here using precatalyst **1a** are supportive of the active catalyst species bearing a resemblance to either of those proposed by Stein, Lewis, Roy and Kühn, although the exact composition and structure remain to be resolved.

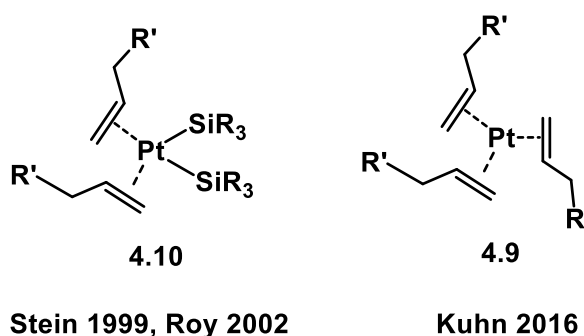
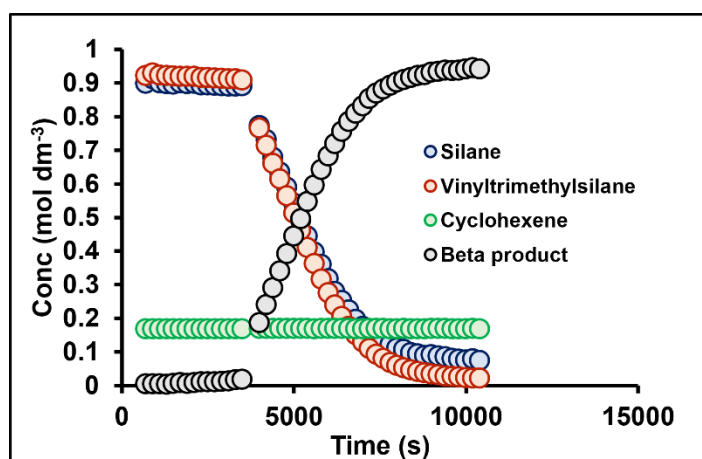


Figure 4.32. Proposed (generic) structures of the active catalyst species in platinum-catalysed hydrosilylation according to the literature.^{2,19,183} Kühn noted that addition spectator ligands should be thought of as part of the species denoted as [Pt].

4.6 Effect of alkene on the active species

The notion that **VTMS** competes for metal sites with **MD'M** was suggested by the preceding results; therefore, cyclohexene, *trans*-2-octene and norbornadiene, substrates known to be reluctant to undergo hydrosilylation in the model system (see chapter 3), were added to the reaction with **MD'M** and **VTMS**, to probe their role as inhibitors. For all experiments in this series, precatalyst **1b** was used (0.0025 M) and the initial concentrations of **MD'M** and **VTMS** were 0.8 – 1.1 M. The relevant alkene was added in at the same time as the **MD'M** and **VTMS** (0.15 M cyclohexene, 0.09 M *trans*-2-octene, 0.14 M norbornadiene), and then the sample was inserted into the spectrometer for ~1 h to monitor the latency period, before being irradiated for 120 s with the 365 nm LED. The sample was then returned to the spectrometer and the concentration of beta product forming over time was monitored by in-situ ¹H NMR spectroscopy. The kinetics were probed using the initial rates method, monitoring the rate of beta product formation for the first 5 data points after catalytic activity had been established. Errors were calculated using the linear regression model (LINEST) in Microsoft Excel. The reported errors are the estimated standard error from the model. The concentration-time profile for the sample with doped-in cyclohexene is detailed in Figure 4.33, along with the table of initial rates to compare to the rate observed in the absence of cyclohexene.



Ratio	Initial Rate (mol dm ⁻³ s ⁻¹)
1 Si-H : 1 vinyltrimethylsilane : 0.15 cyclohexene	$(2.54 \pm 0.02) \times 10^{-4}$
1 Si-H : 1 vinyltrimethylsilane	$(5.2 \pm 0.1) \times 10^{-4}$

Figure 4.33. Concentration-time profiles of beta product formation and **MD'M** and **VTMS** consumption during the photoactivated hydrosilylation reaction between **MD'M** and **VTMS** with cyclohexene doped in. Reaction conditions as detailed in section 4.6.

The addition of 0.15 M cyclohexene proved to dramatically slow down the rate of hydrosilylation, but still reached completion. Indeed, the rate is 2.1 x slower than that observed in the absence of cyclohexene ($5.2 \pm 0.1 \times 10^{-4} \text{ mol dm}^{-3} \text{ s}^{-1}$ compared to $2.54 \pm 0.02 \times 10^{-4} \text{ mol dm}^{-3} \text{ s}^{-1}$). Furthermore, no hydrosilylation of the cyclohexene substrate is observed. The slower rate observed in the presence of cyclohexene could be attributed to this latter substrate competing for binding sites on the metal centre. This implies that the active species released from precatalyst **1b** in the hydrosilylation reaction between **MD'M** and **VTMS** has similarities to that proposed by Kühn (Figure 4.34).²

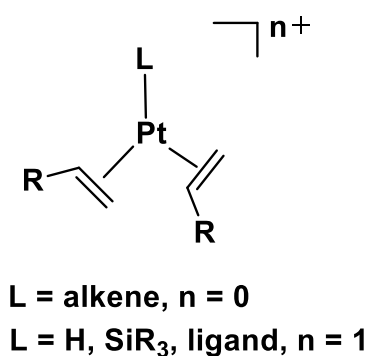
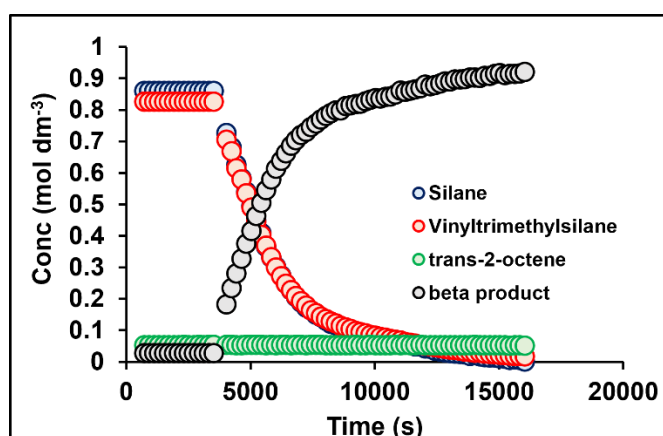


Figure 4.34. Proposed active species formed from precatalyst **1b** in the hydrosilylation reaction between **MD'M** and **VTMS**. Spectator ligands should be thought of as part of the species denoted as [Pt].

In a similar fashion, 0.09 M *trans*-2-octene was added into the reaction mixture with **MD'M** and **VTMS**. The concentration-time profile and table of initial rates are shown in Figure 4.35.



Ratio	Initial Rate (mol dm ⁻³ s ⁻¹)
1 Si-H : 1 vinyltrimethylsilane : 0.09 <i>trans</i> -2-octene	$(2.40 \pm 0.03) \times 10^{-4}$
1 Si-H : 1 vinyltrimethylsilane	$(5.2 \pm 0.1) \times 10^{-4}$

Figure 4.35. Concentration-time profiles of beta product formation and **MD'M** and **VTMS** consumption during the photoactivated hydrosilylation reaction between **MD'M** and **VTMS** with *trans*-2-octene doped in. Reaction conditions as detailed in section 4.6.

In accordance with that observed when cyclohexene was added into the reaction mixture, the addition of 0.09 M *trans*-2-octene proved to slow down catalysis by 2.2 x compared with the corresponding experiment in the absence of *trans*-2-octene ($5.2 \pm 0.1 \times 10^{-4} \text{ mol dm}^{-3} \text{ s}^{-1}$

compared to $2.40 \pm 0.03 \times 10^{-4} \text{ mol dm}^{-3} \text{ s}^{-1}$). There is also no evidence of any hydrosilylation products being formed from the reaction of **MD'M** with *trans*-2-octene. This implies that *trans*-2-octene has a similar inhibiting effect to cyclohexene that could, in part, be related to the binding strength.

In contrast, the addition of 0.14 M norbornadiene proved to completely halt catalytic activity (Figure 4.36). That both cyclohexene and *trans*-2-octene still permit the successful hydrosilylation reaction between **MD'M** and **VTMS**, albeit at a slower rate, yet norbornadiene does not, suggests that this latter substrate binds much more strongly to the active catalyst species than **VTMS**, and inhibits the binding of **VTMS** to the metal centre. This is in line with the kinetic studies conducted by Kühn, where it was reported from Eyring analysis that the activation barriers E_A for the dissociation of norbornadiene ($E_A = 138.6 \pm 7.5 \text{ kJ mol}^{-1}$) were much higher than that for oct-1-ene ($E_A = 60.2 \pm 3.5 \text{ kJ mol}^{-1}$).² Despite the high activation barrier however, Kühn found that Karstedt's catalyst was still effective at catalysing the hydrosilylation reaction between norbornadiene and HSiCl_3 . The inhibition of catalysis by norbornadiene is similar to what was observed when DBCOT was added to the reaction mixture, and inhibition by norbornadiene has been reported for other Pt(0)-based pre-catalysts.⁷³

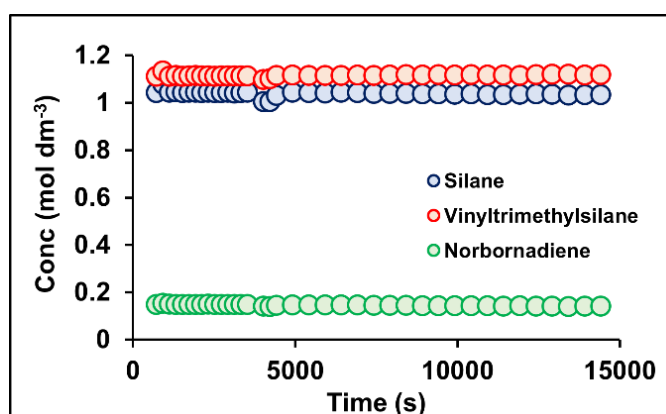
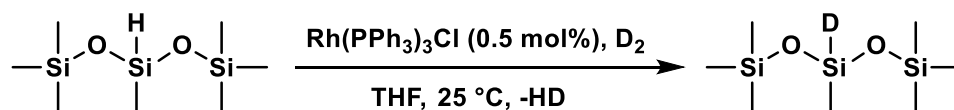


Figure 4.36. Concentration-time profiles of **MD'M**, **VTMS** and norbornadiene during the attempted photoactivated hydrosilylation reaction between **MD'M** and **VTMS** with norbornadiene doped in. Reaction conditions as detailed in section 4.6.

4.7 ^2H NMR studies

To identify the rate-limiting factors and pinpoint the crucial steps and barriers of the hydrosilylation reaction catalysed by the active species generated from precatalysts **1a** and **1b**, a series of ^2H -labelling experiments were conducted. Deuterio **MD'M** was prepared by adding $\text{RhCl}(\text{PPh}_3)_3$ to a THF solution of protio **MD'M**, which was degassed by three successive freeze-pump-thaw (FPT) cycles and then charged with D_2 (3 bar) and stirred vigorously at $25\text{ }^\circ\text{C}$ (Scheme 4.4). The FPT process was repeated after 2 and 4 h to remove excess HD and the solution was each time recharged with D_2 . The product was obtained via distillation as a colourless liquid in a good yield (75%). One distinct ^2H signal is observed in the ^2H NMR spectrum of deuterio **MD'M** at 298 K in dichloromethane (δ 4.63) which corresponds to the Si–D bond (Figure 4.37). The ^1H NMR spectrum of deuterio **MD'M** in d_2 -dichloromethane shows two distinct signals at δ 0.12 and δ 0.10, which correspond to the O–Si–(CH_3)₃ and D–Si– CH_3 protons, respectively (Figure 4.38). The relative integral of the Si–H bond is 0.02, which demonstrates that **MD'M** is > 99% deuterated in the Si–H position.



Scheme 4.4. Synthesis of deuterio **MD'M**.

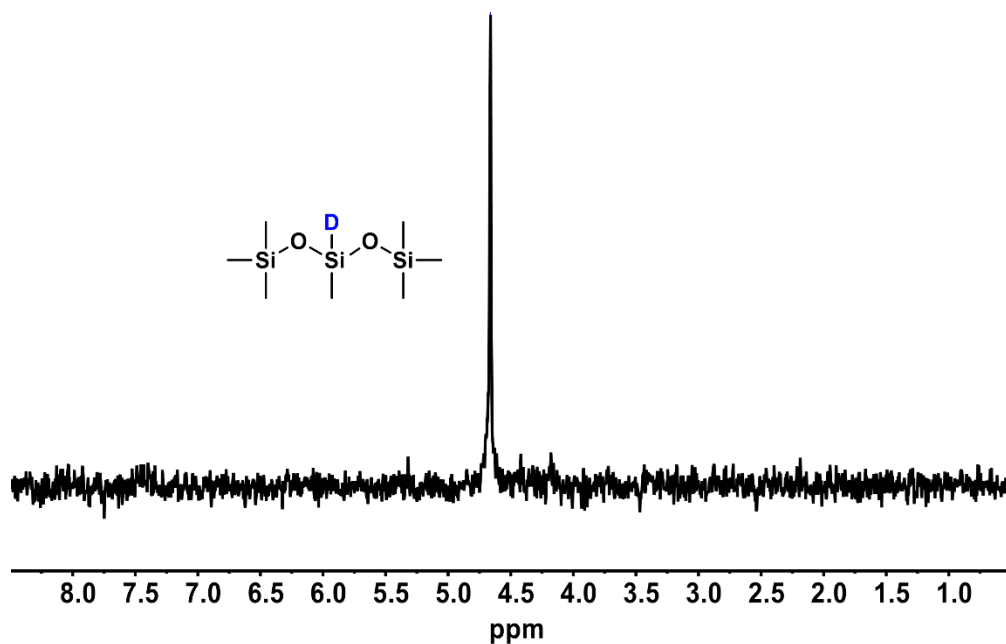


Figure 4.37. ^2H NMR spectrum of deuterio MD'M (92 MHz, dichloromethane, 298 K).

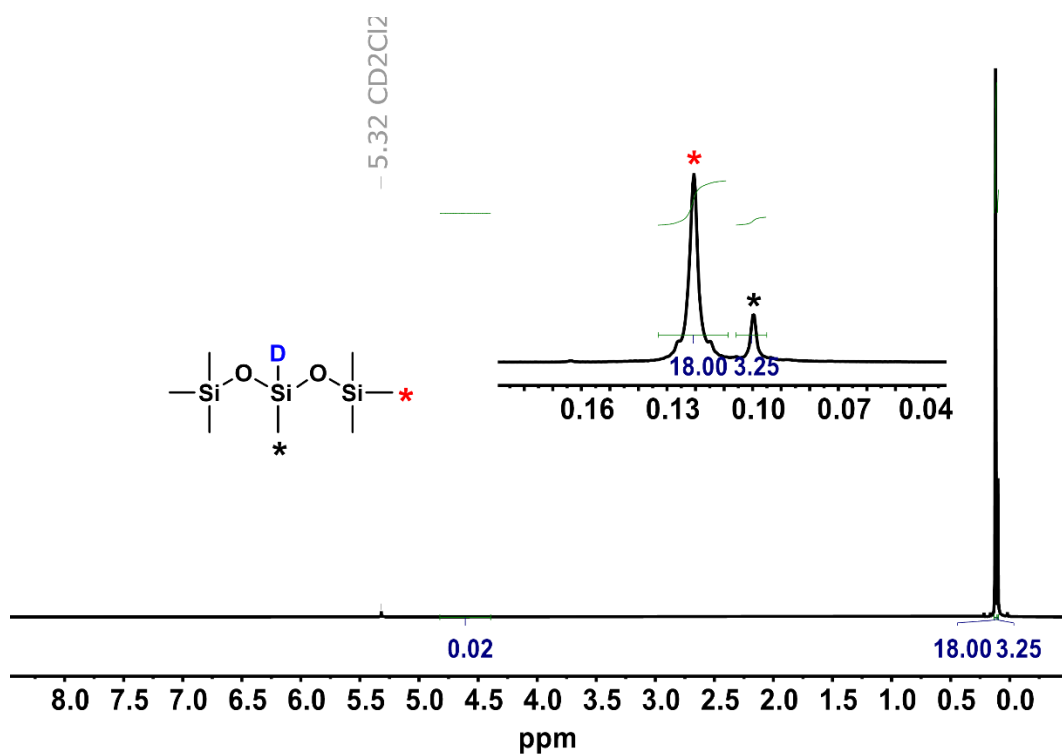


Figure 4.38. ^1H NMR spectrum of deuterio MD'M (600 MHz, d_2 -dichloromethane, 298 K).

4.7.1 Thermal hydrosilylation using deuterio MD'M

To examine any isotope effects observed under thermal conditions, the model reaction was performed in the presence of deuterio **MD'M** using precatalyst **1a** (0.0025 M). The precatalyst was loaded into a J. Young's NMR tube and to it was added d_2 -dichloromethane, along with deuterio **MD'M** (1.1 M), **VTMS** (1.1 M) and mesitylene as an integration standard from a stock solution. The sample was inserted into the NMR spectrometer and an array of ~ 100 ^1H NMR spectra was acquired to monitor the formation of beta product over time. The kinetics were probed using the initial rates method, monitoring the rate of beta product formation over the first 5 data points after catalytic activity had been established. The concentration-time profile along with a table of initial rates for the formation of beta product in the presence of deuterio **MD'M** is shown in Figure 4.39, overlaid with the parallel experiment using protio **MD'M**.

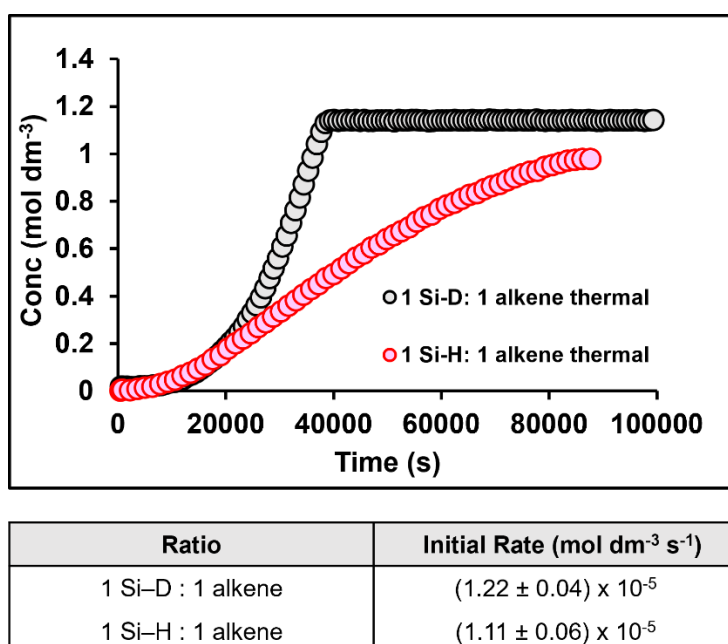


Figure 4.39. Concentration-time profiles of beta product formation during the thermal hydrosilylation reaction between **MD'M** and **VTMS** (pink) and deuterio **MD'M** and **VTMS** (black) using **1a** as a precatalyst. Reaction conditions as detailed in section 4.7.1.

For both experiments, the reaction is characterised by the same induction period during which the catalyst activates: at $\sim 20,000$ s, conversion to the beta product is at 17% and 16% using the

deuterio **MD'M** and protio **MD'M**, respectively. Interestingly after the induction period, the presence of deuterio **MD'M** leads to an accelerated rate of conversion to the beta product relative to the protio **MD'M** counterpart. Indeed at 40,000 s, full conversion has been achieved when deuterio **MD'M** is used, compared with only 44% conversion in the corresponding experiment in the presence of protio **MD'M**. This result was somewhat surprising, as earlier studies by Pregosin have shown a primary kinetic isotope effect ($k_H/k_D = 3.6(2)$) in the thermal hydrosilylation reaction between $\text{Et}_3\text{Si-H}$ and styrene, when using *cis*- $[\text{PtCl}_2(\text{PhCH}=\text{CH}_2)_2]$ as the precatalyst.⁴¹

If precatalyst **1a** proceeds via a Chalk–Harrod type mechanism under thermal conditions (Figure 4.40), a primary kinetic isotope would be expected and would be indicative of either Si–H/D bond breakage (prior to or during the rate-limiting step, step I), or rate-limiting olefin insertion into the Pt–H/D bond (step III). Lewis, Stein and coworkers interpreted the primary kinetic isotope effect ($k_H/k_D = 1.8$) observed in the hydrosilylation of **MD'M** and tris(trimethylsiloxy)vinylsilane using Karstedt's catalyst to be symptomatic of the Si–H/D bond breaking before or during the rate-limiting step, but Kühn and coworkers later argued that the primary KIE arises from the rate-limiting nature of the migratory insertion step.^{2,191} The inverse isotope effect observed for the active catalyst generated from using precatalyst **1a** under thermal conditions ($k_H/k_D = \sim 0.2$, calculated from the first 5 data points following the induction period), implies that **1a** proceeds via a different mechanism under thermal conditions, especially since the formation of the active catalyst appears to proceed at a similar rate regardless of using protio or deuterio **MD'M** (similar induction periods).

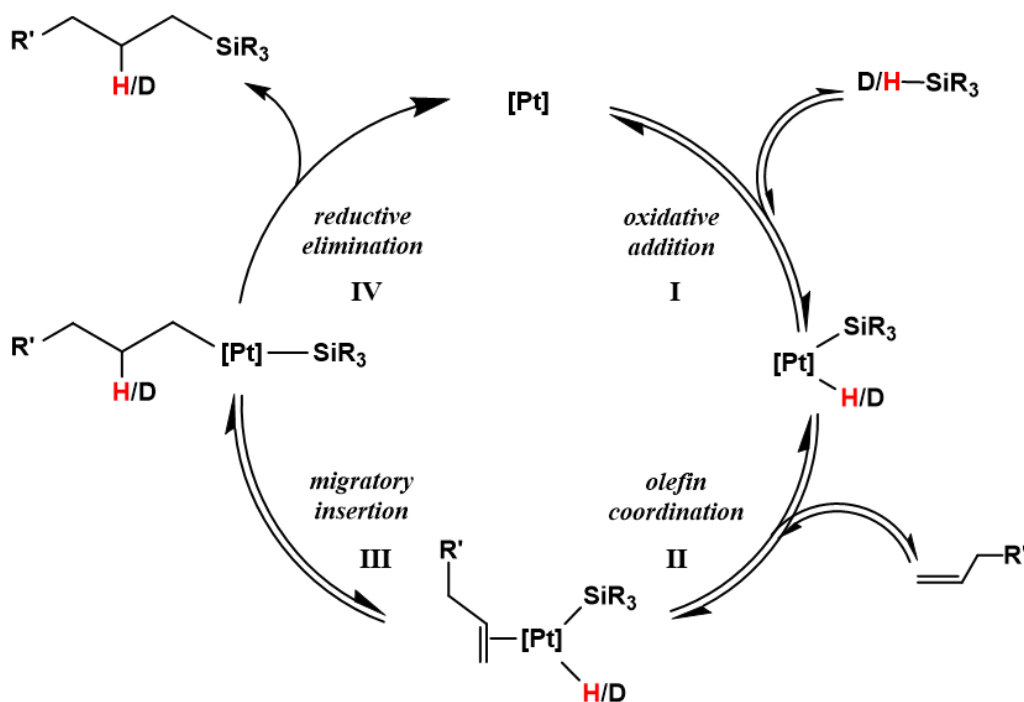


Figure 4.40. Simplified Chalk-Harrod mechanism.³³

To determine whether an inverse isotope effect was also observed under thermal conditions using precatalyst **1b** in the presence of deuterio **MD'M**, the model reaction was conducted in the presence of this precatalyst (0.0025 M **1b**, 0.93 deuterio **MD'M**, 0.93 M **VTMS**). The concentration-time profile for beta product formation along with the table of initial rates for this reaction and the corresponding experiment using protio **MD'M** are shown in Figure 4.41.

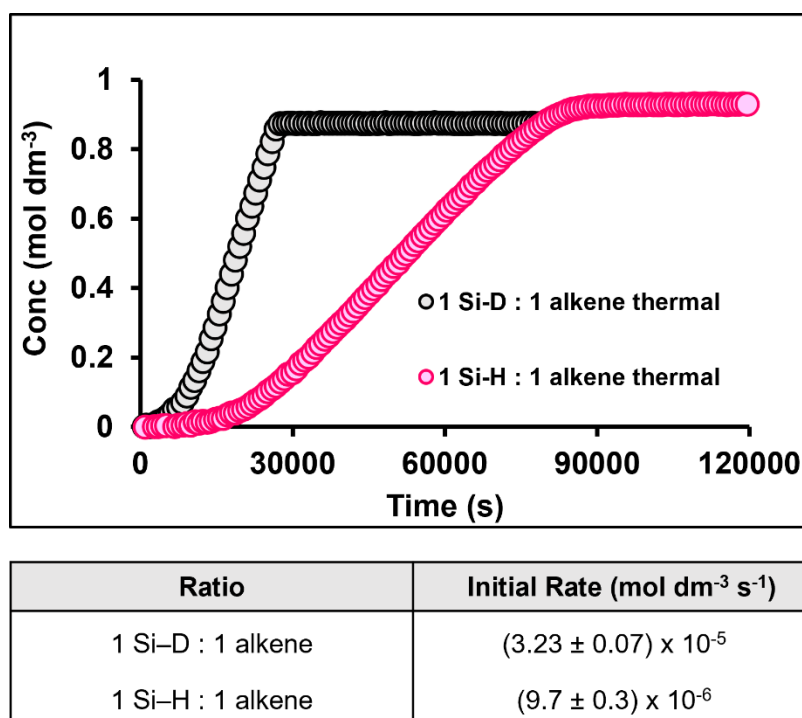


Figure 4.41. Concentration-time profiles of beta product formation during the thermal hydrosilylation reaction between **MD'M** and **VTMS** (pink) and deuterio **MD'M** and **VTMS** (black) using **1b** as a precatalyst. Reaction conditions as detailed in section 4.7.1.

In accordance with that observed when using precatalyst **1a**, using deuterio **MD'M** in the model reaction results in an accelerated rate of catalytic activity compared to the corresponding experiment using protio **MD'M**. The striking difference, however, is that the induction period when using protio **MD'M** is much longer than that observed when using deuterio **MD'M** when precatalyst **1b** is employed. From the initial rate measured after catalytic activity has been established, using deuterio **MD'M** results in rate that is 3.3 x faster than that when protio **MD'M** is used ($k_H/k_D = 0.3$). Furthermore, the times taken to achieve full conversion are 2.7×10^4 s (7.4 h) and 7.96×10^4 s (22.1 h) for using deuterio **MD'M** and protio **MD'M**, respectively. This implies that when using precatalyst **1b**, the isotope effect arises from the formation of the active catalyst and also from an on-cycle step in the mechanism.

To further consolidate mechanistic understanding for the thermal regime, the course of this reaction was followed by ^2H NMR spectroscopy (Figure 4.42). Over time, the signal at δ 4.63 corresponding to the Si-D bond gets consumed, simultaneous with the formation of the beta

product as evidenced by the ethylene signals at δ 0.42. Superimposing the ^1H and ^2H NMR spectra at the end of catalysis shows that there is no difference in product selectivity regardless of whether protio or deuterio **MD'M** is used (Figure 4.43).

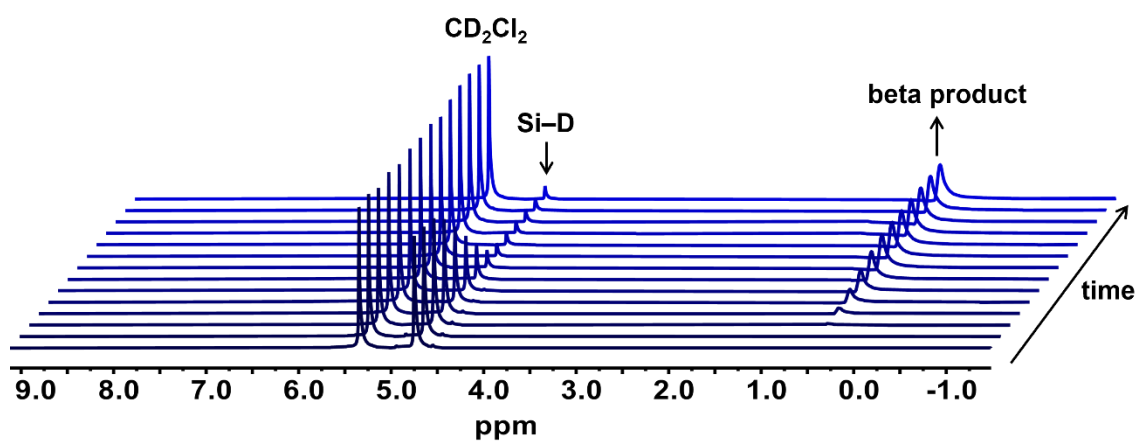


Figure 4.42. In-situ stacked ^2H NMR spectra of the thermal hydrosilylation reaction between deuterated **MD'M** and **VTMS** using **1b** as a precatalyst (92 MHz, dichloromethane, 298 K). Reaction conditions as detailed in section 4.7.1.

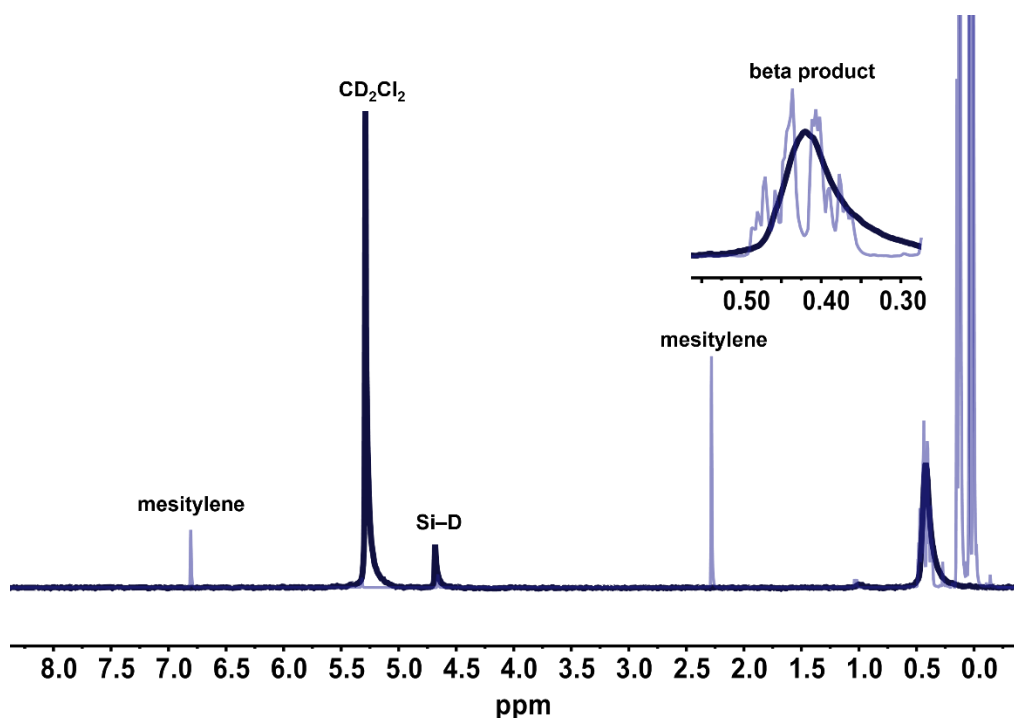


Figure 4.43. Overlaid ^1H (600 MHz, CD_2Cl_2 , 298 K) and ^2H (92 MHz, dichloromethane, 298 K) NMR spectra at the end of the thermal hydrosilylation reaction between **MD'M** and **VTMS** (light blue) and deuterio **MD'M** and **VTMS** (dark blue) using **1b** as a precatalyst. Reaction conditions as detailed in section 4.7.1

4.7.2 Photoactivated hydrosilylation using deuterio **MD'M**

Having observed a significant albeit inverse isotope effect under thermal conditions, deuterio **MD'M** was also employed in the model reaction under photoactivated conditions using precatalyst **1b**. The precatalyst was loaded into a J. Young's NMR tube and to it was added d_2 -dichloromethane, along with deuterio **MD'M** (0.93 M), **VTMS** (0.93 M) and mesitylene as an integration standard from a stock solution. The sample was inserted into the NMR spectrometer and an array of ~ 20 ^1H NMR spectra was acquired to monitor the latency period. Following this, the sample was irradiated for 120 s on the 365 nm LED and returned to the spectrometer. A further array of ~ 20 ^1H NMR spectra was acquired to monitor the formation of beta product over time. The kinetics were probed using the initial rates method, monitoring the rate of beta product formation over the first 5 data points after catalytic activity had been established. The

concentration-time profile along with a table of initial rates for the formation of beta product in the presence of deuterio **MD'M** is shown in Figure 4.44, overlaid with the parallel experiment using protio **MD'M**.

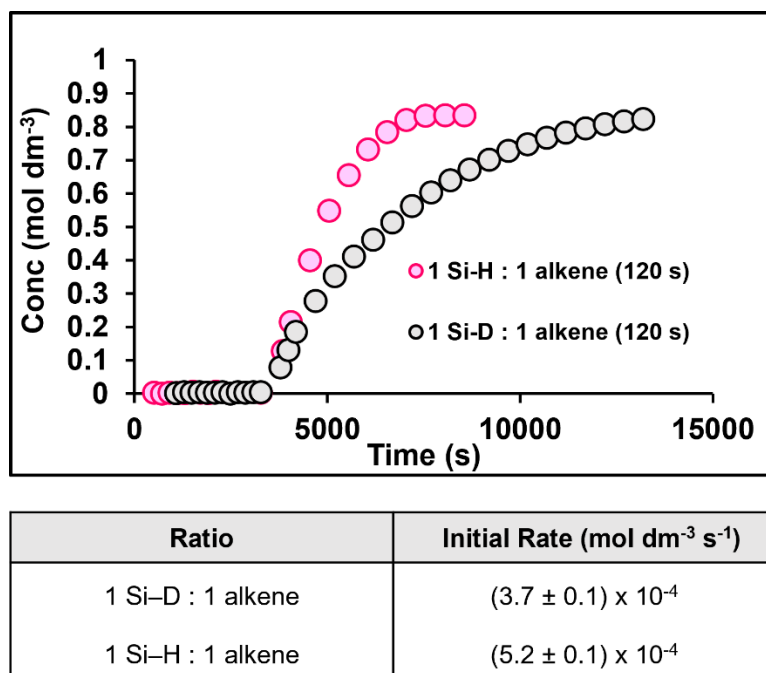


Figure 4.44. Concentration-time profiles of beta product formation during the photoactivated hydrosilylation reaction between **MD'M** and **VTMS** (pink) and deuterio **MD'M** and **VTMS** (black) using **1b** as a precatalyst. Reaction conditions as detailed in section 4.7.2. All plots are time-shifted to 3300 s to show the same latency period. The table shows the initial rates extracted from the first 5 data points following irradiation.

Contrary to what was observed under thermal conditions, there is a marked deceleration in catalytic activity when using deuterio **MD'M** compared with protio **MD'M** under photoactivated conditions. The observed isotope effect on the initial rates for product formation is 1.4 ± 0.2 . This isotope effect is similar to that measured for Karstedt's catalyst combined with similar substrates to those used here (1.8), for which reductive elimination is proposed to be the turnover-limiting step, that is preceded by Si-H bond breaking.¹⁹ However for Karstedt's catalyst combined with chlorosilanes and either norbornene or 1-octene alkene substrates, significantly larger isotope effects are measured, of 2.4(1) and 3.9(4) respectively. In these cases, the turnover-limiting step is proposed to be migratory insertion of the hydride to the alkene.² It is worth noting that whilst

the observed isotope effects prove useful for understanding the catalytic cycle, the used methodology is relatively limited as isotope effects are more accurate when studied for a single elementary step rather than a complex reaction system, but the elusive nature of platinum intermediates makes this very challenging. Nevertheless, in an effort to decipher more mechanistic detail under the photoactivated conditions, the reaction was probed further by in-situ ^2H NMR spectroscopy (Figure 4.45).

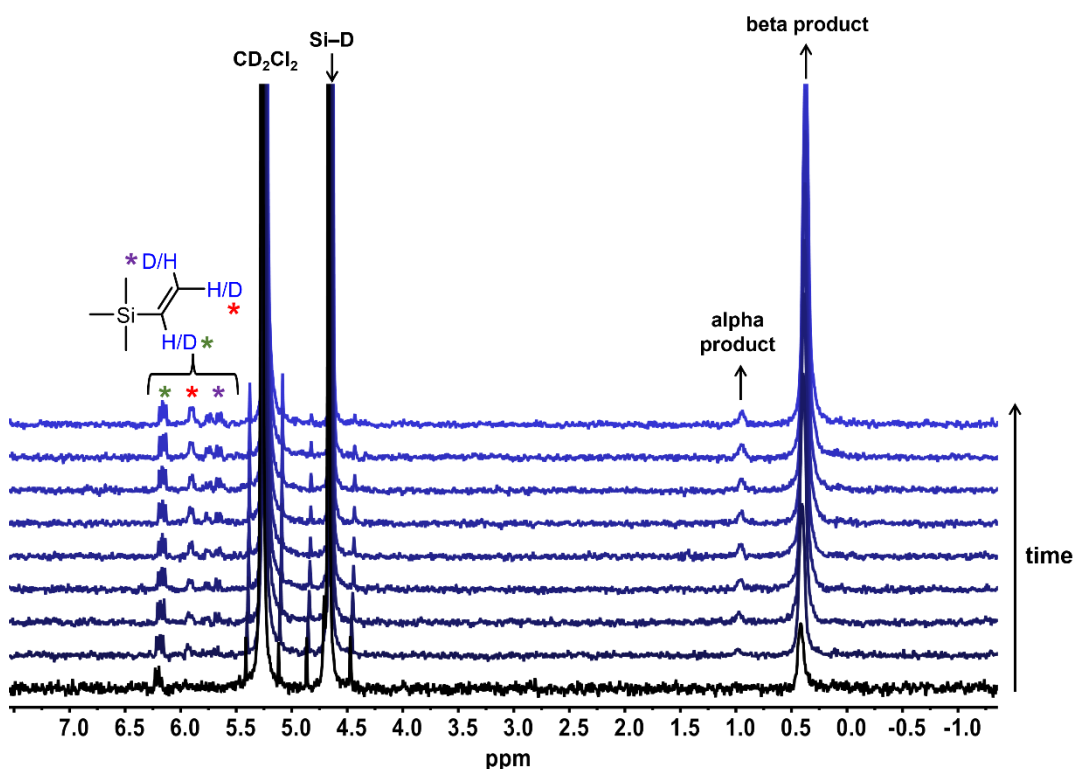


Figure 4.45. In-situ stacked ^2H NMR spectra of the photoactivated hydrosilylation reaction between deuterated **MD'M** and **VTMS** using **1b** as a precatalyst (92 MHz, dichloromethane, 298 K). Reaction conditions as detailed in section 4.7.2.

Monitoring the reaction by ^2H NMR spectroscopy over time shows the consumption of the Si-D bond (δ 4.63) with simultaneous formation of the beta hydrosilylation product (δ 0.42). There is also evidence of the alpha product forming in the ^2H NMR spectrum, but this integrates to give only 1% alpha product compared to 99% beta product. Interestingly, there is also evidence of H/D exchange into all three position of free **VTMS** (δ 6.18, 5.93 and 5.68). At the early stages of

reaction this favours the internal C–H vinyl bond (δ 6.18), but over the course of reaction all the vinyl C–H bonds undergo H/D exchange.

The differences observed under the thermal and photoactivated conditions suggest that the two proceed via different mechanisms: i) an inverse isotope effect is observed under thermal conditions, in contrast to the primary isotope effect observed under photoactivated conditions. ii) There is evidence of deuterium scrambling into all positions of **VTMS** in the photoactivated regime, which is not apparent thermally. iii) Under photoactivated conditions, 1% of alpha product is observed in the ^2H NMR spectrum (this is absent thermally). This shows that migratory insertion into the alpha and beta product occurs, but reductive elimination of the beta product is favoured. Despite the differences implied in the mechanism, the active species under both regimes is most likely homogeneous in nature since both were fractionally poisoned by DBCOT but unaffected by Hg(0).

The observations under photoactivated conditions support all of the following mechanistic conclusions: (i) alkene coordination is reversible, (ii) hydride insertion is reversible, (iii) the overall barrier to give the intermediate for the alpha product is higher than that for the beta product, (iv) reductive elimination is likely the turnover limiting step.

4.7.2.1 Re-charges

The overall isotope effect of 1.4 likely represents a combination of effects arising from precatalyst activation and steps in the catalytic manifold. On the catalytic cycle it is likely that an equilibrium isotope effect (EIE) would result from reversible migratory insertion, and possibly reversible Si–H activation, prior to rate determining reductive elimination. This complexity makes delineating the individual contributions challenging. In an effort to elucidate this, a recharge experiment using precatalyst **1b** (0.0025 M) was conducted where deuterio **MD'M** (1.0 M) was first used and then recharged with protio **MD'M** (1.0 M). The in-situ ^1H NMR experiment was conducted under

the same conditions as described in section 4.3.5, using a 1:1 ratio of **MD'M** and **VTMS**. Importantly, the 120 s irradiation time was selected so that the recharge could be conducted on the same day as the first charge (to prevent possible change / decomposition of the catalyst overnight), and the sample was only irradiated after the ~1 h latency period (no further irradiation upon re-charging). The concentration of beta product was monitored by in-situ ^1H NMR spectroscopy during the entire experiment and the initial rates were calculated using the first 5 data points after catalytic activity had been established (or after the recharge). Figure 4.46 shows the concentration-time profile for the deuterio **MD'M** experiment recharged with protio **MD'M**.

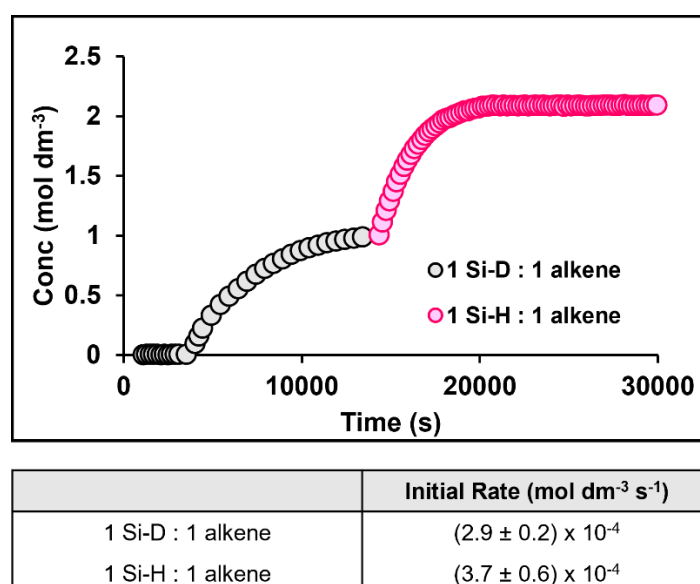


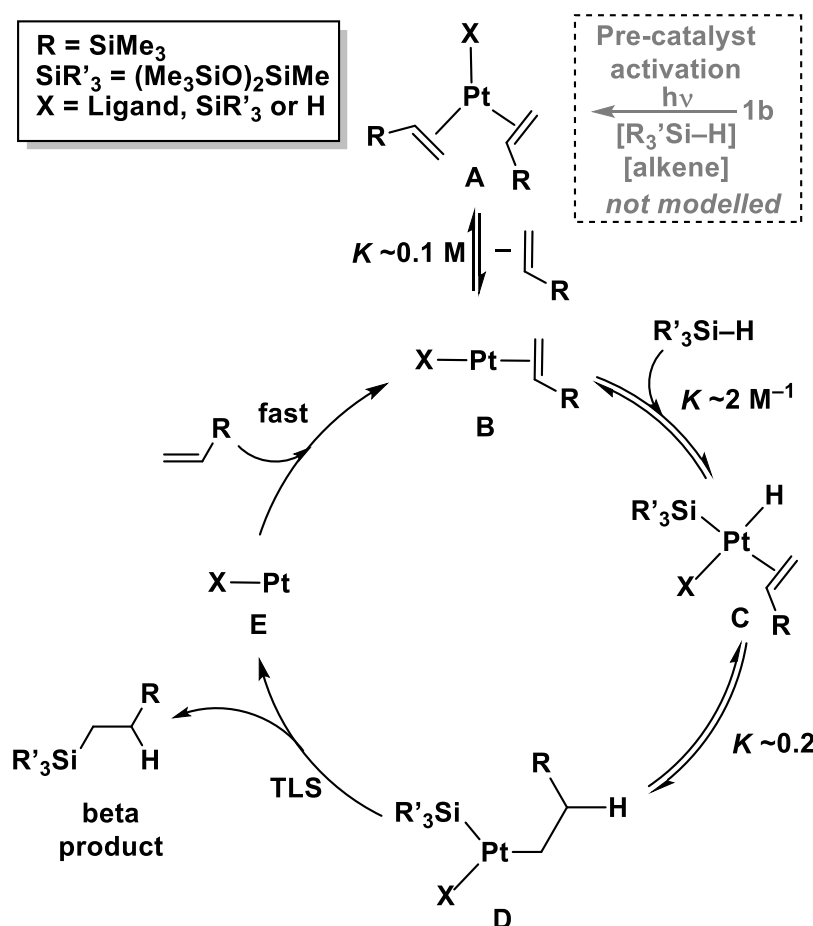
Figure 4.46. Concentration-time profiles for beta product formation during the photoactivated hydrosilylation reaction between deuterio **MD'M** and **VTMS** with a recharge of the same amount of protio **MD'M** and **VTMS** after completion. The table shows the initial rates extracted from the first 5 data points following irradiation, and after the recharge. Reaction conditions as detailed in section 4.7.2.1.

The initial rate of the recharge with protio **MD'M** is ~1.3 x faster than the first charge with deuterio **MD'M**. As catalyst aging will contribute to a deceleration in rate upon recharge, this serves to illustrate that the major contribution to the isotope effect comes from an on-cycle process, since the overall observed isotope effect is 1.4, where the difference in rates observed

between protio and deuterio **MD'M** arises in the kinetics after the active catalyst is formed. That free deuterated **VTMS** was observed in the ^2H NMR experiments demonstrates that the system is in equilibrium to allow for H/D exchange and then alkene loss. This points towards reductive elimination being the rate-determining step, and the overall the observed isotope effect is an equilibrium isotope effect.

4.8 Proposed mechanism for photoactivated hydrosilylation using COPASI

With the preceding observations of precatalyst activation, overall order in substrates and H/D labelling experiments, a reaction mechanism was modelled using COPASI¹⁹² – informed by previous studies on the mechanism of hydrosilylation using Pt-based catalysts.^{2,19,73} All data was modelled by Professor Andrew Weller. Four independent sets of **MD'M:VTMS** starting concentrations were holistically, and simultaneously modelled against the corresponding experimental data after the irradiation period in the photoactivated model reaction. The experimental conditions were ~0.5 M to 2 M for **MD'M** and **VTMS** and a constant concentration of either **1a** or **1b** (0.0025 M) at the 10 s irradiation time. In the absence of any specific measured rate constants, the models only provide overall relative rates rather than absolute values, and some consecutive individual steps were telescoped for simplicity and to avoid over-parameterization. For the same reason, the activation of the precatalyst was not modelled and for the on-cycle steps, only the beta product was modelled. The elementary steps of the model, with the associated relative equilibria and key intermediates are shown in Scheme 4.5.



Scheme 4.5. Simplified catalytic cycle, showing the modelled elementary steps, associated intermediates and selected equilibrium constants as simulated using COPASI. The precise speciation of the catalyst is undetermined (i.e. oxidation state, charge, and identity of X).

Despite the identity of the active catalyst (**A**) being unknown, the model captures an endergonic alkene dissociation to form **B**, which undergoes reversible oxidative addition of Si–H to form **C**. Subsequent migratory insertion affords **D**, followed by turnover-limiting reductive elimination of the beta product and rapid alkene coordination to **E** to return to **B**. This model also supports the proposed isotope effect of 1.4. Notably only one equivalent of silane is added in the catalytic cycle (**B** to **C**), whilst alkene plays a role as both a substrate (**E** to **B**) and an inhibitor (**B** to **A**). This supports the experimental observations that the alkene plays a dominant role in converting the precatalyst to the active catalyst, and that it is inhibitory for catalysis at excess **VTMS** to **MD'M** concentrations. The fits of the simulated and experimental data for precatalyst **1b** are shown in Figure 4.47.

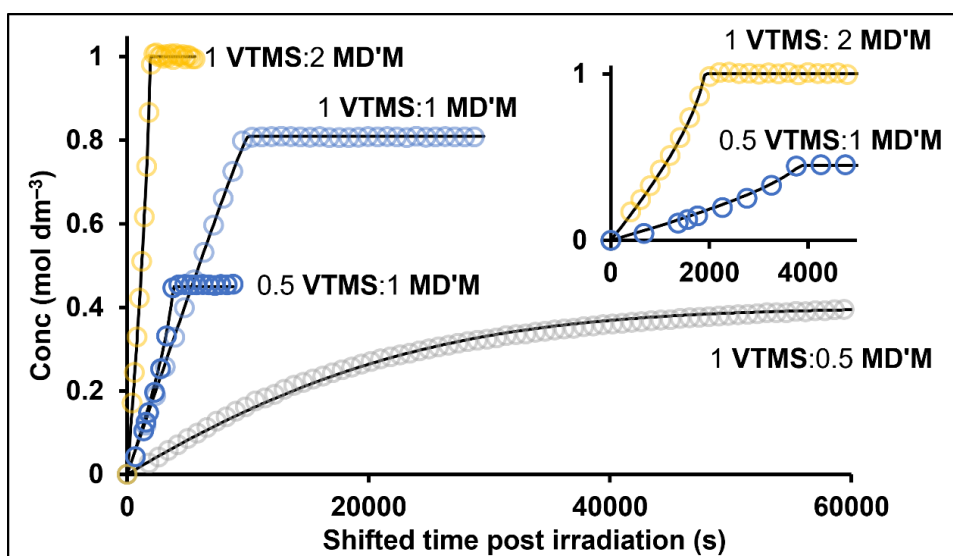


Figure 4.47. Concentration-time profiles of beta product formation for a variety of starting concentrations of **MD'M** and **VTMS** (~0.5 M to 2 M) using pre-catalyst **1b** (0.0025 M, 10 s irradiation time) Open circles = experimental data, solid lines = holistically simulated data derived from the catalytic manifold outlined in . Data are time shifted to remove the latent periods prior to irradiation. Inset shows the first 5000 s for experiments with an excess of **MD'M** that show the increase in rate of turnover with time.

Overall, these high-quality fits capture multiple nuances, which provide confidence that holistically, this is a reasonable solution for the catalytic manifold. For example, the model captures the inhibitory effect of alkene well. When compared to an initial 1:1 ratio of **MD'M:VTMS**, the rate of catalysis at the 0.5:1 ratio (i.e. an excess of alkene) shows a marked deceleration with time. This effect can be attributed to the increasing enrichment in **VTMS** relative to **MD'M** as catalysis proceeds, which in turn inhibits turnover by pushing **B** towards **A** (Scheme 4.5). The opposite effect is observed when **MD'M** is in excess at the 2:1 or 1:0.5 ratios of **MD'M:VTMS**. In these cases, as catalysis evolves, the ratio of **MD'M** / **VTMS** increases, and the inhibitory effect of **VTMS** becomes weaker. This means that the rate of catalysis increases as the substrates become enriched in **MD'M** with each turnover (see inset). When the ratios are balanced and constant throughout the reaction (1:1), an apparent pseudo zero order evolution of beta product is observed. Similar kinetic profiles have been discussed in detail for the anion-initiated trifluoromethylation of ketones using Me_3SiCF_3 . As found in this case, initial rate

measurements showed initiator (anion) and ketone to be first order and the Me_3SiCF_3 approximately inverse order.¹⁴⁹

During the fitting process it became apparent that a universal solution for the four different sets of substrate concentration regimes was not possible using the same catalyst concentration. Although the precatalyst concentration was the same (0.0025 M) for all four sets of **MD'M:VTMS** ratios, successful modelling required different effective catalyst concentrations, $[\text{cat}]_{\text{effective}}$, as shown in Table 4.2. To do this, each individual experiment was manually iterated for different $[\text{cat}]_{\text{effective}}$ and the model was simulated holistically over all four data sets using the same set of rate constants. This model also accounts for less than 5% of the active catalyst being formed (i.e. $[\text{cat}]_{\text{effective}} = 15 \times 10^{-6}$ M or lower). The same process was run for pre-catalyst **1a**, that resulted in a different, but very similar set of $[\text{cat}]_{\text{effective}}$ for those particular starting substrate concentrations (Table 4.3).

Table 4.2. Experimental details of **[VTMS]** and **[MD'M]** used for the COPASI model using precatalyst **1b**, and resulting, iterated, $[\text{cat}]_{\text{effective}}$ used in the fitting. Conditions as detailed in Figure 4.47.

Entry	[VTMS] / M	[MD'M] / M	[VTMS] x [MD'M]	$[\text{cat}]_{\text{effective}} / \times 10^{-6}$ M
1	0.81	0.84	0.6804	6.0
2	0.79	0.40	0.316	2.4
3	1.00	1.94	1.9206	15
4	0.45	0.97	0.4365	3.3

Table 4.3. Experimental details of **[VTMS]** and **[MD'M]** used for the COPASI model using precatalyst **1a**, and resulting, iterated, $[\text{cat}]_{\text{effective}}$ used in the fitting. Conditions as detailed in Figure 4.47.

Entry	[VTMS] / M	[MD'M] / M	[VTMS] x [MD'M]	$[\text{cat}]_{\text{effective}} / \times 10^{-6}$ M
1	0.98	0.99	0.9702	7.0
2	0.96	0.56	0.5376	3.5
3	0.99	2.1	2.079	1.5
4	0.48	1.1	0.528	3.5

The formation of beta product, using the derived rate constants for precatalyst **1b** from the fitting of the experimental data, was also simulated for different $[\text{cat}]_{\text{effective}}$ concentrations using fixed $[\text{MD}'\text{M}]$ and $[\text{VTMS}]$ concentrations. This demonstrates that the model provides a linear, first order relationship between the simulated rate of turnover and $[\text{cat}]_{\text{effective}}$ (Figure 4.48). This is consistent with the observations of a linear relationship between precatalyst irradiation time (10 s, 60 s, 120 s) and initial rate of turnover (Figure 4.49). Note that this holds true for all irradiation times using precatalyst **1a**, but only the 10 s and 60 s irradiation time using precatalyst **1b**. An explanation for this is provided later in this section.

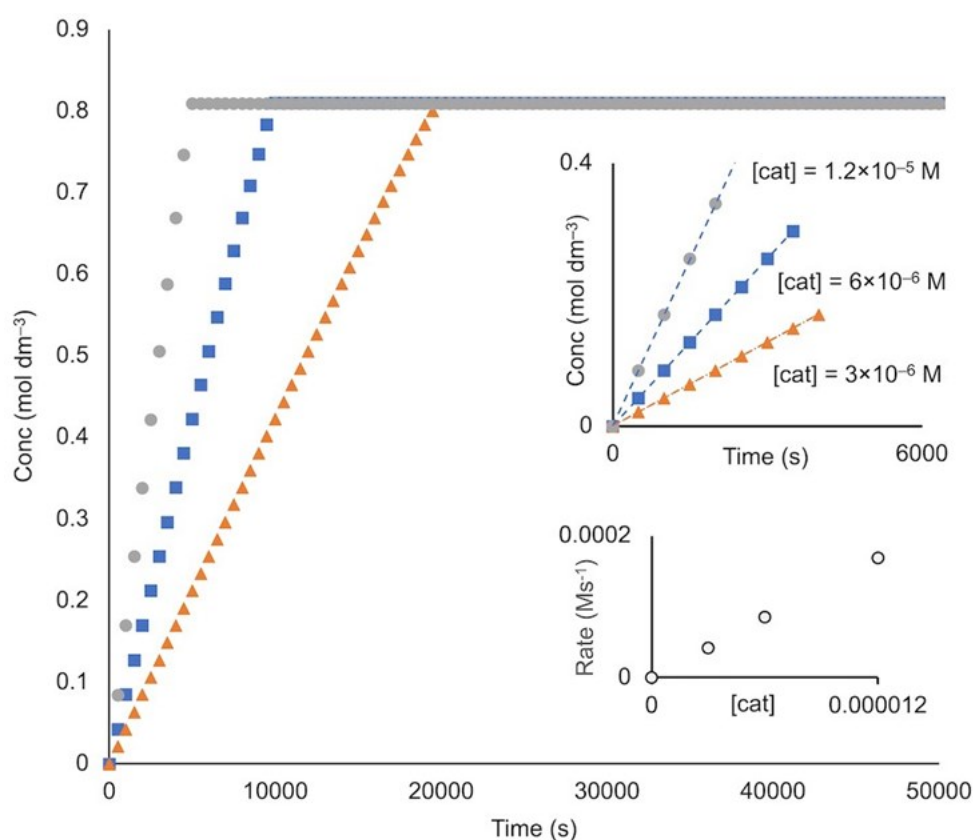


Figure 4.48. COPASI simulated models for the concentration of beta product, using the derived rate constants from fitting **1b** (Figure 4.49) at three different $[\text{cat}]_{\text{effective}}$ ● = 1.2×10^{-5} M; ■ = 6.0×10^{-6} M; ▲ = 3.0×10^{-6} M; $[\text{VTMS}] = 0.81$ M; $[\text{MD}'\text{M}] = 0.84$ M. Simulated post irradiation. Inset: (top) expansion of the first 5000 s of simulation, showing the three different starting $[\text{cat}]_{\text{effective}}$ and linear fits. Inset (bottom): relationship between simulated rates and $[\text{cat}]_{\text{effective}}$.

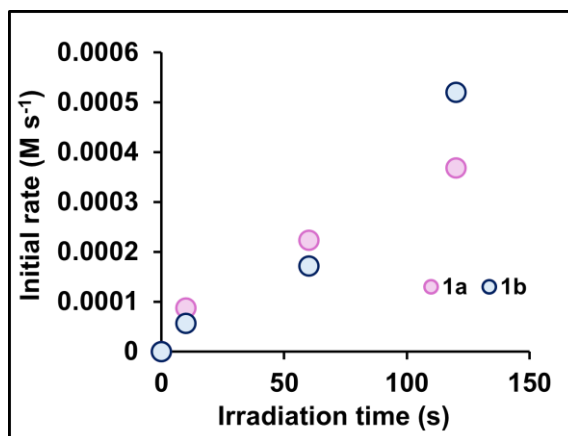


Figure 4.49. Initial rates, post induction period, versus irradiation time for pre-catalyst **1a** and **1b**. Reaction conditions as detailed in section 4.3.

For the pre-catalyst activation step, insight can be obtained by plotting $[\text{cat}]_{\text{effective}}$ used in the successful model against the experimental data of $[\text{silane}] \times [\text{alkene}]$, as this returns a linear relationship (Figure 4.50). This diagram also includes the data for pre-catalyst **1a**, showing that this relationship holds for both systems. This suggests that the amount of pre-catalyst that is converted to active catalyst, i.e. $[\text{cat}]_{\text{effective}}$, is dependent on each set of starting substrate concentrations, demonstrating that both substrates play a role in pre-catalyst activation and productive turnover. This is consistent with the experiments described in section 4.5 (Figure 4.31), which show that the fastest turnover occurs when both **VTMS** and **MD'M** are present during pre-catalyst irradiation.

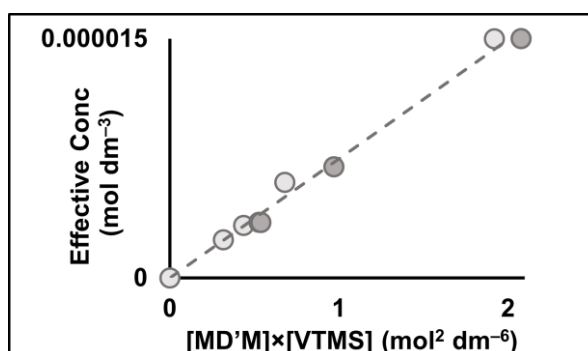


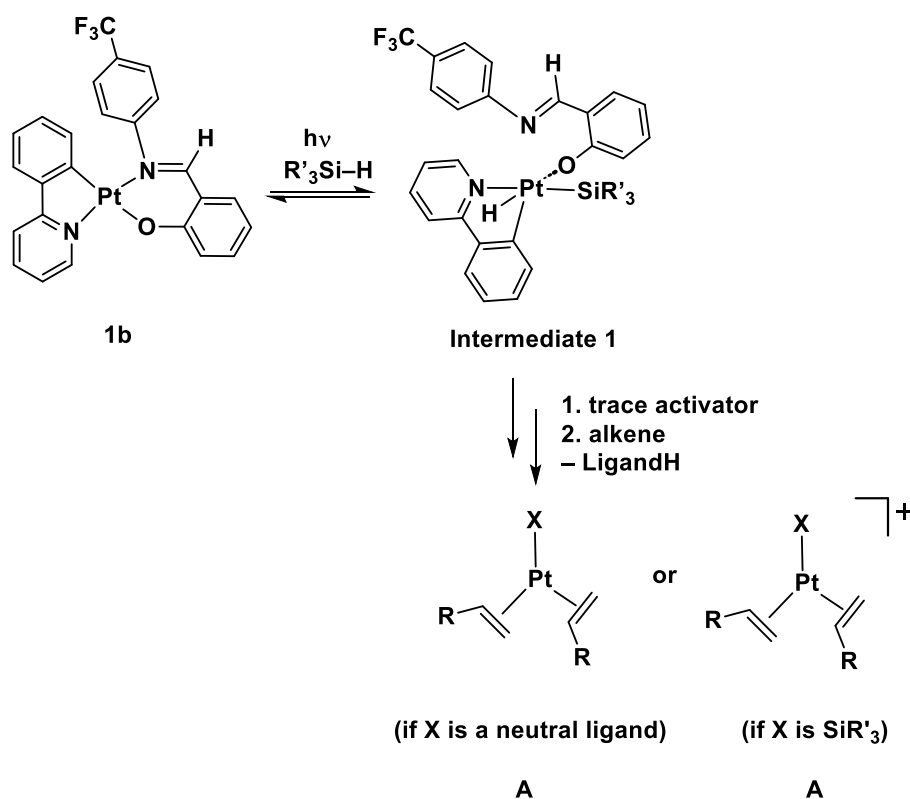
Figure 4.50. Relationship of **[VTMS]** and **[MD'M]** to $[\text{cat}]_{\text{effective}}$ for pre-catalysts **1b** (light grey) and **1a** (dark grey).

These results explain the observed second order behaviour in **MD'M** derived from initial rates in the model reaction, as this reflects a precatalyst photoactivation step that is first order in **MD'M** (not modelled), along with first order in **MD'M** in productive catalysis after photoactivation, i.e. overall pseudo $[\mathbf{MD'M}]^2$. This explanation of second order for **MD'M** differs from that proposed by Kühn² and Girolami⁷³ for Karstedt's catalyst, as they proposed that two equivalents of silane were required per catalytic turnover. Attempts were made to model two equivalents of **MD'M** in the catalytic cycle using precatalyst **1b**, whilst keeping the concentration of [cat] fixed at 2.5×10^{-6} M, but this did not return an acceptable fit (see appendix). This provides further support for a different mechanism being operative herein.

Although an inverse order in **VTMS** was observed using the initial rates method, the COPASI model suggests an apparent positive order in **VTMS** that controls precatalyst activation and thus $[\text{cat}]_{\text{effective}}$. One explanation could be the involvement of a trace activator present in **VTMS** (such as water or alcohol), the concentration of which would scale proportionately with **VTMS**, and that photoactivation is actually zero-order in **VTMS**. The role of trace contaminants, such as water, in modifying catalysis has been previously reported.^{193,194,195} This hypothesis is also consistent with the burst in catalysis measured for different irradiation times, but the same **MD'M** and **VTMS** concentrations (Figure 4.49), that would result from a small concentration of an additional activator that operates under photoactivation conditions in the model reaction. That this doesn't hold for the 120 s irradiation time using precatalyst **1b** could be due to a different batch of **VTMS** being used for this experiment.

Whilst the identity of the active catalyst remains unresolved due to the very low conversion of precatalyst conversion, it must be a highly active species that operates at the ppm-levels. A tentative mechanism for the generation of the photoactivated catalyst is shown in Scheme 4.6. It is proposed that initial activation occurs under photoactivated conditions, likely via coordination and activation of **MD'M** to form **intermediate 1**. This may be facilitated by ligand hemilability. Similar modes of activation that are aided by ligand dissociation have also been proposed for the formation of the active catalyst in $\text{Pt}(\text{acac})_2$ -based photoinitiated

systems.^{79,84,196} The role of the hypothesised trace activator may be to protonate off one, or both, of the ligands. No evidence (from ^1H NMR studies) is observed for the formation of an alkene adduct under the photoactivated conditions, such as reported for the related $\text{Pt}(\text{hfac})_2$ complex that forms a five coordinate ethene adduct upon irradiation at 350 nm, albeit in the absence of silane (see Chapter One, Scheme 1.25).⁸⁴ The fate of the organic ligands remains unresolved, and the challenges associated with determining trace levels of highly active catalyst have been discussed for other catalyst systems.¹⁹⁷

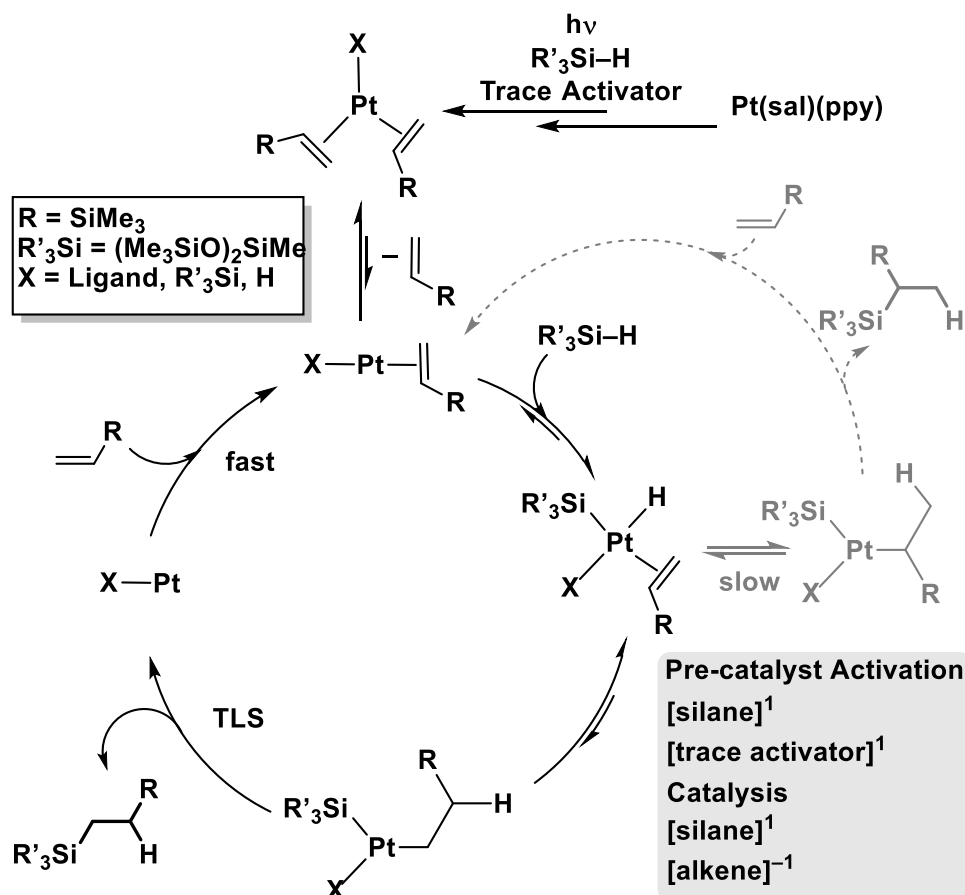


Scheme 4.6. Suggested mechanism of photoactivation of the precatalysts. X = neutral ligand, SiR'_3 or another anionic ligand.

The overall mechanism proposed for photoactivated hydrosilylation using the $\text{Pt}(\text{sal})(\text{ppy})$ complexes is depicted in Scheme 4.7. This mechanism accounts for catalyst activation, the high selectivity towards the beta product, as well as combining the mechanistic observations, kinetics and COPASI simulations. For the systems under consideration here, the identity of X and the oxidation state of the active Pt-species formed in trace quantities remains unresolved. A $\text{Pt}(0)$,

Pt(alkene)₃ species or a Pt(II) species such as [XPt(alkene)₂]⁺ (X = ligand, H, SiR'₃) are possibilities.

Pt(II)/Pt(IV) or Pt(0)/Pt(II) cycles have both been postulated for hydrosilylation.^{2,73,183}



Scheme 4.7. Suggested mechanism for photoactivated hydrosilylation. For simplicity, ligand X in the active species is assumed to be a neutral ligand, but its identity remains unresolved.

4.9 Conclusions

This chapter has presented a detailed kinetic and mechanistic study utilising precatalysts **1a** and **1b** in the photoactivated hydrosilylation reaction between **MD'M** and **VTMS**. Selective poisoning experiments using Hg(0) and DBCOT in the thermal and photoactivated hydrosilylation reactions revealed that the likely active species is homogeneous in nature, as Hg(0) did not impede catalytic activity, whilst the addition of DBCOT led to a significant deceleration in the rate of

hydrosilylation. The elucidation of a homogeneous active species presented the opportunity to explore the kinetic and mechanistic intricacies of photoactivated hydrosilylation using **1a** and **1b**. From the initial rate studies alone, a second order dependence on **MD'M** and a negative order in **VTMS** was determined for both precatalysts at a range of irradiation times (10 s, 60 s, and 120 s). For precatalyst **1b**, the second order dependence on **MD'M** also held up at lower concentrations of catalyst (0.000025 M), and also when using **VTMOS** as the alkene substrate, suggesting a similar precatalyst activation mechanism for both substrates. Control experiments in the presence and absence of either substrate during the irradiation step revealed that optimal catalytic turnover was achieved when both substrates were present during irradiation. The second fastest turnover was achieved when **VTMS** was present during irradiation, followed by when **MD'M** was present during irradiation. This highlighted that the generation of the active catalyst required both substrates, but the effect of **VTMS** dominates. The addition of cyclohexene and *trans*-2-octene to the catalysis solution using **1b** showed that photoactivated hydrosilylation of **VTMS** still proceeded, albeit at a slower rate, but no hydrosilylation of the cyclohexene or *trans*-2-octene substrates was observed. Addition of norbornadiene however, proved to completely shut down the hydrosilylation of **VTMS**, presumably by binding strongly with the Pt centre in a similar fashion to DBCOT. Using deuterated **MD'M** revealed an inverse isotope effect ($k_H/k_D = 0.3$) in the model thermal reaction, while an isotope effect of 1.4 was observed under photoactivated conditions. The experiment where deuterio **MD'M** was used first as a substrate under photoactivation conditions, and then recharging the system without further irradiation revealed that the initial rate of recharge is ~ 1.3 x faster. This suggested that the isotope effect operates mainly in the catalytic manifold, and only a small isotope effect is involved in precatalyst activation. Monitoring the ^2H NMR spectra during the photoactivated hydrosilylation reaction using **1b** showed evidence for deuterium scrambling into all the vinyl C–H bonds, as well as evidence for the formation of a small amount (<1%) of alpha product.

These experimental observations culminated in a mechanistic proposal, modelled using COPASI by Professor Andrew Weller. While the identity of the active species remains to be resolved, the

model is based on the elementary steps of alkene dissociation, oxidative addition of silane, migratory insertion, reductive elimination, and subsequent coordination of alkene. Modelling the experimental data for **1b** on COPASI captured multiple nuances, such as an increased rate when the solution becomes enriched in **MD'M**, and a decelerating effect when the solution becomes enriched in **VTMS**. The model also revealed that different $[\text{cat}]_{\text{effective}}$ concentrations were required to obtain an acceptable fit, and a linear first order relationship was observed for the simulated rate of turnover and $[\text{cat}]_{\text{effective}}$. This was in accordance with the experimental observations of a linear relationship between precatalyst irradiation time and initial rate of turnover. Plotting $[\text{cat}]_{\text{effective}}$ used in the successful model against the experimental data of $[\text{MD'M}] \times [\text{VTMS}]$ also returned a linear relationship, suggesting that the amount of precatalyst that is converted to active catalyst, i.e. $[\text{cat}]_{\text{effective}}$, is dependent on each set of starting substrate concentrations, demonstrating that both substrates play a role in precatalyst activation and productive turnover. This is consistent with the experiments that showed that optimal turnover was achieved when both substrates were present during the irradiation step. These results explained the observed second order behaviour in **MD'M** derived from initial rates in the model reaction, as this reflects a precatalyst photoactivation step that is first order in **MD'M** (not modelled), along with first order in **MD'M** in productive catalysis after photoactivation, i.e. overall pseudo $[\text{MD'M}]^2$. While a negative order in **VTMS** was observed using the initial rates method, the COPASI model indicated a more nuanced mechanism in which photoactivation is zero-order in **VTMS**. The discrepancy between observed and modelled kinetics implicates the role of a trace activator present in **VTMS**. Overall, the suggested mechanism accounts for catalyst activation, the high selectivity towards the beta product, as well as combining the mechanistic observations, kinetics and COPASI simulations. The identity of the active species remains to be resolved, but a Pt(0) or Pt(alkene)₃ species are possibilities.² This work has revealed deeper insight into the mechanism for photoactivated hydrosilylation and will hopefully pave the way for further research in the field, with a particular focus on elucidating the exact nature of the active species.

Chapter 5 – Conclusions and Future Directions

This short section of the thesis provides a comprehensive overview of the key conclusions reached in this project, along with suggestions for further lines of inquiry.

5.1 Key Conclusions

This aim of this project was to develop a series of new Pt-based complexes for use in the photoactivated hydrosilylation reaction. The current most studied photoactivated hydrosilylation catalysts are based on the CpPtMe₃ and Pt(β -diketonate) frameworks.^{5,54,79,84,88} The former catalysts are acutely toxic and volatile, but more reactive than the latter under photohydrosilylation conditions, while the latter suffer from poor solubility in siloxane substrates.^{85,89} The development of further photoactivated hydrosilylation catalysts is of particular interest as they offer spatial and temporal control, as well as providing an increased shelf-life for premixed precatalyst / substrate mixtures.^{3,5,72} This is incredibly useful for certain applications such as in the production of fast-curing films, and in additive or continuous manufacturing processes.⁵ Despite the considerable maturity of the field, the mechanism of hydrosilylation is still not fully understood, and mechanistic studies particularly on photoactivated catalysts, have been relatively scarce in the academic and patent literature.^{2,19,73} This project was designed to address the current limitations in the field of photoactivated hydrosilylation, from precatalyst design, substrate scope exploration, detailed kinetic studies, and mechanistic investigations.

Chapter two presented the synthesis and characterisation of a series of Pt(sal)(ppy) complexes as photoactivated precatalysts for hydrosilylation (Figure 5.1). Two major advantages of these complexes over the current best-studied photohydrosilylation catalysts are that the ligands can be tuned in a modular way via a simple synthetic route, and they do not require handling in a

glovebox. Complexes **1b** and **1d** are known and have well established photophysical properties and are considered to have low cytotoxicity.^{113,114} All the Pt(sal)(ppy) complexes showed relatively wide absorption bands between 220 – 480 nm, which rendered them primed for photoactivation. They also offer the potential for hemilabile reactivity profiles by decoordination of the imine group, which is the current anticipated mode of activation for these complexes.¹¹⁵ All complexes were characterised by NMR and UV-vis spectroscopies along with electrospray ionisation mass spectrometry and elemental analysis. Crystal structures for precatalysts **1a**, **1b**, **1f** and **1g** were obtained, and these complexes were found to adopt a slightly distorted square-planar structure. The distortion was found to be most pronounced in precatalyst **1b** (16.64°) and **1g** (14.95°), and in combination with the different functional groups, this led to different reactivity profiles in the model reaction.

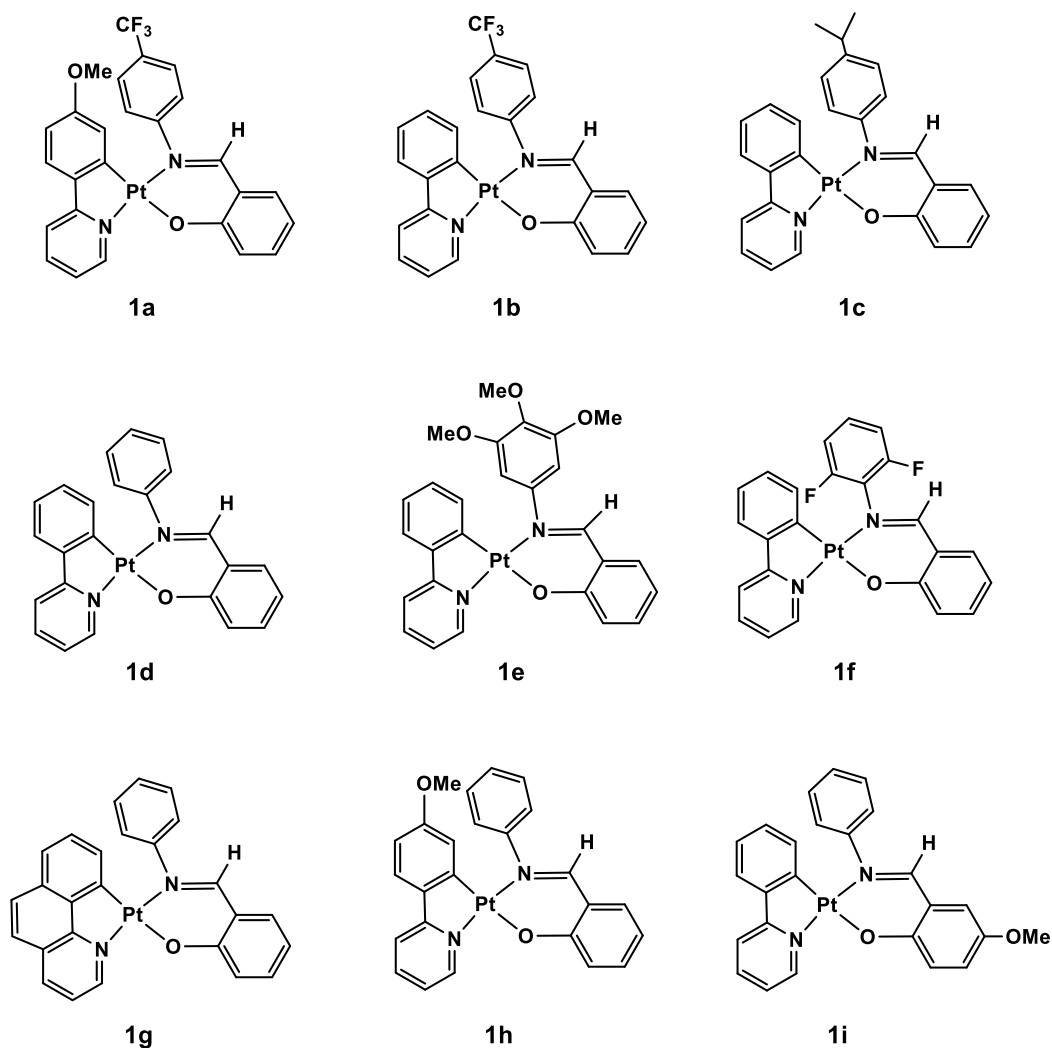


Figure 5.1. Pt(sal)(ppy) complexes synthesised herein (**1a** – **1i**) and used as precatalysts for the hydrosilylation reaction.

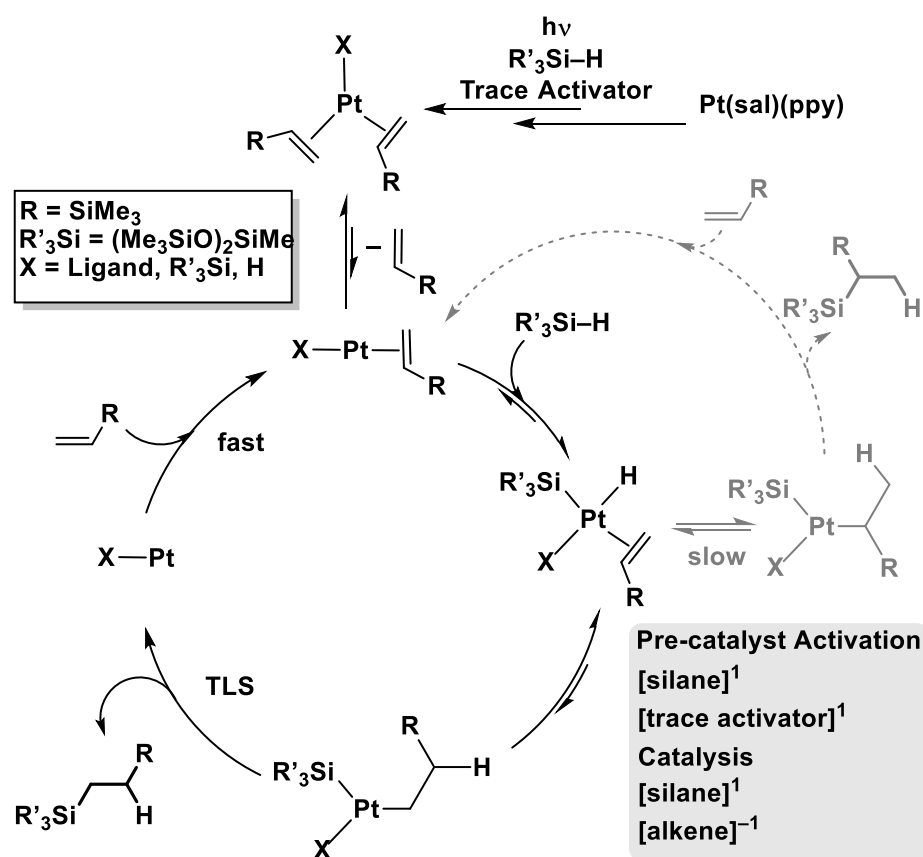
Chapter three presented the development of a model reaction that was used as a platform to assess the performance of precatalysts **1a** to **1i** in thermal and photoactivated hydrosilylation reactions. In all cases, the precatalysts were identified to be effective photoactivated catalysts with excellent selectivity towards the beta product, as turnover continued after the irradiation source was removed. Under thermal conditions, a sigmoidal profile, with an associated induction period and a pseudo-zero order regime at maximum rate of turnover, was observed for all precatalysts except **1c** and **1d**. Precatalysts **1c** and **1d** showed much shorter induction periods and apparent zero-order reaction profiles that operated over nearly all of the reaction profile. The time measured to completion under thermal conditions varied from 1.8 h (**1c**) to 22.4 h (**1a**).

Under photoactivated conditions, the time measured to completion varied from 0.15 h (**1c**) to 4.7 h (**1a**). Whilst a direct trend was not established, as a bigger library of complexes is required, some key structural features of these precatalysts can be related to their catalytic activity. For instance, in the model thermal reaction, **1d** had a shorter induction period than **1g** (5.8×10^2 s compared to 1.2×10^3 s), but **1g** promoted faster turnover overall (1.6×10^4 s for **1d** and 1.5×10^4 s for **1g**). This might suggest that the benzo[*h*]quinoline ligand is more suited than phenylpyridine for providing latent reaction kinetics, due to its higher stability. Precatalyst **1c** promoted faster turnover than **1d** in both the thermal (6.4×10^3 s for **1c** compared to 1.6×10^4 s for **1d**) and photoactivated (7.6×10^2 s for **1c** compared to 1.4×10^3 s for **1d**) model reactions, which suggests that introduction of an alkyl group onto the salicylaldimine ligand is conducive to enhanced photoactivation efficiencies. Precatalysts **1a** and **1b** showed the best latent reaction kinetics and had induction periods of 5.0×10^3 s and 1.0×10^4 s respectively, and after 120 s irradiation, full conversion to the beta product was realised after 5.6×10^3 s and 4.4×10^3 s, respectively. To demonstrate its suitability under commercially relevant conditions, precatalyst **1b** was also shown to catalyse the model reaction at a catalyst loading of 0.0025 mol% (0.000025 M / 14 ppm). Precatalyst **1b** was also shown to successfully catalyse the photoactivated hydrosilylation reactions between **MD'M** and a variety of alkene substrates, including **VTMOS**, **oct-1-ene**, **3-Buten-2-one**, **styrene** and **4-methoxystyrene**. For all alkene substrates **except 3-Buten-2-one**, the main product conformed to the anti-Markovnikov rule and afforded the beta product. Using **VTMOS**, **styrene**, and **4-methoxystyrene** as the alkene substrate also furnished the alpha product under the model reaction conditions, in a range of selectivities. When **oct-1-ene** was employed as the alkene substrate, the beta product was formed as well as 9% isomerisation products. Compared with the model reaction using **VTMS**, the reaction proceeded slower in the presence of all the other studied alkenes **except oct-1-ene**, and **4-methoxystyrene** was identified as the slowest reacting substrate ($\text{ToF}_{\text{app}} < 20 \text{ h}^{-1}$ compared to $\text{ToF}_{\text{app}} = 333 \text{ h}^{-1}$ for **VTMS**). This chapter concluded by demonstrating the ability of several precatalysts to cure the commercially used polysiloxane substrates (**HMS** and **DMS**) at commercially relevant catalyst

loadings (50 ppm). All precatalysts photocured the substrates in a timeframe of 4.8×10^2 s – 2.5×10^3 s. The thermal stability of these precatalysts in the **HMS / DMS** formulations was also examined, and the cure temperatures were found to be in the range of 114 °C – 127 °C. This is similar to that observed for the industry standard catalyst **i-68**, which has a cure temperature of 156 °C.

In chapter four, precatalysts **1a** and **1b** were taken forward for kinetic and mechanistic studies, as despite not promoting the fastest turnover, these complexes showed the best thermal latency. The series of poisoning experiments using the long-established Hg(0) drop test and addition of DBCOT pointed towards the active species being homogenous in nature.^{37,83} These results prompted a detailed kinetic and mechanistic analysis of the reaction mixtures under photohydrosilylation conditions. From the initial rate studies alone, a second order dependence on **MD'M** and a negative order in **VTMS** was observed for both precatalysts. Control experiments in the presence and absence of either substrate during the irradiation step revealed that optimal catalytic turnover was achieved when both substrates were present during irradiation. The second fastest turnover was achieved when **VTMS** was present during irradiation, followed by when **MD'M** was present during irradiation. This highlighted that the generation of the active catalyst required both substrates, but the effect of **VTMS** dominated. The use of deuterated **MD'M** in the model photohydrosilylation reaction revealed an isotope effect of ~ 1.4 , which was determined to be operating mainly in the catalytic manifold. In light of these results, a mechanism was proposed using COPASI by Professor Andrew Weller (Scheme 5.1).¹⁹² The mechanism accounted for the observed second order behaviour in **MD'M** derived from initial rates in the model reaction, as this reflected a precatalyst photoactivation step that is first order in **MD'M** (not modelled), along with first order in **MD'M** in productive catalysis after photoactivation, i.e. overall pseudo $[\text{MD}'\text{M}]^2$. The negative order in **VTMS** was also accounted for, as the COPASI model indicated a more nuanced mechanism in which photoactivation is zero-order in **VTMS**. The discrepancy between observed and modelled kinetics implicated the role of a trace activator present in **VTMS**.^{193,194,195} This mechanism also accounted for the high selectivity

towards the beta product. Combined, the resulting kinetic and mechanistic observations pointed to a catalytic cycle where the turnover limiting step is reductive elimination of the beta product, while pre-catalyst activation is dependent on the concentrations of solutions of silane and alkene used. The identity of the active species remains to be resolved, but a Pt(0) or Pt(alkene)₃ species are possibilities and have been previously suggested.^{2,73} Overall, this work has revealed deeper insight into the mechanism for photoactivated hydrosilylation and will hopefully pave the way for further research in the field.



Scheme 5.1. Suggested mechanism for photoactivated hydrosilylation.

5.2 Future Directions

5.2.1 Combining the precatalyst with inhibitors

As discussed in detail in chapter 3, inhibitors can play a crucial role in extending latency periods and providing controlled release of the precatalyst.¹ Combining the precatalyst systems developed herein with an inhibitor may offer the opportunity to prolong latency periods for extended shelf-lives whilst enabling rapid release for on-demand catalysis. Many known inhibitors such as maleates and fumarates require heating to be removed, so an ideal system would combine the precatalyst with an inhibitor that stabilises the precatalyst and formulation but is quickly removed upon exposure to UV-light.

5.2.2 Expanding the substrate scope

Whilst the catalytic activity of precatalyst **1b** with a variety of alkenes has been investigated, further studies are warranted to systematically investigate the reactivity and selectivity towards a broader range of functional groups. This should include alkynes, carbonyls, and conjugated dienes.

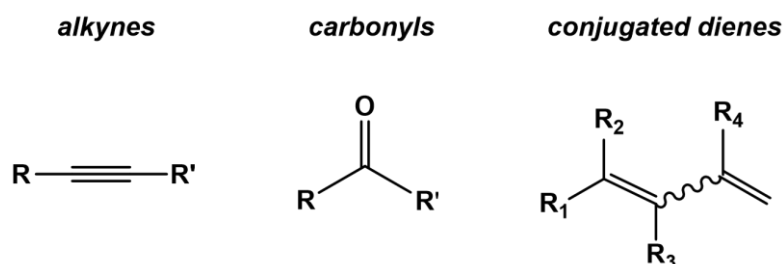


Figure 5.2. Alternative unsaturated substrates to test in the model reaction based on alkynes, carbonyls and conjugated dienes.

The compatibility of the catalytic system with a variety of silanes remains to be fully explored. Future work should focus on evaluating the activity and selectivity towards various silane functionalities, such as alkylsilanes, phenylsilanes and chlorosilanes.

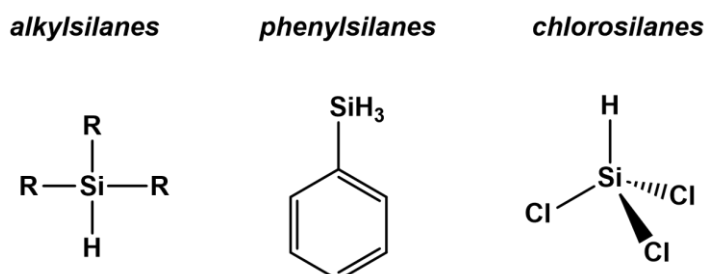


Figure 5.3. Alternative silanes to test in the model reaction based on alkylsilanes, phenylsilanes and chlorosilanes.

Systematically varying a broader range of substrates will provide insights into the scope and limitations of the Pt(sal)(ppy) catalyst systems. Whilst substrate scope has been explored extensively in conventional thermal hydrosilylation, harnessing photoactivation may unlock new synthetic pathways and enable the efficient synthesis of a diverse array of organosilicon compounds with enhanced functionalities.⁴

5.2.3 Time-resolved spectroscopic methods for identifying the active species

Utilising time-resolved spectroscopic methods to identify the active species during catalysis represents a promising avenue for future research.¹⁹⁸ As discussed in chapter four, the signal integrals corresponding to the precatalyst in the ¹H NMR spectrum are unchanged at the end of catalysis, and no new signals which may indicate a change or decomposition of the precatalyst can be identified. The identification of the active species present in the catalytic cycle of hydrosilylation has been a long-standing issue, as these species are highly reactive.^{2,41} Techniques such as time-resolved infrared spectroscopy, in collaboration with computational

methods, may enable the identification of reactive intermediates present during the catalytic cycle. Exploiting these techniques may also allow for identification of the active species that forms from the precatalyst and validate the proposed mechanism. The insights gained from this research will enable the rational design of improved platinum-based catalysts for photoactivated hydrosilylation, leading to improved catalytic activity and selectivity.

Chapter 6 – Experimental methods

6.1 General techniques

6.1.1 Nuclear Magnetic Resonance (NMR) spectroscopy

NMR spectra were recorded on a Bruker Avance III 500 MHz NMR spectrometer or a Bruker Ultrashield 400 MHz or 600 MHz NMR spectrometer at 298 K unless otherwise specified. Residual protio solvent was used as a reference for ^1H and $^{13}\text{C}\{^1\text{H}\}$ NMR spectra in deuterated solvent samples. ^{19}F spectra were externally referenced to CFCl_3 , and ^{29}Si NMR spectra were externally referenced to TMS. All chemical shifts (δ) are quoted in ppm and coupling constants (J) in Hz. NMR assignments were aided by 2D spectra ($^1\text{H},^1\text{H}$ -COSY, $^1\text{H},^{13}\text{C}$ -HSQC, $^1\text{H},^{13}\text{C}$ -HMBC) where required. Coupling constants to ^{195}Pt are listed where satellites are observed. The satellites are generally quite broad. For the in-situ ^1H NMR hydrosilylation experiments, the time between FID encodings (d_1) was set to 45 s to ensure accurate quantitative analysis.

6.1.2 Ultraviolet–visible spectroscopy

All UV-vis absorption spectra were recorded using an Evolution Array UV-vis spectrophotometer, with a window of 190–1100 nm. Data was processed using VISIONcollect software. ‘Background’ absorption spectra of the solvents used were subtracted from sample spectra. Herein, the wavelengths of maximum absorption (λ_{max}) are given in nm, and molar absorption coefficients (ϵ) are reported in $\text{mol}^{-1} \text{dm}^3 \text{cm}^{-1}$.

6.1.3 Mass spectrometry

Electrospray Ionisation Mass Spectrometry (ESI-MS) was carried out using a Bruker compact® Time of Flight mass spectrometer by Mr Karl Heaton at the University of York. All platinum complexes are quoted for ^{195}Pt .

6.1.4 Elemental microanalysis

Elemental analyses were conducted by Dr Graeme McAllister and Dr Scott Hicks at the University of York, or by Dr Orfhlaith McCullough at London Metropolitan University.

6.1.5 Transmission Electron Microscopy

TEM images were collected at the University of York Jeol Nanocentre using a EOL 2010 TEM conventional (2Å) High Resolution TEM.

6.1.6 Differential Scanning Calorimetry

All experiments were carried out on a NETZSCH DSC 204F1 Phoenix. The heating rate for each experiment was 5°C min^{-1} in an open aluminium crucible with the lid (hole) under a nitrogen atmosphere with a gas flow of 60 mL min^{-1} . Analysis conditions (DSC): keeping at 30°C for 3 min, heating $0\rightarrow 200^\circ\text{C}$ at 5°C min^{-1} , then cooling to room temperature.

6.2 UV photoreactor

The UV photoreactor comprised four Osram LZ1-00UV0R LEDs (radiant flux 1.36 W, emission centred at 365 nm with full width at half maximum 11 nm) mounted vertically in a square array to surround a 5 mm NMR tube at a distance of 8.5 mm. The angular distribution at half-maximum radiant flux is ca. 60 degrees. Cooling compressed air was purged through the reactor housing, and a thermocouple located close to the NMR tube showed that there was only a minimal increase in temperature during photolysis (maximum of 2 °C rise over 160 s). The controller provided power and timing control (10–120 s).

6.3 Catalytic procedures

All catalytic procedures were performed under an atmosphere of nitrogen, using standard Schlenk line and glove-box techniques, unless otherwise specified. Glassware was oven-dried at 110 °C overnight and flamed under vacuum prior to use. NMR spectra were acquired on a Bruker Ultrashield 400 MHz spectrometer at 298 K. Residual protio solvent was used as reference for ^1H spectra in deuterated solvent samples. For the in-situ ^1H NMR hydrosilylation experiments, the time between FID encodings (d1) was set to 45 s to ensure accurate quantitative analysis.

6.3.1 Reagents

Commercially sourced solvents and reagents were purchased from Acros Organics, Alfa Aesar, Fisher Scientific, Fluorochem or Sigma-Aldrich and used as received unless otherwise noted. The synthesis of the $[\text{Pt}\{\text{NC}_5\text{H}_4\text{-6-(4'-R-C}_6\text{H}_3)\}\text{Cl}(\kappa_1\text{-S-dmsO})]$ and $\text{Pt}(\text{sal})(\text{ppy})$ complexes was performed under a nitrogen atmosphere despite the air stability of the complexes, the main concern being the oxidative and thermal stability of reaction intermediates at elevated temperatures (< 110 °C). Dichloromethane- d_2 (CD_2Cl_2), hexamethylsiloxymethylsilane (**MD'M**),

vinyltrimethylsilane (**VTMS**) and mesitylene were dried overnight with CaH_2 before vacuum transfer and subsequent degassing by three freeze-pump-thaw (FPT) cycles and were stored over 3 Å molecular sieves. Other substrates used in catalysis were degassed by either purging with nitrogen or by three FPT cycles.

6.3.2 Method for in-situ reaction monitoring

All manipulations were performed under a nitrogen atmosphere using standard Schlenk line and glove-box techniques. Glassware was oven-dried at 130 °C overnight and flamed under vacuum prior to use. NMR tubes for hydrosilylation procedures were wrapped in foil during transportation to avoid light activation. The time between FID encodings (d_1) was set to 45 s to ensure accurate quantitative analysis. To assess and compare the catalytic activity of precatalysts **1a–1i** in the model hydrosilylation reaction, a series of NMR experiments were conducted. For each experiment, the precatalyst (0.0025 M) was loaded into a J. Young's NMR tube and to it was added d_2 -dichloromethane, along with **MD'M** (0.8 – 1.0 M), **VTMS** (0.8 – 1.0 M) and mesitylene as an internal standard (0.10 M) from a stock solution. The sample was inserted into the NMR spectrometer and an array of ~ 20 ^1H NMR spectra was acquired to determine the thermal latency period over ~ 1 h. The sample was then removed from the spectrometer and irradiated using the bespoke 365 nm LED for either 10, 60 or 120 s before being returned to the spectrometer (note that this step is omitted for experiments conducted under thermal conditions). An array of 10–100 ^1H NMR spectra was acquired with appropriate delays between each acquisition (depending on the catalytic activity) and the concentrations of **MD'M**, **VTMS** and beta product were calculated using the absolute quantitation method (Equation 6.1). The absolute NMR integrals of the Si–H (δ 4.63), olefinic CH (δ 6.18) and Si–CH₂–CH₂–Si (δ 0.42) resonances were compared with the (CH₃)₃ (δ 2.29) resonance of the internal standard. The kinetics were probed using the initial rates method, monitoring the rate of beta product

formation over the first 3 – 5 data points after catalytic activity had been established. For the thermal profiles with an associated induction period, the initial rate was measured after the induction period, at the maximum rate of turnover. Errors were calculated using the linear regression model (LINEST) in Microsoft Excel. The reported errors are the estimated standard error from the model.

$$C_x = \frac{I_x}{I_{std}} \cdot \frac{N_{std}}{N_x} \cdot C_{std}$$

Equation 6.1. Calculation to determine absolute concentration of analytes by NMR.

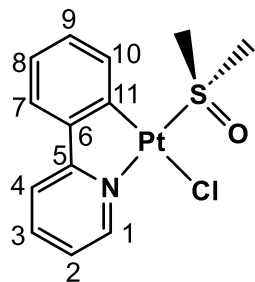
6.4 Chapter Two Experimental

6.4.1 Synthesis and characterisation of [Pt{NC₅H₄-6-(4'-R-C₆H₃)}Cl(κ₁-S-dmsso)] complexes

All dmsso complexes were synthesised in the same way, via a literature reported procedure.^{122,120}

For **1-dmsso**, K₂PtCl₄ (1.00 g, 2.41 mmol) solubilised in the minimum amount of hot water was added to a solution of 2-phenylpyridine (0.376 g, 2.42 mmol) in acetic acid (100 mL). The mixture was stirred under a nitrogen atmosphere and heated to reflux overnight. The orange precipitate was recovered by filtration and washed with water (10 mL) to afford crude [Pt(N[^]C)(μ-Cl)]₂, which was used in the next step without further purification. The [Pt(N[^]C)(μ-Cl)]₂ complex (590 mg, 0.762 mmol) was then dissolved in dmsso (10 mL) and heated to reflux with stirring for 1 h (4 h for **2-dmsso**). The solvent was removed *in vacuo* to afford **1-dmsso** in good yield (604 mg, 1.30 mmol, 83%). All complexes are known and the acquired NMR data matches the literature reported data.^{122,121}

6.4.1.1 1-dmsso yield (604 mg, 1.30 mmol, 83%).



^1H NMR (600 MHz, d_2 -dichloromethane, 298 K): δ 9.61 (d, 1H, $^3J_{\text{H-H}} = 5.9$ Hz, $^3J_{\text{H-Pt}} = 35.6$ Hz, H-1), 8.30–8.28 (m, 1H, $^3J_{\text{H-Pt}} = 43.7$ Hz, H-10), 7.91 (t, $^3J_{\text{H-H}} = 7.7$ Hz, 1H, H-3), 7.78 (d, 1H, $^3J_{\text{H-H}} = 8.0$ Hz, H-4), 7.57–7.54 (m, 1H, H-7), 7.27 (t, 1H, $^3J_{\text{H-H}} = 6.8$ Hz, H-2), 7.20–7.17 (m, 2H, H-8/9), 3.60 (s, 6H, $^3J_{\text{H-Pt}} = 23.4$ Hz, 2 x CH₃).

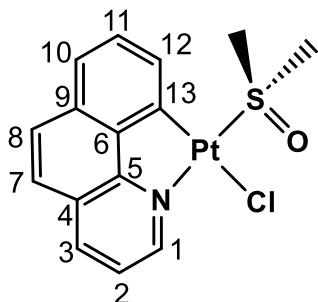
$^{13}\text{C}\{^1\text{H}\}$ NMR (151 MHz, d_2 -dichloromethane, 298 K): δ 166.5 (s, C-5/6/11), 150.5 (s, $^2J_{\text{C-Pt}} = 25.1$ Hz, C-1), 145.2 (s, C-5/6/11), 141.1 (s, C-5/6/11), 134.6 (s, $^2J_{\text{C-Pt}} = 50.2$ Hz, C-10), 131.0 (s, $^2J_{\text{C-Pt}} = 50.2$ Hz, C-8/9), 125.6 (s, C-8/9), 124.3 (s, $^3J_{\text{C-Pt}} = 41.7$, C-7), 122.6 (s, $^3J_{\text{C-Pt}} = 29.3$ Hz, C-2), 119.3 (s, $^3J_{\text{C-Pt}} = 39.6$ Hz, C-4), 47.7 (s, $^2J_{\text{C-Pt}} = 60.1$ Hz, 2 x CH₃).

These NMR data are in accordance with the literature reported data.¹²¹

ESI-MS (CH₂Cl₂): m/z [M-Cl]⁺ 427.0434 (calc. 427.0439) with the correct isotope pattern.

UV-Vis (CH₂Cl₂): λ_{max} /nm [$\log(\epsilon \text{ dm}^3 \text{ mol}^{-1} \text{ cm}^{-1})$] 242 (4.77), 282 (4.55), 316 (4.22), 328 (4.22).

6.4.1.2 2-dmsol yield (228 mg, 0.47 mmol, 47%).



^1H NMR (600 MHz, d_1 -chloroform, 298 K): δ 9.83 (d, 1H, $^3J_{\text{H-H}} = 5.5$ Hz, $^3J_{\text{H-Pt}} = 32.9$ Hz, H-1), 8.50 (d, 1H, $^3J_{\text{H-H}} = 7.4$ Hz, $^3J_{\text{H-Pt}} = 43.6$ Hz, H-12), 8.35–8.33 (m, 1H, H-10), 7.82–7.80 (m 1H, H-7/8), 7.69–7.67 (m, 1H, H-3), 7.60–7.58 (m, 3H, C-2/7/8/11), 3.74 (s, 6 H, $^3J_{\text{H-Pt}} = 21.5$ Hz, 2 x CH_3).

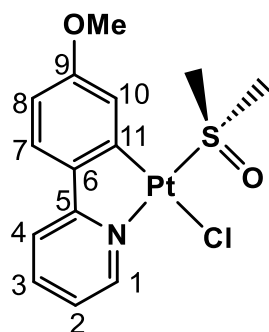
$^{13}\text{C}\{^1\text{H}\}$ NMR (151 MHz, d_1 -chloroform, 298 K): δ 155.1 (s, C-4/5/6/9/13), 149.3 (s, $^2J_{\text{C-Pt}} = 28.2$ Hz, C-1), 141.0 (s, C-4/5/6/9/13), 139.3 (s, C-10), 138.2 (s, C-4/5/6/9/13), 134.1 (s, C-4/5/6/9/13), 131.9 (s, $^2J_{\text{C-Pt}} = 55.5$ Hz, C-12), 130.2 (s, C-2/7/8/11), 129.9 (s, C-7/8), 126.9 (s, C-4/5/6/9/13), 123.7 (s, H-3), 123.0 (s, C-2/7/8/11), 120.9 (s, C-4/5/6/9/13), 47.5 (s, $^2J_{\text{C-Pt}} = 60.7$ Hz, 2 x CH_3).

These NMR data are in accordance with the literature reported data.¹²¹

ESI-MS (CH_2Cl_2): m/z $[\text{M}+\text{Na}]^+$ 509.0027 (calc. 509.0025) with the correct isotope pattern.

UV-Vis (CH_2Cl_2): $\lambda_{\text{max}}/\text{nm}$ [$\log(\text{e dm}^3 \text{ mol}^{-1} \text{ cm}^{-1})$] 228 (4.83), 250 (4.78), 301 (4.39), 395 (3.73).

6.4.1.3 3-dmsO yield (209 mg, 0.42 mmol, 39%).



^1H NMR (600 MHz, d_2 -dichloromethane, 298 K): δ 9.56 (d, 1H, $^3J_{\text{H-H}} = 5.9$ Hz, $^3J_{\text{H-Pt}} = 31.3$ Hz, H-1), 7.92 (d, 1H, $^4J_{\text{H-H}} = 2.5$ Hz, $^3J_{\text{H-Pt}} = 52.3$ Hz, H-10), 7.83 (t, 1H, $^3J_{\text{H-H}} = 7.8$ Hz, H-3), 7.62 (d, 1H, $^3J_{\text{H-H}} = 8.2$ Hz, H-4), 7.48 (d, 1H, $^3J_{\text{H-H}} = 8.5$ Hz, H-7), 7.16 (t, 1H, $^3J_{\text{H-H}} = 6.7$ Hz, H-2), 6.72 (dd, $^3J_{\text{H-H}} = 8.5$ Hz, $^4J_{\text{H-H}} = 2.5$ Hz, H-8), 3.83 (s, 3H, $-\text{OCH}_3$), 3.67 (s, 6H, $^3J_{\text{H-Pt}} = 21.3$ Hz, 2 x CH_3).

$^{13}\text{C}\{^1\text{H}\}$ NMR (151 MHz, d_2 -dichloromethane, 298 K): δ 166.4 (s, C-5), 161.7 (s, C-9), 150.1 (s, $^2J_{\text{C-Pt}} = 22.3$ Hz, C-1), 143.0 (s, C-6/11), 140.8 (s, C-3), 137.7 (s, C-6/11), 125.7 (s, $^3J_{\text{C-Pt}} = 49.2$ Hz, C-7), 121.2 (s, $^3J_{\text{C-Pt}} = 30.0$ Hz, C-2), 119.3 (s, $J_{\text{C-Pt}} = 54.0$ Hz, C-10), 118.6 (s, $^3J_{\text{C-Pt}} = 38.6$ Hz, C-4), 111.6 (s, C-8), 55.9 (s, $-\text{OCH}_3$), 47.6 (s, $^3J_{\text{C-Pt}} = 58.5$ Hz, 2 x CH_3).

These NMR data are in accordance with the literature reported data.¹²²

ESI-MS (CH_2Cl_2): m/z $[\text{M}-\text{Cl}]^+$ 457.0539 (calc. 457.0544) with the correct isotope pattern.

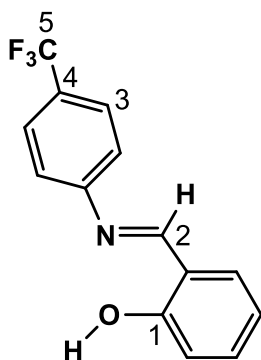
UV-Vis (CH_2Cl_2): $\lambda_{\text{max}}/\text{nm}$ [$\log(\epsilon \text{ dm}^3 \text{ mol}^{-1} \text{ cm}^{-1})$] 239 (4.68), 298 (4.59), 336 (4.16), 381 (4.06).

6.4.2 Synthesis and characterisation of Schiff base ligands

All Schiff base ligands **L-a** to **L-i** were prepared by the same procedure as reported in the literature.¹²⁷ As an example, For **L-a**, an ethanol solution (15 mL) of salicylaldehyde (1.34 g, 0.011 mol) was added to an ethanol solution (15 mL) of 4-(trifluoromethyl)aniline (1.77 g, 0.011 mol)

and stirred at room temperature for 1 h. The mixture was then heated to reflux until complete consumption of the starting materials was observed. Subsequently, ethanol was removed under reduced pressure and crude **L-a** was purified by dissolving in minimal dichloromethane and layering with hexane. The pure material was obtained as a yellow crystalline solid in excellent yield (2.77 g, 0.010 mol, 95%). All ligands are known and the acquired analytical data match the literature reported data.^{128,129,130,131,132}

6.4.2.1 **L-a** yield (2.77 g, 0.010 mol, 95%).



¹H NMR (500 MHz, *d*₂-dichloromethane, 298 K): δ 12.77 (s, 1H, OH), 8.66 (s, 1H, H-2), 7.71–7.70 (m, 2H, H-3), 7.47–7.43 (m, 2H, Ar), 7.42–7.38 (m, 2H, Ar), 7.03–6.97 (m, 2H, Ar).

¹³C{¹H} NMR (126 MHz, *d*₂-dichloromethane, 298 K): δ 165.4 (s, C-2), 161.8 (s, C-1), 152.4 (s, Ar), 134.4 (s, Ar), 133.4 (s, Ar), 129.3–128.5 (q, ²*J*_{C-F} = 32.6 Hz, H-4), 128.1–121.6 (q, ¹*J*_{C-F} = 272.5 Hz, C-5), 127.2–127.1 (q, ³*J*_{C-F} = 3.8 Hz, C-3), 122.1 (s, Ar), 119.9 (s, Ar), 119.6 (s, Ar), 117.7 (s, Ar).

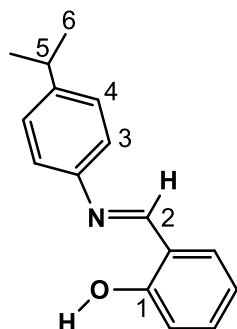
¹⁹F NMR (565 MHz, *d*₂-dichloromethane, 298 K): δ –62.5 (s).

These NMR data are in accordance with the literature reported data.¹²⁸

ESI-MS (CH₂Cl₂): *m/z* [M+H]⁺ 266.0786 (calc. 266.0787).

UV-Vis (CH₂Cl₂): λ_{max} /nm [log(*e* dm³ mol⁻¹ cm⁻¹)] 232 (4.83), 274 (4.70), 340 (4.57).

6.4.2.2 L-c yield (3.37 g, 0.014 mol, 94%).



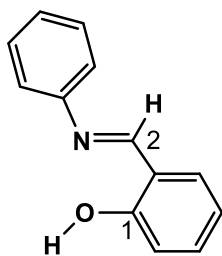
^1H NMR (600 MHz, d_2 -dichloromethane, 298 K): δ 13.29 (s, 1H, OH), 8.67 (s, 1H, H-2), 7.43 (dd, 1H, $^3J_{\text{H-H}} = 7.7$ Hz, $^4J_{\text{H-H}} = 1.7$ Hz, Ar), 7.37 (t, 1H, $^3J_{\text{H-H}} = 7.7$ Hz, Ar), 7.31–7.30 (m, 2H, H-3/4), 7.27–7.25 (m, 2H, H-3/4), 6.99 (d, 1H, $^3J_{\text{H-H}} = 8.4$ Hz, Ar), 6.95 (t, 1H, $^3J_{\text{H-H}} = 7.4$ Hz, Ar), 2.95 (sept, 1H, $^3J_{\text{H-H}} = 6.9$ Hz, H-5), 1.28 (d, 6H, $^3J_{\text{H-H}} = 6.9$ Hz, H-6).

$^{13}\text{C}\{^1\text{H}\}$ NMR (151 MHz, d_2 -dichloromethane, 298 K): δ 162.6 (s, C-2), 161.7 (s, C-1), 148.7 (s, Ar), 146.8 (s, Ar), 133.4 (s, Ar), 132.8 (s, Ar), 128.0 (s, C-3/4), 121.6 (s, C-3/4), 120.0 (s, Ar), 119.5 (s, Ar), 117.5 (s, Ar), 34.4 (s, H-5), 24.3 (s, H-6).

ESI-MS (CH_2Cl_2): m/z $[\text{M}+\text{H}]^+$ 240.1380 (calc. 240.1383).

UV-Vis (CH_2Cl_2): $\lambda_{\text{max}}/\text{nm}$ [$\log(\epsilon \text{ dm}^3 \text{ mol}^{-1} \text{ cm}^{-1})$] 232 (4.95), 270 (4.73), 308 (4.69), 322 (4.76), 344 (4.81).

6.4.2.3 L-d yield (2.25 g, 0.011 mol, 95%).



^1H NMR (600 MHz, d_2 -dichloromethane, 298 K): δ 13.18 (s, 1H, OH), 8.67 (s, 1H, H-2), 7.47-7.45 (m, 3H), 7.40 (1H, t, $^3J_{\text{H-H}} = 7.6$ Hz), 7.33-7.30 (m, 3H), 7.02 (d, 1H, $^3J_{\text{H-H}} = 8.3$ Hz), 6.97 (t, 1H, $^3J_{\text{H-H}} = 7.6$ Hz).

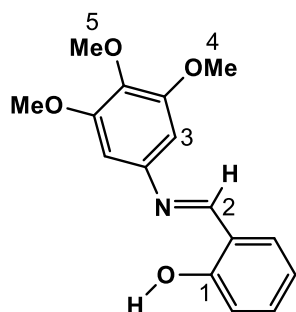
$^{13}\text{C}\{^1\text{H}\}$ NMR (151 MHz, d_2 -dichloromethane, 298 K): δ 163.5 (s, C-2), 161.7 (s, C-1), 149.1 (s, Ar), 133.7 (s, Ar), 133.0 (s, Ar), 130.0 (s, Ar), 127.5 (s, Ar), 121.7 (s, Ar), 119.9 (s, Ar), 119.6 (s, Ar), 117.6 (s, Ar).

These NMR data are in accordance with the literature reported data.¹²⁹

ESI-MS (CH_2Cl_2): m/z $[\text{M}+\text{H}]^+$ 198.0908 (calc. 198.0913).

UV-Vis (CH_2Cl_2): $\lambda_{\text{max}}/\text{nm}$ [$\log(\epsilon \text{ dm}^3 \text{ mol}^{-1} \text{ cm}^{-1})$] 230 (4.99), 270 (4.80), 302 (4.69), 318 (4.73), 340 (4.76).

6.4.2.4 L-e yield (3.96 g, 0.014 mol, 92%).



^1H NMR (600 MHz, d_2 -dichloromethane, 298 K): δ 13.14 (s, 1H, OH), 8.66 (s, 1H, H-2), 7.45 (d, 1H, $^3J_{\text{H-H}} = 7.6$ Hz), 7.38 (t, 1H, $^3J_{\text{H-H}} = 7.6$ Hz), 7.00–7.95 (m, 2H), 6.57 (s, 2H, H-3), 3.88 (s, 6H, 2 x OCH_3), 3.80 (s, 3H, OCH_3).

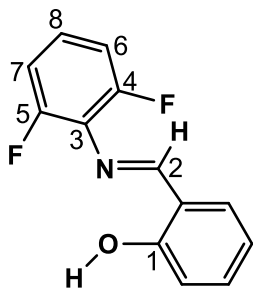
$^{13}\text{C}\{^1\text{H}\}$ NMR (151 MHz, d_2 -dichloromethane, 298 K): δ 162.5 (s, C-2), 161.6 (s, C-1), 154.5 (s, Ar), 144.8 (s, Ar), 137.9 (s, Ar), 133.6 (s, Ar), 132.9 (s, Ar), 119.6 (s, Ar), 117.6 (s, Ar), 99.1 (s, C-3), 93.0 (s, Ar), 61.1 (s, C-5), 56.7 (s, C-4).

These NMR data are in accordance with the literature reported data.¹³⁰

ESI-MS (CH_2Cl_2): m/z $[\text{M}+\text{H}]^+$ 288.1231 (calc. 288.1230).

UV-Vis (CH_2Cl_2): $\lambda_{\text{max}}/\text{nm}$ [$\log(\text{e dm}^3 \text{ mol}^{-1} \text{ cm}^{-1})$] 266 (4.38), 352 (4.51).

6.4.2.5 L-f yield (1.56 g, 0.007 mol, 94%).



^1H NMR (600 MHz, d_2 -dichloromethane, 298 K): δ 12.84 (s, 1H, OH), 8.89 (s, 1H, H-2), 7.44–7.71 (m, 2H), 7.21–7.16 (m, 1H), 7.06–7.01 (m, 3H), 6.97 (t, 1H, $^3J_{\text{H-H}} = 7.6$ Hz).

$^{13}\text{C}\{^1\text{H}\}$ NMR (151 MHz, d_2 -dichloromethane, 298 K): δ 169.6 (t, $^4J_{\text{C-F}} = 5.0$ Hz, C-2), 162.0 (s, C-1), 157.4 (d, $^1J_{\text{C-F}} = 255.5$ Hz, C-4), 157.3 (d, $^1J_{\text{C-F}} = 245.6$ Hz, C-5), 134.5 (s, Ar), 133.5 (s, Ar), 127.3 (t, $^3J_{\text{C-F}} = 10.0$ Hz, C-8), 126.0 (t, $^2J_{\text{C-F}} = 12.9$ Hz, C-3), 119.8 (s, Ar), 199.7 (s, Ar), 117.9 (s, Ar), 112.7 (d, $^2J_{\text{C-F}} = 19.3$ Hz, C-6), 112.6 (d, $^2J_{\text{C-F}} = 19.3$ Hz, C-7).

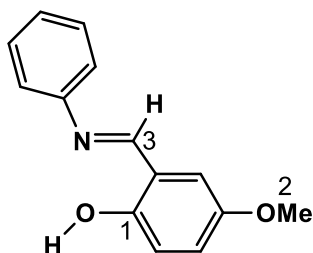
^{19}F NMR (565 MHz, d_2 -dichloromethane, 298 K): δ -123.8 (m).

These NMR data are in accordance with the literature reported data.¹³¹

ESI-MS (CH_2Cl_2): m/z $[\text{M}+\text{H}]^+$ 234.0719 (calc. 234.0725).

UV-Vis (CH_2Cl_2): $\lambda_{\text{max}}/\text{nm}$ [$\log(\epsilon \text{ dm}^3 \text{ mol}^{-1} \text{ cm}^{-1})$] 230 (4.69), 270 (4.57), 300 (4.46), 316 (4.45), 344 (4.45).

6.4.2.6 L-i yield (2.45 g, 0.012 mol, 90%).



^1H NMR (600 MHz, d_2 -dichloromethane, 298 K): δ 12.70 (s, 1H, OH), 8.63 (s, 1H, H-3), 7.44 (t, 2H, $^3J_{\text{H-H}} = 7.8$ Hz), 7.31–7.29 (m, 3H), 7.01–6.99 (m, 1H), 6.94–6.92 (m, 2H), 3.80 (s, 3H, OCH₃).

$^{13}\text{C}\{^1\text{H}\}$ NMR (151 MHz, d_2 -dichloromethane, 298 K): δ 163.2 (s, C-3), 155.9 (s, C-1), 152.9 (s, Ar), 149.2 (s, Ar), 130.0 (s, Ar), 127.5 (s, Ar), 121.7 (s, Ar), 121.0 (s, Ar), 119.5 (s, Ar), 118.4 (s, Ar), 116.0 (s, Ar), 56.4 (s, C-2).

These NMR data are in accordance with the literature reported data.¹³²

ESI-MS (CH_2Cl_2): m/z [M+H]⁺ 228.1019 (calc. 228.1025).

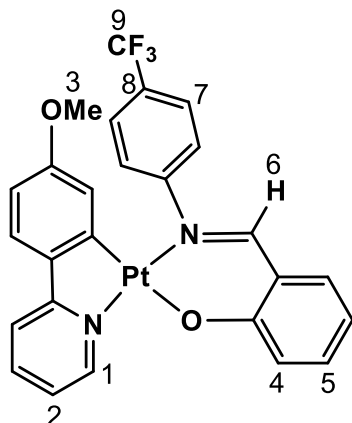
UV-Vis (CH_2Cl_2): $\lambda_{\text{max}}/\text{nm}$ [$\log(\text{e dm}^3 \text{ mol}^{-1} \text{ cm}^{-1})$] 240 (4.63), 274 (4.43), 294 (4.39), 308 (4.38), 376 (4.26).

6.4.3 Synthesis and characterisation of Pt(sal)(ppy) complexes

All Pt(sal)(ppy) complexes were prepared by the same procedure modified from the literature.¹¹³

In the literature procedure, the Pt(sal)(ppy) complexes were synthesised from the [Pt(N[^]C)(μ-Cl)]₂ complexes directly, but herein the [Pt{NC₅H₄-6-(4'-R-C₆H₃)}Cl(κ₁-S-dmsO)] complexes were synthesised first. As an example, for **1a**, a solution of **3-dmsO** (340 mg, 0.69 mmol), 3 equiv. of **L-a** (549 mg, 2.07 mmol) and 10 equiv. of Na₂CO₃ (731 mg, 6.9 mmol) in 2-methoxyethanol (50 mL) was heated to reflux for 20 h under a nitrogen atmosphere. The solvent was then removed under reduced pressure and hexane (15 mL) was added gradually to give an orange precipitate that was subsequently filtered and washed with water (10 mL). Subsequent freeze-drying followed by recrystallisation by slow diffusion of hexane into a dichloromethane solution of the complex resulted in the formation of **1a** in moderate yield (240 mg, 0.37 mmol, 54%). Complexes **1b** and **1d** are known, and the acquired analytical data match the literature reported data.¹¹³

6.4.3.1 1a yield (240 mg, 0.37 mmol, 54%).



^1H NMR (600 MHz, d_2 -dichloromethane, 298 K): δ 9.42 (d, 1H, $^3J_{\text{H-H}} = 5.8$ Hz, $^3J_{\text{H-Pt}} = 33.2$ Hz, H-1), 8.25 (s, 1H, $^3J_{\text{H-Pt}} = 70.6$ Hz, H-6), 7.81–7.78 (m, 3H, ppy), 7.71–7.69 (m, 2H, sal), 7.53–7.49 (m, 2H, sal), 7.36 (d, 1H, $^3J_{\text{H-H}} = 7.9$ Hz, ppy), 7.32 (d, 1H, $^3J_{\text{H-H}} = 8.5$ Hz, ppy), 7.18 (t, 1H, $^3J_{\text{H-H}} = 6.7$ Hz, H-2), 7.06 (d, 1H, $^3J_{\text{H-H}} = 8.6$ Hz, sal), 6.61 (t, 1H, $^3J_{\text{H-H}} = 7.4$ Hz, sal), 6.44 (dd, 1H, $^3J_{\text{H-H}} = 8.5$ and 2.5 Hz, H-5), 5.30 (d, 1H, $^3J_{\text{H-H}} = 2.5$ Hz, H-4), 3.23 (s, 3H, H-3).

$^{13}\text{C}\{^1\text{H}\}$ NMR (151 MHz, d_2 -dichloromethane, 298 K): δ 168.0 (s, ppy), 166.8 (s, sal), 164.5 (s, C-6), 160.3 (s, ppy), 158.2 (s, ppy), 146.6 (s, ppy), 141.3 (s, ppy), 139.4 (s, ppy), 138.9 (s, ppy), 136.6 (s, sal), 135.2 (s, sal), 129.9 (q, $^2J_{\text{C-F}} = 32.3$ Hz, C-8), 126.9 (s, sal), 126.8 (q, $^3J_{\text{C-F}} = 3.8$ Hz, C-7), 124.6 (q, $^1J_{\text{C-F}} = 273.1$ Hz, C-9), 124.9 (s, ppy), 123.3 (s, ppy), 122.3 (s, sal), 120.2 (s, ppy), 118.7 (s, ppy), 118.2 (s, sal), 116.2 (s, sal), 111.0 (s, sal), 55.2 (s, C-3).

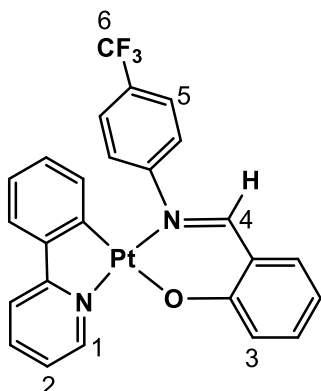
^{19}F NMR (565 MHz, d_2 -dichloromethane, 298 K): δ -62.5 (s).

ESI-MS (CH_2Cl_2): m/z $[\text{M}+\text{H}]^+$ 644.1127 (calc. 644.1119) with the correct isotope pattern.

Elemental analysis found (calc. for $\text{C}_{26}\text{H}_{19}\text{F}_3\text{N}_2\text{O}_2\text{Pt}$): C 48.77 (48.53) H 3.30 (2.98) N 4.05 (4.35).

UV-Vis (CH_2Cl_2): $\lambda_{\text{max}}/\text{nm}$ [$\log(\epsilon \text{ dm}^3 \text{ mol}^{-1} \text{ cm}^{-1})$] 228 (4.66), 268 (4.75), 362 (4.29), 394 (4.07).

6.4.3.2 1b yield (64 mg, 0.104 mmol, 48%).



^1H NMR (600 MHz, d_2 -dichloromethane, 298 K): δ 9.51 (d, 1H, $^3J_{\text{H-H}} = 5.7$ Hz, $^3J_{\text{H-Pt}} = 33.5$ Hz, H-1), 8.27 (s, 1H, $^3J_{\text{H-Pt}} = 70.5$ Hz, H-4), 7.86 (1H, t, $^3J_{\text{H-H}} = 7.7$ Hz, ppy), 7.74–7.73 (m, 2H, sal), 7.69–7.66 (m, 3H, 1 ppy + 2 sal), 7.51 (t, 1H, $^3J_{\text{H-H}} = 7.7$ Hz, ppy), 7.41 (d, 1H, $^3J_{\text{H-H}} = 7.7$ Hz, ppy), 7.37 (d, 1H, $^3J_{\text{H-H}} = 7.7$ Hz, sal), 7.29 (t, 1H, $^3J_{\text{H-H}} = 5.7$ Hz, H-2), 7.07 (m, 1H, ppy), 6.87 (t, 1H, $^3J_{\text{H-H}} = 7.4$ Hz, sal), 6.62 (t, 1H, $^3J_{\text{H-H}} = 7.4$ Hz, sal), 6.55 (t, 1H, $^3J_{\text{H-H}} = 7.4$ Hz, sal), 5.63 (d, 1H, $^3J_{\text{H-H}} = 7.8$ Hz, $^4J_{\text{H-Pt}} = 35.2$ Hz, H-3).

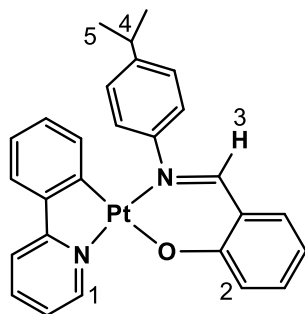
$^{13}\text{C}\{^1\text{H}\}$ NMR (151 MHz, d_2 -dichloromethane, 298 K): δ 176.0 (s, ppy), 168.2 (s, ppy), 166.7 (s, C-4), 164.1 (s, ppy), 152.3 (s, ppy), 158.3 (s, sal), 147.0 (s, ppy), 146.3 (s, sal), 139.6 (s, ppy), 139.1 (s, ppy), 136.5 (s, ppy), 135.2 (s, ppy), 135.0 (s, sal), 129.8 (s, ppy), 129.6 (s, ppy), 129.0 (s, sal), 126.6 (q, $^3J_{\text{C-F}} = 3.7$ Hz, C-5), 122.6 (q, $^1J_{\text{C-F}} = 313.8$ Hz, C-6), 123.3 (s, sal), 122.3 (s, sal), 119.4 (s, sal), 118.9 (s, sal), 116.2 (s, sal).

^{19}F NMR (565 MHz, d_2 -dichloromethane, 298 K): δ -62.5 (s).

ESI-MS (CH_2Cl_2): m/z $[\text{M}+\text{H}]^+$ 614.1005 (calc. 614.0943) with the correct isotope pattern.

UV-Vis (CH_2Cl_2): $\lambda_{\text{max}}/\text{nm}$ [$\log(\epsilon \text{ dm}^3 \text{ mol}^{-1} \text{ cm}^{-1})$] 228 (4.55), 264 (4.69), 362 (4.13), 396 (3.86).

These analytical data are in accordance with the literature reported data.¹¹³

6.4.3.3 1c yield (154 mg, 0.26 mmol, 27%).

¹H NMR (500 MHz, *d*₂-dichloromethane, 298 K): δ 9.54 (d, 1H, ³*J*_{H-H} = 6.1 Hz, ³*J*_{H-Pt} = 33.5 Hz, H-1), 8.27 (s, 1H, ³*J*_{H-Pt} = 73.8 Hz, H-3), 7.85 (t, 1H, ³*J*_{H-H} = 7.7 Hz, ppy), 7.66 (m, 1H, ppy), 7.48 (m, 3H, 1 ppy + 2 sal), 7.39 (dd, 1H, *J*_{H-H} = 7.7 and 1.4 Hz, ppy), 7.36 (dd, 1H, *J*_{H-H} = 7.9 and 1.7 Hz, ppy), 7.28 (m, 3H, 1 ppy + 2 sal), 7.07 (m, 1H, ppy), 6.85 (t, 1H, ³*J*_{H-H} = 7.4 Hz, sal), 6.59 (t, 1H, ³*J*_{H-H} = 7.4 Hz, sal), 6.52 (t, 1H, ³*J*_{H-H} = 7.7 Hz, sal), 5.60 (d, 1H, ³*J*_{H-H} = 8.1 Hz, ⁴*J*_{H-Pt} = 38.2 Hz, H-2), 2.99 (sept, 1H, ³*J*_{H-H} = 6.9 Hz, H-4), 1.30 (d, 6H, ³*J*_{H-H} = 6.9 Hz, H-5).

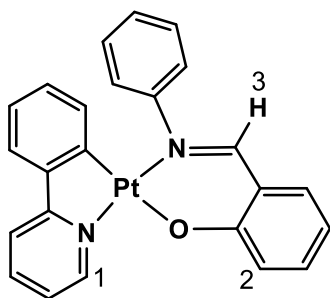
¹³C{¹H} NMR (126 MHz, *d*₂-dichloromethane, 298 K): δ 168.3 (s, ppy), 166.2 (s, ppy), 163.5 (s, C-3), 153.3 (s, sal), 149.1 (s, sal), 146.9 (s, ppy) 146.2 (s, ppy), 139.5 (s, ppy), 139.4 (s, ppy) 135.8 (s, sal), 135.2 (s, sal), 135.0 (s, sal), 128.7 (s, sal), 127.2 (s, ppy), 125.9 (s, sal), 123.3 (s, ppy), 123.1 (s, ppy), 122.9 (s, ppy), 122.4 (s, sal), 121.4 (s, sal), 118.8 (s, ppy), 115.8 (s, sal), 34.4 (s, C-4), 24.5 (s, C-5).

ESI-MS (CH₂Cl₂): *m/z* [M+H]⁺ 588.1608 (calc. 588.1609) with the correct isotope pattern.

The sample is pure to the detection limit of NMR spectroscopy.

UV-Vis (CH₂Cl₂): λ_{max}/nm [log(*e* dm³ mol⁻¹ cm⁻¹)] 266 (4.54), 310 (4.02), 362 (3.99), 398 (3.76).

6.4.3.4 1d yield (365 mg, 0.67 mmol, 48%).



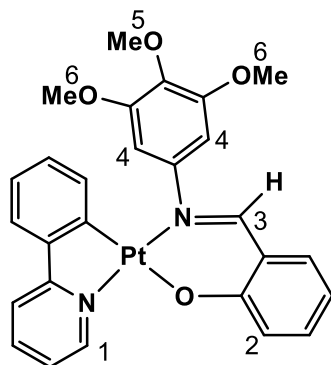
^1H NMR (400 MHz, d_2 -dichloromethane, 298 K): δ 9.54 (d, 1H, $^3J_{\text{H-H}} = 6.0$ Hz, $^3J_{\text{H-Pt}} = 34.9$ Hz, H-1), 8.27 (s, 1H, $^3J_{\text{H-Pt}} = 76.5$ Hz, H-3), 7.85 (t, 1H, $^3J_{\text{H-H}} = 7.8$ Hz, ppy), 7.67–7.65 (m, 1H, ppy), 7.58–7.57 (m, 2H, sal), 7.48 (t, 1H, $^3J_{\text{H-H}} = 7.7$ Hz, ppy), 7.42–7.33 (m, 5H, 2 ppy + 3 sal), 7.28 (t, 1H, $^3J_{\text{H-H}} = 6.7$ Hz, ppy), 7.07–7.05 (m, 1H, ppy), 6.85 (t, 1H, $^3J_{\text{H-H}} = 7.4$ Hz, sal), 6.60 (t, 1H, $^3J_{\text{H-H}} = 7.4$ Hz, sal), 6.54 (t, 1H, $^3J_{\text{H-H}} = 7.5$ Hz, sal), 5.68 (d, 1H, $^3J_{\text{H-H}} = 7.7$ Hz, $^4J_{\text{H-Pt}} = 35.4$ Hz, H-2).

$^{13}\text{C}\{^1\text{H}\}$ NMR (151 MHz, d_2 -dichloromethane, 298 K): δ 168.3 (s, ppy), 166.3 (s, sal), 163.9 (s, C-3), 155.5 (s, sal), 147.0 (s, ppy), 146.2 (s, ppy), 139.4 (s, ppy), 135.9 (s, ppy), 135.1 (s, sal), 129.4 (s, sal), 128.9 (s, sal), 127.8 (s, ppy), 126.2 (s, ppy), 123.4 (s, ppy), 123.1 (s, ppy), 123.0 (s, sal), 122.4 (s, sal), 121.4 (s, ppy), 118.8 (s, ppy), 115.9 (s, sal).

ESI-MS (CH_2Cl_2): m/z $[\text{M}+\text{H}]^+$ 546.1146 (calc. 546.1140) with the correct isotope pattern.

UV-Vis (CH_2Cl_2): $\lambda_{\text{max}}/\text{nm}$ [$\log(\epsilon \text{ dm}^3 \text{ mol}^{-1} \text{ cm}^{-1})$] 228 (4.33), 266 (4.45), 308 (3.91), 362 (3.89), 398 (3.64).

These analytical data are in accordance with the literature reported data.¹¹³

6.4.3.5 1e yield (109 mg, 0.17 mmol, 36%).

^1H NMR (600 MHz, d_2 -dichloromethane, 298 K): δ 9.58 (d, 1H, $^3J_{\text{H-H}} = 5.7$ Hz, $^3J_{\text{H-Pt}} = 33.7$ Hz, H-1), 8.35 (s, 1H, $^3J_{\text{H-Pt}} = 71.4$ Hz, H-3), 7.85 (t, 1H, $^3J_{\text{H-H}} = 7.7$ Hz, ppy), 7.67–7.66 (m, 1H, ppy), 7.49 (t, 1H, $^3J_{\text{H-H}} = 7.7$ Hz, ppy), 7.40 (dd, 1H, $J_{\text{H-H}} = 7.6$ and 1.2 Hz, ppy), 7.37 (dd, 1H, $J_{\text{H-H}} = 7.9$ and 1.6 Hz, ppy), 7.27 (t, 1H, $^3J_{\text{H-H}} = 6.7$ Hz, ppy), 7.06 (d, 1H, $^3J_{\text{H-H}} = 8.4$ Hz, ppy), 6.89 (t, 1H, $^3J_{\text{H-H}} = 7.4$ Hz, sal), 6.83 (s, 2H, H-4), 6.65 (t, 1H, $^3J_{\text{H-H}} = 7.6$ Hz, sal), 6.61 (t, 1H, $^3J_{\text{H-H}} = 7.4$ Hz, sal), 5.79 (d, 1H, $^3J_{\text{H-H}} = 7.9$ Hz, H-2), 3.81 (s, 3H, H-5), 3.76 (s, 6H, H-6).

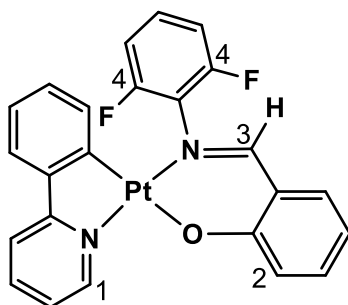
$^{13}\text{C}\{^1\text{H}\}$ NMR (151 MHz, d_2 -dichloromethane, 298 K): δ 168.4 (s, ppy), 166.3 (s, ppy), 163.2 (s, C-3), 153.7 (s, sal), 151.2 (s, sal), 146.9 (s, sal), 139.4 (s, ppy), 138.2 (s, ppy), 135.9 (s, ppy), 135.0 (s, sal), 128.9 (s, sal), 123.3 (s, ppy), 123.1 (s, ppy), 123.0 (s, ppy), 122.2 (s, sal), 121.3 (s, sal), 119.9 (s, ppy), 118.8 (s, ppy), 118.1 (s, ppy), 115.9 (s, sal), 104.3 (s, sal), 93.0 (s, sal), 61.5 (s, C-5), 56.9 (s, 2 x C-6).

ESI-MS (CH_2Cl_2): m/z $[\text{M}+\text{H}]^+$ 636.1468 (calc. 636.1457) with the correct isotope pattern.

The sample is pure to the detection limit of NMR spectroscopy.

UV-Vis (CH_2Cl_2): $\lambda_{\text{max}}/\text{nm}$ [$\log(\epsilon \text{ dm}^3 \text{ mol}^{-1} \text{ cm}^{-1})$] 228 (4.45), 264 (4.44), 310 (3.94), 362 (3.92), 396 (3.67).

6.4.3.6 1f yield (136 mg, 0.23 mmol, 54%).



^1H NMR (600 MHz, d_2 -dichloromethane, 298 K): δ 9.55 (d, 1H, $^3J_{\text{H-H}} = 5.8$ Hz, $^3J_{\text{H-Pt}} = 35.5$ Hz, H-1), 8.19 (s, 1H, $^3J_{\text{H-Pt}} = 73.1$ Hz, H-3), 7.84 (t, 1H, $^3J_{\text{H-H}} = 7.7$ Hz, ppy), 7.66–7.65 (m, 1H, ppy), 7.56 (t, 1H, $^3J_{\text{H-H}} = 7.7$ Hz, sal), 7.45 (d, 1H, $^3J_{\text{H-H}} = 7.7$ Hz, ppy), 7.36–7.31 (m, 2H, sal), 7.27 (t, 1H, $^3J_{\text{H-H}} = 6.6$ Hz, ppy), 7.11–7.07 (m, 3H, ppy), 6.92 (t, 1H, $^3J_{\text{H-H}} = 7.4$ Hz, sal), 6.65–6.59 (m, 2H, sal), 5.60 (d, 1H, $^3J_{\text{H-H}} = 7.9$ Hz, $^4J_{\text{H-Pt}} = 37.2$ Hz, H-2).

$^{13}\text{C}\{^1\text{H}\}$ NMR (151 MHz, d_2 -dichloromethane, 298 K): δ 168.1 (s, C-3), 166.7 (d, $^3J_{\text{C-F}} = 4.8$ Hz, sal), 158.2–156.6 (dd, 2C, $^1J_{\text{C-F}} = 249.9$ and $^3J_{\text{C-F}} = 3.5$ Hz, C-4), 146.9 (s, ppy), 146.7 (s, ppy), 139.4 (s, ppy), 137.6 (s, ppy), 136.8 (s, ppy), 135.2 (s, sal), 132.2 (s, sal), 129.0 (s, ppy), 128.6 (t, $^2J_{\text{C-F}} = 9.6$ Hz, sal), 123.9 (s, ppy), 123.6 (s, ppy), 123.5 (s, sal), 122.0 (s, sal), 121.5 (s, sal), 118.8 (s, ppy), 116.2 (s, ppy), 112.9 (d, $^2J_{\text{C-F}} = 19.7$ Hz, sal), 112.7 (d, $^2J_{\text{C-F}} = 19.7$ Hz, sal).

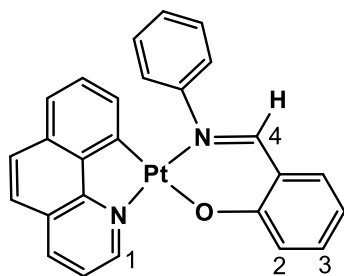
^{19}F NMR (565 MHz, d_2 -dichloromethane, 298 K): δ -120.1 (dd).

ESI-MS (CH_2Cl_2): m/z $[\text{M}+\text{H}]^+$ 582.0943 (calc. 582.0951) with the correct isotope pattern.

Elemental analysis found (calc. for $\text{C}_{24}\text{H}_{16}\text{F}_2\text{N}_2\text{OPT}$): C 49.96 (49.57) H 3.09 (2.77) N 4.69 (4.82).

UV-Vis (CH_2Cl_2): $\lambda_{\text{max}}/\text{nm}$ [$\log(\epsilon \text{ dm}^3 \text{ mol}^{-1} \text{ cm}^{-1})$] 230 (4.54), 260 (4.67), 300 (4.17), 362 (4.19).

6.4.3.7 1g yield (31 mg, 0.055 mmol, 38%).



^1H NMR (600 MHz, d_1 -chloroform, 298 K): δ 9.76 (d, 1H, $^3J_{\text{H-H}} = 5.2$ Hz, $^3J_{\text{H-Pt}} = 33.4$ Hz, H-1), 8.29–8.26 (m, 2H, H-4/ ppy), 7.69–7.68 (m, 1H, ppy), 7.62–7.59 (m, 3H, ppy), 7.53–7.50 (m, 2H, ppy), 7.47–7.44 (2H, t, $^3J_{\text{H-H}} = 7.6$ Hz, sal), 7.39–7.35 (m, 3H, sal), 7.18 (d, 1H, $^3J_{\text{H-H}} = 8.4$ Hz, sal), 6.97 (t, 1H, $^3J_{\text{H-H}} = 7.6$ Hz, H-3), 6.62 (t, 1H, $^3J_{\text{H-H}} = 7.4$ Hz, sal), 5.65 (d, 1H, $^3J_{\text{H-H}} = 7.6$ Hz, H-2).

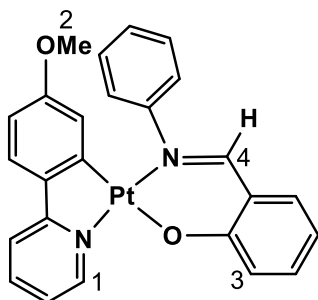
$^{13}\text{C}\{^1\text{H}\}$ NMR (151 MHz, d_1 -chloroform, 298 K): δ 165.7 (s, C-4), 163.0 (s, ppy), 157.1 (s, ppy), 155.4 (s, ppy), 145.6 (s, ppy), 142.7 (s, sal), 137.5 (ppy), 135.6 (s, sal), 135.5 (s, sal), 134.7 (s, sal), 133.3 (s, sal), 132.1 (s, sal), 129.7 (s, ppy), 129.2 (s, ppy), 127.4 (s, ppy), 126.6 (s, ppy), 125.8 (s, ppy), 122.9 (s, sal), 122.7 (s, sal), 121.9 (s, ppy), 121.3 (s, sal), 119.9 (s, ppy), 115.7 (s, sal).

ESI-MS (CH_2Cl_2): m/z $[\text{M}+\text{H}]^+$ 570.1142 (calc. 570.1140) with the correct isotope pattern.

The sample is pure to the detection limit of NMR spectroscopy.

UV-Vis (CH_2Cl_2): $\lambda_{\text{max}}/\text{nm}$ [$\log(\text{e dm}^3 \text{ mol}^{-1} \text{ cm}^{-1})$] 240 (4.51), 288 (3.93), 318 (3.92), 344 (3.94), 364 (3.80), 408 (3.62).

6.4.3.8 1h yield (42 mg, 0.073 mmol, 38%).



^1H NMR (600 MHz, d_2 -dichloromethane, 298 K): δ 9.50 (d, 1H, $^3J_{\text{H-H}} = 5.7$ Hz, $^3J_{\text{H-Pt}} = 33.2$ Hz, H-1), 8.28 (s, 1H, $^3J_{\text{H-Pt}} = 70.7$ Hz, H-4), 7.78 (t, 1H, $^3J_{\text{H-H}} = 7.5$ Hz, ppy), 7.66 (d, 2H, $^3J_{\text{H-H}} = 7.6$ Hz, sal), 7.53 (d, 1H, $^3J_{\text{H-H}} = 7.9$ Hz, ppy), 7.47 (t, 1H, $^3J_{\text{H-H}} = 7.5$ Hz, ppy), 7.42 (t, 2H, $^3J_{\text{H-H}} = 7.3$ Hz, sal), 7.35–7.30 (m, 3H, 1 ppy + 2 sal), 7.18 (1H, t, $^3J_{\text{H-H}} = 6.3$ Hz, ppy), 7.06 (d, 1H, $^3J_{\text{H-H}} = 8.6$ Hz, ppy), 6.60 (t, 1H, $^3J_{\text{H-H}} = 7.3$ Hz, sal), 6.43 (1H, d, $^3J_{\text{H-H}} = 8.3$ Hz, sal), 5.42 (s, 1H, H-3), 3.24 (s, 3H, H-2).

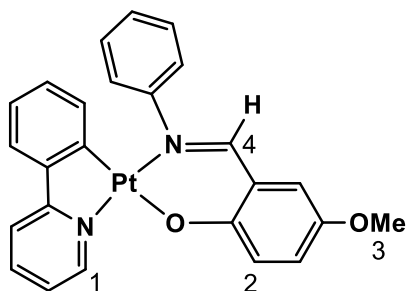
$^{13}\text{C}\{^1\text{H}\}$ NMR (151 MHz, d_2 -dichloromethane, 298 K): δ 168.1 (s, sal), 166.4 (s, C-4), 164.4 (s, ppy), 160.2 (s, ppy), 155.4 (s, sal), 146.6 (s, ppy), 141.7 (s, ppy), 139.3 (s, ppy), 138.8 (s, ppy), 136.0 (s, ppy), 135.1 (s, sal), 129.6 (s, sal), 128.0 (s, ppy), 126.2 (s, ppy), 124.8 (s, ppy), 123.0 (s, sal), 122.5 (s, ppy), 120.1 (s, sal), 118.5 (s, sal), 118.1 (s, sal), 116.0 (s, sal), 111.0 (s, sal), 55.5 (s, C-2).

ESI-MS (CH_2Cl_2): m/z $[\text{M}+\text{H}]^+$ 576.1251 (calc. 576.1245) with the correct isotope pattern.

Elemental analysis found (calc. for $\text{C}_{25}\text{H}_{20}\text{N}_2\text{O}_2\text{Pt}$): C 52.44 (52.17) H 3.21 (3.50) N 4.80 (4.87).

UV-Vis (CH_2Cl_2): $\lambda_{\text{max}}/\text{nm}$ [$\log(\text{e dm}^3 \text{ mol}^{-1} \text{ cm}^{-1})$] 230 (4.51), 270 (4.63), 360 (4.18), 394 (3.96).

6.4.3.9 1i yield (82.5 mg, 0.143 mmol, 44%).



^1H NMR (600 MHz, d_2 -dichloromethane, 298 K): δ 9.58 (d, 1H, $^3J_{\text{H-H}} = 5.8$ Hz, $^3J_{\text{H-Pt}} = 33.2$ Hz, H-1), 8.26 (s, 1H, $^3J_{\text{H-Pt}} = 74.6$ Hz, H-4), 7.84 (t, 1H, $^3J_{\text{H-H}} = 7.8$ Hz, ppy), 7.66 (d, 1H, $^3J_{\text{H-H}} = 7.9$ Hz, ppy), 7.58–7.56 (m, 2H, ppy), 7.42–7.38 (m, 3H, 2 ppy + 1 sal), 7.34–7.32 (m, 1H, sal), 7.27 (t, 1H, $^3J_{\text{H-H}} = 6.7$ Hz, ppy), 7.19–7.16 (m, 1H, sal), 7.03–7.00 (m, 1H, sal), 6.85 (t, 1H, $^3J_{\text{H-H}} = 7.5$ Hz, sal), 6.77 (1H, d, $^3J_{\text{H-H}} = 3.2$ Hz, sal), 6.53 (t, 1H, $^3J_{\text{H-H}} = 7.5$ Hz, sal), 5.68 (d, 1H, $^3J_{\text{H-H}} = 8.0$ Hz, $^4J_{\text{H-Pt}} = 37.5$ Hz, H-2), 3.75 (s, 3H, H-3).

$^{13}\text{C}\{^1\text{H}\}$ NMR (151 MHz, d_2 -dichloromethane, 298 K): δ 168.3 (s, ppy), 163.1 (s, C-4) 162.0 (s, sal), 155.6 (s, sal), 150.2 (s, sal), 146.9 (s, ppy), 146.2 (s, ppy), 139.8 (s, sal), 139.4 (s, ppy), 135.1 (s, ppy), 129.3 (s, sal), 128.8 (s, sal), 127.7 (s, ppy), 126.8 (s, sal), 126.3 (s, ppy), 124.1 (s, sal), 123.4 (s, sal), 123.0 (s, ppy), 121.4 (s, ppy), 120.6 (s, ppy), 118.8 (s, ppy), 113.8 (s, sal), 56.4 (s, C-3).

ESI-MS (CH_2Cl_2): m/z $[\text{M}+\text{H}]^+$ 576.1254 (calc. 576.1245) with the correct isotope pattern.

Elemental analysis found (calc. for $\text{C}_{25}\text{H}_{20}\text{N}_2\text{O}_2\text{Pt}$): C 52.50 (52.17) H 3.12 (3.50) N 4.81 (4.87).

UV-Vis (CH_2Cl_2): $\lambda_{\text{max}}/\text{nm}$ [$\log(\epsilon \text{ dm}^3 \text{ mol}^{-1} \text{ cm}^{-1})$] 230 (4.68), 266 (4.77), 310 (4.25), 366 (4.22), 408 (4.01), 476 (3.86).

6.5 Chapter Three Experimental

6.5.1 Performance of Pt(sal)(ppy) complexes in thermal and photoactivated hydrosilylation reactions

Hydrosilylation was conducted as per the standard procedure outlined in section 6.3.2, using precatalysts **1a** – **1i** at 0.0025 M. Each precatalyst was assessed under thermal (no irradiation) and photoactivated (10 – 120 s irradiation) conditions.

6.5.2 Substrate scope

Hydrosilylation was conducted as per the standard photoactivated procedure outlined in section 6.3.2, but **VTMS** was replaced by a variety of alkene substrates (0.8 – 1.2 M). In each case, the reaction was monitored thermally for ~1 h to determine the latency period, and then irradiated for 120 s. **MD'M** and the alkene substrate (vinyltrimethoxysilane, 3-Buten-2-one, styrene, 4-methoxystyrene, oct-1-ene, cyclohexene, norbornadiene, *trans*-2-octene or acetone) were used in a 1:1 ratio. The selectivity of each substrate was determined by ^1H NMR and / or ^{29}Si NMR spectroscopy.

Hydrosilylation of vinyltrimethylsilane

^1H NMR (400 MHz, d_2 -dichloromethane, 298 K): beta product, δ 0.48 – 0.40 (m, 4H, Si-CH₂-CH₂-Si), 0.13 (s, 18H, 2 x Si(CH₃)₃), 0.04 (s, 3H, Si-CH₃), 0.01 (s, 9H, Si(CH₃)₃). These analytical data match the values reported in the literature.¹⁰⁵

^{29}Si NMR (119 MHz, d_2 -dichloromethane, 298 K): beta product, δ 6.9 (s, 2 x Si(CH₃)₃), 3.1 (s, Si(CH₃)₃), -20.7 (s, Si-CH₃).

Hydrosilylation of vinyltrimethoxysilane

¹H NMR (400 MHz, *d*₂-dichloromethane, 298 K): beta product, δ 3.54 (s, 9H, Si-(OCH₃)₃), 0.59 – 0.44 (m, 4H, Si-CH₂-CH₂-Si), 0.11 (s, 18H, 2 x Si-(CH₃)₃), 0.03 (s, 3H, Si-CH₃). These analytical data match the values reported in the literature.¹⁹⁹

¹H NMR (400 MHz, *d*₂-dichloromethane, 298 K): alpha product, δ 1.05 (d, 3H, ³J_{H-H} = 7.4 Hz, CH₃). No other signals can be distinguished due to signal overlap with the beta product.

²⁹Si NMR (119 MHz, *d*₂-dichloromethane, 298 K): beta product, δ 7.2 (s, 2 x Si-(CH₃)₃), -21.5 (Si-CH₃), -41.5 (s, Si-(OCH₃)₃). These analytical data match the values reported in the literature.¹⁹⁹

²⁹Si NMR (119 MHz, *d*₂-dichloromethane, 298 K): alpha product, δ 7.2 (s, 2 x Si-(CH₃)₃), -23.1 (s, Si-CH₃), -42.5 (s, Si-(OCH₃)₃).

Hydrosilylation of oct-1-ene

¹H NMR (400 MHz, *d*₂-dichloromethane, 298 K): beta product, δ 1.33–1.31 (m, 12H, 6 x CH₂), 0.91–0.89 (m, 3H, CH₃), 0.51–0.47 (m, 2H, Si-CH₂), 0.12 (s, 18H, 2 x Si-(CH₃)₃), 0.03 (s, 3H, Si-CH₃). These analytical data match the values reported in the literature.^{105,159}

²⁹Si NMR (119 MHz, *d*₂-dichloromethane, 298 K): beta product, δ 6.8 (s, 2 x Si-(CH₃)₃), -21.2 (s, Si-CH₃).

Hydrosilylation of 3-Buten-2-one

¹H NMR (400 MHz, *d*₂-dichloromethane, 298 K): beta product, δ 2.43 (q, 2H, ³J_{H-H} = 7.4 Hz, CH₂), 1.80 (s, 3H, CH₃), 1.03 (t, 2H, ³J_{H-H} = 7.4 Hz, Si-CH₂), 0.10 (s, 18H, 2 x Si-(CH₃)₃).

¹H NMR (400 MHz, *d*₂-dichloromethane, 298 K): alpha product, δ 4.77 (q, 1H, ³J_{H-H} = 6.8 Hz, C-H), 1.74 (s, 1H, CH₃-C=O), 1.54 (d, 3H, ³J_{H-H} = 6.8 Hz, CH₃), 0.13 (s, 18H, 2 x Si-(CH₃)₃).

Hydrosilylation of styrene

¹H NMR (400 MHz, *d*₂-dichloromethane, 298 K): beta product selected signals, δ 2.74–2.72 (m, 2H, CH₂), 0.94–0.92 (m, 2H, CH₂), 0.22 (s, 18H, 2 x Si–(CH₃)₃). Not all signals assigned due to significant signal overlap with starting materials. These analytical data match the values reported in the literature.¹⁶⁰

¹H NMR (400 MHz, *d*₂-dichloromethane, 298 K): alpha product selected signals, δ 2.18 (q, 1H, ³J_{H-H} = 7.4 Hz, C–H), 1.43 (d, 3H, ³J_{H-H} = 7.4 Hz, CH₃), 0.23 (s, 18H, 2 x Si–(CH₃)₃). Not all signals assigned due to significant signal overlap with starting materials.

Hydrosilylation of 4-methoxystyrene

¹H NMR (400 MHz, *d*₂-dichloromethane, 298 K): beta product selected signals δ 3.80 (s, 3H, O–CH₃), 2.66–2.63 (m, 2H, CH₂), 0.87–0.84 (m, 2H, CH₂), 0.18 (s, 18H, 2 x Si–(CH₃)₃). Not all signals assigned due to significant signal overlap with starting materials. These analytical data match the values reported in the literature.¹⁶⁰

¹H NMR (400 MHz, *d*₂-dichloromethane, 298 K): alpha product selected signals δ 3.83 (s, 3H, O–CH₃), 2.09 (q, 1H, ³J_{H-H} = 7.5 Hz, C–H), 1.36 (d, 3H, ³J_{H-H} = 7.5 Hz, CH₃), 0.11 (s, 18H, 2 x Si–(CH₃)₃). Not all signals assigned due to significant signal overlap with starting materials.

6.5.3 Recharges with inert substrates

Hydrosilylation was conducted as per the standard photoactivated (120 s irradiation) procedure outlined in section 6.3.2, but stopped after complete conversion of **MD'M** and **VTMS** was observed. A batch of **MD'M** and alkene (cyclohexene, *trans*-2-octene or norbornadiene) at the 1:1 ratio was then added to the NMR tube without further irradiation.

6.5.4 Curing times in commercial substrates

This set of experiments were conducted as part of a placement at Johnson Matthey Technology Centre with the assistance of Dr Samuel Douglas. To assess the curing times of precatalysts **1a**, **1b**, **1d** and **1i** in the commercial substrates, a series of cuvette tests were conducted. In this proof-of-concept study, the precatalyst (50 ppm) was dissolved in dichloromethane (100 μ L) and added to the commercially used methylhydrosiloxane / dimethylsiloxane co-polymer (**HMS**, \sim 1000 g/mol) and vinyl-terminated polydimethylsiloxane (**DMS**, \sim 6000 g/mol) substrates at a ratio of 6.8 **HMS**: 100 **DMS** (2 g total), in line with the established industrial protocol. The mixture was vigorously shaken in a sample vial and then transferred to a cuvette. A stirrer bar was added to the cuvette and then the cuvette was positioned on a stirrer set 110 mm away from a commercial 300 W Xe arc lamp (Oriel instruments model 6259). The lamp was then switched on and a timer was started. The curing time was determined by the time needed for the stirrer bar to stop stirring, due to the increased viscosity of the formulation once cured. No precautions for the ingress of air or water were taken, and the sample was not cooled.

6.5.5 Thermal stability studies

To determine the cure temperatures in the presence of precatalysts **1a**, **1b**, **1d** and **1i**, a stock solution of the precatalyst (50 ppm) in the **HMS/ DMS** (2 g) formulation was prepared and 10 μ L of this solution was pipetted onto an aluminium sample pan for analysis by differential scanning calorimetry. The parameters used are detailed in section 6.1.6.

6.6 Chapter Four Experimental

6.6.1 Tests for determining the active species

6.6.1.1 Mercury poisoning

Hydrosilylation was conducted as per the standard procedure outlined in section 6.3.2. After ~40% conversion to the hydrosilylation product, an excess of elemental mercury (ca. 0.05 mL) was added to the NMR tube which was shaken vigorously. No inhibition of catalysis was observed under thermal or photoactivated conditions, consistent with homogenous catalysis.

6.6.1.2 Dibenzo[a,e]cyclooctatetraene fractional poisoning

Hydrosilylation was conducted as per the standard procedure outlined in section 6.3.2. After ~30% conversion to the hydrosilylation product, 0.3 equiv. (relative to catalyst) of DBCOT in 0.05 mL CD₂Cl₂ was added to the NMR tube. A decrease in catalytic activity was observed under thermal and photoactivated conditions, consistent with homogeneous catalysis.

6.6.2 Determining order in silane

Hydrosilylation was conducted as per the standard procedure outlined in section 6.3.2, but using a 5-fold range of **MD'M** concentrations (0.1 – 2.0 M). A fixed **VTMS** concentration (0.8 – 1.1 M) was used.

6.6.3 Recharges

Hydrosilylation was conducted as per the standard procedure outlined in section 6.3.2, and stopped after full conversion to the hydrosilylation product was observed. A fresh batch of the appropriate stock solution was then added into the NMR tube. Importantly, the 120 s irradiation time was selected so that the recharge could be conducted on the same day as the first charge (to prevent possible change/ decomposition of the catalyst overnight), and the sample was only irradiated after the ~1 h latency period (no further irradiation upon recharging).

6.6.4 Determining order in alkene

Hydrosilylation was conducted as per the standard procedure outlined in section 6.3.2, but using a 3-fold range of **VTMS** concentrations (0.5 – 2 M). A fixed **MD'M** concentration (0.8 – 1.0 M) was used.

6.6.5 Adding substrates before and after irradiation

For all experiments in this series, precatalyst **1a** was used (0.0025 M) and the initial concentrations of **MD'M** and **VTMS** were 0.95 – 1.0 M. The experiments were performed as per the procedure outlined in section 6.3.2, except the latency period was not monitored and substrates were added sequentially as detailed below.

- I. **1a** in d_2 -dichloromethane irradiated 10 s then added **MD'M** and **VTMS**.
- II. **1a** and **MD'M** in d_2 -dichloromethane irradiated 10 s then added **VTMS**.
- III. **1a** and **VTMS** in d_2 -dichloromethane irradiated 10 s then added **MD'M**.

6.6.6 Experiments to determine the effect of alkene on the active species

For all experiments in this series, precatalyst **1b** was used (0.0025 M) in d_2 -dichloromethane and the initial concentrations of **MD'M** and **VTMS** were 0.8 – 1.1 M. The relevant alkene was added in at the same time as **MD'M** and **VMTS** (0.15 M cyclohexene, 0.09 M *trans*-2-octene, 0.14 M norbornadiene), and then the sample was inserted into the spectrometer for ~1 h to monitor the latency period, before being irradiated for 120 s with the 365 nm LED. The sample was then returned to the spectrometer and the concentration of beta product forming over time was monitored by in-situ ^1H NMR spectroscopy. The kinetics were probed using the initial rates method, monitoring the rate of beta product formation for the first 5 data points after catalytic activity had been established.

6.6.7 Preparation of d_1 -hexamethylsiloxymethylsilane

Deuterated hexamethylsiloxymethylsilane was prepared in accordance with the literature procedure.²⁰⁰ To a solution of hexamethylsiloxymethylsilane (8.0 g, 36 mmol) in THF (10 mL) was added $\text{Rh}(\text{PPh}_3)_3\text{Cl}$ (190 mg, 0.19 mmol). The mixture was degassed by three successive freeze-pump-thaw (FPT) cycles and then charged with D_2 (3 bar) and stirred vigorously at 25 °C. The FPT process was repeated after 2 and 4 h to remove excess HD and the solution was each time recharged with D_2 (3 bar). The product was obtained as a colourless liquid via distillation in good yield (6.0 g, 27 mmol, 75%). The ^1H and ^2H NMR data indicate 99.8% D-incorporation.

6.6.8 Hydrosilylation reactions using d_1 -hexamethylsiloxymethylsilane

Hydrosilylation was conducted as per the standard procedure outlined in section 6.3.2, but using d_1 -hexamethylsiloxymethylsilane (0.9 – 1.1 M) labelled at the Si–D position in place of protio hexamethylsiloxymethylsilane. A fixed **VTMS** concentration was used (0.9 – 1.1 M).

6.6.9 Recharge of the solution using d_1 -hexamethylsiloxymethylsilane

Hydrosilylation was conducted as per the standard procedure outlined in section 6.3.2, but using d_1 -hexamethylsiloxymethylsilane (1.0 M) labelled at the Si–D position in place of protio hexamethylsiloxymethylsilane, and stopped after full conversion to the hydrosilylation product was observed. A fresh batch of protio hexamethylsiloxymethylsilane (1.0 M) and vinyltrimethylsilane (1.0 M) from the appropriate stock solution was then added into the NMR tube. Importantly, the 120 s irradiation time was selected so that the recharge could be conducted on the same day as the first charge (to prevent possible change / decomposition of the catalyst overnight), and the sample was only irradiated after the ~1 h latency period (no further irradiation upon re-charging).

6.7 Crystallographic data

	1a	1b	1f	1g
<i>Chemical formula</i>	C ₂₆ H ₁₉ F ₃ N ₂ O ₂ Pt	C ₂₅ H ₁₇ F ₃ N ₂ OPt	C ₂₄ H ₁₆ F ₂ N ₂ OPt	C ₂₆ H ₁₈ N ₂ OPt
<i>Formula weight</i>	643.52	613.49	581.48	569.51
<i>Temperature (K)</i>	110	110	110	150
<i>Crystal system</i>	Monoclinic	Monoclinic	Monoclinic	Monoclinic
<i>Space group</i>	P2 ₁ /c	P2 ₁ /c	P2 ₁ /n	Cc
<i>a (Å)</i>	23.8137(2)	22.76126(10)	15.4703(2)	19.6072(3)
<i>b (Å)</i>	6.10822(5)	5.95793(2)	7.4355(1)	6.2393(1)
<i>c (Å)</i>	15.27755(13)	14.84159(7)	16.5876(2)	15.9568(2)
<i>α (°)</i>	90	90	90	90
<i>β (°)</i>	107.8118(9)	98.2179(4)	100.756(1)	97.249(1)
<i>γ (°)</i>	90	90	90	90
<i>V (Å³)</i>	2115.74(3)	1991.999(15)	1874.54(4)	1936.48(5)
<i>Z</i>	4	4	4	4
<i>r_{calc} (g cm⁻³)</i>	2.020	2.046	2.060	1.953
<i>μ (mm⁻¹)</i>	12.893	13.615	14.343	13.715
<i>Reflections collected</i>	19796	52402	12228	14021
<i>Unique reflections</i>	4347	4195	3581	3664
<i>Restraints/parameters</i>	0/308	0/289	0/271	2/272
<i>R_{int}</i>	0.0281	0.0363	0.0322	0.0261
<i>R₁ [I > 2σ(I)]</i>	0.0200	0.0179	0.0192	0.0217
<i>wR₂ [I > 2σ(I)]</i>	0.0531	0.0466	0.0435	0.0554
<i>GoF</i>	1.071	1.086	1.054	1.037
<i>Residual electron density (e Å⁻³)</i>	1.21/ -0.63	0.51/ -0.94	0.47/ -0.68	0.47/ -0.95
<i>CCDC no.</i>	2313862	2313861	2313863	n/a

Appendix

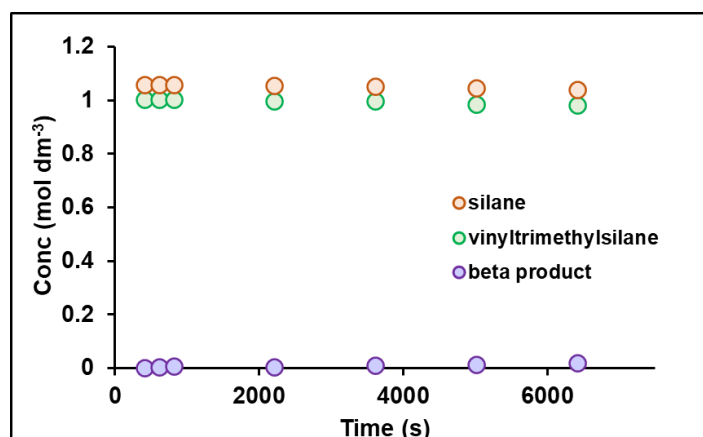
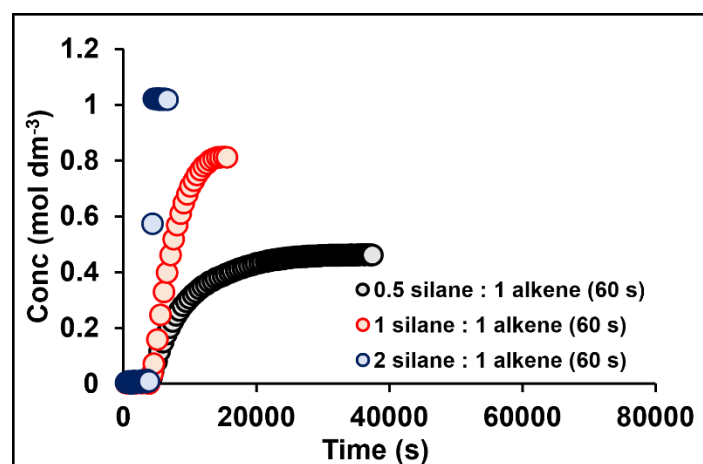
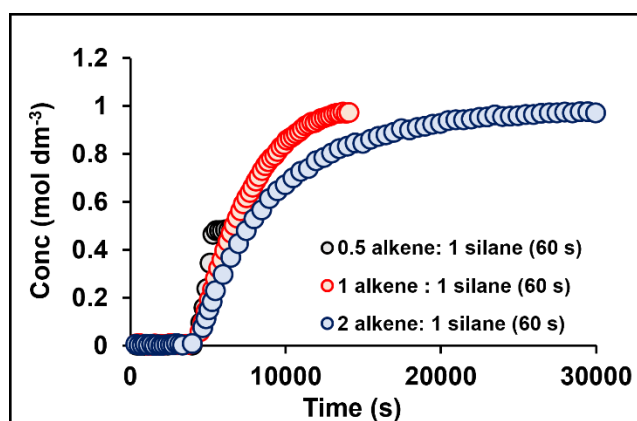


Figure A.1. Expanded region of the latency period in the thermal hydrosilylation reaction detailed in Figure 3.11.



Ratio	Initial Rate (mol dm ⁻³ s ⁻¹)
0.5 silane : 1 alkene	$(7.36 \pm 0.18) \times 10^{-5}$
1 silane : 1 alkene	$(1.71 \pm 0.01) \times 10^{-4}$
2 silane : 1 alkene	-

Figure A.2. Concentration-time profiles of beta product formation during the photoactivated hydrosilylation reaction between **MD'M** and **VTMS** using **1b** as a precatalyst. Reaction conditions as detailed in section 4.3.2, with 60 s irradiation. All plots are time-shifted to 3000 s to show the same latency period. The table shows the initial rates extracted from the first 5 data points following irradiation.



Ratio	Initial Rate (mol dm ⁻³ s ⁻¹)
0.5 alkene : 1 silane	$(4.4 \pm 0.5) \times 10^{-4}$
1 alkene : 1 silane	$(2.23 \pm 0.03) \times 10^{-4}$
2 alkene : 1 silane	$(1.89 \pm 0.04) \times 10^{-4}$

Figure A.3. Concentration-time profiles of beta product formation during the photoactivated hydrosilylation reaction between **MD'M** and **VTMS** using **1a** as a precatalyst. Reaction conditions as detailed in section 4.4.1, with 60 s irradiation. All plots are time-shifted to 4500 s to show the same latency period. The table shows the initial rates extracted from the first 5 data points following irradiation.

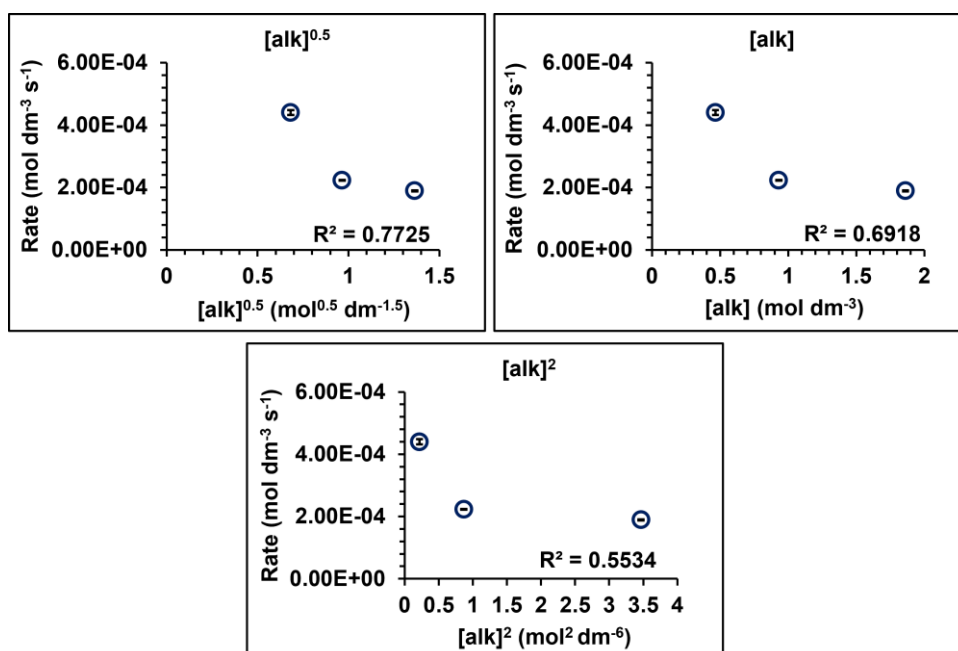
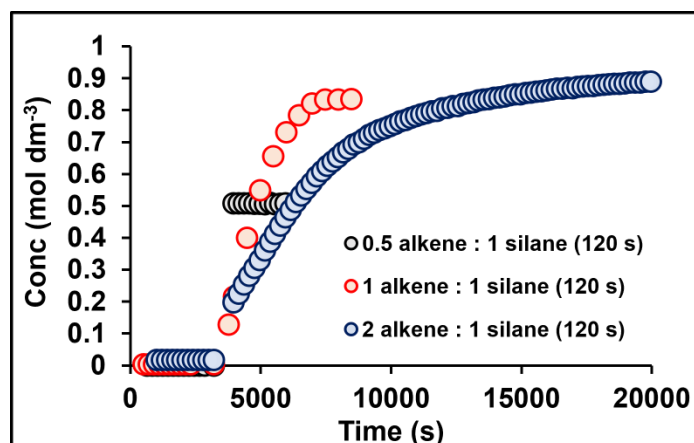


Figure A.4. Rate-concentration profiles for half, first and second order in **VTMS** using the rates for beta product formation in the hydrosilylation reaction between **MD'M** and **VTMS** with precatalyst **1a**. Reaction conditions as detailed in section 4.4.1, with 60 s irradiation.



Ratio	Initial Rate (mol dm ⁻³ s ⁻¹)
0.5 alkene : 1 silane	-
1 alkene : 1 silane	$(5.23 \pm 0.12) \times 10^{-4}$
2 alkene : 1 silane	$(6.01 \pm 0.02) \times 10^{-5}$

Figure A.5. Concentration-time profiles of beta product formation during the photoactivated hydrosilylation reaction between **MD'M** and **VTMS** using **1b** as a precatalyst. Reaction conditions as detailed in section 4.4.2, with 120 s irradiation. All plots are time-shifted to 3200 s to show the same latency period. The table shows the initial rates extracted from the first 5 data points following irradiation.

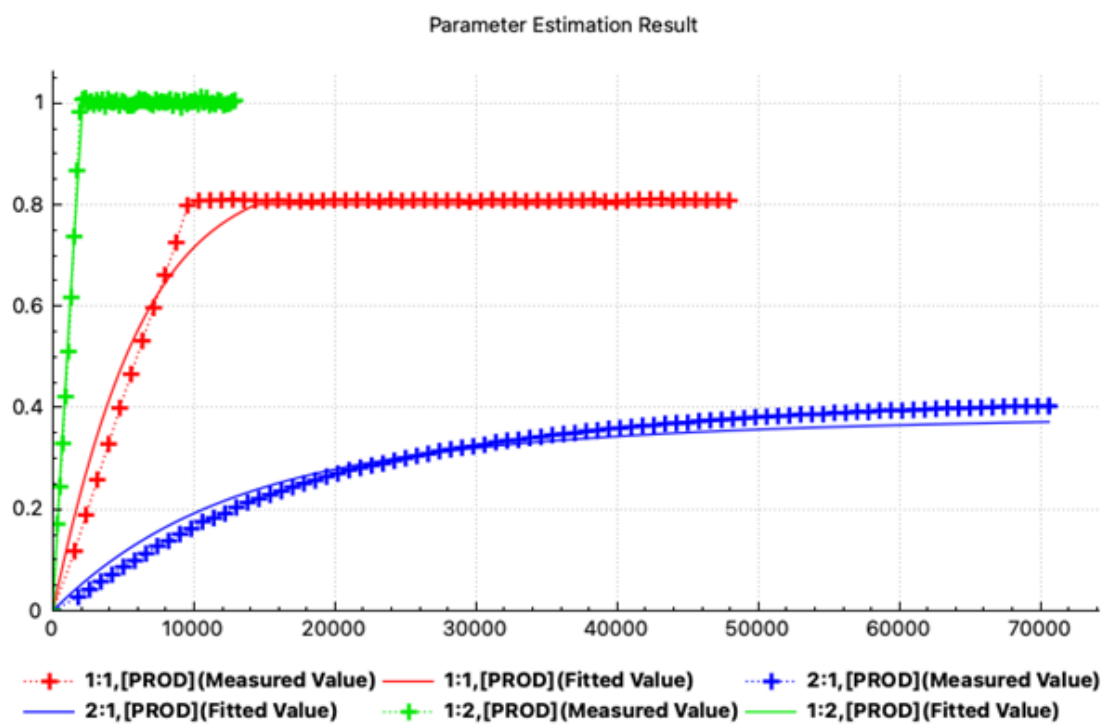


Figure A.6. COPASI simulated models using the Kühn/Girolami model that requires two equivalents of silane to be involved in the catalytic cycle. [cat **1b**] = 2.5×10^{-6} M. Concentrations as detailed in Figure 4.47.

Abbreviations

Å	Angstrom
acac	acetylacetonate
AIPE	aggregation-induced phosphorescent emission
Ar	aryl
bpy	2,2'-bipyridine
calc.	calculated
[cat]	catalyst
COD	1,5-cyclooctadiene
COSY	correlation spectroscopy
Cp	cyclopentadienyl
CTX	2-chlorothioxanthen-9-one
Cy	cyclohexyl
δ	chemical shift in ppm
d	doublet
dba	dibenzylideneacetone
DBCOT	dibenzo[<i>a,e</i>]cyclooctatetraene
dcm	dichloromethane
DFT	density functional theory
DLS	dynamic light scattering
dms	dimethyl sulphide
DMS	vinyl-terminated polydimethylsiloxane
dmso	dimethyl sulfoxide
DSC	differential scanning calorimetry
dvtms	1,3-divinyl-1,1,3,3-tetramethyldisiloxane
EIE	equilibrium isotope effect
equiv.	equivalents
ESI-MS	electrospray ionisation mass spectrometry
Et	ethyl
EXAFS	extended X-ray absorption fine structure
FPT	freeze-pump-thaw
g	gram(s)
HAT	hydrogen atom transfer
hfac	hexafluoroacetylacetonate
HMBC	heteronuclear multiple bond correlation

HMS	methylhydrosiloxane / dimethylsiloxane co-polymer
HSQC	heteronuclear single quantum coherence
Hz	Hertz
ⁱ Pr	isopropyl
IR	infrared spectroscopy
<i>J</i>	coupling constant in Hz
K	Kelvin
<i>k</i>	rate constant
KIE	kinetic isotope effect
LC	ligand centred
LED	light-emitting diode
LLCT	ligand-to-ligand charge transfer
M	mol dm ⁻³
MALLS	multi angle laser light scattering
MD'M	hexamethylsiloxymethylsilane
Me	methyl
ml	millilitre
MLCT	metal-to-ligand charge transfer
mmol	millimole
μmol	micromole
mol%	mole percentage
m/z	mass to charge ratio
nm	nanometre
NBD	norbornadiene
NHC	<i>N</i> -heterocyclic carbene
NMR	nuclear magnetic resonance
NOESY	nuclear Overhauser effect spectroscopy
NTC	nortricyclane
OEt	ethoxy
OMe	methoxy
P-DSC	photo-differential scanning calorimetry
Ph	phenyl
PMHS	polymethylhydrosiloxane
ppb	parts per billion
ppm	parts per million
ppy	2-phenylpyridine
q	quartet

QNMR	quantitative nuclear magnetic resonance spectroscopy
R	generic group
rt	room temperature
s	seconds
sal	salicylaldimine
SEC	size exclusion chromatography
sept	septet
std	standard
t	triplet
TEM	transmission electron microscopy
TGA	thermogravimetric analysis
THF	tetrahydrofuran
TOF	turnover frequency
TON	turnover number
TOF _{app}	apparent turnover frequency
TON _{app}	apparent turnover number
UV	ultraviolet
UV-vis	ultraviolet-visible spectroscopy
VE	valence electron
VTMOS	vinyltrimethoxysilane
VTMS	vinyltrimethylsilane
W	watt
°C	degrees Celsius

References

1. D. Troegel and J. Stohrer, *Coord. Chem. Rev.*, 2011, **255**, 1440-1459.
2. T. K. Meister, K. Riener, P. Gigler, J. Stohrer, W. A. Herrmann and F. E. Kühn, *ASC Catal.*, 2016, **6**, 1274-1284.
3. R. J. Hofmann, M. Vlatkovic and F. Wiesbrock, *Polymers.*, 2017, **9**.
4. Y. Nakajima and S. Shimada, *RSC Adv.*, 2015, **5**, 20603-20616.
5. A. V. Radchenko and F. Ganachaud, *Ind. Eng. Chem. Res.*, 2022, **61**, 7679-7698.
6. L. N. Lewis, J. Stein, Y. Gao, R. E. Colborn and G. Hutchins, *Platinum Met. Rev.*, 1997, **41**, 66.
7. A. K. Roy, *Adv. Organomet. Chem.*, 2007, **55**, 1-59.
8. T. Galeandro-Diamant, M.-L. Zanota, R. Sayah, L. Veyre, C. Nikitine, C. d. Bellefon, S. Marrot, V. Meille and C. Thieuleux, *Chem. Commun.*, 2015, **51**, 16194-16196.
9. J. Y. Corey, *Chem. Rev.*, 2011, **111**, 863-1071.
10. L. H. Sommer, E. W. Pietrusza and F. C. Whitmore, *J. Am. Chem. Soc.*, 1947, **69**, 188.
11. *US Pat.*, 2637738, 1953.
12. *US Pat.*, 2823218, 1958.
13. J. L. Speier, J. A. Webster and G. H. Barnes, *J. Am Chem. Soc.*, 1957, **79**, 974-979.
14. I. Ojima, *The Chemistry of Organic Silicon Compounds*, Wiley, 1989.
15. J. C. Saam and J. L. Speier, *J. Am Chem. Soc.*, 1958, **80**, 4104.
16. F. Stoessel, H. Fierz, P. Lerena and G. Kille, *Org. Process Res. Dev.*, 1997, **1**, 428.
17. S. I. K. Kato, Y. Wada, E. Higashi, Y. Suzuki, K. Kubota, K. Nakano and Y. Wada, *J. Chem. Thermodyn.*, 2011, **43**, 1229.
18. *US Pat.*, 3775452, 1973.
19. J. Stein, L. N. Lewis, Y. Gao and R. A. Scott, *J. Am. Chem. Soc.*, 1999, **121**, 3693-3703.
20. I. E. Marko, S. Sterin, O. Buisine, G. Mignani, P. Branland, B. Tinant and J.-P. Declercq, *Science*, 2002, **298**, 204-206.
21. O. Buisine, G. Berthon-Gelloz, J. F. Briere, S. Sterin, G. Mignani, P. Branlard, B. Tinant, J. P. Declercq and I. E. Marko, *Chem. Commun*, 2005, 3856-3858.
22. B. P. Maliszewski, N. V. Tzouras, S. G. Guillet, M. Saab, M. Belis, K. V. Hecke, F. Nahra and S. P. Nolan, *Dalton Trans.*, 2020, **49**, 14673-14679.
23. I. Rodstein, A. Doppiu and V. H. Gessner, *Organometallics.*, 2023, **42**, 1021-1029.
24. X. Wu, G. Ding, W. Lu, L. Yang, J. Wang, Y. Zhang, X. Xie and Z. Zhang, *Org. Lett.*, 2021, **23**, 1434-1439.
25. V. Srinivas, Y. Nakajima, W. Ando, K. Sato and S. Shimada, *Catal. Sci. Technol.*, 2015, **5**, 2081-2084.

26. A. M. Tondreau, C. Carmen, H. Atienza, K. J. Weller, S. A. Nye, K. M. Lewis, J. G. P. Delis and P. J. Chirik, *Science*, 2012, **335**, 567-570.
27. A. Gorczyński, M. Zaranek, S. Witomska, A. Bocian, A. R. Stefankiewicz, M. Kubicki, V. Patroniak and P. Pawluć, *Catal. Commun.*, 2016, **78**, 71-74.
28. A. D. Ibrahim, S. W. Entsminger, L. Zhu and A. R. Fout, *ACS Catal.*, 2016, **6**, 3589-3593.
29. H. Maciejewski, B. Marciniec and I. Kownacki, *J. Organomet. Chem.*, 2000, **597**, 175.
30. I. Buslov, J. Becouse, S. Mazza, M. Montandon-Clerc and X. Hu, *Angew. Chem.*, 2015, **127**, 14731-14734.
31. L. F. Groux and D. Zargarian, *Organometallics.*, 2003, **22**, 4759-4769.
32. D. Noda, A. Tahara, Y. Sunada and H. Nagashima, *J. Am. Chem. Soc.*, 2016, **138**, 2480-2483.
33. A. J. Chalk and J. F. Harrod, *J. Am Chem. Soc.*, 1965, **87**, 16-21.
34. S. Sakaki, M. Ogawa, Y. Musashi and T. Arai, *J. Am Chem. Soc.*, 1994, **116**, 2844.
35. G. Giorgi, F. D. Angelis, N. Re and A. Sgmaellotti, *J. Mol. Struct.: THEOCHEM*, 2003, **623**, 277.
36. W. J. Ryan and J. L. Speier, *J. Am Chem. Soc.*, 1964, **86**, 895.
37. R. H. Crabtree and D. R. Anton, *Organometallics.*, 1983, **2**, 855.
38. P. Steffanut, J. A. Osborn, A. DeCian and J. Fisher, *Chem. Eur. J.*, 1998, **4**, 2008.
39. Z. V. Belyakova, E. A. Chernyshev, P. A. Storozhenko, P. S. Knyazev, G. N. Turkel'taub, E. V. Parshina and A. V. Kisin, *Russ. J. Gen. Chem.*, 2006, **76**.
40. T. W. Hambley, T. Maschmeyer and A. F. Masters, *Organomet. Chem.*, 1992, **6**, 253-260.
41. W. Caseri and S. P. Pregosin, *Organomet. Chem*, 1988, **356**, 259-269.
42. J. Y. Corey and J. Braddock-Wilking, *Chem. Rev.*, 1999, **99**, 175-292.
43. R. J. Puddephatt, *Coord. Chem. Rev.*, 2001, 157-185.
44. J. C. Mitchener and M. S. Wrighton, *J. Am Chem. Soc.*, 1981, **103**, 975.
45. P. Braunstein and M. Knorr, *J. Organomet. Chem.*, 1995, **500**, 21.
46. F. Seitz and M. S. Wrighton, *Angew. Chem. Int. Ed. Engl.*, 1988, **27**, 289.
47. C. L. Reichel and M. S. Wrighton, *Inorg. Chem.*, 1980, **19**, 3858.
48. S. B. Duckett and R. N. Perutz, *Organometallics*, 1992, **11**, 90.
49. D. M. Haddleton and R. N. Perutz, *J. Chem. Soc., Chem. Commun.*, 1985, 1372.
50. A. Millan, M. J. Fernandez, P. Bentz and P. M. Maitlis, *J. Mol. Catal.*, 1984, **26**, 89.
51. A. Millan, E. Towns and P. M. Maitlis, *Chem. Commun.*, 1981, 673.
52. L. A. Oro, M. J. Fernandez, M. A. Esteruelas and M. S. Jimenez, *J. Mol. Catal.*, 1986, **37**, 151.
53. M. Brookhart and B. E. Grant, *J. Am Chem. Soc.*, 1993, **115**, 2151.
54. L. D. Boardman, *Organometallics.*, 1992, **11**, 4194-4201.

55. J. L. Speier, *Adv. Organomet. Chem.*, 1979, **17**, 407.
56. U. Schubert, *Transition Met. Chem.*, 1991, **16**, 136.
57. X.-L. Luo, G. J. Kubas, C. J. Burns, J. C. Bryan and C. J. Unkefer, *J. Am Chem. Soc.*, 1995, **117**.
58. S. Sakaki and M. Ieki, *J. Am Chem. Soc.*, 1993, **115**, 2373.
59. C. J. Levy and R. J. Puddephatt, *Organometallics.*, 1995, **14**, 5019-5020.
60. S. Roy, R. J. Puddephatt and J. D. Scott, *Dalton Trans.*, 1989, 2121.
61. K. Ackermann, J. Muller, G. Scholz, U. Schubert and B. Worle, *J. Organomet. Chem.*, 1986, **306**, 303.
62. U. Schubert, *Adv. Organomet. Chem.*, 1990, **30**, 151.
63. P. M. Bailey, P. O. Bentz, M. J. Fernandez, T. F. Koetzle and P. M. Maitlis, *J. Am Chem. Soc.*, 1984, **106**, 5458.
64. J. M. Asensio, D. Bouzouita, P. W. N. M. v. Leeuwen and B. Chaudret, *Chem. Rev.*, 2019.
65. L. N. Lewis, *J. Am Chem. Soc.*, 1990, **112**, 5998-6004.
66. L. N. Lewis and R. J. Uriarte, *Organometallics.*, 1990, **9**, 621-625.
67. E. E. Finney and R. G. Finke, *Inorg. Chim. Acta.*, 2006, **359**, 2879-2887.
68. M. A. Brook, H. A. Ketelson, F. J. LaRonde and R. Pelton, *Inorg. Chim. Acta.*, 1997, **264**, 124-135.
69. B. P. S. Chauhan and J. S. Rathore, *J. Am Chem. Soc.*, 2005, **127**, 5790-5791.
70. Y. Bai, S. Zhang, Y. Deng, J. Peng, J. Li, Y. Hu, X. Li and G. Lai, *J. Colloid. Interface Sci.*, 2013, **394**, 428-433.
71. M. R. Buchner, B. Bechlars and K. Ruhland, *J. Organomet. Chem.*, 2013, **744**, 60-67.
72. L. Ibáñez-Ibáñez, A. Lázaro, C. Mejuto, M. Crespo, C. Vicent, L. Rodríguez and J. A. Mata, *J. Catal.*, 2023, **428**, 115155.
73. S. Liu and G. S. Girolami, *J. Am Chem. Soc.*, 2021, **143**, 17492-17509.
74. M. N. Jagaeesh, W. Thiel, J. Kohler and A. Fehn, *Organometallics.*, 2002, **21**, 2076-2087.
75. *EU Pat.*, 3606665B1, 2018.
76. M. Moro, P. Zardi, M. Rossi and A. Biffis, *Catalysts*, 2022, **12**, 307.
77. A. L. Prignano and W. C. Trogler, *J. Am Chem. Soc.*, 1987, **109**, 3586-3595.
78. T. Mayer, D. Burget, G. Mignani and J. P. Fouassier, *J. Polym. Sci. A*, 1996, **34**, 3141-3146.
79. F. D. Lewis and G. D. Salvi, *Inorg. Chem.*, 1995, **34**, 3182-3189.
80. A. W. Adamson, W. L. Waltz, E. Zinato, D. W. Watts, P. D. Fleischauer and R. D. Lindholm, *Chem. Rev.*, 1968, **68**, 541-585.
81. R. S. Paonessa, A. L. Prignano and W. C. Trogler, *Organometallics*, 1985, **4**, 647-657.
82. M. Ciriano, M. Green, J. A. K. Howard, J. Proud, J. L. Spencer, F. G. A. Stone and C. A. Tsipis, *J. Chem. Soc., Dalton Trans.*, 1978, 801-808.

83. G. M. Whitesides, M. Hackett, R. L. Brainard, J. P. M. Lavalleye, A. F. Sowinski, A. N. Izumi, S. S. Moore, D. W. Brown and E. M. Staudt, *Organometallics.*, 1985, **4**, 1819.
84. F. Wang, W. Xiaosong, A. A. Pinkerton, P. Kumaradhas and D. C. Neckers, *Inorg. Chem.*, 2001, **40**, 6000-6003.
85. B. E. Fry, A. Guo and D. C. Neckers, *J. Organomet. Chem.*, 1997, 7003.
86. G. B. Zhang, J. Kong, X. D. Fan, X. G. Li, W. Tian and M. R. Huang, *Appl. Organometal. Chem.*, 2009, **23**, 277-282.
87. J. A. Creighton and D. G. Eadon, *Faraday Trans.*, 1991, **87**, 3881.
88. V. Jakubek and A. J. Lees, *J. Inorg. Chem.*, 2004, **43**, 6869-6871.
89. S. Marchi, M. Sangermano, P. Meier and X. Kornmann, *J. Photochem. Photobiol. Chem.*, 2015, **303**, 86-90.
90. *US Pat.*, 4510094A, 1985.
91. J. V. Crivello and M. Jang, *J. Photoch. Photobio. A Chem.*, 2003, **159**, 173.
92. L. Xi, Z. Liu, J. Su, Y. Bei, H. Xiang and X. Lio, *J. Appl. Polym. Sci.*, 2019, **136**, 48251.
93. J. V. Obligation and P. J. Chirik, *Nat. Rev. Chem.*, 2018, **2**, 15-34.
94. J. L. Speier, J. A. Webster and G. H. Barnes, *J. Am Chem. Soc.*, 1957, **79**, 974-979.
95. C. J. Kong, S. E. Gilliland, B. R. Clark and B. F. Gupton, *Chem. Commun.*, 2018, **54**, 13343-13346.
96. D. A. D. Vekki, *Russ. J. Gen. Chem.*, 2011, **81**, 1480-1492.
97. T. Lippert, J. Dauth, B. Deubzer, J. Weis and A. Wokaun, *Radiat. Phys. Chem.*, 1996, **47**, 889-897.
98. H. Watanabe, T. Kitahara, T. Motegi and Y. Nagai, *J. Organomet. Chem.*, 1977, **139**, 215-222.
99. T. Muraoka, I. Matsuda and K. Itoh, *Tetrahedron Lett.*, 1998, **39**, 7325-7328.
100. I. Ojima, M. Nihonyanagi and Y. Nagai, *Chem. Commun.*, **1972**, 938.
101. J. Matthey, Price Charts., <https://matthey.com/products-and-markets/pgms-and-circularity/pgm-management>, (accessed January 9th 2024).
102. J. Stein, L. N. Lewis, Y. Gao and R. A. Scott, *J. Am Chem. Soc.*, 1999, **121**, 3693.
103. L. N. Lewis and N. Lewis, *J. Am Chem. Soc.*, 1986, **108**, 7228-7231.
104. I. E. Marko, S. Sterin, O. Buisine, G. Berthon, G. Michaud, B. Tinant and J. P. Declercq, *Adv. Synth. Catal.*, 2004, **346**, 1429-1434.
105. B. P. Maliszewski, T. A. C. A. Bayrakdar, P. Lambert, L. Hamdouna, X. Trivelli, L. Cavallo, A. Poater, M. Belis, O. Lafon, K. V. Hecke, D. Ormerod, C. S. J. Cazin, F. Nahra and S. P. Nolan, *Chem. Eur. J.*, 2023, **29**, 40.
106. J. Zheng, S. Elangovan, D. A. Valyaev, R. Brousses, V. Cesar, J.-B. Sortais, C. Darcel, N. Lugan and G. Lavigne, *Adv. Synth. Catal.*, 2014, **356**, 1093-1097.

107. D. Kumar, A. P. Prakasham, L. P. Bheeter, J.-B. Sortais, M. Gangwar, T. Roisnel, A. C. Kalita, C. Darcel and P. Ghosh, *J. Organomet. Chem.*, 2014, **762**, 81-87.
108. *EU Pat.*, EP3862405A1, 2021.
109. *EU Pat.*, EP3868836A1, 2021.
110. *US Pat.*, US20210179783A1, 2021.
111. F. Wang, X. Wu, A. A. Pinkerton, P. Kumaradhas and D. C. Neckers, *Inorg. Chem.*, 2001, **40**, 6000-6003.
112. D. A. d. Vekki and N. K. Skvortsov, *Russ. J. Gen. Chem.*, 2006, **76**, 119-124.
113. S. Lin, H. Pan, L. Li, R. Liao, S. Yu, Q. Zhao, H. Sun and W. Huang, *J. Mater. Chem. C.*, 2019, **7**, 7893.
114. S. Liu, H. Sun, Y. Ma, S. Ye, X. Liu, X. Zhou, X. Mou, L. Wang, Q. Zhao and W. Huang, *J. Mater. Chem.*, 2012, **22**, 22167-22173.
115. C. M. Manna, A. Kaur, L. M. Yablon, F. Haeffner, B. Li and J. A. Byers, *J. Am Chem. Soc.*, 2015, **137**, 14232-14235.
116. Q. Zhao, C. Huang and F. Li, *Chem. Soc. Rev.*, 2011, **40**, 2508-2524.
117. V. Guerschais and J.-L. Fillaut, *Coord. Chem. Rev.*, 2011, **255**, 2448-2457.
118. J. J. Zhong, C. Yang, X. Y. Chang, C. Zou, W. Lu and C. M. Che, *Chem. Commun.*, 2017, **53**, 8948-8951.
119. J. Brooks, Y. Babayan, S. Lamansky, P. I. Djurovich, I. Tsyba, R. Bau and M. E. Thompson, *Inorg. Chem.*, 2002, **41**, 3055-3066.
120. A. Santoro, A. C. Whitwood, J. A. G. Williams, V. N. Kozhevnikov and D. W. Bruce, *Chem. Mater.*, 2009, **21**, 3871-3882.
121. N. Godbert, T. Pugliese, I. Aiello, A. Bellusci, A. Crispini and M. Ghedini, *Eur. J. Inorg. Chem.*, 2007, **32**, 5105-5111.
122. C. P. Newman, K. Casey-Green, G. J. Clarkson, G. W. V. Cave, W. Errington and J. P. Rourke, *Dalton Trans.*, 2007, 3170-3182.
123. T. Liu, Y. Chen, D. Tan and F. Han, *J. Organomet. Chem.*, 2022, **977**.
124. M. S. More, P. G. Joshi, Y. K. Mishra and P. K. Khanna, *Mater. Today Chem.*, 2019, **14**, 100195.
125. K. Upendranath, T. Venkatesh, Y. A. Nayaka, M. Shashank and G. Nagaraju, *Inorg. Chem. Commun.*, 2022, **139**, 109354.
126. M. S. Refat, H. A. Saad, A. A. Gobouri, M. Alsawat, A. M. A. Adam and S. M. El-Megharbel, *J. Mol. Liq.*, 2022, **345**, 117140.
127. P. Altmann, M. Cokoja and F. E. Kuhn, *J. Organomet. Chem.*, 2012, **701**, 51-55.
128. T. S. I. Cassells, A. T. Hutton, S. Prince, G. S. Smith *J. Biol. Inorg. Chem.*, 2018, **23**, 763-774.

129. Y. Belay, A. Muller, D. T. Ndinteh, O. A. Kolawole, S. A. Adeyinka and T. Y. Fonkui, *J. Mol. Struct.*, 2023, **1275**.
130. S. Acharya, M. Maji, R. Raturaj, K. Purkait, A. Gupta and A. Mukherjee, *Inorg. Chem.*, 2019, **58**, 9213-9224.
131. A. Parssinen, T. Luhtanen, M. Klinga, T. Pakkanen, M. Leskela and T. Repo, *Eur. J. Inorg. Chem.*, 2005, **2005**, 2100-2109.
132. S. Y. Li, X. B. Wang and L. Y. Kong, *Eur. J. Med. Chem.*, 2014, **71**, 36-45.
133. J. Zhang, L. Wang, A. Zhong, G. Huang, F. Wu, D. Li, M. Teng, J. Wang and D. Han, *Dyes Pigm.*, 2019, **162**, 590-598.
134. J. L. Serrano, L. Garcia, J. Perez, E. Perez, J. Garcia, G. Sanchez, G. Lopez and M. Liu, *Eur. J. Inorg. Chem.*, 2008, **2008**, 4797-4806.
135. M. N. Jagadeesh, W. Thiel, J. Kohler and A. Fehn, *Organometallics*, 2002, **21**, 2076-2087.
136. L. Gambut and L. Garel, *Recent Res. Dev. Org. Chem.*, 2000, **4**, 121-131.
137. L. N. Lewis, J. Stein, Y. Gao, R. E. Colborn and G. Hutchins, *Platinum Metals Rev.*, 1997, **41**, 66-75.
138. L. N. Lewis, J. Stein, R. E. Colborn, Y. Gao and J. Dong, *J. Organomet. Chem.*, 1996, **521**, 221-227.
139. F. Faglioni, M. Blanco, W. A. Goddard and D. Saunders, *J. Phys. Chem. B*, 2002, **106**, 1714-1721.
140. *EU Pat.*, EP0761759, 2003.
141. *EU Pat.*, EP0602638, 1996.
142. *EU Pat.*, EP0994159, 2001.
143. L. Xi, Z. Liu, J. Su, Y. Bei, H. Xiang and X. Lio, *J. Appl. Polym. Sci.*, 2019, DOI: 10.1002/APP.48251.
144. Z. Xue, J. Strouse, D. K. Shuh, C. B. Knobler, H. D. Kaesz, R. F. Hicks and R. S. Williams, *J. Am Chem. Soc.*, 1989, **111**, 8779.
145. Y. Ben-Tal, P. J. Boaler, H. J. A. Dale, R. E. Dooley, N. A. Fohn, Y. Gao, A. Garcia-Dominguez, K. M. Grant, A. M. R. Hall, H. L. D. Hayes, M. M. Kucharski, R. Wei and G. C. Lloyd-Jones, *Prog. Nucl. Magn. Reson. Spectosc.*, 2022, **129**, 28-106.
146. C. H. Cullen, G. J. Ray and C. M. Szabo, *Magn. Reson. Chem.*, 2013, **51**, 705-713.
147. S. K. Bharti and R. Roy, *Trends Anal. Chem.*, 2012, **35**, 5-26.
148. J. R. Pankhurst, M. Curcio, S. Sproules, G. C. Lloyd-Jones and J. B. Love, *Inorg. Chem.*, 2018, **57**, 5915-5928.
149. C. P. Johnston, T. H. West, R. E. Dooley, M. Reid, A. B. Jones, E. J. King, A. G. Leach and G. C. Lloyd-Jones, *J. Am Chem. Soc.*, 2018, **140**, 11112-11124.
150. M. P. Robinson and G. C. Lloyd-Jones, *ACS Catal.*, 2018, **8**, 7484-7488.

151. F. Susanne, D. S. Smith and A. Codina, *Org. Process Res. Dev.*, 2012, **16**, 61-64.
152. A. M. R. Hall, J. C. Chouler, A. Codina, P. T. Gierth, J. P. Lowe and U. Hintermair, *Catal. Sci. Technol.*, 2016, **6**, 8406-8417.
153. T. Bartik, B. Bartik, B. E. Hanson, T. Glass and W. Bebout, *Inorg. Chem.*, 1992, **31**, 2667-2670.
154. D. A. Foley, A. L. Dunn and M. T. Zell, *Magn. Reson. Chem.*, 2016, **54**, 451-456.
155. B. Wrackmeyer, E. Khan, S. Bayer, O. L. Tok, E. V. Klimkina, W. Milius and R. Kempe, 2010, **65**, 725-744.
156. H. Primasova, P. Bigler and J. Furrer, *Annu. Rep. NMR Spectrosc.*, 2017, **92**.
157. J. F. Sonnenberg and R. H. Morris, *Catal. Sci. Technol.*, 2014, **4**, 3426-3438.
158. A. J. Holwell, *Platinum Metals Rev.*, 2008, **52**, 243-246.
159. B. P. Maliszewski, E. Casillo, P. Lambert, F. Nahra, C. S. J. Cazin and S. P. Nolan, *Chem. Commun.*, 2023, **59**, 14017.
160. A. Vivien, L. Veyre, R. Mirgalet, C. Camp and C. Thieuleux, *Green Chem.*, 2023, **25**, 7721-7728.
161. R. A. Benkeser and J. J. Kong, *J. Organomet. Chem.*, 1980, **185**, 9.
162. H. G. Kuivila and C. R. Warner, *J. Org. Chem.*, 1964, **29**, 2845-2851.
163. M. A. Guseva, D. A. Alentiev, E. V. Bermesheva, I. A. Zamilatskov and M. V. Bermeshev, *RSC Adv.*, 2019, **9**, 33029-33037.
164. V. Cesar, S. Bellemin-Laponnaz and L. H. Gade, *Chem. Soc. Rev.*, 2004, **33**, 619-636.
165. G. Z. Zheng and T. H. Chan, *Organometallics*, 1995, **14**, 70-79.
166. T. Luchs, P. Lorenz and A. Hirsch, *ChemPhotoChem*, 2020, **4**, 52-58.
167. M. F. Rettig and R. S. Drago, *J. Am Chem. Soc.*, 1969, **91**, 1361-1370.
168. R. B. King and F. G. A. Stone, *Inorg. Synth.*, 1963, **7**, 99-101.
169. S. Marchi, M. Sangermano, P. Meier and X. Kornmann, *Macromol. React. Eng.*, 2015, **9**, 360-365.
170. J. A. Widegreen and R. G. Finke, *J. Mol. Catal. A: Chem.*, 2003, **198**, 317.
171. C. A. Jaska and I. Manners, *J. Am Chem. Soc.*, 2004, **126**, 9776-9785.
172. R. M. Laine, *J. Mol. Catal.*, 1982, **14**, 137.
173. Y. Lin and R. G. Finke, *Inorg. Chem.*, 1994, **33**, 4891-4910.
174. M. A. Watzky and R. G. Finke, *J. Am Chem. Soc.*, 1997, **119**, 10382-10400.
175. J. Huang, Z. Liu, X. Liu, C. He, S. Y. Chow and J. Pan, *Langmuir.*, 2005, **21**, 699-704.
176. L. N. Lewis and N. Lewis, *J. Am Chem. Soc.*, 1986, **108**, 7228-7231.
177. M. J. Russell, C. White and P. M. Maitlis, *J. Chem. Soc., Chem. Commun.*, 1977, 427.
178. R. H. Crabtree, M. F. Mellea, J. M. Mihelcic and J. M. Quirk, *J. Am Chem. Soc.*, 1982, **104**, 107.

179. G. M. Whitesides, M. Hackett, R. L. Brainard, J. P. P. M. Lavelleye, A. F. Sowinski, A. N. Izumi, S. S. Moore, D. W. Brown and E. M. Staudt, *Organometallics.*, 1985, **4**, 1819-1830.
180. C. Paal and W. Hartmann, *Chem. Ber.*, 1918, **51**, 711.
181. K. A. Johnson, *Polymer Preprints.*, 2000, **41**, 1525.
182. L. N. Lewis, R. J. Uriarte and N. Lewis, *J. Catal.*, 1991, **127**, 67-74.
183. A. K. Roy and R. B. Taylor, *J. Am Chem. Soc.*, 2002, **124**, 9510-9524.
184. E. E. Ondar, J. V. Burykina and V. P. Ananikov, *Catal. Sci. Technol.*, 2022, **12**, 1173-1186.
185. A. Hopf and K. H. Dotz, *J. Mol. Catal. A.*, 2000, **164**, 191.
186. J. W. Sprengers, M. J. Agerbeek and C. J. Elsevier, *Organometallics.*, 2004, **23**, 3117.
187. X. Coqueret and G. Wegner, *Organometallics.*, 1991, **10**, 3139.
188. J. Stein, L. N. Lewis, K. A. Smith and K. X. Lettko, *J. Inorganomet. Polym.*, 1991, **1**, 325.
189. J. W. Sprengers, M. J. Mars, M. A. Duin, K. J. Cavell and C. J. Elsevier, *J. Organomet. Chem.*, 2003, **679**, 149-152.
190. M. I. Rybinskaya, L. V. Rybin and A. A. Pogrebnyak, *J. Organomet. Chem.*, 1981, **217**, 373-383.
191. L. L. J. Stein, Yan Gao, R. A. Scott, *J. Am Chem. Soc.*, 1999, **121**, 3693.
192. S. Hoops, S. Sahle, R. Gauges, C. Lee, J. Pahle, N. Simus, M. Singhal, L. Xu, P. Mendes and U. Kummer, *Bioinformatics*, 2006, **22**, 3067-3074.
193. C. Alamillo-Ferrer, G. Hutchinson and J. Bures, *Nature Rev. Chem.*, 2023, **7**, 26-34.
194. J. T. W. Bray, M. J. Ford, P. B. Karadakov, A. C. Whitwood and I. J. S. Fairlamb, *React. Chem. Eng.*, 2019, **4**, 122-130.
195. C. N. Brodie, T. M. Boyd, L. Sotorrios, D. E. Ryan, E. Magee, S. Huband, J. S. Town, G. C. Lloyd-Jones, D. M. Haddleton, S. A. Macgregor, A. S. Weller and *J. Am Chem. Soc.*, 2021, **143**, 21010-21023.
196. B. E. Fry and D. C. Neckers, *Macromol.*, 1996, **29**, 5306-5312.
197. L. H. Do, J. A. Labinger and J. E. Bercaw, *ACS Catal.*, 2013, **3**, 2582-2585.
198. B. L. Greene, G. E. Vansuch, B. C. Chica, M. W. W. Adams and R. B. Dyer, *Acc. Chem. Res.*, 2017, **50**, 2718-2726.
199. K. L. Lee, *Angew. Chem.*, 2017, **56**, 3665-3669.
200. C. Cheng and J. F. Hartwig, *J. Am Chem. Soc.*, 2014, **136**, 12064-12072.